Advanced Computational Fluid Dynamics models for liquid metal flows

Candidato: FILIPPO MENGHINI

Coordinatore Dottorato:

PROF. VINCENZO PARENTI CASTELLI

Relatore:

PROF. SANDRO MANSERVISI

Contents

Abstract

In this thesis it is shown the development, implementation and numerical solution of several computational fluid dynamics models for the study of liquid metal flows. The work is organized in two main parts in which different modeling techniques are analyzed. These two parts are introduced by a brief chapter on the finite element methods and on the computational platform developed during the Ph.D. studies which have been the basis for the implementation and numerical solution of all the developed mathematical models.

In the first part, turbulence modeling based on Reynolds Averaged Navier Stokes equations is considered for the study of turbulent heat transfer in liquid metal flows. A new four parameter turbulence model is introduced and validated in two different k-ϵ and k-ω formulations. Several results in four geometries interesting for the fast nuclear reactor field are reported in order to assess and prove the feasibility of this model for the study of turbulent heat transfer in liquid metal flows.

In the second part the adjoint optimal control theory is introduced. Some numerical cases are presented by solving the optimality system with state and adjoint variables. The first application is a temperature boundary optimal control in which an improved way of setting boundary conditions in weak form has been developed. The second application is a distributed optimal control problem for the RANS system. Numerical simulations in two and three dimensions have been carried on for this type of applications and are reported in the final chapter.

Introduction

The study of computational methods for solving numerical approximation of partial differential equations dates back in the second half of the last century, when finite differences solvers have first been implemented in computers to solve simple differential equations. Since then the use of computational methods steadily increased among universities and companies with the growing computational power. At the present time, simulation and modeling are commonly used by physicist, mathematicians and engineers with applications ranging from the understanding of basic physical phenomena, to the study of complex equation properties, to design and optimization of engineering devices. The high computational power available nowadays allows to improve and study accurately complex systems that a few years ago could only be studied with experimental tests on prototypes. It is easy to understand that in the future, simulation of physical systems will become always more important for engineering design, biomedical applications and basic scientific research. However many problems remain open and there is still a strong need of models to overcome the complexity of the real engineering problems.

One of the main issues in computational fluid-dynamics is the presence of turbulence in the vast majority of simulated flows. With few exceptions in some narrow application fields, nearly all the flows in nature and engineering are turbulent. It is well known that the Navier-Stokes system of equations can reproduce the onset of turbulence as instabilities on the flow due to the non-linear advection term. Turbulent fields are characterized by random fluctuations of the variables around an average value. The intensity and frequency of these fluctuations can vary a lot depending on the specific flow and physical properties of the fluid. To properly account for all the instabilities in the flow it is necessary to compute the fluid flow with a mesh size that can resolve the scales of the smallest eddies, namely the Kolmogorov scales. At these scales the energy of the fluid flow is dissipated into heat by the molecular viscosity of the fluid. The Kolmogorov length scale is

$$\eta = \left(\frac{\nu^3}{\epsilon} \right)^{1/4}$$

3

where ν is the molecular kinematic viscosity of the fluid and ϵ is the average rate of dissipation of turbulence kinetic energy. This length scale can vary much among different flows and in different flowing regions. For example, in an atmospheric flow where the large eddies have length scales on the order of kilometers the Kolmogorov scale is around 1 millimeter. This example suggests that with current available computational resources and also in the near future it will not be possible to resolve numerically all the turbulent flow important details. Direct Numerical Simulation (DNS) of turbulent flows are becoming important and may be employed to study simple and low Reynolds number flows with the purpose to better understand the physical processes involved in the development of turbulence and of flow instabilities.

Many methods have been developed to address the turbulence simulation in fluid flows. A very popular one in engineering is the use of a turbulence model based on Reynolds Averaged Navier-Stokes (RANS) closure. In these models the fields of Navier-Stokes system are split into fluctuating and steady parts and then an averaging process is performed on the equations. The resulting system is solved for the averaged fields and turbulence is taken into account by introducing average tensor quantities which are functions of the fluctuating fields. Another method which is considered for the solution of turbulent flows is the Large Eddy Simulation. In this approach a sub-grid model is used and the numerical mesh needs to be fine enough to resolve the flow large eddies. The smallest eddies are considered to be independent on the flow so that they can be modeled in the same way for any geometry and type of flow. In recent years the use of hybrid RANS-LES models started to grow in order to improve the accuracy of the firsts and enhancing the applicability of the last ones.

In the framework of RANS modeling the turbulent heat flux $\mathbf{q}_\theta$ is usually computed by mean of an eddy thermal diffusivity as

$$\mathbf{q}_\theta = -\alpha_t \, \nabla T \, .$$

By defining the turbulent Prandtl number $Pr_t = \nu_t/\alpha_t$, where ν_t is the eddy viscosity, and assigning a constant value to Pr_t it is straightforward to compute the turbulent heat flux from the above definition. Unfortunately the hypothesis of a constant turbulent Prandtl number relies on a similarity between the dynamical and thermal turbulence which does not hold for fluids with low-Prandtl number, as it is shown later. In this thesis it is reported the development and validation of a four parameter turbulence model for liquid metal flows that takes into account dissimilarities between the dynamical and thermal time scales of turbulence. This is necessary because liquid metals are characterized by a high thermal conductivity and low viscosity, thus resulting in a very low Prandtl number.

Liquid metal flows have also the property of being responsive to electromagnetic fields. In theory a liquid metal flow could be controlled from the environment by applying electromagnetic forces on the fluid, as it is done in plasma technologies for nuclear fusion. With this approach different objectives could be obtained such as a deviation of the flow towards a chosen direction. However, the effects of a force applied on a complex fluid flow could be difficult to predict and understand. In particular this is true when complex objectives such as re-laminarization or increase in the heat exchange are chosen. The use of adjoint optimal control theory to treat these problems could lead to great improvements in the design and optimization of engineering devices. This technique can be used also in the design of heat exchanger or mixer when a certain temperature needs to be obtained in a certain region of the domain. In these cases it is usually possible to apply heat fluxes on the walls or to inject fluid with a certain temperature in some parts of the domain. These are typical problems to be solved through inverse or adjoint techniques. This thesis contains a brief summary of adjoint optimal control theory, which is used to solve some design problems such as the ones described above. In particular we focus on thermal and dynamical problems by studying a boundary optimal control for the energy equation and a distributed optimal control for the RANS system.

The thesis is divided in two main parts dealing with the two main subjects just described. The first part is devoted to turbulent heat transfer computations in heavy liquid metal flows by assessing the turbulence modeling needed in this problem. In the second part we study adjoint optimal control problems for the energy equation and for the RANS system closed with a two-equation turbulence model.

Chapter 1

Mathematical and finite elements notation

In this work advanced Computational Fluid Dynamics models are studied to analyze liquid metal flows and heat transfer. These models have been developed in the framework of a computational platform in which the numerical algorithms obtained with a Finite Element Method discretization have been implemented.

The Finite Element Method is a powerful tool used to solve numerically boundary value problems based on Partial Differential Equations. By applying this method to a continuous boundary value problem on a defined domain it is possible to obtain a system of algebraic equations that, once solved, gives an approximated solution to the continuous problem over a finite number of degrees of freedom. This class of numerical methods has been used first to solve structural mechanics problems and then gradually they have been employed in all the fields where mathematical models are based on PDEs, such as heat transfer, fluid-dynamics, diffusion-reaction problems, and many others. The Finite Element Methods are based on a solid mathematical background, for a comprehensive review on this subject the interested reader is referred to [20, 39, 51, 85, 115, 116, 117].

In this Chapter we aim at giving some basic notations about the Finite Element Methods. In the first Section of this Chapter we give a brief description of the computational platform that is being developed in our research group. This platform is based on finite element solvers and it allows the coupling with external codes to solve multi-scale and multi-physics problems. External codes are used when the solver cannot be developed inside the platform or it is better to use well tested software like one-dimensional system codes for nuclear power plant design. In the second Section some notations about function spaces are given. In the third Section the weak form of the

energy and Navier-Stokes system of equations are derived. In the fourth Section some Lagrangian Finite Elements are described together with their shape functions and in the last Section a few considerations on the numerical errors arising in the finite element discretization process are given.

1.1   The FEM computational platform

The computational platform used and developed in this thesis is based on a C++ main program that handles several external open source libraries. The *libmesh* library is a C++ finite element library used in our computational platform to generate and handle the numerical mesh and to refine it with multiple levels [64]. The Portable, Extensible Toolkit for Scientific Computation (*PETSc*) is a C++ library for linear and non-linear algebra developed using *LASPack* cores written in Fortran and other solvers. A key feature of this library is its ability to handle parallel solutions of systems of equations with solvers designed to scale very well with the increasing number of nodes by defining parallel vectors and matrices classes [12, 13, 14]. By using *OpenMPI* parallel applications together with *PETSc* library we can solve complex numerical problems with a high number of nodes [37]. The HDF5 suite comprises a data model, file format, API, library, and tools used to handle large data sets in binary format. Using this data format it is possible to save solutions on mesh composed of several nodes using a quantity of hard disk memory that is order of magnitude smaller than the one required by the simpler text file ASCII format [1]. By using the features of these open source libraries the main program can solve very complex problems with fast parallel computation and small memory requirements relying on *PETSc* and HDF5.

The C++ main program is called *FEMus* which stands for Finite Element MUltigrid Solver. This program is built with hierarchical C++ classes that allow the user to develop its own application and assembly functions without interfering with the main platform. Many users can work on the same installation of *FEMus* and several solvers have been developed until now. These includes a basic Laplacian solver, a transient diffusion-advection equation solver, two Navier-Stokes solvers that implement a fully coupled and a penalty-projection algorithm, different solvers for two and four equation turbulence models, a Fluid-Structure Interaction solver based on a monolithic approach, a Volume of Fluid solver for multiphase flows and the two adjoint optimal control algorithms as reported in Chapters 6 and 7. Since it is possible to couple without effort different physical solvers, this code is capable of multi-physics solutions by coupling the solvers named above. Moreover the

finite element solver is multigrid-based by using *PETSc* solvers as solution kernels of single multigrid steps [11, 15, 19, 73]. The temperature and turbulence model equations are discretized with standard Lagrangian quadratic finite elements. For the Navier-Stokes equations we use Taylor-Hood finite elements which are elements with linear shape functions to approximate the pressure and quadratic shape functions to approximate the velocity, see the spaces definition in Section 1.5. As it is reported in that Section, this is necessary to fulfill the *Inf-Sup* condition (1.36).

The computational platform is being further developed to couple the solution of *FEMus* solvers with external codes solutions. This has been accomplished through the use of *MEDMEM* libraries that are part of the *SALOME* platform [22]. The aim of this project is to simulate multi-scale problems by including dedicated software that has been developed by external groups like the one-dimensional system codes for the simulation of nuclear power plant loops. At the present time the system code *Cathare* is integrated in the platform together with the neutronic codes *Dragon-Donjon* [2, 23]. The coupling can be obtained through the boundary conditions or a volumetric force for the CFD code while for system codes it is better to use a defective approach by using a source term inside specific elements of the loop that simulate the effects of the CFD simulation like pressure drops or heat generation or removal. Multi-scale simulations could lead to great improvements in the study and design of complex systems where some elements need to be simulated with a high resolution CFD code because the one-point or one-dimensional assumptions do not hold [25].

1.2 Function spaces

In this thesis we make use of some notations on functional spaces that are briefly reported here. For a wide discussion on these spaces and their properties the reader is referred to [7, 20].

We define the space of integrable functions at the power n over the domain $\Omega \subset \mathbb{R}^d$, where d is the space dimension of the domain, as

$$L^n(\Omega) = \left\{ f \; : \; \int_\Omega |f(\mathbf{x})|^n d\Omega < \infty \right\} \; . \tag{1.1}$$

It can be easily proven that this space is a vector space, indeed given the linearity of the integral operator the conditions

$$f + g \in L^n(\Omega) \; , \; \alpha f \in L^n(\Omega) \text{ with } f, g \in L^n(\Omega) \text{ and } \alpha \in \mathbb{R} \; , \tag{1.2}$$

are necessary and sufficient to define a vector space and are verified for $L^n(\Omega)$. The space of continuous function over Ω is defined as $C^0(\Omega)$ and the space with continuous derivative until order k over Ω as $C^k(\Omega)$. We can define the space of infinitely differentiable functions that are null on the boundary of Ω as $C_0^\infty(\Omega)$ and we remark that all of these spaces are vector spaces.

In the spaces $C^k(\Omega)$ the derivative is defined in the strong form as

$$f'(x) = \lim_{h \to 0} \frac{f(x+h) - f(x)}{h} , \tag{1.3}$$

but we need a weak form of the derivatives in order to define the Sobolev spaces. We define the first weak derivative $f'(\mathbf{x})$ for a function $f(\mathbf{x})$ defined over Ω as

$$\int_\Omega f'(\mathbf{x}) \, \psi(\mathbf{x}) \, d\Omega = - \int_\Omega f(\mathbf{x}) \, \psi'(\mathbf{x}) \, d\Omega , \qquad \forall \psi(\mathbf{x}) \in C_0^\infty(\Omega) . \tag{1.4}$$

This definition is a natural extension of the strong form for $f(\mathbf{x})$ function differentiable in the standard way, but it opens the possibility to define the derivative also for other functions.

We can now define the space of differentiable functions in weak sense at the order k over the domain Ω as

$$H^k(\Omega) := \left\{ f(\mathbf{x}) \in L^2(\Omega) \; : \; f(\mathbf{x})^l \in L^2(\Omega) \text{ with } l = 1, 2, \ldots, k \right\} \tag{1.5}$$

where $f^l(\mathbf{x})$ is the weak derivative of order l of the function $f(\mathbf{x})$. These spaces are called *Sobolev spaces*. It is easy to see from the definition that $H^0(\Omega) = L^2(\Omega)$.

A *norm* can be defined for a generic vector space $V(\Omega)$ as a functional that couples a function $f(\mathbf{x}) \in V(\Omega)$ with a real number. A norm must satisfy the following properties

$$\|x\| \geq 0 , \; \forall \, x \in V(\Omega) \text{ and } \|x\| = 0 \Leftrightarrow x = 0$$
$$\|\alpha x\| = \alpha \|x\| , \; \forall \, x \in V(\Omega) \text{ and } \alpha \in \mathbb{R}$$
$$\|x + y\| \leq \|x\| + \|y\| , \; \forall \, x, y \in V(\Omega) .$$

For $L^n(\Omega)$ the natural norm can be defined as

$$\|f(\mathbf{x})\|_{L^n} = \left(\int_\Omega f(\mathbf{x})^n d\Omega \right)^{\frac{1}{n}} , \tag{1.6}$$

while for the norm in $H^1(\Omega)$

$$\|f(\mathbf{x})\|_{H^1} = \left(\int_\Omega \left(f(\mathbf{x})^2 + f(\mathbf{x})'^2 \right) d\Omega \right)^{\frac{1}{2}} , \tag{1.7}$$

and so on for the other Sobolev spaces. A vector space endowed with the metric induced by its norm is called a normed linear space. A complete space V is defined as a metric space in which every Cauchy sequence $\{s_j\}$ of elements of V has a limit $s_j \to s \in V$. A *Banach space* is a normed linear space $(V, \|\cdot\|)$ which is complete with respect to the metric induced by its norm. It can be proven that the Sobolev spaces defined above are all Banach spaces with respect to their natural norms.

A *scalar product* in a linear vector space V can be defined as a bilinear symmetric form that couples two elements $a(\mathbf{x}), b(\mathbf{x}) \in V(\Omega)$ with a real number

$$\langle a(\mathbf{x}), b(\mathbf{x}) \rangle : V(\Omega) \times V(\Omega) \to \mathbb{R} \tag{1.8}$$

and with the following properties

$$\langle a(\mathbf{x}), a(\mathbf{x}) \rangle > 0 \ , \ \forall \, a(\mathbf{x}) \neq 0$$
$$\langle a(\mathbf{x}), b(\mathbf{x}) \rangle \ = \ \langle b(\mathbf{x}), a(\mathbf{x}) \rangle \ , \ \forall \, a(\mathbf{x}), b(\mathbf{x}) \in V(\Omega)$$
$$\langle \alpha a(\mathbf{x}) + b(\mathbf{x}), c(\mathbf{x}) \rangle = \alpha \langle a(\mathbf{x}), c(\mathbf{x}) \rangle + \langle b(\mathbf{x}), c(\mathbf{x}) \rangle \ ,$$
$$\forall \, a(\mathbf{x}), b(\mathbf{x}), c(\mathbf{x}) \in V(\Omega) \text{ and } \alpha \in \mathbb{R} \ .$$

It is easy to define a scalar product for the space $L^2(\Omega)$ that satisfies these properties as

$$\langle f(\mathbf{x}), g(\mathbf{x}) \rangle_{L^2} = \int_\Omega f(\mathbf{x}) g(\mathbf{x}) \, d\Omega \ , \tag{1.9}$$

and for the space $H^1(\Omega)$

$$\langle f(\mathbf{x}), g(\mathbf{x}) \rangle = \int_\Omega (f(\mathbf{x}) g(\mathbf{x}) + f(\mathbf{x})' g(\mathbf{x})') \, d\Omega \ . \tag{1.10}$$

A norm can be generated naturally by the scalar product as

$$\|f(\mathbf{x})\| = \langle f(\mathbf{x}), f(\mathbf{x}) \rangle^{\frac{1}{2}} \ . \tag{1.11}$$

A function space which is equipped with a scalar product and which is a Banach space with respect to the norm induced naturally by the scalar product is called a *Hilbert space*. A Hilbert space has the important property that, given a basis $\{e_i\}_{i=1}^\infty$ of the space $H(\Omega)$, any element of this space $f \in H(\Omega)$ can be expressed as a convergent series

$$f = \sum_{i=1}^\infty \langle f, e_i \rangle e_i \ . \tag{1.12}$$

Using the above definitions for the norm and scalar product of the spaces $L^2(\Omega)$ and $H^k(\Omega)$ it is easy to prove that these spaces are Hilbert spaces. We can define also the dual space of $H_0^k(\Omega)$ as $H^{-k}(\Omega)$ and the trace space for the functions in $H^1(\Omega)$ by $H^{1/2}(\Gamma)$, where $\Gamma = \partial\Omega$.

1.3 Weak formulation

Partial differential equations are equations containing functions and their derivatives of different orders that give local information on how these functions are related. A typical example of a partial differential equation is the heat transfer equation with a thermal source and the heat flux given by Fourier law

$$\nabla \cdot (\lambda \nabla T) + Q = 0 \,, \tag{1.13}$$

where $\lambda = \lambda(\mathbf{x})$ is the heat conductivity of the material, $T = T(\mathbf{x})$ is the temperature and $Q = Q(\mathbf{x})$ is a given source term. This equation is valid on every point of the domain of interest $\forall \mathbf{x} \in \Omega$ and it requires $\lambda(\mathbf{x})$ to be at least differentiable once and $T(\mathbf{x})$ to be at least differentiable twice, i.e. $\lambda(\mathbf{x}) \in C^1(\Omega)$ and $T(\mathbf{x}) \in C^2(\Omega)$. We name this form of the equation *strong form*.

The strong requirements on the smoothness of the solution and data needed by this formulation make the solution of this equation not trivial in several situations. For example this equation in strong form with the requirements defined above cannot model the heat conduction in a domain composed of two materials with different λ because on the interface between the two materials the function $\lambda(\mathbf{x}) \notin C^1(\Omega)$. A possible solution to this problem is to split the domain in the two materials, solve the equation on each domain and impose the continuity of the temperature and of the heat fluxes on the interface. However every situation needs a different approach and it becomes obvious to ask if this is the best formulation possible to obtain the solution in interesting cases.

The weak formulation is an integral formulation of the partial differential equation that allows to weak the hypothesis on the functions that are solution to the PDE. It is obtained by multiplying the equation with a smooth test function and then integrating over the whole domain. Using (1.13) as an example we can multiply it with a test function $\phi \in H^1(\Omega)$ and integrate over the whole domain Ω

$$\int_\Omega \nabla \cdot (\lambda \nabla T)\, \phi\, d\Omega + \int_\Omega Q\, \phi\, d\Omega = 0 \,. \tag{1.14}$$

Of course this relation is true whichever test function we choose, so we write

$$\int_\Omega \nabla \cdot (\lambda \nabla T)\, \phi\, d\Omega + \int_\Omega Q\, \phi\, d\Omega = 0 \qquad \forall \phi \in H^1(\Omega) \,. \tag{1.15}$$

Now we can use the divergence theorem to rewrite the first integral as in an integration by parts

$$-\int_\Omega \lambda \nabla T \cdot \nabla \phi\, d\Omega + \int_{\partial\Omega} (\lambda \nabla T) \cdot \mathbf{n}\, \phi\, d\Gamma + \int_\Omega Q\, \phi\, d\Omega = 0 \quad \forall \phi \in H^1(\Omega) \,, \tag{1.16}$$

where $\partial\Omega$ is the boundary of the domain Ω and the vector $\mathbf{n}$ is the unit normal to the surface $\partial\Omega$. By doing so we see that the requirements on the functions $\lambda(\mathbf{x})$ and $T(\mathbf{x})$ are less stringent. We see that $\lambda(\mathbf{x})$ only needs to be integrable over Ω and $T(\mathbf{x})$ needs to be differentiable once, $\lambda(\mathbf{x}) \in L^2(\Omega)$ and $T(\mathbf{x}) \in H^1(\Omega)$. In this setting the simple case of a non continuous heat conductivity like in a domain composed of two materials is well defined. Moreover we can see that an integral over the boundary of the domain appears, and one can easily understand that this is related with the boundary conditions of the problem. As a matter of fact, in a weak formulation the boundary conditions are already incorporated in the integral equation through two types of boundary conditions which are named *natural* or *essential*. The *natural* boundary conditions are those which appear directly in the equation, like in this case the definition of the heat flux through the boundary of the domain which is a Neumann or Robin boundary condition. The *essential* boundary conditions are Dirichlet and are obtained by assuming a proper space for the test functions ϕ. To better understand this difference let us consider the boundary $\partial\Omega = \Gamma_n \cup \Gamma_d$ where Γ_n is the surface where Neumann boundary conditions are imposed and Γ_d the surface where Dirichlet boundary conditions are used,

$$\lambda\nabla T \cdot \mathbf{n} = -q_w \qquad \text{on} \qquad \Gamma_n \tag{1.17}$$

$$T = T_b \qquad \text{on} \qquad \Gamma_d. \tag{1.18}$$

The surface integral in (1.16) can be split into

$$\int_{\partial\Omega} (\lambda\nabla T) \cdot \mathbf{n}\,\phi\,d\Gamma = \int_{\Gamma_n} (\lambda\nabla T) \cdot \mathbf{n}\,\phi\,d\Gamma + \int_{\Gamma_d} (\lambda\nabla T) \cdot \mathbf{n}\,\phi\,d\Gamma, \tag{1.19}$$

where in the first term on the right hand side the heat flux is known to be $-q_w$. The second term is unknown but since we have a Dirichlet boundary condition in here we can assume that the test functions are always zero on this surface because we already know the solution to be $T = T_b$. The space of the test functions thus becomes $H^1_{\Gamma_d}(\Omega)$ and this surface integral term vanishes. This condition is called *essential* because it involves the space where the test functions are defined. On the other hand, the Neumann condition is called *natural* because the term defined in the boundary condition appears directly in the surface integral and can be substituted. The weak formulation thus becomes

$$\int_\Omega \lambda\nabla T \cdot \nabla\phi\,d\Omega + \int_{\Gamma_n} q_w\,\phi\,d\Gamma - \int_\Omega Q\,\phi\,d\Omega = 0 \quad \forall\phi \in H^1(\Omega). \tag{1.20}$$

We report also the weak formulation of the Navier-Stokes equations since it is used in every application of this thesis. In order to introduce these

equations, consider three Hilbert spaces $V(\Omega), P(\Omega)$ and $W(\Gamma)$ and set

$$a(\mathbf{v}, \mathbf{u}) = \int_{\Omega} \nabla \mathbf{v} : \nabla \mathbf{u} \, d\Omega \,, \tag{1.21}$$

$$b(\mathbf{u}, q) = -\int_{\Omega} q \nabla \cdot \mathbf{u} \, d\Omega \,, \tag{1.22}$$

$$c(\mathbf{v}, \mathbf{u}, \mathbf{s}) = \int_{\Omega} (\mathbf{v} \cdot \nabla) \mathbf{u} \cdot \mathbf{s} \, d\Omega \,, \tag{1.23}$$

for all $\mathbf{u}$, $\mathbf{v}$, $\mathbf{s} \in V(\Omega)$ and $q \in P(\Omega)$ and define the Reynolds number as

$$Re = \frac{\rho U L}{\mu} \,, \tag{1.24}$$

where ρ, U, L, μ denote the reference values for density, velocity, length and dynamic viscosity, respectively. Given $\mathbf{v}_0 \in W(\Gamma)$, we seek $(\mathbf{v}, p, \mathbf{t}) \in V(\Omega) \times P(\Omega) \times V^{-1}(\Omega)$ such that

$$\frac{1}{Re} a(\mathbf{v}, \mathbf{u}) + c(\mathbf{v}, \mathbf{v}, \mathbf{u}) + b(\mathbf{u}, p) + (\mathbf{t}, \mathbf{u}) = 0 \qquad \forall \mathbf{u} \in V(\Omega) \tag{1.25}$$

$$b(\mathbf{v}, q) = 0 \qquad \forall q \in P(\Omega) \,, \tag{1.26}$$

where $\mathbf{v} = \mathbf{v}_0$ on Γ and $\mathbf{t}$ is the stress boundary vector.

The weak formulations of the heat transfer (1.20) and Navier-Stokes (1.25-1.26) problems have been written for functions in the infinite dimensional spaces $L^2(\Omega)$ and $H^1(\Omega)$. It is very easy to obtain a numerical approximation of these equations by replacing the infinite dimensional spaces with finite dimensional ones that are subsets of the firsts. By properly choosing these finite dimensional spaces one can obtain the finite element approximation of the weak form of the equations. In this thesis we consider only the Petrov-Galerkin method which assumes that both the unknown functions and the test functions are chosen in the same spaces. Other methods are available that suggest to use different approximation spaces for the unknown and the test functions, but we focus on Petrov-Galerkin method since it is the simplest and widely used approach among the finite element methods. In the next Section we describe some Finite Elements that are widely used to obtain a numerical approximation of PDEs weak forms.

1.4   Finite elements

The finite element methods rely on the definition of suitable finite dimensional spaces for the numerical approximation of functions. This definition
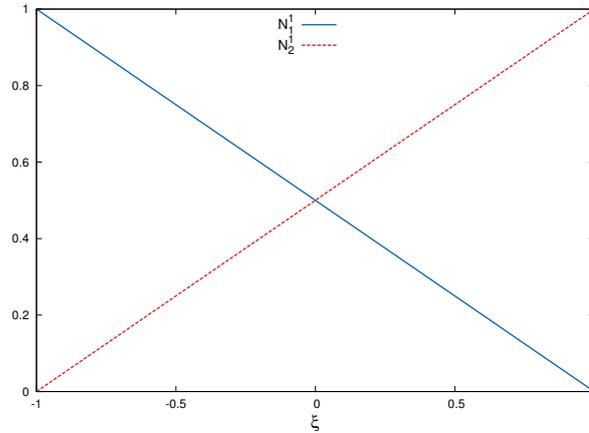
Figure 1.1:   Linear shape functions for a one-dimensional EDGE2 element.

is in turn the definition of a basis for the function space. It is very common to assume that the basis functions have compact support, i.e. they are defined as $\phi_i(\mathbf{x}) = \phi_i(\mathbf{x})$ if $\mathbf{x} \in \Omega_s \subset \Omega$ and $\phi_i(\mathbf{x}) = 0$ if $\mathbf{x} \notin \Omega_s$. The support is usually defined in a reference configuration Ω_s^*. We define the shape functions N_j^i of order i related to j node of the reference element Ω_s^* as the restriction of the basis function on Ω_s^*. We define *finite element* the set of the reference support Ω_s^* and shape functions N_j^i defined over it. To approximate any domain Ω with a set of Ω_s^*, a coordinate transformation of the type $t_s : \Omega_s^* \to \Omega_s$ can be developed to obtain $\Omega = \cup_s \Omega_s = \cup_s t_s^{-1} \Omega_s^*$. By doing so the definition of the finite element is completely disjointed from the geometrical properties of the domain Ω while this information is kept by the transformation t_s which is defined for every geometry.

With these preliminary considerations it is easy to understand why the definition of finite elements can be done without any information on the geometry that will be simulated and conversely why any geometry can be well approximated by using the appropriate type of finite elements and a suitable coordinate transformation. We briefly describe a few Lagrangian finite elements which are very commonly employed, but we remark that several other finite elements have been developed with respect to the geometry and the basis functions chosen [115, 116, 117].

The definition of piecewise constant basis functions is trivial in any dimension, $\phi_i^*(\mathbf{x}) = 1$ if $\mathbf{x} \in \Omega_s^*$, for any chosen Ω_s^*. When piecewise constant basis functions are used the method is called Discontinuous Galerkin method which is a discretization very similar to the one obtained with finite volumes techniques.

Consider a one-dimensional domain $\Omega = [0, 1]$ and a subdivision with N
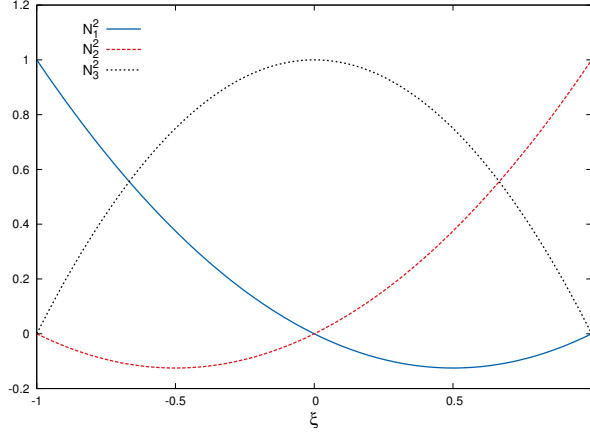
Figure 1.2:   Quadratic shape functions for a one-dimensional EDGE3 element.

intervals $\Omega_i = [x_i, x_{i+1}]$ for $i = 0, 1, \ldots, N$ with $x_0 = 0$ and $x_N = 1$. A basis for the space $H^1(\Omega)$ can be obtained with linear Lagrangian polynomials as

$$
\phi_i^1(x) = \begin{cases} \dfrac{x - x_{i-1}}{x_i - x_{i+1}} & \text{if } x \in [x_{i-1}, x_i] \\ \dfrac{x_{i+1} - x}{x_{i+1} - x_i} & \text{if } x \in [x_i, x_{i+1}] \\ 0 & \text{otherwise}. \end{cases} \tag{1.27}
$$

Note that with the definition (1.27) the basis function is equal to 1 on the node x_i and null outside the sub interval, so it has compact support. We can define a reference $1-$D element based on an interval in the variable $\xi \in [-1, 1]$. As already explained with a transformation $t^{-1} : \Omega_i \to \Omega_i^*$ we can transform any $\Omega_i = [x_i, x_{i+1}]$ interval into the reference interval $\Omega_i^* = [-1, 1]$. This transformation can be defined with linear or quadratic polynomials, for example.

The finite dimensional space $X_h^1(0, 1)$ can be defined as the function space with (1.27) as basis functions,

$$
X_h^1(0, 1) = \left\{ f \in H^1(0, 1) \; : f = \sum_{i=0}^{N-1} \alpha_i \phi_i^1 \;, \; \alpha_i \in \mathbb{R} \right\}, \tag{1.28}
$$

It can be proven that this space is a dense subset of $H^1(0, 1)$ and that for $N \to \infty$ the space $X_h^1(0, 1) \to H^1(0, 1)$. Given the reference element Ω_i^* the
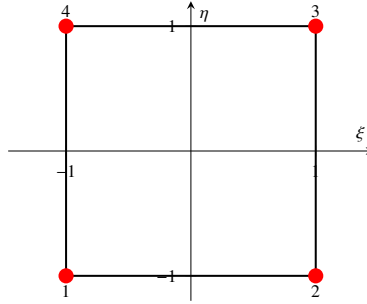
Figure 1.3: Linear two-dimensional element QUAD4.
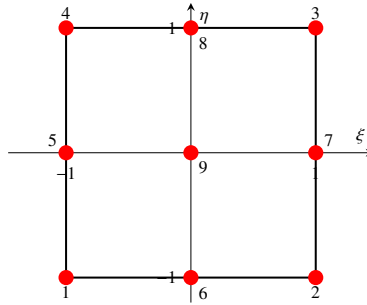

Figure 1.4: Quadratic two-dimensional element QUAD9.

linear shape functions for this element are

$$N_1^1(\xi) = \frac{1 - \xi}{2} \tag{1.29}$$

$$N_2^1(\xi) = \frac{1 + \xi}{2} .$$

These shape functions are reported in Figure 1.1.

With the same subdivision in N intervals $[x_i, x_{i+1}]$ for $i = 0, 1, \ldots, N$ we can also define a basis with quadratic polynomials by considering even and odd nodes as different. If i is even we get

$$\phi_i^2(x) = \begin{cases} \dfrac{(x - x_{i-1})(x - x_{i-2})}{(x_i - x_{i-1})(x_i - x_{i-2})} & \text{if } x \in [x_{i-2}, x_i] \\ \dfrac{(x - x_{i+1})(x - x_{i+2})}{(x_i - x_{i+1})(x_i - x_{i+2})} & \text{if } x \in [x_i, x_{i+2}] \\ 0 & \text{otherwise} \end{cases} , \tag{1.30}$$

and if i is odd

$$\phi_i^2(x) = \begin{cases} \dfrac{(x - x_{i-1})(x - x_{i+1})}{(x_i - x_{i-1})(x_i - x_{i+1})} & \text{if } x \in [x_{i-1}, x_{i+1}] \\ 0 & \text{otherwise} \end{cases} . \tag{1.31}$$
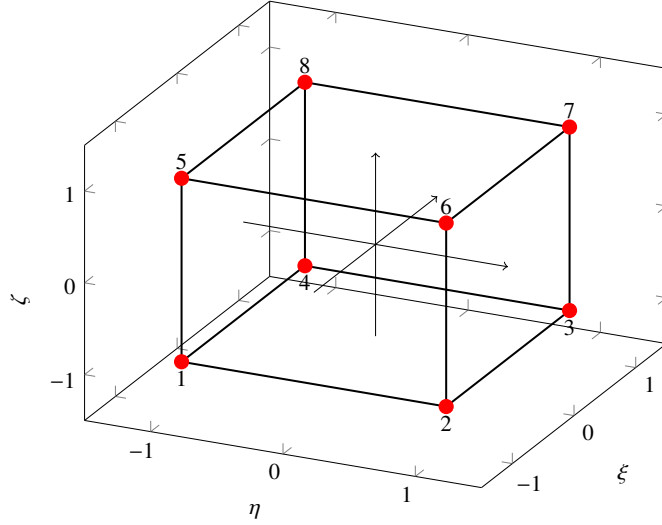
Figure 1.5:   Linear three-dimensional element HEX8.

This basis function defines a finite dimensional space of quadratic functions $X_h^2(0,1)$ as

$$X_h^2(0,1) = \left\{ f \in H_1(0,1) \; : f = \sum_{i=0}^{N-1} \alpha_i \phi_i^2 \; , \; \alpha_i \in \mathbb{R} \right\} \; , \tag{1.32}$$

which is also a dense subset of $H^1(0,1)$. With this quadratic function basis we define the element as composed of three nodes, $\Omega_i = [x_i, x_{i+2}]$, and thus we have three shape functions on every reference element Ω_i^*,

$$\begin{aligned} N_1^2(\xi) &= -\frac{1-\xi}{2}\xi \\ N_2^2(\xi) &= \frac{1+\xi}{2}\xi \\ N_3^2(\xi) &= (1-\xi)(1+\xi) \, . \end{aligned} \tag{1.33}$$

These shape functions are reported in Figure 1.2. The one-dimensional elements with linear shape functions are called *EDGE2* and are composed of two nodes. The one-dimensional elements with quadratic shape functions are called *EDGE3* and have three nodes.

Using these basic one-dimensional elements and shape functions the multi-dimensional square (two-dimensional) and hexahedron (three-dimensional) elements can be easily constructed. We can define the linear square element *QUAD4*. This element is defined in a reference domain with two coordinates,
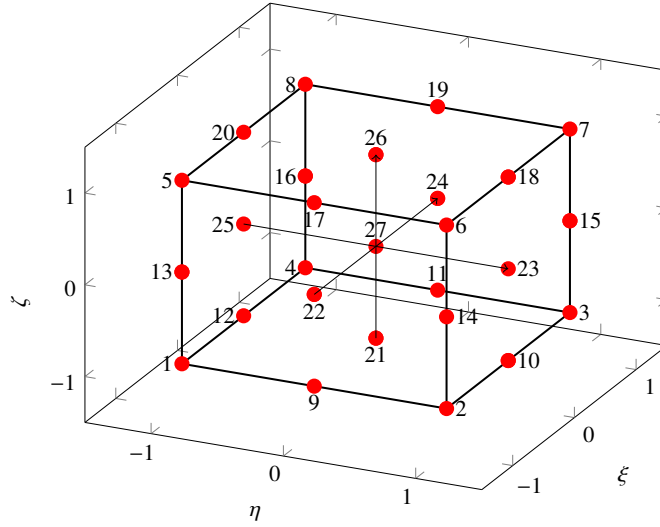
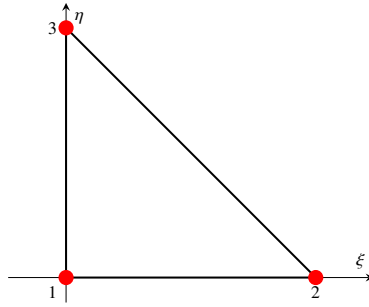Figure 1.6:   Quadratic three-dimensional element HEX27.

Figure 1.7:   Linear two-dimensional element TRI3.

ξ and η, and with four nodes, one for each vertex of the square, as reported in Figure 1.3. This element can be generated by two *EDGE2* elements connected at the end and so the shape functions for this element can be defined using the (1.29) as

$$N_{ij}^1(\xi, \eta) = N_i^1(\xi)\, N_j^1(\eta)\,.$$

In a similar way the quadratic square element obtained by connecting three *EDGE3* elements is called *QUAD9* and it is reported in Figure 1.4. The quadratic shape functions for this element can be obtained in the same way as the linear shape functions from the definition (1.33)

$$N_{ij}^2(\xi, \eta) = N_i^2(\xi)\, N_j^2(\eta)\,.$$

The hexahedron elements can be obtained starting from the one-dimensional *EDGE* elements or from the two-dimensional *QUAD* elements. The shape
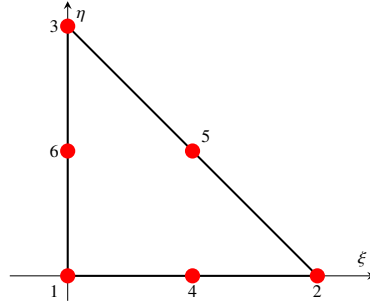
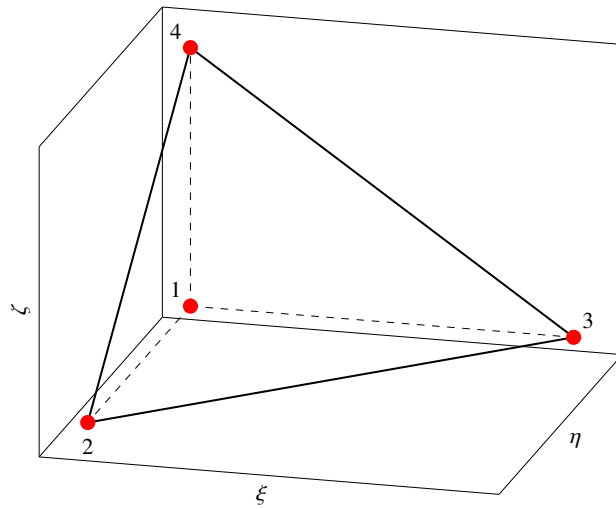Figure 1.8:   Quadratic two-dimensional element TRI6.

Figure 1.9:   Linear three-dimensional element TET4.

functions of these elements are obtained recursively from the (1.29) and (1.33). By doing so the three-dimensional linear element *HEX8* can be obtained as depicted in Figure 1.5 with shape functions

$$N_{ijk}^1(\xi, \eta, \zeta) = N_i^1(\xi)\, N_j^1(\eta)\, N_k^1(\zeta)\,.$$

The three-dimensional quadratic element *HEX27* is depicted in Figure 1.6 and it has the shape functions

$$N_{ijk}^2(\xi, \eta, \zeta) = N_i^2(\xi)\, N_j^2(\eta)\, N_k^2(\zeta)\,.$$

Another important set of elements is based on triangular shapes. This type of elements can be more suitable to approximate complex and curved domains with respect to the quadrilateral ones. The standard linear two-dimensional triangular element is called *TRI3* and it is depicted in Figure
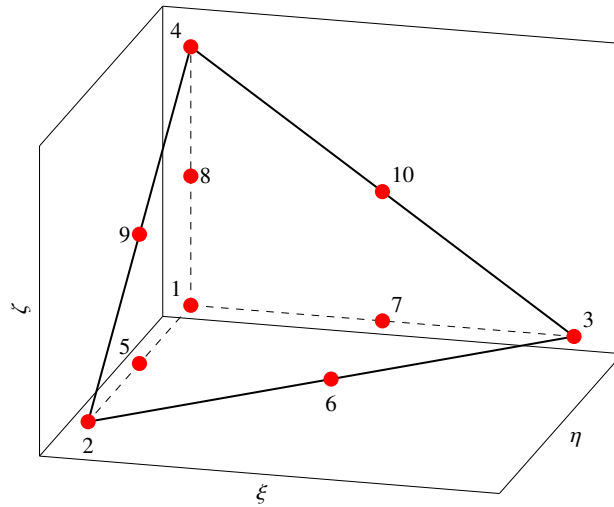
Figure 1.10:   Quadratic three-dimensional element TET10.

1.7 with the three nodes at the vertices of the triangle. Usually the standard Cartesian coordinate system is not used for this type of elements but a coordinate system based on surfaces or volumes is preferred. Any point inside the element is connected through straight lines with the vertices of the element. The ratio between the surface or volume of each smaller element obtained in this way and the total surface or volume is the triangular coordinate. In two dimensions the first coordinate r is the one obtained using the surface of the small triangle built on the vertical side of the main triangle, the second s is obtained using the surface of the small triangle built on the horizontal side of the main triangle and the third coordinate is computed as $1 - r - s$. With this coordinate the node 1 of Figure 1.7 has coordinate $(0,0)$, node 2 is in $(1,0)$ and node 3 in $(0,1)$. The linear shape functions in this coordinate system are therefore simply equal to the triangular coordinate,

$$N_1^1(r,s) = 1 - r - s$$
$$N_2^1(r,s) = r$$
$$N_3^1(r,s) = s \,.$$

The quadratic two-dimensional triangular element has six nodes, it is called *TRI6* and it is depicted in Figure 1.8. One can understand that with this element it is very easy to obtain grid refinements because by connecting the middle side nodes one can obtain four new triangular elements *TRI3* that can be made quadratic *TRI6* through a simple middle point refinement on every side. The quadratic shape functions in triangular coordinates for this

element are

$$N_1^2(r, s) = 2\,(1 - r - s)\,((1 - r - s) - 0.5)$$
$$N_2^2(r, s) = 2\,r\,(r - 0.5)$$
$$N_3^2(r, s) = 2\,s\,(s - 0.5)$$
$$N_4^2(r, s) = 4\,r\,(1 - r - s)$$
$$N_5^2(r, s) = 4\,r\,s$$
$$N_6^2(r, s) = 4\,s\,(1 - r - s)\,.$$

To obtain the three dimensional tetrahedral elements the procedure is exactly the same and the tetrahedral coordinate system is composed of three variables based on volume ratios computation (p, q, t). The linear three dimensional element has four nodes, is called *TET4* and is depicted in Figure 1.9. The nodes are collocated on the tetrahedral coordinate system as $1 : (0, 0, 0)$, $2 : (1, 0, 0)$, $3 : (0, 1, 0)$ and $4 : (0, 0, 1)$ and the linear shape functions are simply

$$N_1^1(p, q, t) = 1 - p - q - t$$
$$N_2^1(p, q, t) = p$$
$$N_3^1(p, q, t) = q$$
$$N_4^1(p, q, t) = t\,.$$

By looking at these very simple shape functions it is easy to understand why this coordinate system has been chosen. Finally the quadratic three dimensional tetrahedral elements has ten nodes, is called *TET10* and is depicted in Figure 1.10. This element has the same feature of element *TRI6* to allow for a very easy mesh refinement since the *TET4* elements can be obtained by connecting the middle side nodes. The quadratic shapes for this element are

$$N_1^2(p, q, t) = (1 - p - q - t)\,(2(1 - p - q - t) - 1)$$
$$N_2^2(p, q, t) = p\,(2\,p - 1)$$
$$N_3^2(p, q, t) = q\,(2\,q - 1)$$
$$N_4^2(p, q, t) = t\,(2\,t - 1)$$
$$N_5^2(p, q, t) = 4\,p\,(1 - p - q - t)$$
$$N_6^2(p, q, t) = 4\,p\,q$$
$$N_7^2(p, q, t) = 4\,q\,(1 - p - q - t)$$
$$N_8^2(p, q, t) = 4\,t\,(1 - p - q - t)$$
$$N_9^2(p, q, t) = 4\,p\,t$$
$$N_{10}^2(p, q, t) = 4\,q\,t\,.$$

Other three-dimensional elements can be build combining the elements we have described. For example the linear pyramidal element is composed of a *QUAD4* as basis and four *TRI3* elements as vertical faces. To obtain the second order element one can simply use the quadratic elements *QUAD9* and *TRI6* or consider to use a central point in the volume. Prism elements built using two *TRI3* elements as bottom and up faces and three *QUAD4* elements as vertical faces are sometimes used to obtain a mesh which uses quadrilateral elements in the flow direction and triangular ones on the section. By doing so one can build a mesh that approximate very well a channel with a curved section in the direction normal to the axis. Many other elements have been built with different geometries and shape functions, for a more comprehensive review one can see [20, 115, 116, 117].

1.5 Discrete approximation properties

The weak forms derived in Section 1.3 can be used to obtain a Finite Element discretization by substituting the finite dimensional spaces X_h defined in the previous Section 1.4 with the infinite dimensional ones. When this is done an approximation error arise and we need some information on how this error decreases with the order of the discretization and the element main dimensions. To this end, let $X_h(\Omega) \subset H^1(\Omega)$ and $S_h(\Omega) \subset L^2(\Omega)$ be two families of finite dimensional subspaces parametrized by a main dimension h that tends to zero as the approximation improves. We also denote $X_{h0}(\Omega) \subset H_0^1(\Omega)$ and $S_{h0}(\Omega) \subset L_0^2(\Omega)$. Furthermore consider $(\mathbf{v}_h, p_h) \in X_h(\Omega) \times S_h(\Omega)$ to be the approximations of the variables $(\mathbf{v}, p)$ in the finite dimensional spaces.

We make the following assumptions on $X_h(\Omega)$ and $S_h(\Omega)$. The first is the approximation hypotheses that says that there exists an integer l and a constant C, independent of h, $(\mathbf{v}, p)$ such that for $1 \leq k \leq l$ we have

$$\inf_{\mathbf{v}_h \in X_h(\Omega)} \|\mathbf{v}_h - \mathbf{v}\|_1 \leq Ch^k \|\mathbf{v}\|_{k+1} \qquad \forall \mathbf{v} \in H^{k+1}(\Omega) \cap H_0^1(\Omega) \qquad (1.34)$$

$$\inf_{p_h \in S_h(\Omega)} \|p_h - p\| \leq Ch^k \|p\|_k \qquad \forall p \in H^k(\Omega) \cap L_0^2(\Omega). \qquad (1.35)$$

The *Inf-Sup* Condition assures the stability of the discretized Navier-Stokes equations if and only if

$$\inf_{q_h \in S_h} \sup_{\mathbf{v}_h \in X_h} \frac{|b(\mathbf{v}_h, q_h)|}{\|v_h\|_1 \|q_h\|} > 0. \qquad (1.36)$$

This is true if the spaces are chosen properly and it can be verified for Taylor-Hood spaces in dimension n,

$$V_h = \left\{ \mathbf{v} \in \prod_i^n V_h^k : \mathbf{v} = 0 \quad \text{on } \Gamma \right\} \tag{1.37}$$

$$P_h = \left\{ q \in V_h^{k-1} : \int_\Omega q(\mathbf{x}) d\Omega = 0 \right\}, \tag{1.38}$$

where V_h^k are the spaces of C^0 polynomials of degree k on a mesh of a polygonal domain $\Omega \subset \mathbb{R}^n$ with a maximum element length of h [20]. Thus if the spaces $X_h(\Omega)$ and $S_h(\Omega)$ are chosen as Taylor-Hood spaces the stability of the discretized Navier-Stokes equations is assured by (1.36).

Now we examine the advective trilinear form $c(\mathbf{v}, \mathbf{u}, \mathbf{s})$ defined in (1.23). To preserve the antisymmetry of this form we introduce the modified trilinear form

$$\tilde{c}(\mathbf{v}, \mathbf{u}, \mathbf{s}) = \frac{1}{2}(c(\mathbf{v}, \mathbf{u}, \mathbf{s}) - c(\mathbf{v}, \mathbf{s}, \mathbf{u})) \qquad \forall \mathbf{v}, \mathbf{u}, \mathbf{s} \in H^1(\Omega). \tag{1.39}$$

This modified form has some interesting properties,

$$\tilde{c}(\mathbf{v}, \mathbf{u}, \mathbf{s}) = -\tilde{c}(\mathbf{v}, \mathbf{s}, \mathbf{u}) \qquad \forall \mathbf{v}, \mathbf{u}, \mathbf{s} \in H^1(\Omega), \tag{1.40}$$

$$\tilde{c}(\mathbf{v}, \mathbf{u}, \mathbf{u}) = 0 \qquad \forall \mathbf{v}, \mathbf{u} \in H^1(\Omega). \tag{1.41}$$

Moreover there exist some interesting bounds for this form in the two dimensional case. For all $\mathbf{v}, \mathbf{u}, \mathbf{s} \in H^1(\Omega)$ we have

$$|\tilde{c}(\mathbf{v}, \mathbf{u}, \mathbf{s})| \leq C_1 \|\mathbf{v}\|_1 \|\mathbf{u}\|_1 \|\mathbf{s}\|_1, \tag{1.42}$$

$$|\tilde{c}(\mathbf{v}, \mathbf{u}, \mathbf{s})| \leq C_2 \|\mathbf{v}\|^{\frac{1}{2}} \|\mathbf{u}\|^{\frac{1}{2}} \|\mathbf{s}\|^{\frac{1}{2}} \|\nabla \mathbf{v}\|^{\frac{1}{2}} \|\nabla \mathbf{u}\|^{\frac{1}{2}} \|\nabla \mathbf{s}\|^{\frac{1}{2}}. \tag{1.43}$$

Using the approximation property (1.34) we can also derive a boundary approximation property valid for the restriction of the velocity on the boundary $\Gamma = \partial \Omega$ of the domain Ω. Let $Q_h = X_h|_\Gamma$ be the space of the restrictions of the functions belonging to $X_h(\Omega)$ on the boundary Γ and $Q_{h0} = Q_h \cap H_0^1(\Gamma)$. Then there exists an integer k and a constant C_3, independent of h and $\mathbf{s}$ such that for $1 \leq m \leq k$ we have

$$\inf_{\mathbf{s}_h \in Q_h(\Gamma)} \|\mathbf{s}_h - \mathbf{s}\|_s \leq C_3 h^{m-s+\frac{1}{2}} \|\mathbf{s}\|_{m+\frac{1}{2}} \qquad \forall \mathbf{s} \in H_0^1(\Gamma). \tag{1.44}$$

It can be proven that the weak formulation (1.25-1.26) of Navier-Stokes equations discretized with Finite Elements based on the Taylor-Hood spaces as defined in (1.37) admits solutions for any value of Reynolds number [20, 116]. Moreover the solution is unique if the kinematic viscosity $\mu = \nu/\rho$ is "large enough", i.e. if the diffusion term is more important than the advection one. For more details on this result see Theorem 1 in Chapter 7 and the reference book [109].

Part I

Heat Transfer in Liquid Metals

Chapter 2

Liquid metals

2.1 Physical properties

The study of heavy liquid metals started in the last century and it is still important nowadays for the engineering community since these fluids are often considered for new advanced industrial applications. There is a broad range of applications where liquid metals are involved, in nuclear and non-nuclear fields. Regarding the first we mention Accelerator Driven Systems, fast and breeding fission reactors, fusion reactors [27, 41, 93, 99]. In non-nuclear field liquid metals are studied in the metallurgy industry and are considered as heat transfer fluids for innovative concentrated solar power plants [35, 68]. Recently some European research programmes have been dedicated to the study of liquid metal physical and chemical properties, heat transfer and thermal-hydraulics in general, neutron properties and other research fields. Specific features of liquid metals comprise neutron properties, which are very interesting for the design of fast nuclear reactors, electromagnetic properties useful for electromagnetic control of the flow and peculiar thermodynamical properties with respect to common fluids. Here we focus our attention on thermodynamical properties for thermal-hydraulics purposes.

This class of fluids is characterized by a very high thermal conductivity and low molecular viscosity. The Prandtl number is defined for a fluid as

$$Pr = \frac{\nu}{\alpha} = \frac{\mu \, C_p}{\lambda} \, , \qquad (2.1)$$

where ν is the kinematic viscosity, α is the heat diffusivity, μ is the dynamic viscosity, C_p is the heat capacity and λ the thermal conductivity. This number represents the ratio between momentum and heat transport. For fluids with $Pr \sim 1$, like water and air, a similarity between the thermal and dynamical boundary layers can be observed. If a fluid has a high Prandtl number,

	ρ [Kg/m^3]	μ [Pa $\cdot$ s]	λ [W/(m K)]	C_p [J/(Kg K)]	Pr
Pb	10801	$3.86 \cdot 10^{-3}$	14.7	155.45	0.041
Bi	10115	$2.12 \cdot 10^{-3}$	12.09	121.17	0.021
LBE	10419	$2.23 \cdot 10^{-3}$	11.06	146.4	0.029
Hg	13040	$1 \cdot 10^{-3}$	13.1	136	0.01
Na	896.9	$4.15 \cdot 10^{-4}$	80.1	1334	0.0069

Table 2.1: Physical transport properties at $T = 500$ K of some heavy liquid metals considered for industrial applications.

like oils, it means that the transport of momentum is faster than heat transfer so that the fluid is very viscous and thermally insulating. If a fluid has a very low Prandtl number, like liquid metals, the opposite is true and the heat transfer is fast while the momentum transport is poor. This feature of liquid metals is really desirable from a thermal-hydraulics point of view because it results in a strong heat transfer and very low pressure drops when pumped in a loop, so they are ideal coolants. Moreover electromagnetic fields applied from outside the pool or the main loop could be used to actively control the fluid flow to enhance the mixing and heat transfer or to modify the flow pattern to decrease the pressure drops.

In table 2.1 the physical properties of several heavy liquid metals considered nowadays for industrial applications are reported for a reference temperature of 500 K [34]. The metals Lead, Bismuth and Lead Bismuth Eutectic (44.5 % Pb and 55.5 % Bi in mass) are studied for some fast nuclear reactor designs. Sodium has been used in the last century to operate fast breeder reactors, like Phoenix reactor in France, but it is less considered nowadays for safety reasons because sodium reacts with water inflaming and exploding. Mercury is a peculiar metal with a very low melting point, such that it is liquid at room temperature and it boils at not too high temperatures. All of these fluids are characterized by a very low Prandtl number which is a function of the temperature. For the first three metals we report the recommended correlations for the physical properties as functions of the temperature [34].

Lead

$\rho = 11441 - 1.2795\, T$

$\mu = 4.55 \cdot 10^{-4} \exp\left(\dfrac{1069}{T}\right)$

$\lambda = 9.2 + 0.011\, T$

$C_p = 176.2 - 4.923 \cdot 10^{-2}\, T + 1.544 \cdot 10^{-5}\, T^2 - 1.524 \cdot 10^{6}\, T^{-2}$

Metal	T_l [K]	T_g [K]
Pb	600.6	2021
Bi	544.6	1831
LBE	398	1927
Hg	234.3	629.9
Na	370.7	1153

Table 2.2:   Melting and boiling temperatures of some heavy liquid metals considered for industrial applications.

Bismuth

$\rho = 10725 - 1.22\,T$

$\mu = 4.456 \cdot 10^{-4} \exp\left(\dfrac{780}{T}\right)$

$\lambda = 7.34 + 0.0095\,T$

$C_p = 118.2 + 5.934 \cdot 10^{-3}\,T + 7.183 \cdot 10^6\,T^{-2}$

LBE

$\rho = 11065 - 1.293\,T$

$\mu = 4.94 \cdot 10^{-4} \exp\left(\dfrac{754}{T}\right)$

$\lambda = 3.284 + 0.0167\,T - 2.305 \cdot 10^{-6}\,T^2$

$C_p = 164.8 - 3.94 \cdot 10^{-2}\,T + 1.25 \cdot 10^{-5}\,T^2 - 4.56 \cdot 10^5\,T^{-2}$

These formulas can be implemented in a computational code used for the design of a fast reactor in which one of these metals is employed.

In table 2.2 the melting and boiling temperatures are reported for the same metals. In this table it can be seen that the choice of LBE for nuclear reactors relies on its low melting temperature which allows to operate the reactor in a wider and lower range of temperatures. Moreover, by keeping a low pool temperature, maintenance is easier and corrosion rates remain low.

Despite these advantages with respect to ordinary fluids liquid metals are not commonly used because of several reasons. The main one is that in order to use these fluids appropriately, very precise information on their heat transfer and physical behavior is needed but, because of the discrepancy among experimental data, the definition of heat transfer correlations and physical properties need to be employed with attention because of the limited range of validity and possible experimental errors. Experimental studies are difficult to perform because heavy liquid metals are solid at room temperature and

must be kept liquid by a substantial increase of environmental temperature, so experimental data cannot be collected easily with standard measurement devices. Profiles of velocity, temperature and their turbulent fluctuations are available mainly through DNS at low Reynolds numbers, while for engineering applications at higher Reynolds numbers one must rely on integral heat transfer data. Furthermore there are many open problems in the comprehension of physics of turbulent heat transfer and in the consistency between experimental observations, since data collected by different authors often do not agree [27]. In the next section we describe the problem of turbulent heat transfer modeling with a special emphasis on liquid metals.

2.2   Turbulent Heat Transfer Modeling

In fluids such as air or water with $Pr \sim 1$ it is widely accepted that similarity between the thermal and dynamical boundary layer holds. With this hypothesis the turbulent heat transfer can be easily modeled using information coming from turbulent dynamical modeling. It is common practice to define a turbulent heat diffusivity α_t and an effective heat diffusivity as the sum of the molecular and turbulent heat diffusivities, $\alpha_e = \alpha + \alpha_t$. Therefore the only modification in the energy equation due to turbulence is the substitution of α with α_e in the diffusion term. In a similar way as done with the
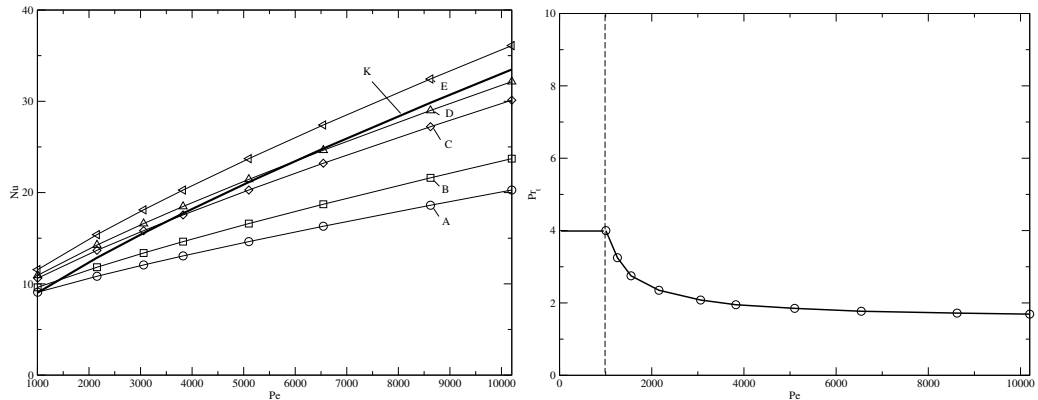
Figure 2.1:   On the left Nusselt number as a function of Peclet number in a cylindrical geometry flow heated with constant heat flux on the wall. Kirillov experimental correlation (K) is reported and compared with CFD computations with constant $Pr_t = 4$ (A), 3 (B), 2 (C), 1.8 (D) and 1.5 (E). On the right values of the turbulent Prandtl number needed to match experimental correlation for the cylinder pipe heated with constant heat flux as a function of the Peclet number.

Prandtl number it is common to define a turbulent Prandtl number

$$Pr_t = \frac{\nu_t}{\alpha_t} \,, \tag{2.2}$$

where ν_t is the turbulent or eddy viscosity defined appropriately in the dynamical turbulence model. For fluids with $Pr \sim 1$ it is common to assume Pr_t constant by using a Simple Eddy Diffusivity (SED) model. The value of Pr_t is usually set to $0.85 - 0.9$ and the turbulent heat transfer can be easily modeled by computing α_t from (2.2).

Fluids with very low Prandtl number show different thermal characteristics from ordinary coolants. This is mainly due to the difference of time scales between the thermal and dynamical turbulence, since the heat transfer is due to a mix of conduction and convection transport phenomena. For this reason the SED model with the hypothesis of a constant turbulent Prandtl number does not hold for these fluids and therefore it should not be used in Computational Fluid Dynamics (CFD) simulations. As an example of common mistakes in turbulent heat transfer predictions by using the SED model we compare the experimental correlation proposed by Kirillov-Ushakov for simple cylindrical geometry heated with constant heat flux with a set of CFD data obtained with the SED model [26, 27, 61, 62]. In Figure 2.1 the asymptotic Nusselt numbers of this experimental correlation and computed with CFD simulations are reported as a function of Peclet number. On the left side of Figure 2.1 the correlation curve is labeled with the letter K. As one can see the CFD computations with constant $Pr_t = 4$ (A), 3 (B), 2 (C), 1.8 (D) and 1.5 (E) cannot reproduce the Kirillov correlation curve K. The cases with $Pr_t = 1.8$-1.5 are very close but only in a limited range of Peclet numbers.

In order to match experimental data many formulas have been suggested for the turbulent Prandtl number Pr_t which are valid for different geometries and types of flow. For example the curve K can be reproduced if the turbulent Prandtl number is set as a function of Peclet number as shown in Figure 2.1 on the right side [27]. Unfortunately this is true only for this particular geometry and a new set of turbulent Prandtl numbers should be defined for each different geometry and boundary condition configuration. Indeed it has been proven that computational models based on the same constant turbulent Prandtl number fail to reproduce the available heat transfer experimental correlations in different geometries [26, 27, 56]. Some expressions for a variable Pr_t as a function of the distance from the wall or of the turbulent-molecular viscosity ratio have been proposed, like the Kays model [32, 59], but they need to be assessed in several geometries and for wider range of Peclet numbers. To summarize, the Simple Eddy Diffusivity model with a

constant turbulent Prandtl number may be valid for water and air but it does not seem to be appropriate for liquid metals.

To accurately predict turbulent heat transfer in liquid metal cooled reactors two possibilities are available at the present time: an improved turbulence modeling for the heat transfer and/or reliable experimental correlations for the geometry chosen. In the next section we report the heat transfer correlations currently available for the predictions of Nusselt number of fully developed or developing flows, while in this section we report briefly the ideas underlying turbulent heat transfer modeling currently employed. In the following two chapters we focus on two different four parameter turbulence models based on a k-ϵ or k-ω formulation.

The use of a turbulence model that takes into account thermal turbulence effects and dissimilarities between thermal and dynamical turbulent fields may solve the problems of the SED model. On the last several years, two-equation heat transfer models have been developed starting from the Algebraic Flux Model (AFM) based on implicit or explicit formulation [5, 65, 101]. Implicit methods rely on an algebraic solution of the corresponding transport equation computing directly the heat flux by solving a high non-linear algebraic equation. Explicit methods approximate the implicit term by introducing the velocity and temperature time scales and are based on a term that is a product between the turbulent viscosity and the inverse turbulent Prandtl number [3, 52, 54, 65, 86, 87, 89]. Heat transfer two-equation models have been tested against DNS simulations for low Reynolds numbers in very simple Cartesian geometries but a full test against experimental correlations and data has not been yet investigated in a satisfactory way [30, 56, 89]. The explicit formulation choice leads to k-ϵ-k_θ-ϵ_θ four parameter turbulence models or to similar ones [3, 52, 88, 89]. Unlike the SED model, where the value of Pr_t has to be assigned for each geometry, this modeling approach should be valid in complex geometries and transient flows. Moreover, by using the SED model one is not able to compute the local heat transfer and to take into account advection and transport of thermal turbulence quantities.

In this thesis we focus our attention on new RANS models for applications in liquid metal flows with $Pr \ll 1$. The turbulent heat transfer is computed with the aid of a thermal two equation turbulence model. The complete turbulence model is obtained by coupling the Reynolds-Averaged Navier-Stokes and energy equations with four additional transport equations needed to close the dynamical and thermal problems. These four equations consist of two transport equations for the turbulent kinetic energy k and its dissipation ϵ or specific dissipation rate ω, and two equations for the thermal turbulent quantities k_θ, which is the average square temperature fluctuation, and its dissipation ϵ_θ or specific dissipation rate ω_θ.

These four parameter turbulence models could have some limitations due to the isotropy of the model. In fact, there is an open discussion about turbulent mixing in tight lattice bundles because some experimental and numerical results have shown that there may exist an additional macroscopic flow process in the regions adjacent to the gaps and that in some cases a secondary flow could develop [26]. In order to detect secondary flows, anisotropic turbulent models must be used [26]. Moreover when dealing with turbulent buoyant flows it is necessary to take into account the specific features of these flows. In literature some anisotropic k-ϵ-k_θ-ϵ_θ models are available and they should be considered for further model improvements to study anisotropic and buoyant flows [49]. In this work we focus on forced convection fully developed flows and report several numerical results that prove the usefulness of this type of models in many industrial applications where an accurate turbulent heat flux computation is needed.

2.3 Heat transfer correlations

2.3.1 Cylindrical Channel

Heat transfer in cylindrical geometry is an important topic because this type of flow can be considered as the reference one and simplest to study. For this reason several experimental studies are carried out using different liquid metals to obtain heat transfer correlations and physical information in this geometry. The most common and studied liquid metals are sodium, mercury, lead, sodium-potassium and LBE alloys. The molecular Prandtl number depends on temperature but sodium-potassium (NaK), mercury, lead and LBE are close with values in the range of 0.01-0.03, as we have shown in Table 2.1. We consider $Pr = 0.025$ as the reference value since many heat transfer correlations are based on experiments performed with a fluid with this molecular Prandtl number. Most experiments are performed for engineering applications in the range of Peclet numbers between 1000 and 10000 and the heat transfer data are reported through the heat transfer coefficient h. In the case of a constant heat flux on the wall it is defined as $h = q_w/\Delta T$. The quantity q_w is the heat flux through the solid surface and $\Delta T = T_w - T_b$ the temperature difference between the wall T_w and the surrounding bulk coolant temperature T_b. This quantity is defined over the section surface A as

$$T_b = \frac{\int_A \mathbf{v} \cdot \mathbf{n}\, T\, dA}{\int_A \mathbf{v} \cdot \mathbf{n}\, dA}\,, \qquad\qquad (2.3)$$
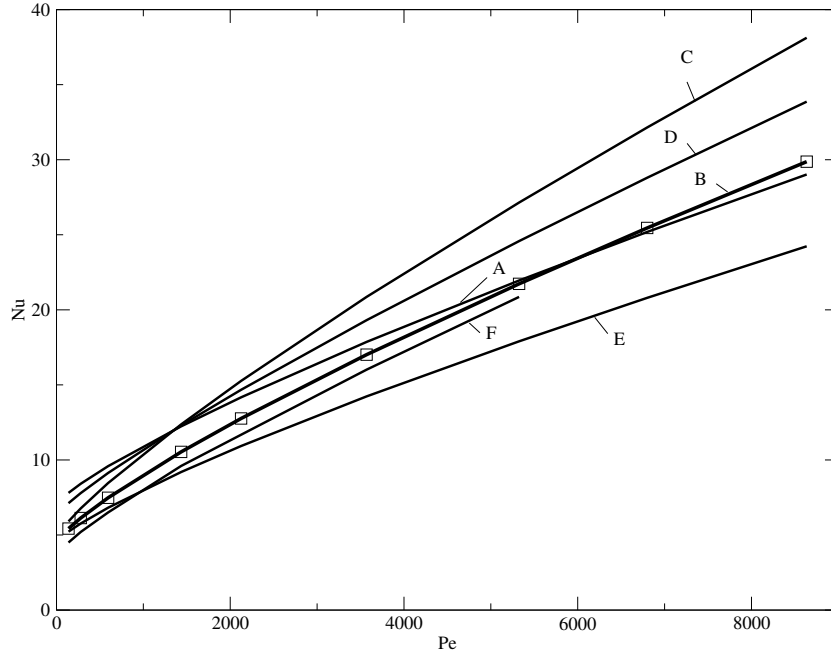
Figure 2.2: Nusselt number correlations for the cylindrical channel from different authors ($Pr = 0.025$) as a function of Pe number. Lyon with $Pr_t = 1.8$ (A), Kirillov (B), Skupinski (C), Sleicher (D), Ibragimov (E) and Stromquist (F).

with **n** the unit normal to the surface. The coefficient h is usually computed in non-dimensional form with the introduction of the Nusselt number which is the most important parameter for integral heat transfer calculations in the design of a heat transport system:

$$Nu = \frac{D_h \, h}{\lambda} = \frac{D_h \, q_w}{\lambda \, \Delta T} \, , \tag{2.4}$$

where D_h is the hydraulic diameter of the channel and λ the thermal conductivity of the fluid.

Several correlations are available for liquid metal flows in a cylindrical geometry heated with constant wall heat flux. Most of them can be written as

$$Nu = A + a \, Pe^n \, , \tag{2.5}$$

where A, a and n are constant positive real numbers. One of the first heat transfer correlation for liquid metals was proposed by Lyon. Applying the Reynolds analogy for momentum and energy transfer he obtained a semi-empirical equation to calculate the heat transfer. This correlation reads

[69, 70]

$$Nu = 7.0 + 0.025 \Big(\frac{Pe}{Pr_t} \Big)^{0.8},\qquad (2.6)$$

where the Pr_t is the turbulent Prandtl number. During a large period of time the collection of data on liquid metals has produced many independent and contradictory correlations. We report some of them

$$Nu = 7.0 + 0.025 \Big(Pe \frac{Pr(\frac{\epsilon_M}{\nu})_{max}^{1.4} - 1.82}{Pr(\frac{\epsilon_M}{\nu})_{max}^{1.4}} \Big) \qquad 10^4 \le Re \le 5 \cdot 10^6, \qquad (2.7)$$

$$Nu = 4.82 + 0.0185\,Pe^{0.827} \qquad\qquad 10^4 \le Re \le 5 \cdot 10^6, \qquad (2.8)$$

$$Nu = 6.3 + 0.0167\,Pe^{0.85}\,Pr^{0.08} \qquad\quad 10^4 \le Re \le 5 \cdot 10^6, \qquad (2.9)$$

$$Nu = 4.5 + 0.014\,Pe^{0.8} \qquad\qquad\quad 10^4 \le Re \le 5 \cdot 10^6, \quad (2.10)$$

$$Nu = 3.6 + 0.018\,Pe^{0.8} \qquad\qquad\qquad 88 < Pe < 4000. \quad (2.11)$$

The correlation (2.7) was proposed by Dwyer [33]. Based on experimental NaK heat transfer test data, the correlations in (2.8) and (2.9) were written by Skupinski and Sleicher [102, 103]. Performing heat transfer tests in LBE pipe flows Ibragimov proposed his correlation reported in (2.10), [53]. Stromquist carried out a systematic work with mercury over a large range of Peclet number, after his studies he proposed (2.11), [105]. Recently Kirillov and Ushakov, after a long analysis on existing correlations and experimental data, recommended the following expression [62]

$$Nu = 4.5 + 0.018\,Pe^{0.8} \quad 10^4 \le Re \le 5 \cdot 10^6. \qquad (2.12)$$

In Figure 2.2 we show the Nusselt number of the different above mentioned correlations calculated with $Pr = 0.025$: Lyon with $Pr_t = 1.8$ (A), Kirillov (B), Skupinski (C), Sleicher (D), Ibragimov (E) and Stromquist (F). It is important to remark that there exists a large discrepancy between data collected from different fluids and from different authors but Kirillov correlation is taken as reference correlation as usually done in the most recent literature. Skupinski (C) and Sleicher (D) correlations, based on NaK test data, give higher heat transfer coefficients than other correlations proposed for Mercury and LBE flows. In the low Peclet number region, the correlations of Kirillov and Ibragimov show a similar heat transfer while Stromquist correlation is different, whereas at high Peclet number, the Stromquist correlation predicts a higher heat transfer coefficient than the Ibragimov correlation. The correlation of Lyon with the standard turbulent Prandtl number $Pr_t = 0.9$ gives much higher heat transfer coefficients than any other correlation considered. Therefore this correlation has been modified setting the turbulent Prandtl number to 1.8.

2.3.2   Triangular rod bundle

The most consistent and numerous heat transfer experimental data for rod bundle geometries are those in triangular geometry that are reported in form of experimental heat transfer correlations. This geometry is defined in Figure 2.3, where a triangular bundle configuration is shown. In a nuclear core the fuel pellets are located inside the cylindrical tubes and the coolant flows in the gaps between the tubes. In this figure the rod diameter is labeled by D and the bundle crosswise transverse pitch by P. The so called pitch-to-diameter ratio $\chi = P/D$ is an important data in the parametric investigation since many experimental data are grouped with respect to χ because of the similarity of flow patterns encountered studying geometries with similar χ. Triangular rod bundle correlations are important also because they can be compared with experimental results in hexagonal bundle geometries because of the similarity between these two geometries [93]. In many cases, however, the experimental data collected from different authors should be used with care since they exhibit extreme sensitivity to experimental conditions such as depositions of impurities on rod surfaces and surface roughness [27].

In Figure 2.4 different heat transfer correlations obtained from experimental data are shown for different pitch-to-diameter ratios χ. In this figure the Nusselt number is shown as a function of Peclet number for $\chi = 1.2$ on top, 1.3 on the middle and 1.5 on the bottom. The first correlations for heat
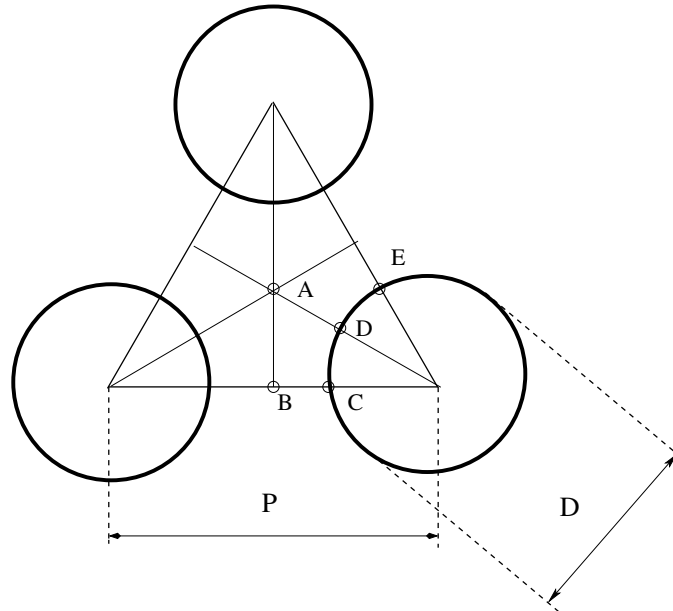
Figure 2.3:   Triangular rod bundle geometry.
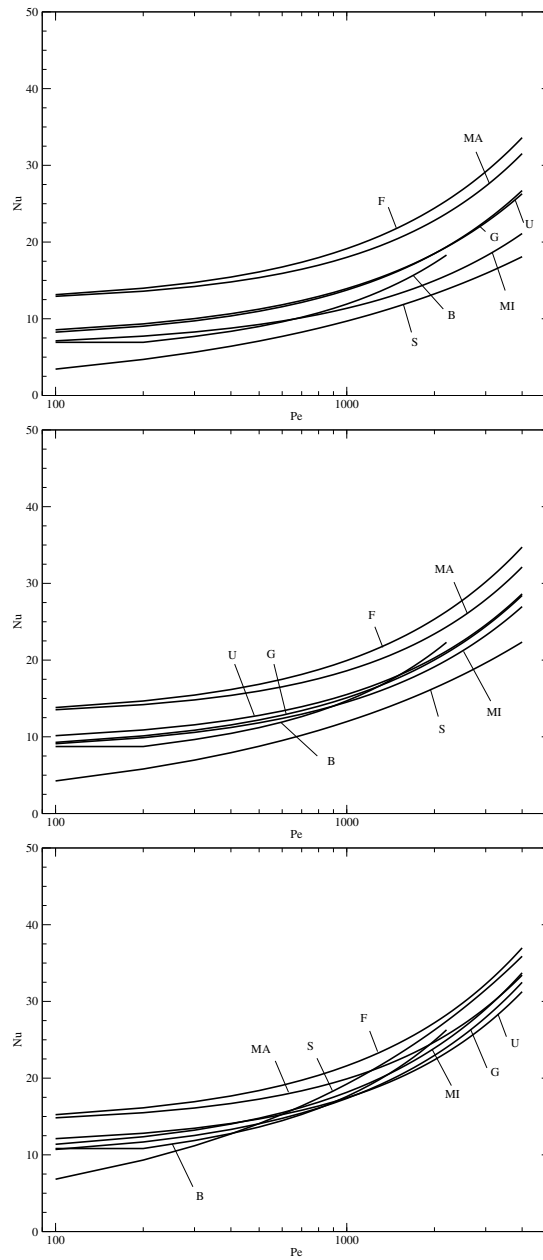
Figure 2.4: Nusselt number as a function of Peclet number in the triangular rod bundle geometry from Friedland (F), Mareska (MA), Subbotin (S), Graber (G), Ushakov (U) and Mikityuk (MI) correlations and for different pitch-to-diameter ratio $\chi = 1.2$ (top), 1.3 (middle) and 1.5 (bottom).

transfer of liquid metal flowing in a triangular bundle of circular rods were derived by Dwyer and Friedland. These correlations are semi-empirical and

they are based on different assumptions about the velocity profile. Dwyer correlation reads [33]

$$Nu = 0.93 + 10.81\,\chi - 2.01\,\chi^2 + 0.0252\,\chi^{0.273}\,(\psi Pe)^{0.8} \qquad (2.13)$$

while Friedland correlation is [36]

$$Nu = 7.0 + 3.8\,\chi^{1.52} + 0.027\,\chi^{0.27}\,(\psi Pe)^{0.8}\,, \qquad (2.14)$$

where ψ is the ratio between the eddy diffusivity of heat and the eddy diffusivity of momentum, which is basically the inverse of the turbulent Prandtl number. The ratio of the eddy diffusivities of heat and momentum in this correlation is assumed equal to one if the analogy hypothesis between heat and momentum transfer is assumed to be true as for air, water and similar fluids. The correlation (2.13) is valid for Peclet numbers of 70 up to 10^4 and pitch-to-diameter ratios of 1.375 up to 2.2, while the range of applicability of the second correlation, shown in Figure 2.4 with label F, is defined for $Pe = 0$-10^5 and $\chi = 1.3$-10.

Early experimental investigations have been performed at the Brookhaven National Laboratories in a 13-pin-bundle cooled with mercury and in a 19-pin-bundle cooled with a sodium-potassium alloy (NaK) and arranged in an equilateral triangular lattice with the pitch-to-diameter ratio χ of 1.75. These experimental results lead to the following Mareska-Dwyer heat transfer correlation [80]

$$Nu = 6.66 + 3.126\chi + 1.184\chi^2 + 0.0155\,(\psi Pe)^{0.86}\,, \qquad (2.15)$$

where the factor ψ can be approximated by the empirical equation

$$\psi = 1 - \frac{1.82}{Pr(\epsilon_M/\nu)_{max}^{1.4}}\,, \qquad (2.16)$$

$$\log(\epsilon_M/\nu)_{max} \approx 0.864\,\log(Re) - 0.24\,\chi - 2.12\,. \qquad (2.17)$$

The correlation (2.15), shown (for $\psi = 1$) in Figure 2.4 with label (MA), is valid for triangular bundles in the range 70-10^4 Pe and pitch-to-diameter ratio χ of 1.3-3.

Subbotin proposes the following correlation for the flow of liquid metal in a triangular rod lattice with the pitch-to-diameter ratio of 1.1-1.5 and Peclet numbers of 80-4000 [107]

$$Nu = 0.58\left(\frac{2\sqrt{3}}{\pi}\chi^2 - 1\right)^{0.55} Pe^{0.45}\,. \qquad (2.18)$$

This correlation, shown in Figure 2.4 with label S, is based on theoretical consideration by using the D_{eq}/D ratio for the triangular lattice as

$$\frac{D_{eq}}{D} = \frac{2\sqrt{3}}{\pi}\chi^2 - 1 \,, \tag{2.19}$$

where D_{eq} and D are the hydraulic diameter and the rod diameter, respectively.

Borishanski performed experimental tests on seven tubes of 22 mm of diameter arranged in equilateral triangular bundles with four different pitch-to-diameter ratios $P/D = 1.1$, 1.3, 1.4 and 1.5. Three working fluids were analyzed with Prandtl numbers 0.007, 0.03 and 0.024. The total of 230 (Nu, Pe) points were measured. On the basis of this data, the following correlation was derived [17]

$$Nu_l = 24.15 \log(-8.12 + 12.76\,\chi - 3.65\chi^2) \quad Pe < 200 \tag{2.20}$$
$$Nu = Nu_l + 0.0174\,(1 - e^{-6(\chi-1)})(Pe - 200)^{0.9} \quad Pe \geq 200 \,. \tag{2.21}$$

Eq. 2.21, shown in Figure 2.4 with label B, is recommended for triangular bundles in the range of Peclet numbers 60-2200 and pitch-to-diameter ratios 1.1-1.5.

Graber correlation reads [40]

$$Nu = 0.025 + 6.2\chi + (0.032\chi - 0.007)\,Pe^{0.8 - 0.024\chi} \quad Pe \leq 2500 \,. \tag{2.22}$$

Three sets of experimental data were measured by Graber with the test sections consisting of 31 tubes of 12 mm of diameter arranged in equilateral triangular bundles with pitch-to-diameter ratios of 1.25, 1.6 and 1.95. The working fluid was NaK at temperatures from 100° to 425^oC. The Prandtl number varied with temperatures from 0.011 to 0.024. A total of 246 data pairs (Nu, Pe) were given for the range of the Peclet numbers 110-4300. As one can see from Figure 2.4 the Graber correlation (labeled with G) and the Ushakov correlation (labeled with U) are very close for pitch-to-diameter ratio of 1.2-1.3.

The reference correlation for triangular bundle geometry nowadays is Ushakov correlation [63]

$$Nu = 7.55\,\chi - 20/\chi^{13} + (0.041/\chi^2)\,Pe^{0.56 + 0.19\chi} \,. \tag{2.23}$$

This correlation is shown in Figure 2.4 with label U and it is recommended for the study of heat transfer in liquid metal flows in a triangular rod lattice with pitch-to-diameter ratio of 1.3-2.0 and Peclet numbers up to 4000 [34].

We recall also the recent Mikityuk correlation [83]

$$Nu = 0.025 + 6.2\chi + (0.032\chi - 0.007)\, Pe^{0.8-0.024\chi} \quad 30 \leq Pe \leq 4000\,. \quad (2.24)$$

The correlation in (2.24), shown in Figure 2.4 with label MI, refers to a statistical correlation obtained by the collection of several data obtained in rod bundle geometry.

2.3.3 Square rod bundle

The square rod bundle geometry has been considered for the design of the core of nuclear reactors and it consists of a bundle of parallel cylindrical tubes with diameter D arranged with their axis forming a square with side P. In Figure 2.5 a scheme of this geometry is reported. Some heat transfer correlations for the prediction of the Nusselt number as a function of Peclet number and $\chi = P/D$ ratio are available for fully developed flows of heavy liquid metals with low-Prandtl number in square lattice bare rod bundle geometries. In the following we review the most important ones. There are no many experimental data for the flow configuration of interest, so the correlations should be used with care. In many cases the correlations for square lattice geometry are obtained from the corresponding correlations for triangular rod bundle geometry.

In the work by Subbotin et al. a correlation derived for the triangular lattice is applied to the square lattice by adjusting the ratio D_h/D to $\frac{2}{\pi}\chi^2 - 1$,
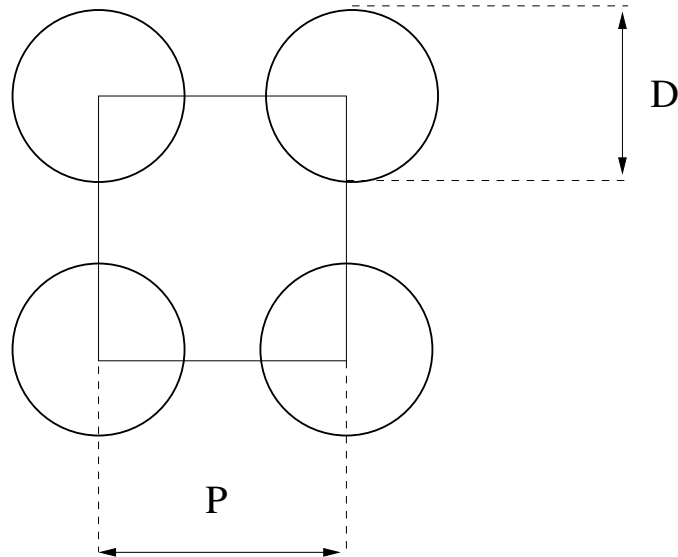
Figure 2.5: Geometry of a square lattice bare rod bundle.
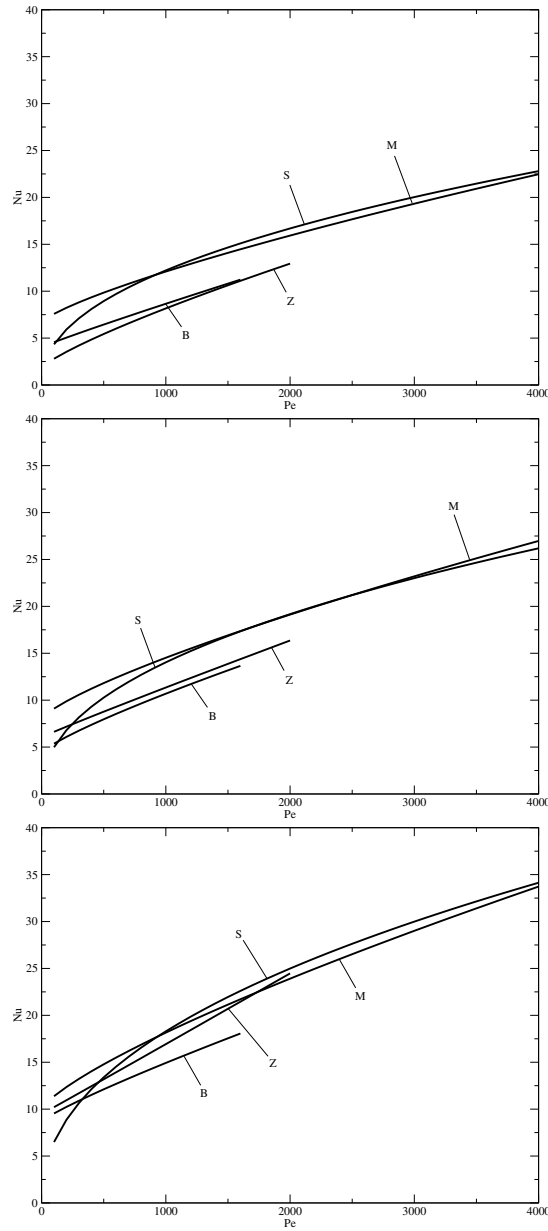
Figure 2.6: Experimental heat transfer correlations for the prediction of the Nusselt number as a function of the Peclet number for heavy liquid metal flows in square lattice bare rod bundle geometries. Subbotin, Zhukov, BREST and Mikityuk correlations are labeled by (S), (Z), (B) and (M). From top to bottom $\chi = 1.22$, 1.3 and 1.5.

see [107]. For square lattices it takes the form

$$Nu = 0.58 \left(\frac{4}{\pi} \chi^2 - 1 \right)^{0.55} Pe^{0.45} . \tag{2.25}$$

This correlation is proposed for a square lattice of rods with pitch-to-diameter ratio of 1.1-1.5 and Peclet numbers of 80-4000.

The report issued in frame of the BREST lead-cooled reactor recommends also for square arrays a correlation which is derived by the triangular arrays one using equivalent pin flow area in triangular (hexagonal) and square lattice bare rod bundle arrangements [6]. The BREST correlation reads

$$Nu = 7.55\,\chi - 20\chi^{-5} + \frac{0.00354}{\chi^2}\,Pe^{0.64+0.246\chi} \tag{2.26}$$

It is reported that (2.26) was verified for P/D ratios of 1.28 and 1.46 in the range $100 < Pe < 1600$.

An experimental investigation in square lattice bare rod bundles has been performed by Zhukov, see [114]. The experimental results were correlated by

$$Nu = 7.55\,\chi - 14\chi^{-5} + 0.007\,Pe^{0.64+0.246\chi}\,, \tag{2.27}$$

for the case of tube bundles with no spacers. The working section of this experimental program consisted of 25 tubes with diameter $D = 12$ mm. Four groups of experimental data with pitch-to-diameter ratios of 1.25, 1.28, 1.34 and 1.46 were measured. However only a total of 36 data pairs (Nu, Pe) are given in this experimental work for the range of the Peclet numbers of 60-2000.

Finally we report the correlation by Mikityuk who recently obtained a heat transfer correlation for liquid metals from a wide database of both triangular and square lattice bare rod bundle experimental studies [83]. The correlation is claimed to be valid for rod lattices with $\chi = 1.1\text{-}1.95$ and $Pe = 30\text{-}5000$ and it reads

$$Nu = 0.047\left(1 - \exp^{-3.8(\chi-1)}\right)\left(Pe^{0.77} + 250\right)\,. \tag{2.28}$$

Due to the limited availability of experimental data for square lattice bare rod bundles in this database, Mikityuk recommends caution in the use of the correlation for this geometry [83]. More experimental results or CFD analysis are needed in order to better understand the differences in the heat transfer between triangular and square lattice bare rod bundles.

In Figure 2.6 we report all these correlations for the three considered geometries. From top left to bottom right the four correlations are plotted for the parameter $\chi = 1.22$, 1.3 and 1.5, respectively. Subbotin correlation (S), Zhukov (Z), BREST (B) and Mikityuk (M) are reported. From these figures it can be seen that Subbotin and Mikityuk correlations predict high heat transfer, while Zhukov and BREST ones are more conservative. For the case $\chi = 1.5$ Zhukov correlation shows a peculiar behavior with a quite high slope, crossing the lines of the other correlations.

Chapter 3

Turbulence model k-ϵ-k_θ-ϵ_θ

In this Chapter we describe the four equation turbulence model k-ϵ-k_θ-ϵ_θ and report several numerical results obtained with the implementation of this model in a finite element code for multiphysics simulations. In the first section the mathematical formulation of the model is reported together with a discussion on the boundary conditions to be used. The second section is dedicated to numerical results obtained in several geometries interesting in the nuclear engineering field. Results obtained in plane, cylindrical, triangular rod bundle and square rod bundle geometries are reported and compared with DNS data and experimental correlations. The overall estimation of heat transfer of this model can be considered satisfactory for these flows.

3.1   Mathematical formulation

The motion of incompressible fluids is based on Navier-Stokes and energy balance equations. Since liquid metals in normal operative conditions can be considered as incompressible fluids, it is customary to use Navier-Stokes system to simulate liquid metal flows. In order to describe turbulent flows, one can apply the Reynolds averaging procedure to the fundamental dynamic equations and obtain a set of transport equations for averaged fields. In order to solve for the flow variables $(\mathbf{u}, p, T)$ we consider the incompressible Navier-Stokes system

$$\nabla \cdot \mathbf{u} = 0\,, \tag{3.1}$$

$$\rho \frac{\partial \mathbf{u}}{\partial t} + \rho(\mathbf{u} \cdot \nabla)\mathbf{u} = \nabla \cdot \sigma - \nabla \cdot (\rho \overline{\mathbf{u}'\mathbf{u}'}) + \rho \mathbf{g}\,, \tag{3.2}$$

$$\rho C_p \left(\frac{\partial T}{\partial t} + (\mathbf{u} \cdot \nabla)T \right) = \nabla \cdot \mathbf{q} - \nabla \cdot (\rho C_p \overline{\mathbf{u}'T'}) + Q\,, \tag{3.3}$$

where $\mathbf{u}$ and T are the average velocity and temperature fields. Moreover, the Reynolds stress tensor $\overline{\mathbf{u'u'}}$ is the average product of velocity fluctuations while the turbulent heat flux vector $\overline{\mathbf{u'}T'}$ is the average product of velocity and temperature fluctuations. We also define the stress tensor σ and the velocity deformation tensor $\mathbf{S}$ as

$$\sigma_{ij} := -p\delta_{ij} + \mu S_{ij} \qquad S_{ij} := \frac{\partial u_i}{\partial x_j} + \frac{\partial u_j}{\partial x_i} , \qquad (3.4)$$

where μ is the molecular viscosity and p the so-called average static pressure. In (3.2-3.3) the unknown Reynolds stress $\overline{\mathbf{u'u'}}$ and the turbulent heat flux $\overline{\mathbf{u'}T'}$ can be seen as solutions of two transport equations: the Reynolds stress transport equation and the turbulent heat flux transport equation [82].

Direct solutions of Reynolds stress transport equation and of turbulent heat flux transport equation are difficult to obtain. By using the concept of the eddy viscosity one may model the Reynolds stresses. For general flow situations the eddy viscosity model may be written as

$$\rho\overline{u_i'u_j'} = -\nu_t \left(\frac{\partial u_i}{\partial x_j} + \frac{\partial u_j}{\partial x_i} \right) + \frac{2k}{3}\,\delta_{ij} , \qquad (3.5)$$

where k and ν_t are the turbulent kinetic energy and the turbulent viscosity, respectively. The last term in (3.5) assures that the sum of the normal stresses is equal to $2k$, which is required by the definition of k. The normal stresses act like pressure forces, so they can be absorbed into the pressure-gradient term and the static pressure is replaced as an unknown quantity by the modified pressure.

One of the most popular model to compute the turbulent viscosity ν_t is

$$\nu_t := C_\mu\, k\tau_{lu} \qquad (3.6)$$

where $C_\mu = 0.09$ and τ_{lu} is the local dynamical characteristic time that takes into account the corrections near the wall region. The turbulent kinetic energy, its dissipation and its specific dissipation are defined by

$$k := \frac{1}{2}\overline{u_i'u_i'} \qquad \epsilon := \nu\overline{\left(\frac{\partial u_i'}{\partial x_j} \right) \left(\frac{\partial u_i'}{\partial x_j} \right)} . \qquad (3.7)$$

The equation for k can be written in the following form

$$\frac{\partial k}{\partial t} + (\mathbf{u} \cdot \nabla)k = \nabla \cdot \left[\left(\nu + \frac{\nu_t}{\sigma_k} \right) \nabla k \right] + P_k - \epsilon . \qquad (3.8)$$

with

$$P_k := -\overline{\mathbf{u'u'}} : \nabla\mathbf{u} = \nu_t\mathbf{S} : \nabla\mathbf{u} . \qquad (3.9)$$

The local dynamical characteristic time τ_{lu} can be modeled in many ways with the introduction of the proper dynamical characteristic time $\tau_u = k/\epsilon$. Since we intend to study also low Reynolds number flows and a near wall approach for the solution of the velocity field, a second order expansion around the wall can be written as [4, 88]

$$\tau_{lu} = \left(f_{1\mu} \, A_{1\mu} + f_{2\mu} \, A_{2\mu} \right), \tag{3.10}$$

where the functions $f_{1\mu}$, $A_{1\mu}$, $f_{2\mu}$ and $A_{2\mu}$ are appropriate for modeling the near wall behavior. We set

$$f_{1\mu} = (1 - \exp(-0.0714 \, R_\delta))^2 \tag{3.11}$$

$$A_{1\mu} = \tau_u \tag{3.12}$$

$$f_{2\mu} = f_{1\mu} \, \exp(-2.5 \times 10^{-5} \, R_t^2) \tag{3.13}$$

$$A_{2\mu} = \tau_u \, \frac{5}{R_t^{3/4}} \tag{3.14}$$

where $R_t = k^2/\nu\epsilon$ and $R_\delta = \delta(\epsilon\nu)^{1/4}/\nu$ with δ the distance from the wall are the turbulent Reynolds number and a non dimensional distance from the wall. The term labeled with 1 is the bulk term that vanishes on the wall with τ_u. The term labeled with 2 is the second order term that modifies the incorrect behavior of ν_t as it approaches the wall. This model can reproduce the near-wall turbulence asymptotic behavior, i.e., $k \propto \delta^2$, $\epsilon \propto \delta^0$ and $\nu_t \propto \delta^3$ for δ tending to zero. For details one can see [4, 88].

The turbulent energy dissipation ϵ can be computed by using a two-equation k-ϵ turbulence model. For this purpose one can write the equation for the dissipation ϵ as

$$\frac{\partial \epsilon}{\partial t} + (\mathbf{u} \cdot \nabla)\epsilon = \nabla \cdot \left[\left(\nu + \frac{\nu_t}{\sigma_\epsilon} \right) \nabla \epsilon \right] + C_{1\epsilon} \frac{\epsilon}{k} P_k - C_{2\epsilon} \, f_\epsilon \frac{\epsilon^2}{k}, \tag{3.15}$$

with $C_{1\epsilon} = 1.5$, $C_{2\epsilon} = 1.9$, $C_\mu = 0.09$, $\sigma_k = 1.4$, $\sigma_\epsilon = 1.4$, P_k defined by (3.9) and f_ϵ defined as

$$f_\epsilon = (1 - \exp(-0.3226 \, R_\delta))^2 \left(1 - 0.3 \exp(-0.0237 \, R_t^2) \right). \tag{3.16}$$

In a similar way we can approximate the turbulent heat flux transport equation with an algebraic solution which needs a two-equation turbulence model to be computed. For this transport equation we may approximate the solution as

$$\rho C_p \overline{\mathbf{u}'T'} = -\alpha_t \, \nabla T, \tag{3.17}$$

where α_t is the turbulent thermal diffusivity. In analogy with the dynamical case the thermal diffusivity α_t may be defined as

$$\alpha_t = C_\theta \, k \tau_{l\theta} \,, \tag{3.18}$$

where $C_\theta = 0.1 = C_\mu/0.9$ and $\tau_{l\theta}$ is the local thermal characteristic time that takes into account the corrections near the wall region. In analogy with the definitions in (3.7) we introduce the average square temperature fluctuation k_θ, its dissipation ϵ_θ and its specific dissipation ω_θ as

$$k_\theta := \frac{1}{2}\overline{T'^2} \,, \qquad \epsilon_\theta := \alpha\overline{(\nabla T')^2} \,, \tag{3.19}$$

and define the characteristic time $\tau_\theta = k_\theta/\epsilon_\theta$ and the ratio $R = \tau_\theta/\tau_u = \epsilon\, k_\theta/(\epsilon_\theta\, k)$ between the thermal turbulent characteristic time and the dynamical turbulent characteristic time.

The local thermal characteristic time $\tau_{l\theta}$ can be modeled in a similar way as done in the dynamical case with the introduction of the proper thermal characteristic time $\tau_\theta = k_\theta/\epsilon_\theta$ as

$$\tau_{l\theta} = \left(f_{1\theta}\, B_{1\theta} + f_{2\theta}\, B_{2\theta} \right) , \tag{3.20}$$

where $f_{1\theta}$, $B_{1\theta}$, $f_{2\theta}$ and $B_{2\theta}$ are appropriate functions. We set

$$f_{1\theta} = (1 - \exp(-0.0526\,\frac{R_\delta}{\sqrt{Pr}}))\,(1 - \exp(-0.0714\,R_\delta)) \tag{3.21}$$

$$B_{1\theta} = \tau_u\, C_\infty \tag{3.22}$$

$$f_{2\theta}\, B_{2\theta} = \tau_u \left(f_{2a\theta}\,\frac{2\,R}{R + C_\gamma} + f_{2b\theta}\sqrt{\frac{2\,R}{Pr}}\,\frac{1.3}{\sqrt{Pr}R_t^{3/4}} \right) , \tag{3.23}$$

where $C_\gamma = 0.3$, $C_\infty = 0.9$, $f_{2a\theta} = f_{1\theta}\,\exp(-4{\cdot}10^{-6}\,R_t^2)$, $f_{2b\theta} = f_{1\theta}\,\exp(-2.5{\cdot}10^{-5}\,R_\delta{}^2)$. There are three characteristic times in this modeling: the asymptotic dynamical time τ_u, the thermal time $\tau_\theta = R\,\tau_u$ and the mixed time τ_m, which is defined as $1/\tau_m = 1/\tau_u + 1/\tau_\theta = (R + C_\gamma)/(2\,\tau_u\,R)$. The dynamical time τ_u is proportional to the turbulent viscosity through (3.6). Near the wall α_t/τ_u is proportional to $\sqrt{R}$ while in the asymptotic region α_t is independent of the time ratio. In the intermediate regions α_t/τ_u is proportional to $2\,R/(R + C_\gamma)$. The model functions f_j blend different behaviors in different regions. For details one can refer to [4, 30, 50, 52, 88] and references therein.

The average square temperature fluctuation k_θ is defined by the following transport equation [50]

$$\frac{\partial k_\theta}{\partial t} + (\mathbf{u} \cdot \nabla)k_\theta = \nabla \cdot \left(\alpha + \frac{\alpha_t}{\sigma_{k_\theta}} \right) \nabla k_\theta + P_\theta - \epsilon_\theta \,, \tag{3.24}$$

where

$$P_\theta := -\overline{\mathbf{u}'T'} \cdot \nabla T = \alpha_t \, \nabla T \cdot \nabla T \,. \tag{3.25}$$

By following the same procedure as in the dynamical case the equation for ϵ_θ can be written as [50]

$$\frac{\partial \epsilon_\theta}{\partial t} + (\mathbf{u} \cdot \nabla)\epsilon_\theta = \nabla \cdot \left[\left(\alpha + \frac{\alpha_\theta}{\sigma_{\epsilon_\theta}} \right) \nabla \epsilon_\theta \right] +$$
$$\frac{\epsilon_\theta}{k_\theta} \left(C_{p1} \, P_\theta - C_{d1} \, \epsilon_t \right) + \frac{\epsilon_\theta}{k} \left(C_{p2} \, P_k - C_{d2} \, \epsilon \right), \tag{3.26}$$

where P_k is defined by (3.9) and P_θ by (3.25). For heavy liquid metals, with $Pr \approx 0.025$, we have used the coefficients defined in [3, 89], namely $C_{d1} = 0.9$, $C_{p2} = 0.9$, $\sigma_{k_\theta} = 1.4$ $\sigma_{\epsilon_\theta} = 1.4$. The coefficient C_{p1} has been chosen to be 0.925 and

$$C_{d2} = (1.9 \, (1 - \exp(-0.1754 \, R_\delta)^2) - 1) \, (1 - 0.3 \, \exp(-0.0237 \, R_t^2)) \,. \tag{3.27}$$

For details one can see [50, 52, 65].

If the system (3.24)-(3.26) is solved then the function R can be computed as $(k/\epsilon)/(k_\theta/\epsilon_\theta)$, and the corresponding turbulent thermal diffusivity α_t and the turbulent heat flux can be substituted in the energy equation.

In order to complete the definition of the problem, appropriate boundary conditions must be imposed. The boundary conditions and the use of appropriate wall functions for the k_θ-ϵ_θ system are under broad discussion [50, 52]. This is a very important issue since they can modify the solution and the computational effort. We consider a near-wall approach for both the dynamical and thermal fields. In literature three types of boundary conditions are considered: constant temperature, constant heat flux and mixed boundary conditions [3, 89, 96].

The constant temperature boundary condition assumes that the wall temperature is uniform in space and constant in time, therefore the average temperature squared fluctuations have to be set to zero on the wall. For fixed temperature boundary conditions we consider the following expansion for thermal fields around a wall point

$$T' \approx b\delta + c\delta^2 + \ldots \tag{3.28}$$

$$k_\theta = \frac{\overline{T'^2}}{2} \approx \frac{\overline{b^2}}{2}\delta^2 + \ldots \tag{3.29}$$

$$\epsilon_\theta = \alpha \overline{\left(\frac{\partial T'}{\partial x_j} \right)^2} \approx \alpha \overline{b^2} + \ldots, \tag{3.30}$$

where δ is the distance from the wall. This is easily imposed by using

$$\frac{dk_\theta}{d\delta} \approx \frac{2\,k_\theta}{\delta} \quad \epsilon_\theta \approx \alpha \frac{2\,k_\theta}{\delta^2} \ . \tag{3.31}$$

Some authors assume full isotropy for all the gradient components on the walls and set $\epsilon_\theta \approx 6\,\alpha k_\theta/\delta^2$ instead of (3.31). Since this expansion is true also for k and ϵ we have

$$\frac{dk}{d\delta} \approx \frac{2\,k}{\delta} + \ldots \qquad \epsilon \approx \nu \frac{2\,k}{\delta^2} + \ldots \ , \tag{3.32}$$

and therefore

$$R = \frac{\epsilon\,k_\theta}{k\,\epsilon_\theta} \approx Pr \ . \tag{3.33}$$

This implies that for uniform wall temperature boundary conditions the time ratio R must tend to Pr at the wall, as seems to be correct from physical considerations and is assumed in many DNS computations [56, 57, 58, 100].

The constant heat flux boundary condition assumes that the wall heat flux is uniform in space and constant in time. This implies that the wall normal derivative of the average square temperature fluctuation has to be set to zero. In this case temperature fluctuations are possible and k_θ may be different from zero on the wall. For constant uniform wall heat flux boundary condition we consider the following expansion for thermal fields

$$T^{'} \approx a + c\delta^2 + \ldots \tag{3.34}$$

$$k_\theta = \frac{\overline{T^{'2}}}{2} \approx \frac{\overline{a^2}}{2} + \overline{ac}\delta^2 + \frac{\overline{c^2}\delta^4}{2} + \ldots \tag{3.35}$$

$$\epsilon_\theta = 2\,\alpha \Big(\frac{\partial \sqrt{k_\theta - k_{\theta w}}}{\partial \delta}\Big)^2 \approx 2\alpha\,\overline{ac} + \ldots \ . \tag{3.36}$$

This means that

$$\frac{dk_\theta}{d\delta} \approx 0 + \ldots \quad \epsilon_\theta \approx 2\alpha\,\overline{ac} + \ldots \ , \tag{3.37}$$

and

$$R = \frac{\epsilon\,k_\theta}{k\,\epsilon_\theta} \approx Pr\frac{\overline{a^2} + 2\overline{ac}\delta^2 + \overline{c^2}\delta^4}{d\,\delta^4} + \ldots \ . \tag{3.38}$$

From (3.38) if k_θ does not tend to zero, $\overline{a^2}$ does not tend to zero and R cannot be finite for $\delta \to 0$. However this behavior of R may not be important

since the behavior of the turbulent viscosity can still give finite values of the thermal diffusivity α_t close to the wall.

The mixed boundary conditions assumes that the wall heat flux is uniform in space and the temperature constant in time. The average square temperature fluctuation is set to zero on the wall and the time ratio R is equal to Pr on the wall. For a detailed discussion on the boundary conditions one can refer to [96, 104, 111].

3.2   Numerical simulations

This section is devoted to the evaluation of the performance of the k-ϵ-k_θ-ϵ_θ heat transfer model in several geometries in forced turbulent flows with no gravity. As already explained in the previous section, this model consists of the k-ϵ system for the transport of turbulent momentum in (3.8-3.16) and the k_θ-ϵ_θ two-equation model for the transport of turbulent energy in (3.18) and (3.20-3.27). In order to validate the four parameter model for heavy liquid metals in the range of 0.01 to 0.03 we consider the reference Prandtl number $Pr = 0.025$. This Prandtl number is the reference value for this class of fluids since a relatively large amount of experimental data and DNS computations are available for comparison, see Chapter 2 for more details.

In the next section the results obtained with the k-ϵ-k_θ-ϵ_θ turbulence model is compared with DNS data in plane geometry. DNS data are available for fully developed flows and over a limited low Reynolds number range. As we have discussed in Section 2.3.1, the most consistent and numerous heat transfer experimental data can be found for cylindrical geometry as experimental heat transfer correlations. In particular, the reference correlation for this molecular Pr number is Kirillov correlation. The purpose of the next two sections is to compare the numerical results of the four parameter model with plane DNS computations at low Reynolds numbers and extend the comparison to the high Reynolds numbers in order to reproduce the available data in cylindrical geometry [74].

In the following third and four sections two more complex geometries are studied, the triangular and square rod bundle geometries [75, 76]. Simulations are performed in a wide range of pitch-to-diameter ratios and Peclet numbers. The comparison is performed with available experimental correlations for this class of geometry of interest in the nuclear field, see Sections 2.3.2 and 2.3.3 for more details on these geometrical configurations.

3.2.1   Plane channel

The plane channel heat transfer problem has been studied extensively by many authors in the past as this type of geometry is the limiting case for other more complex geometries such as rectangular, cylindrical and annular ones. The DNS data in plane geometry have been presented by several authors [3, 5, 56, 60, 71, 89]. We refer mainly to the work in [56] since the results are reported in a database available on the web while writing this thesis. In this work the authors performed Direct Numerical Simulation of channel flows to study the effect of Reynolds and Prandtl numbers on turbulent heat transport. Three DNS cases with thermal computations, $Pr = 0.025$ and friction Reynolds number $Re_\tau = 180, 395, 640$ are available in this database. The bulk Reynolds numbers are in the range of $Re_m \approx 5500$ to 25000 with velocity, in our reference configuration, from 0.0162 to 0.068 m/s. Since these low velocities are not suitable for engineering applications, in order to extend computations to higher Reynolds we use the correlation for the cylindrical geometry in the following section, where experimental data are more numerous and accurate.

For this series of tests we consider a plane geometry, as shown in Figure 3.1 (top), with a fully developed turbulent liquid metal flowing between two plates located at a distance $L_y = 2l = 2 \cdot 0.03025$ m heated by uniform wall fluxes and with infinite length in the other two dimensions. Physical properties of the fluid are given in Table 3.1 (bottom) with corresponding molecular Prandtl number $Pr = 0.025$. We can subdivide the boundary of the computational domain into inlet, outlet, symmetry regions and solid
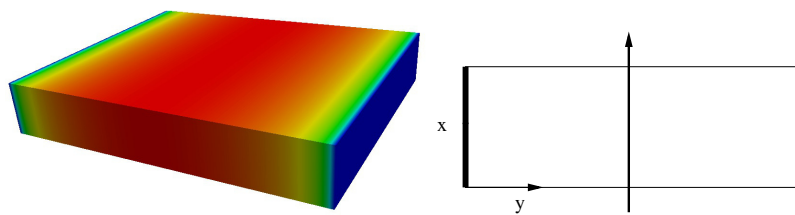
Properties		Values	Units
Density	ρ	10340.	kg/m^3
Dynamic viscosity	μ	18.1×10^{-4}	$Pa \cdot s$
Thermal conductivity	λ	10.72	$W/(m \cdot K)$
Specific heat capacity	C_p	145.75	$J/(kg \cdot K)$

Figure 3.1:   Plane case. Geometry (top) and physical properties at the reference temperature for $Pr = 0.025$ (bottom).

walls, which will be denoted by Γ_i, Γ_o, Γ_s and Γ_w, respectively.

The boundary conditions for the k-ϵ model are enforced by using the near-wall approach. The boundary conditions on the solid surfaces are imposed on a plane surface at a distance δ from the wall. The distance δ depends on the mesh size of the boundary layer region. We refine the mesh until the surface defined by the distance δ lies in the viscous laminar region ($y^+ < 1$), then we enforce the near-wall boundary condition asymptotic expansions

$$\tau_w := \frac{\rho\,\nu}{\delta}\,u_\tau\,, \quad u_n := 0\,, \quad k := k_{wl}\delta^2\,, \quad \epsilon := 2\nu k_{wl} = 2\frac{\nu k}{\delta^2}\,, \qquad (3.39)$$

on Γ_w. Since the constant k_{wl} is not known the condition has been applied in logarithmic form as $dk/dn = 2k/\delta$ on Γ_w.

It is well known that in a fully developed flow the bulk and wall temperature are linear. The slope of the linear profile for unit of vertical length ΔT_b can be computed by writing an energy balance in the volume as

$$2\,L_x\,L_z\,q_0 = C_p\,\dot{m}\Delta T_b\,L_x\,, \qquad (3.40)$$

with $\dot{m} = 2l\,\rho\,\bar{v}\,L_z$ the constant mass flow rate. The steady energy equation can be written as

$$(\mathbf{u}\cdot\nabla)\,T = \nabla\cdot\left[(\alpha + \alpha_t)\nabla T\right]\,, \qquad (3.41)$$

together with appropriate boundary conditions.

In the case of fully developed flow with uniform flux q_0, we may set

$$\lambda\frac{dT}{dn} := q_0 \qquad \text{on } \Gamma_w\,, \qquad (3.42)$$

$$T := T|_{\Gamma_i} + L_x\,\Delta T_b \qquad \text{on } \Gamma_o\,, \qquad (3.43)$$

where L_x is the axial length computational domain and $T|_{\Gamma_i}$ is the inlet temperature. This problem has not a unique solution since the integral form of (3.41), which is basically the (3.40), and (3.43) give the condition (3.42) under fully developed flow hypotheses. The solution becomes unique if one fixes the average value of T. This is equivalent to fix a point on the wall, i.e. the temperature of the first point of the wall is set to zero [96].

In many DNS computations the temperature results are reported in non-dimensional quantities dividing by reference friction variables. In order to define these quantities one can consider the temperature solution T in the form

$$T = T_{w0} + x\,\Delta T_b - \theta\,, \qquad (3.44)$$

where ΔT_b and T_{w0} are constant quantities and θ is the temperature distribution which is zero on the walls Γ_w. After introducing (3.44) into (3.41) we

have

$$(\mathbf{u} \cdot \nabla)\,\theta = \nabla \cdot [(\alpha + \alpha_t)\,\nabla\,\theta] + \frac{v\,q}{l\,\rho\,C_p\,\bar{v}} \quad, \tag{3.45}$$

with constant heat flux (CHF) boundary conditions

$$\theta := 0 \qquad \frac{dk_\theta}{dy} := 0 \qquad \epsilon_\theta := 2\,\alpha\Big(\frac{\partial\sqrt{k_\theta - k_{\theta w}}}{\partial y}\Big)^2 \quad \text{on } \Gamma_w\,, \tag{3.46}$$

$$\theta := \theta|_{\Gamma_o} \qquad k_\theta := k_\theta|_{\Gamma_o} \qquad \epsilon_\theta := \epsilon_\theta|_{\Gamma_o} \quad \text{on } \Gamma_i\,. \tag{3.47}$$

The (3.47) defines periodic boundary conditions for $T - \theta$, k_θ and ϵ_θ. In DNS simulations usually mixed boundary conditions for uniform heat flux (MX) are used, where the average square temperature fluctuation k_θ is set to zero on the wall. In this case the system (3.45-3.47) is the same but the condition $dk_\theta/dy = 0$ is substituted with $k_\theta = 0$. In mixed boundary condition the thermal boundary conditions for the k_θ-ϵ_θ system are similar to those for the k-ϵ system and they can be written as

$$k_\theta|_{\Gamma_w} = k_{\theta wl}\delta^2\,, \quad \epsilon_\theta|_{\Gamma_w} = 2\alpha k_{wl} = 2\frac{\alpha k_\theta}{\delta^2}\,. \tag{3.48}$$

The last condition for ϵ_θ on the wall is equivalent to set $R = Pr$.

Here we report the results obtained from seven different simulations with $Re \approx 5500$ (A), 13500 (B), 23250 (C), 40100 (D), 86200 (E), 204000 (F) and 345000 (G). They correspond to a mean velocity field from 0.0162 m/s to 1.0146 m/s in our reference configuration. The friction Reynolds numbers for these seven cases are $Re_\tau \approx 180$ (A), 395 (B), 640 (C), 1010 (D), 2000 (E), 4400 (F) and 7200 (G). The solution is obtained with the finite element code described in Chapter 1 but in two steps. First we reach convergence with regard to the velocity and k-ϵ fields and then we solve for the temperature and k_θ-ϵ_θ variables. This allows to use different solving parameters in order to obtain a better and faster convergence.

The mean velocity distribution of the axial component v for case A ($Re_\tau = 180$) and for case E ($Re_\tau = 2000$) is shown respectively on the left and right side of Figure 3.2. The behavior of other cases is similar and the linear and logarithmic regions are well reproduced. The velocity and length are non-dimensionalized based on friction velocity. We define the wall friction velocity and the friction Reynolds number in the following way

$$v_\tau = \sqrt{\frac{\tau_w}{\rho}} \qquad Re_\tau = \frac{v_\tau l}{\nu}\,, \tag{3.49}$$

in order to compute the non-dimensional velocity and distance from the wall as

$$v^+ = \frac{v}{v_\tau} \qquad y^+ = \frac{v_\tau y}{\nu}\,. \tag{3.50}$$
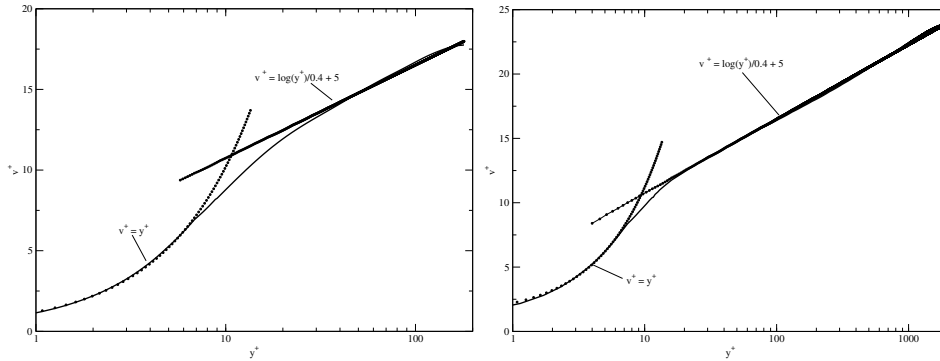
Figure 3.2: Plane case. Mean velocity distribution for $Re_\tau = 180$ (left) and $Re_\tau = 2000$ (right).
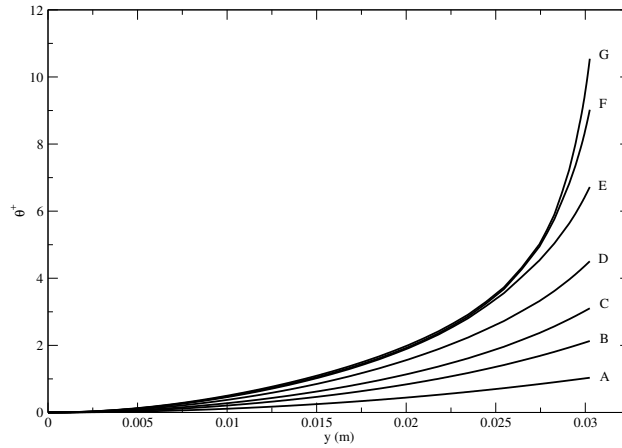
Figure 3.3: Plane case. Temperature distribution θ^+ for different velocities $Re_\tau = 180$ (A), 395 (B), 640 (C), 1010 (D), 2000 (E), 4400 (F) and 7200 (G).

In the linear region the normalized velocity follows the equation $v^+ = y^+$ while in the logarithmic region the equation $v^+ = (\log y^+)/0.4 + 5$.

In Figures 3.3-3.4 temperature distributions are shown for different velocities corresponding to $Re_\tau = 180$ (A), 395 (B), 640 (C), 1010 (D), 2000 (E), 4400 (F) and 7200 (G). In Figure 3.3 one can see the temperature $\theta = T - T_{w0} - x\,\Delta T_b$ which is the difference between the temperature and the linear behavior characteristic of the fully developed flow. This drop in temperature from the wall to the center of the channel is shown in non-dimensional unit $\theta^+ = \theta/T_\tau$ as a function of the dimensional distance from the wall y. The reference temperature T_τ is the so-called friction temperature which is $T_\tau = q/(v_\tau \rho C_p)$. In this case θ^+ is independent of the heat source which is assumed to be 360000 W/m^2. We remark the change in the profile
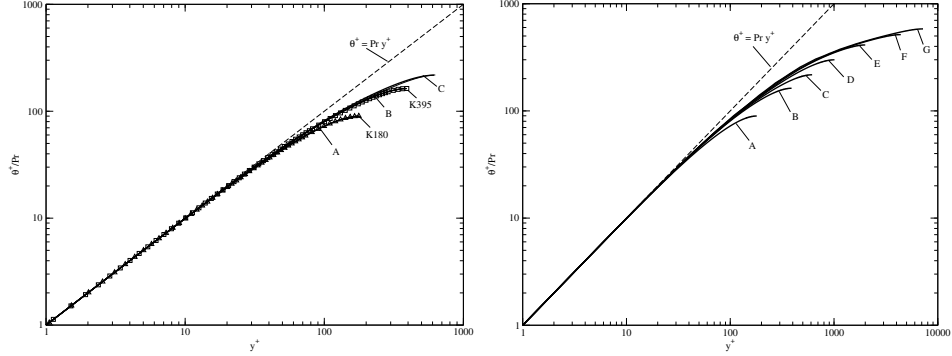
Figure 3.4: Plane case. Temperature distribution θ^+/Pr for different $Re_\tau = 180$ (A), 395 (B), 640 (C), 1010 (D), 2000 (E), 4400 (F) and 7200 (G) and comparison with DNS data for $Re_\tau = 180$ (K180) and $Re_\tau = 395$ (K395) on the left.

between case A with low Reynolds number, where the temperature follows a linear profile in nearly all the domain, and the case G with the highest velocity field, where the temperature slope is very high far from the wall.

In Figure 3.4 the non-dimensional temperature profiles θ^+/Pr are shown as functions of the non-dimensional coordinate y^+ and compared with DNS cases of $Re_\tau = 180$ (K180) and 395 (K395). This comparison can be seen on the left of Figure 3.4 where the DNS data (K180 triangles and K395 squares) are very close to the results obtained with the k-ϵ-k_θ-ϵ_θ model reported on the lines (A) and (B). Dividing by the Prandtl number we can show the linear behavior of the temperature distribution near the wall. A line $\theta^+ = y^+ Pr$ is plotted against the results obtained where it is visible the correct linear behavior predicted near the wall. For completeness on the right of the same Figure all the curves are reported enhancing the different behavior at higher Reynolds numbers. This log-log plot shows that all the curves are still linear about 20-30 y^+.

In Figure 3.5 the root-mean-square temperature fluctuation

$$\frac{{\theta_{rms}}^+}{Pr} = \frac{\sqrt{2k_\theta}}{(T_\tau Pr)} \tag{3.51}$$

for different velocities $Re_\tau = 180$ (A), 395 (B) and 640 (C) is shown on the left as a function of the non-dimensional wall distance y^+ together with the DNS data [56, 58]. The DNS simulation for $Re_\tau = 180$ is labeled K180 (square) and the DNS simulation for $Re_\tau = 395$ is labeled K395 (circle). The agreement between the k-ϵ-k_θ-ϵ_θ model results and the DNS simulation is very good. For completeness on the right of Figure 3.5 the root-mean-square temperature
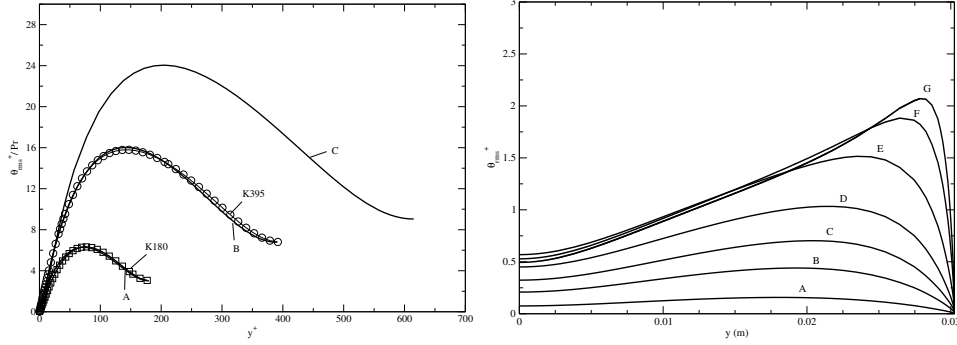
Figure 3.5: Plane case. On the right root-mean-square temperature fluctuations $\theta_{rms}{}^+$ for different $Re_\tau = 180$ (A), 395 (B) and 640 (C), 1010 (D), 2000 (E), 4400 (F) and 7200 (G) and comparison on the left of $\theta_{rms}{}^+/Pr$ with DNS data for $Re_\tau = 180$ (K180) and $Re_\tau = 395$ (K395) on the left.
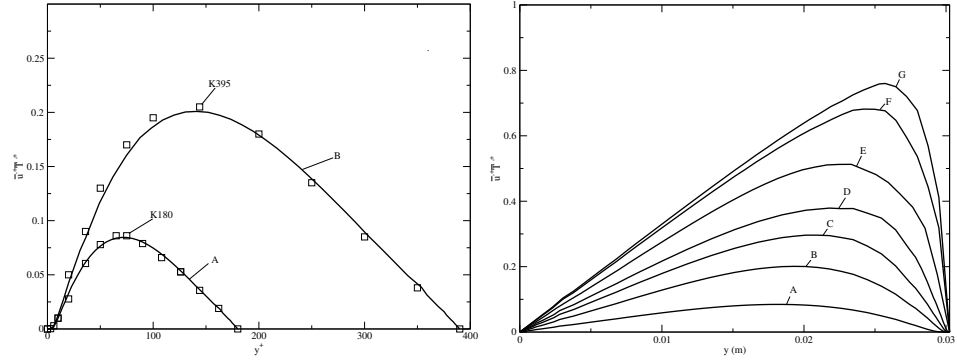
Figure 3.6: Plane case. Non-dimensional turbulent heat flux $\overline{u'T'}^+$ as a function of the coordinate y (on the right) and of the non-dimensional distance y^+ (on the left) for different $Re_\tau = 180$ (A), 395 (B), 640 (C), 1010 (D), 2000 (E), 4400 (F) and 7200 (G). The square dots are the DNS results for $Re_\tau = 180$ ($K180$) and $Re_\tau = 395$ ($K395$) on the left.

fluctuation $\theta_{rms}{}^+$ is reported as a function of a dimensional coordinate that starts from the center line of the channel, i.e. $y = 0.03025$ is the wall. In this Figure distributions are shown for all the different velocities simulated $Re_\tau = 180$ (A), 395 (B), 640 (C), 1010 (D), 2000 (E), 4400 (F) and 7200 (G).

Another very interesting result in these computations is the turbulent heat flux $q_\theta = \overline{\mathbf{u}'T'}$ in the normal direction to the wall, which in this model is computed as $-\alpha_t \, \partial T/\partial y$. In Figure 3.6 the non-dimensional turbulent heat flux $\overline{u'T'}^+$ is shown as a function of the dimensional coordinate y (on the right) and of the non-dimensional distance from the wall y^+ (on the left) for
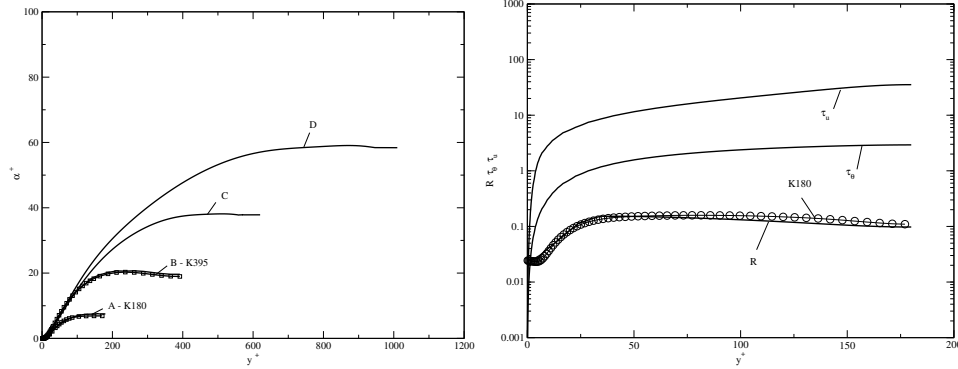
Figure 3.7: Plane case. Non-dimensional turbulent heat diffusivity α_t (on the left) for different $Re_\tau = 180$ (A), 395 (B), 640 (C) and 1010 (D). The DNS results are reported with squares as $K180$ and $K395$ lines on the left. On the right the characteristic time τ_θ, τ_u and their time ratio R for case with $Re_\tau = 180$. The circle line on the right is the DNS result (K180).

case	Re_τ	$< Pr_t >$
A	180	2.38
B	395	1.70
C	640	1.59
D	1010	1.55
E	2000	1.39
F	4400	1.19
G	7200	1.12
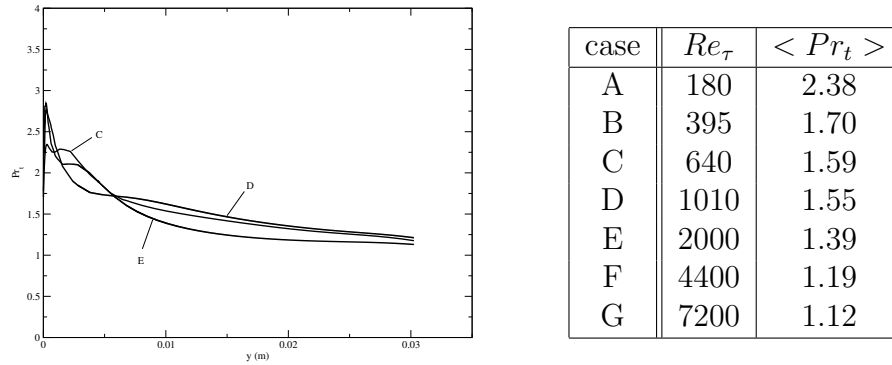
Figure 3.8: Plane case. The turbulent Prandtl number (left) for different $Re_\tau = 640$ (C), 1010 (D) and 2000 (E) and the average turbulent Prandtl number (right) for the considered cases A-G.

different $Re_\tau = 180$ (A), 395 (B), 640 (C), 1010 (D), 2000 (E), 4400 (F) and 7200 (G). On the left of Figure 3.6 a comparison between DNS results and the k-ϵ-k_θ-ϵ_θ model results is reported. The square dots $K180$ and $K395$ are from DNS data [56, 58] while the thick line (A) and (B) are the results of the k-ϵ-k_θ-ϵ_θ model for $Re_\tau = 180$ and $Re_\tau = 395$, respectively. Again the agreement is rather good.

Finally, interesting details can be seen from the turbulent thermal diffusivity α_t which is reported in Figure 3.7 on the left. In this figure the non-dimensional turbulent diffusivity α_t^+ for different $Re_\tau = 180$ (A), 395 (B), 640 (C) and 1010 (D) is reported together with the DNS results. The

Re_τ	Nu (DNS)	Nu (k_θ-ϵ_θ)	Nu (K)
180	5.48	5.50	5.42
395	6.6	6.40	6.32
640	7.89	7.4	7.48
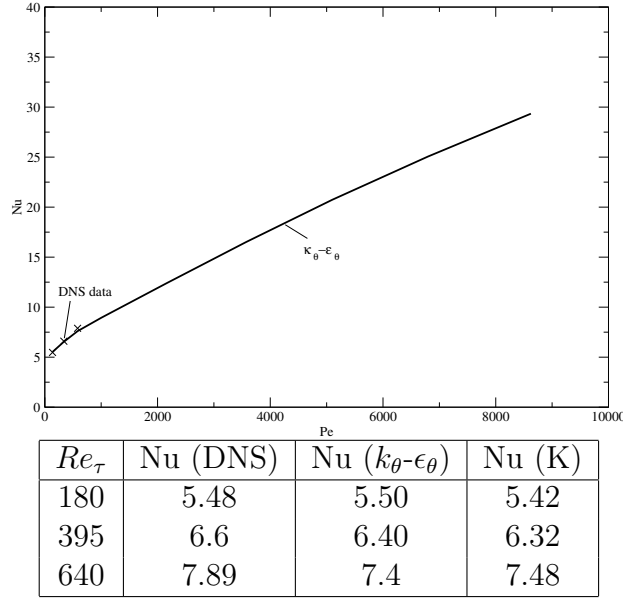
Figure 3.9: Plane case. On top Nusselt number (thick line) and DNS values (cross) for different Peclet number. On the bottom table of Nusselt number for the k-ϵ-k_θ-ϵ_θ model, DNS computations and Kirillov correlation (Nu (K) cylindrical geometry)

DNS results are reported with squares along the $K180$ and $K395$ lines. For $Re_\tau = 180$ case in Figure 3.7 on the right, the characteristic time τ_θ, τ_u and their time ratio R can be seen. The circle line is for the DNS result (K180). On the left of Figure 3.8, the turbulent Prandtl number for $Re_\tau = 640$ (C), 1010 (D) and 2000 (E) as a function of y is shown. On the right the average turbulent Prandtl number is reported for all the cases considered.

From the engineering point of view the heat exchange is defined by the Nusselt number. In Figure 3.9 on the top, we report the Nusselt number Nu, as a function of Peclet number Pe, for the plane geometry. In the Table on the bottom of Figure 3.9 one can see the number extracted from DNS [56, 58] and from the k-ϵ-k_θ-ϵ_θ model. The Nusselt value for $Re_\tau = 180$ extracted from DNS is a point of calibration for our model and the match is almost perfect. The Nusselt number obtained by DNS data for $Re_\tau = 640$ is quite high. It is greater even than the one predicted by the experimental Kirillov correlation for cylindrical geometry. The present model is calibrated to reproduce DNS low-Reynolds data and high-Reynolds experimental data collected in Kirillov correlation. In the regions where they differ the k_θ-ϵ_θ may reproduce only a compromise between these two sets of data.

The mixed boundary condition with uniform flux and $k_\theta = 0$ imposed
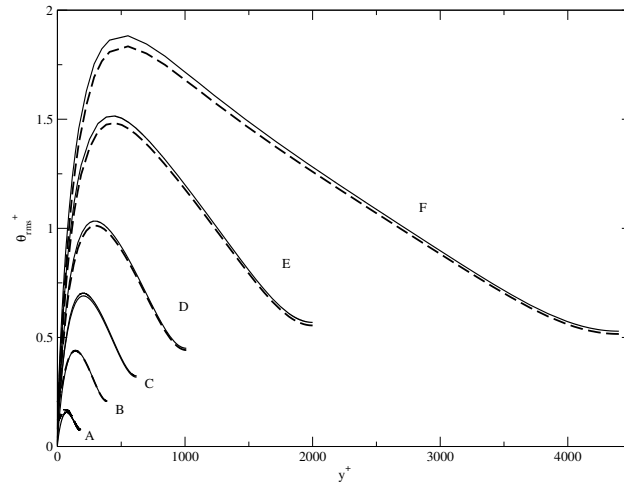
Figure 3.10: Plane case. Non-dimensional root-mean-square temperature fluctuations $\theta_{rms}{}^+$ for different velocities $Re_\tau = 180$ (A), 395 (B), 640 (C), 1010 (D), 2000 (E), 4400 (F) and for different boundary conditions on the wall: thick line $k_\theta = 0$ (MX), dashed line $dk_\theta/dy = 0$ (CHF).
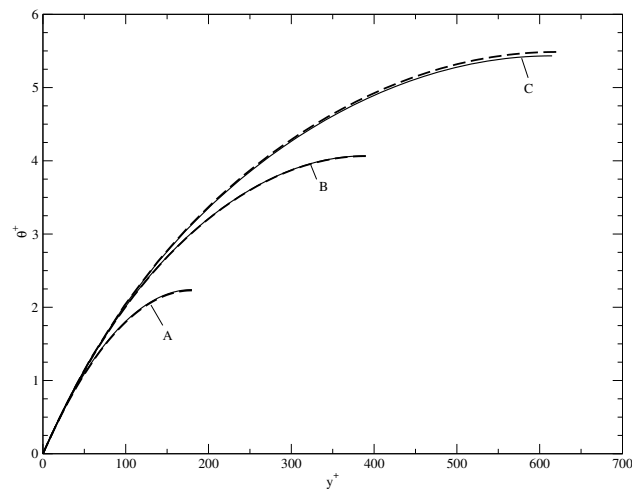
Figure 3.11: Plane case. Temperature distribution θ^+ for different velocities $Re_\tau = 180$ (A), 395 (B), 640 (C) and for different boundary conditions on the wall: thick line $k_\theta = 0$ (MX), dashed line $dk_\theta/dx = 0$ (CHF).

on the wall in the DNS computations are rather ideal. This is true if the temperature turbulent oscillations generated in the fluid are damped out on the wall boundary. If this hypothesis is not true then standard CHF

boundary condition must be applied

$$\frac{dk_\theta}{dn} = 0 \qquad \epsilon_\theta = 2\,\alpha\Big(\frac{\partial\sqrt{k_\theta}}{\partial\delta}\Big)^2 \quad \text{on } \Gamma_w\,. \qquad (3.52)$$

Temperature distribution θ^+ and its root-mean-square temperature fluctuation $\theta_{rms}{}^+$ for uniform heat flux boundary conditions with wall temperature square fluctuation (CHF) and with $k_\theta = 0$ on the wall (MX) are compared in Figures 3.10-3.11. The mixed case (MX) is the case studied in the DNS simulations and compared so far.

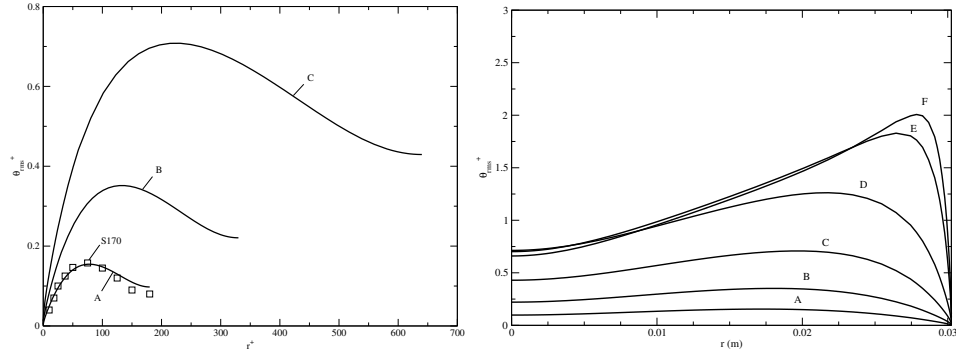In Figure 3.10 one can see non-dimensional root-mean-square temperature fluctuation $\theta_{rms}{}^+$ for different velocities $Re_\tau = 180$ (A), 395 (B), 640 (C), 1010 (D), 2000 (E), 4400 (F) and for different wall boundary conditions. Thick lines are for mixed boundary conditions (MX) $k_\theta = 0$ and dashed lines for $dk_\theta/dy = 0$. The boundary condition $dk_\theta/dy = 0$ does affect the wall value of k_θ which is different from zero, but the profile in the interior region of the domain remains approximately very close to the previous one, especially for the high Reynolds number cases. This was already pointed out in [96, 104, 111] for DNS simulations when performed with other than mixed boundary conditions. In Figure 3.11 temperature distributions θ^+ for different velocities $Re_\tau = 180$ (A), 395 (B), 640 (C) are shown. Uniform heat flux boundary conditions with (MX) and without (CHF) wall temperature fluctuation are reported in thick and dashed lines, respectively. The introduction of the wall temperature fluctuation, $k_\theta \neq 0$, does not seem to affect significantly the mean temperature θ^+ and therefore the heat exchange and the Nusselt number.

3.2.2 Cylindrical channel

In this section we report the numerical results obtained in cylindrical geometry by using the four parameter k-ϵ turbulence model. We compare our results with DNS data, when available, and with the experimental correlation by Kirillov, see Section 2.3.1 for other experimental correlations in cylindrical channel.

The DNS data in cylindrical and annular pipes with $Pr = 0.025$ have been presented by a few authors, see [92, 96, 98, 100] and references therein. We refer mainly to the work in [100], where a direct numerical simulation of turbulent heat transfer in pipe flows with bulk flow Reynolds number of approximately 5000 ($Re_\tau = 170$) and Prandtl number 0.025 is presented. The work in [100] examines the effect of pipe length for different resolution and discusses the convergence of thermal turbulence statistics. In [98] a similar direct numerical simulation of turbulent heat transfer in pipe flows is

presented. In this case the friction Reynolds number Re_τ is 180 but $Pr = 0.026$.

In order to compare these DNS computations and the mentioned correlation we consider a pipe with radius $R_e = 0.03025$ m and fluid properties listed in Table 3.1 with corresponding $Pr \approx 0.025$. All tests are performed in this reference configuration with fully developed flow and average velocity ranging from 0.0162 to 1.016 m/s. The heat exchange is studied with uniform wall flux boundary conditions. As already explained in the plane case Section 3.2.1, we can have two types of boundary conditions with uniform wall heat flux: MX and CHF boundary conditions. The mixed boundary condition is imposed when the constant heat flux is set with vanishing average square temperature fluctuation (MX), i.e., $k_\theta = 0$. On the other hand the CHF boundary condition implies that the normal derivative of k_θ is set to zero. We have shown that the results in term of average temperature and Nusselt number are very close and therefore we adopt the mixed boundary conditions (MX) since all the DNS simulations are solved with this type of conditions. For completeness at the end of this Section we present and discuss the other class of boundary conditions.

As already pointed out, many authors do not report the results directly in temperature variable but in a reduced non-dimensional variable θ^+. The solution T can be written as

$$T(r, z) = T_{w0} + z \, \Delta T_b - \theta(r) \, , \tag{3.53}$$

with ΔT_b the variation of the bulk temperature along the unit length in the axial direction z. θ is the profile of the temperature of the fully developed flow that tends to zero on the walls. The profile of the inlet temperature is $T_{w0} - \theta$ while the profile of the outlet temperature is $T_{w0} + L_z \, \Delta T_b - \theta$. Since θ is zero on the wall, the constant T_{w0} can be identified with the arbitrary inlet temperature over the wall. The value of ΔT_b can be calculated from the energy balance resulting in $2 \, \pi \, R_e \, q = C_p \, \dot{m} \Delta T_b$ where $\dot{m} = \pi R_e^2 \, \rho \, \bar{v}$ is the constant mass flow rate and $\bar{v}$ is the average velocity over a transverse section.

We can subdivide the boundary of the computational domain into an inlet, an outlet and solid walls, which will be denoted by Γ_i, Γ_o and Γ_w respectively. The boundary conditions for the k-ϵ model are enforced by using the near-wall approach. As done in the previous section, we refine the mesh until the surface on which we impose boundary conditions lies in the viscous laminar region, then we enforce the near-wall boundary condition
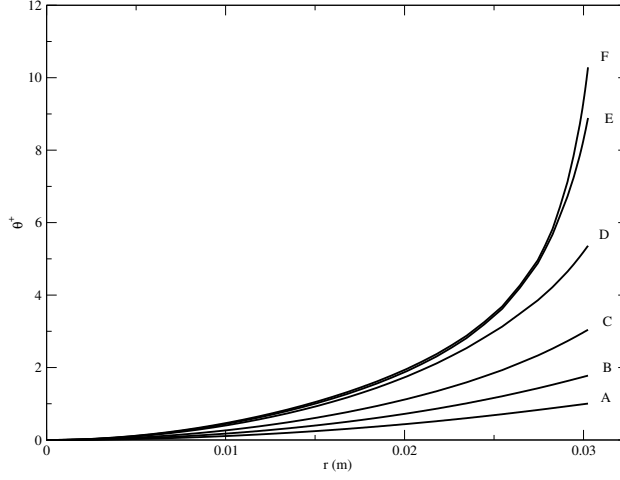
Figure 3.12: Cylinder case. Non-dimensional temperature drop distribution θ^+ for different friction velocities $Re_\tau = 180$ (A), 395 (B), 640 (C), 1400 (D), 4500 (E) and 7150 (F).

asymptotic expansions

$$\tau_w := \frac{\rho \, \nu}{\delta} \, u_t \, , \quad u_n := 0 \, , \tag{3.54}$$

$$k := k_{wl}\delta^2 \, , \quad \epsilon := 2\nu k_{wl} = 2\frac{\nu k}{\delta^2} \quad \text{on } \Gamma_w \, ,$$

and periodic boundary conditions between the inlet and outlet surfaces. Since the constant k_{wl} is not known the condition is applied in logarithmic form as $dk/dr|_{\Gamma_w} = 2k/\delta$. For temperature and k_θ-ϵ_θ system we use mixed boundary conditions (MX). We set

$$T = T_{w0} + z\Delta T_b \quad k_\theta = k_{\theta wl}\delta^2 \, , \, \epsilon_\theta = 2\nu k_\theta/Pr\,\delta^2 \quad \text{on } \Gamma_w \quad (3.55)$$
$$T = T_{\Gamma_i} + L_z\,\Delta T_b \quad k_\theta = k_\theta|_{\Gamma_i} \, , \quad \epsilon_\theta| = \epsilon_\theta|_{\Gamma_i} \quad \text{on } \Gamma_o . (3.56)$$

The boundary condition of ϵ_θ on Γ_w can be substituted by the equivalent condition $R|_{\Gamma_w} = k_\theta\,\epsilon/(k\,\epsilon_\theta) = Pr$. With the transformation (3.53) the boundary conditions at the outlet Γ_o are now simple periodic boundary conditions for all the variables θ, k_θ and ϵ_θ.

In the following the results from six different simulations with $Re \approx 5500$ (A), 11150 (B), 23750 (C), 57500 (D), 213000 (E) and 345000 (F) are reported. In the above proposed configuration they correspond to a mean velocity field ranging approximately from 0.016 m/s to 1.016 m/s. The friction Reynolds numbers for these six cases are $Re_\tau = 180$ (A), 395 (B), 640
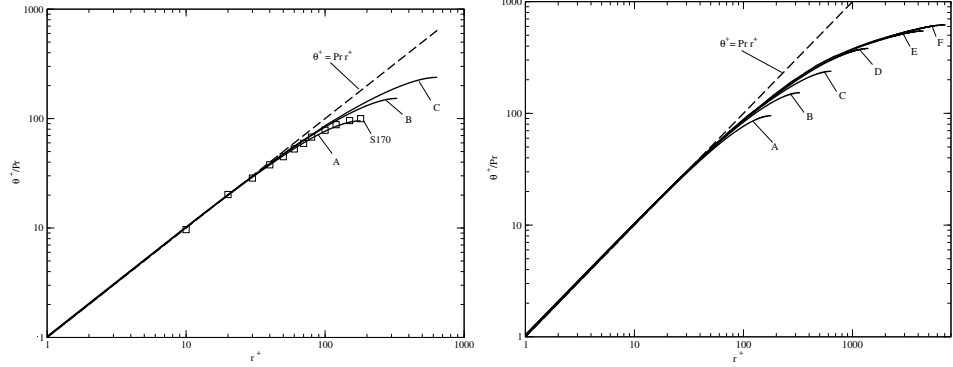
Figure 3.13: Cylinder case. Temperature distribution θ^+/Pr for different friction velocities $Re_\tau = 180$ (A), 395 (B), 640 (C), 1400 (D), 4500 (E) and 7150 (F) and comparison with DNS data for $Re_\tau = 170$ (S170) on the left.

Figure 3.14: Cylinder case. Non-dimensional root-mean-square temperature fluctuations $\theta_{rms}{}^+$ for different friction velocities $Re_\tau = 180$ (A), 395 (B), 640 (C), 1400 (D), 4500 (E) and 7150 (F) and comparison with DNS data for $Re_\tau = 170$ (S170) on the left.

(C), 1400 (D), 4500 (E) and 7150 (F). Using the Blasius friction factor correlation for smooth pipes, the friction Reynolds number can be approximately evaluated from the bulk Reynolds number as [100]

$$Re_\tau = \frac{u_\tau D}{2\nu} = 99.436 \cdot 10^{-3} Re_D^{7/8} \,. \tag{3.57}$$

The comparison with the DNS data is reported only for the case $Re_\tau = 170$, i.e., when these data are available [100]. As in the plane case in order to use the k-ϵ model in low-Reynolds number the second order approximation in [3, 50, 89] has been used together with appropriate mixed boundary conditions (MX).
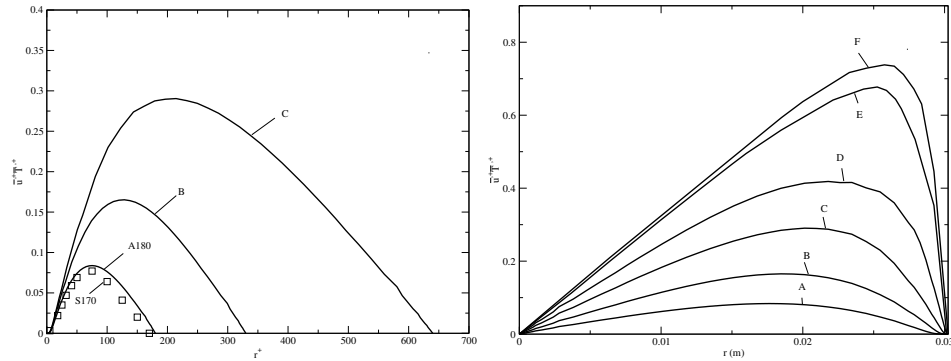
Figure 3.15: Cylinder case. Non-dimensional turbulent heat flux $\overline{u'T'}^+$ as a function of the axial coordinate r (on the right) and of the non-dimensional distance r^+ (on the left) for different friction velocities $Re_\tau = 180$ (A), 395 (B), 640 (C), 1400 (D), 4500 (E) and 7150 (F). The square lines are the DNS results for $Re_\tau = 170$ ($S170$).
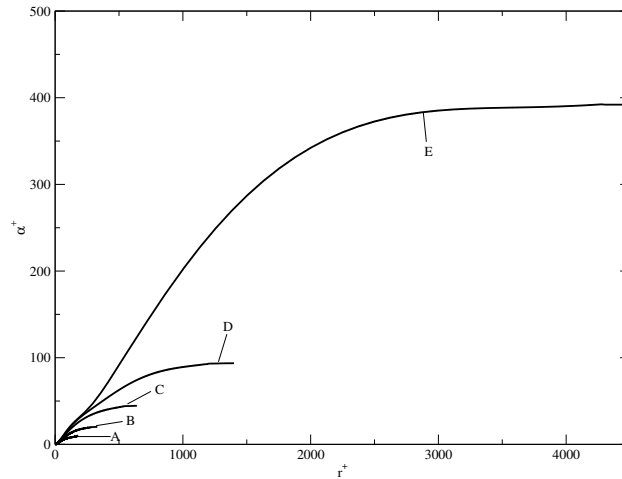
Figure 3.16: Cylinder case. Non-dimensional turbulent thermal diffusivity α^+ for different friction velocities $Re_\tau = 180$ (A), 395 (B), 640 (C), 1400 (D), 4500 (E) and 7150 (F).

In Figures 3.12-3.13 temperature distributions are shown for different velocities corresponding to $Re_\tau = 180$ (A), 395 (B), 640 (C), 1400 (D), 4500 (E) and 7150 (F). In Figure 3.12 one can see the temperature difference $\theta = T - T_{w0} - z\Delta T_b$ between the temperature and the linear behavior characteristic of the fully developed flow. This drop in temperature from the wall to the center of the channel is shown in non-dimensional unit as $\theta^+ = \theta/T_\tau$. The profile of the non-dimensional temperature drop along the radius changes its
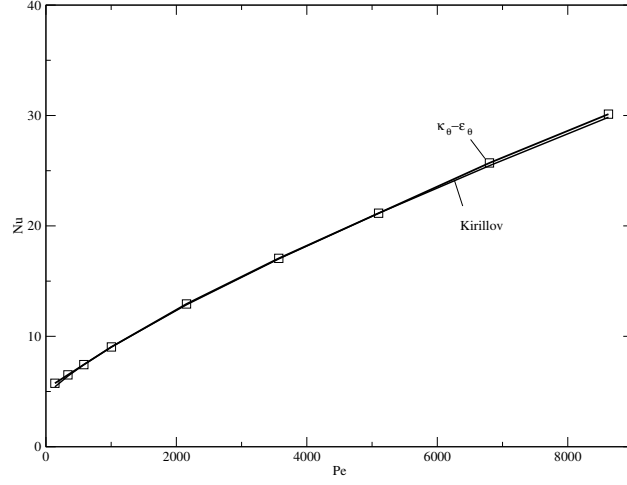
Figure 3.17: Cylinder case. Nusselt number (square) and Kirillov correlation for cylindrical geometry (thick line).

shape and intensity between the case A with low Reynolds number and the case F with higher velocity field.

In Figure 3.13 the non-dimensional temperature profiles divided by the Prandtl number are shown as functions of the non-dimensional coordinate r^+. Dividing by the molecular Prandtl number one can evaluate the linear behavior of the temperature distribution near the wall. The comparison between the k-ϵ-k_θ-ϵ_θ model and the DNS solution for $Re_\tau = 170$, (S170), can be seen on the left of Figure 3.13. The results are good if we take into account that the DNS data (S170 square) and the k-ϵ-k_θ-ϵ_θ solution are obtained for slightly different Re_τ. For completeness on the right of the same Figure all the curves are reported enhancing the different behavior at higher Reynolds numbers. In this Figure 3.13 the log-log plot shows that all the temperature profiles are still linear until about 30-40 r^+.

In Figure 3.14 on the left the root-mean-square temperature fluctuation $\theta_{rms}{}^+$ for different velocities $Re_\tau = 180$ (A), 395 (B) and 640 (C) is shown as a function of the non-dimensional wall distance r^+ together with the DNS simulation [100]. The DNS simulation for $Re_\tau = 170$ is labeled $S170$ (square). The agreement between the k-ϵ-k_θ-ϵ_θ model and the DNS simulation is good considering the slight different Reynolds number. On the right of Figure 3.14 the root-mean-square temperature fluctuation $\theta_{rms}{}^+$ is reported as a function of the channel radius. In this Figure the distributions are shown for all the simulated cases with $Re_\tau = 180$ (A), 395 (B), 640 (C), 1400 (D), 4500 (E) and 7150 (F).

Another important variable in the turbulent heat transfer framework is
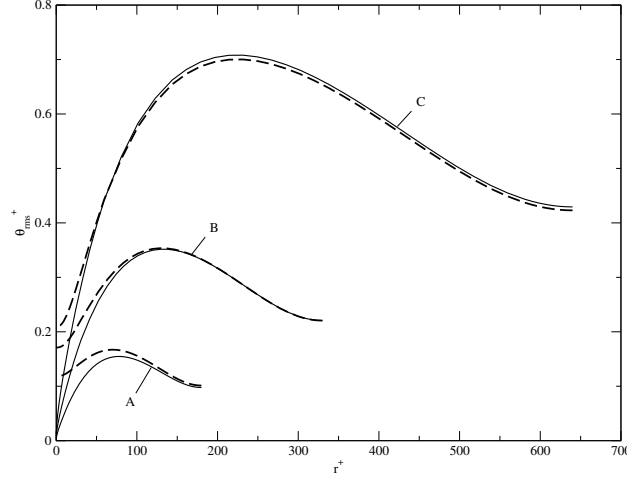
Figure 3.18: Cylinder case. Non-dimensional root-mean-square temperature fluctuations θ_{rms}^+ for different $Re_\tau = 180$ (A), 330 (B), 640 (C) and for different boundary conditions on the wall: thick line $k_\theta = 0$ (MX), dashed line $dk_\theta/dr = 0$ (CHF).

the heat turbulent flux $q_\theta = \overline{\mathbf{u}'T'}$ normal to the wall, which gives the importance of the turbulent convective heat transfer with respect to the molecular heat transfer. In the k-ϵ-k_θ-ϵ_θ model q_θ is defined basically by the turbulent thermal diffusivity α_t as $q_\theta = \alpha_\theta\,\partial T/\partial r$. In Figure 3.15 one can see the non-dimensional turbulent heat flux $\overline{u'T'}^+$ as a function of the radius r (on the right) and of the non-dimensional radius r^+ (on the left) for different friction velocities $Re_\tau = 180$ (A), 395 (B), 640 (C), 1400 (D), 4500 (E) and 7150 (F). On the left of Figure 3.15 a comparison between DNS results and the k-ϵ-k_θ-ϵ_θ model is reported. The square line $S170$ is from DNS data [100] while the thick line (A) is for the k-ϵ-k_θ-ϵ_θ model for $Re_\tau = 180$.

Finally the eddy thermal diffusivity α_t^+ is reported in Figure 3.16 on the left. In this figure α_t is non dimensional with molecular thermal diffusivity α and it is reported for different friction velocities $Re_\tau = 180$ (A), 395 (B), 640 (C), 1400 (D), 4500 (E) and 7150 (F) together with the DNS results.

The thermal diffusivity α_t defines the corresponding heat exchange and the Nusselt number. In Figure 3.17 we report the Nusselt number Nu, as a function of Peclet number Pe, for the cylindrical geometry. The Nusselt value for $Re_\tau = 180$, which has been calibrated with the plane DNS cases is very close and the matching improves with higher Reynolds numbers. This result is obtained by adapting the k-ϵ-k_θ-ϵ_θ coefficients to DNS data in plane geometry in the range of low-Reynolds numbers and to the data from the Kirillov correlation for high-Reynolds flows.
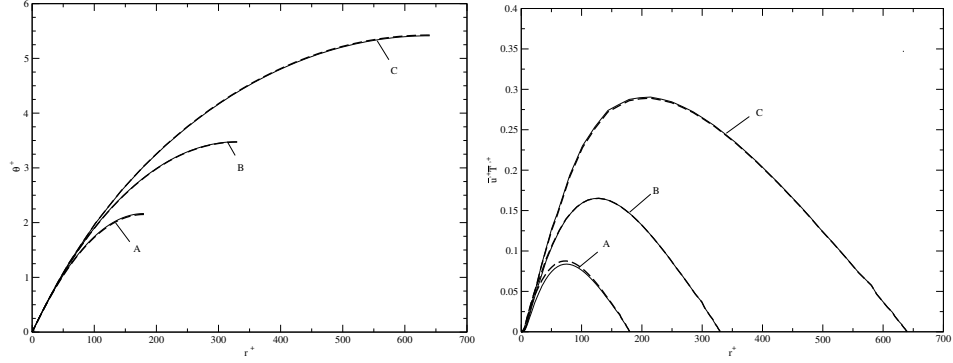
Figure 3.19: Cylinder case. Temperature distribution θ^+ (left) and non-dimensional radial turbulent heat flux $\overline{u'T'}^+$ (right) for different $Re_\tau = 180$ (A), 330 (B), 640 (C) and for different boundary conditions on the wall: thick line $k_\theta = 0$ (MX), dashed line $dk_\theta/dr = 0$ (CHF).

The wall mixed boundary condition with uniform flux and $k_\theta = 0$ imposed on the wall in the DNS computations are not appropriate if the temperature turbulent oscillations generated in the fluid are not damped out on the wall boundary. In this case we must apply standard CHF boundary conditions

$$\frac{dk_\theta}{dn} = 0 \qquad \epsilon_\theta = 2\,\alpha\Big(\frac{\partial\sqrt{k_\theta - k_{\theta w}}}{\partial r}\Big)^2 \quad \text{on } \Gamma_w\,. \qquad (3.58)$$

Temperature distribution $\theta = T_{w0} + z\Delta T_b - T$, its root-mean-square temperature fluctuation θ_{rms}^+ and radial turbulent heat flux $\overline{\mathbf{u}'T'}$ for uniform heat flux boundary conditions with wall temperature squared fluctuation (CHF) and with $k_\theta = 0$ on the walls (MX) are compared in Figures 3.18-3.19. The mixed case (MX) is the case studied in the DNS simulations and compared so far.

In Figure 3.18 one can see the non-dimensional root-mean-square temperature fluctuation θ_{rms}^+ for different $Re_\tau = 180$ (A), 395 (B), 640 (C) and different wall boundary conditions. Thick lines are for mixed boundary conditions (MX) with $k_\theta = 0$ and dashed lines for $\partial k_\theta/\partial r = 0$ (CHF). The root-mean-square temperature fluctuation θ_{rms}^+ with vanishing derivative on the wall shows a constant value near the wall region. Then the curve reaches a maximum and finally tends to decrease again. Both curves, with different boundary conditions, reach the maximum around the same r^+ but for $Re_\tau = 180$ the maximum values are different. For this Reynolds number the two curves merge around $y^+ \approx 120$. For higher Reynolds the matching region moves towards to the wall region and the maximum value of the root-mean-square temperature fluctuation θ_{rms}^+ becomes the same.

In Figure 3.19 non-dimensional temperature distribution θ^+ (left) and non-dimensional radial turbulent heat flux $\overline{\mathbf{u}'T'}^+$ (right) for different velocities $Re_\tau = 180$ (A), 395 (B), 640 (C) are shown. Uniform heat flux boundary conditions with (MX) and without (CHF) wall temperature fluctuation are reported in thick and dashed lines, respectively. The introduction of the wall temperature fluctuation, $k_\theta \neq 0$, does not seem to affect significantly the mean temperature θ^+ and radial turbulent heat flux $\overline{u'T'}^+$. This implies that the Nusselt number remains approximately the same as previously computed.

3.2.3 Triangular rod bundle

In this section we study the triangular rod bundle geometry and show numerical results obtained with different pitch-to-diameter ratios χ at several Peclet numbers. This geometry and the heat transfer correlations available for the prediction of the Nusselt number as a function of the Peclet number have been reported in Section 2.3.2, we report here the geometry of Figure 2.3 in Figure 3.20 for convenience. The reference physical parameters employed in the CFD simulations are shown in Table 3.1. We consider the k_θ-ϵ_θ turbulence model and the simple eddy diffusivity (SED) model with different turbulent Prandtl numbers. The aim of this section is to compare the numerical results obtained by using these heat transfer turbulence models with the experimental correlations introduced in 2.3.2.

We consider periodic boundary conditions in the vertical direction z for all dynamical variables. The solutions for the dynamical variables appear constant along the vertical direction since only a pressure increasing between the inlet and outlet surface is allowed as shown in Figure 3.21 for the vertical component w of the velocity field and the turbulent kinetic energy k.

rod diameter	D	0.0082 m
grid dimension	P	0.00496-0.00615 m
P/D ratio	χ	1.2-1.5
average velocity	w	0.25-2.95 m/s
hydraulic diameter	D_h	0.012-0.0625 m
viscosity	μ	0.00184 Pa $\cdot$ s
density	ρ	10340 Kg/m^3
thermal conductivity	λ	10.72 W/(m K)
heat specific capacity	C_p	145.75 J/(Kg K)

Table 3.1: Physical parameters used in the CFD simulations.
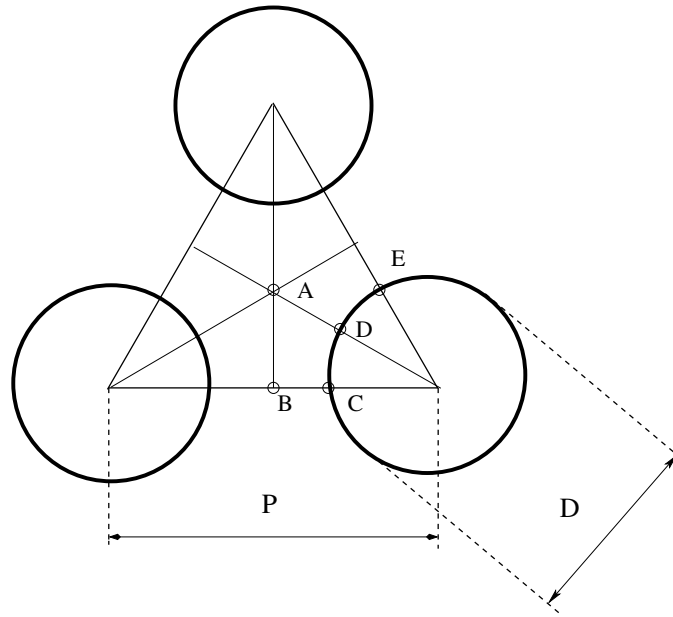
Figure 3.20:   Triangular rod bundle geometry.
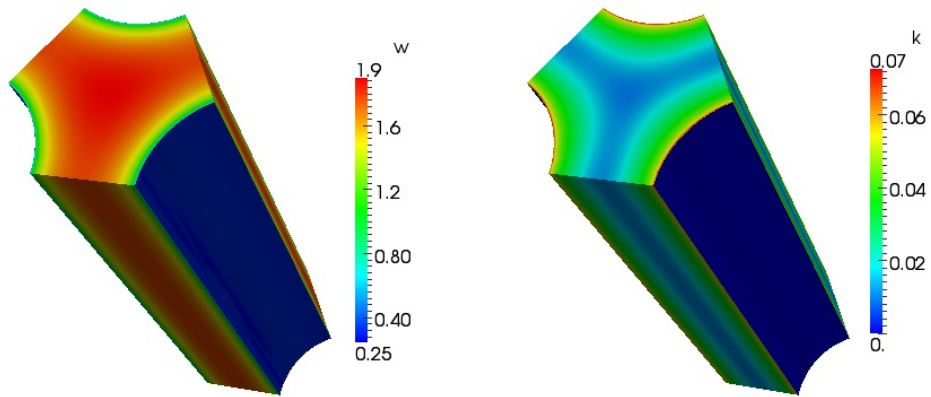
Figure 3.21:   Triangular rod bundle with $\chi = 1.3$. Vertical velocity and turbulent kinetic energy fields in fully developed flow.

With reference to Figure 3.20 let us consider the region $ABCD$ and divide the boundary Γ in four parts: Γ_1 (A-B), Γ_2 (B-C), Γ_w (C-D) and Γ_3 (D-A). Let δ be the distance from the wall defined on the rod surface Γ_w (C-D). The boundary conditions on the solid surfaces Γ_w are imposed on a cylindrical surface at a distance δ from the wall. The distance δ depends on the mesh size of the boundary layer region and, for this reason, it is standard

procedure to refine the mesh until the surface defined by the distance δ lies in the viscous laminar region. When δ is located in the viscous laminar region we enforce the near-wall boundary condition asymptotic expansions in the following form

$$\tau_w|_{\Gamma_w} = \frac{\rho\,\nu}{\delta}\,u_t|_{\Gamma_w} \,, \quad u_n|_{\Gamma_w} = 0 \,, \tag{3.59}$$

$$k|_{\Gamma_w} = k_{wl}\delta^2 \,, \quad \epsilon|_{\Gamma_w} = 2\nu k_{wl} = 2\frac{\nu k_w}{\delta^2} \,. \tag{3.60}$$

Since the constant k_{wl} is not known the condition has to be applied in the form $dk/dn|_{\Gamma_w} = 2k/\delta$. In fact if $k = k_{wl}\delta^2$ then $dk/d\delta = 2k_{wl}\delta = 2k/\delta$ which implies the derivative form of the boundary condition. In the region Γ_1 (*A-B*), Γ_2 (*B-C*) and Γ_3 (*D-A*), where the rod is absent, simple symmetry boundary conditions should be imposed.

As we have already explained in Section 3.2.1, for the k_θ-ϵ_θ system two types of boundary conditions can be applied on Γ_w: the mixed (MX) and constant heat flux (CHF) boundary conditions. The mixed boundary conditions are enforced by the following near-wall asymptotic expansions

$$k_\theta|_{\Gamma_w} = k_{\theta wl}\delta^2 \,, \quad \epsilon_\theta|_{\Gamma_w} = 2\nu k_{tw}/Pr\,\delta^2 \,. \tag{3.61}$$

Also in this case the constant $k_{\theta wl}$ is not known and since $dk_\theta/d\delta = 2k_{\theta wl}\delta = 2k_\theta/\delta$ one can use the logarithmic condition $dk/dn|_{\Gamma_w} = 2k/\delta$ which allows the computation of the unknown constant $k_{\theta wl}$. The mixed boundary conditions, which enforce $k_\theta = 0$ on the wall, are rather ideal since this is true when the temperature turbulent oscillations generated in the fluid are damped out on the wall boundary. If this hypothesis is not true then standard CHF boundary condition must be applied

$$\frac{dk_\theta}{dn} = 0 \quad \epsilon_\theta = 2\alpha\left(\frac{\partial\sqrt{k_\theta}}{\partial\delta}\right)^2 \,. \tag{3.62}$$

Both MX and CHF boundary conditions for the fully developed case can be used to compare to experimental data since the results on the core flow are very similar and they differ only in the very near-wall region as shown in the previous Sections. For this reason we enforce the mixed boundary conditions (MX) with the following near-wall asymptotic expansions

$$\frac{dT}{dn}\Big|_{\Gamma_w} = q \,, \quad k_\theta|_{\Gamma_w} = k_{\theta wl}\delta^2 \,, \quad R|_{\Gamma_w} = Pr \,, \tag{3.63}$$

where the condition on R can be substituted by the equivalent condition $\epsilon_\theta|_{\Gamma_w} = 2\nu k_{tw}/Pr\,\delta^2$. The boundary conditions on Γ_1, Γ_2 and Γ_3 are simple symmetric conditions (i.e., $d\Phi/dn = 0$).

Triangular rod bundle with $P/D = 1.3$

The case with $\chi = 1.3$ may be considered a reference configuration since most experimental data are available in the pitch-to-diameter range $\chi = 1.2$-1.5. For this case our computational domain is characterized by $D = 8.4$
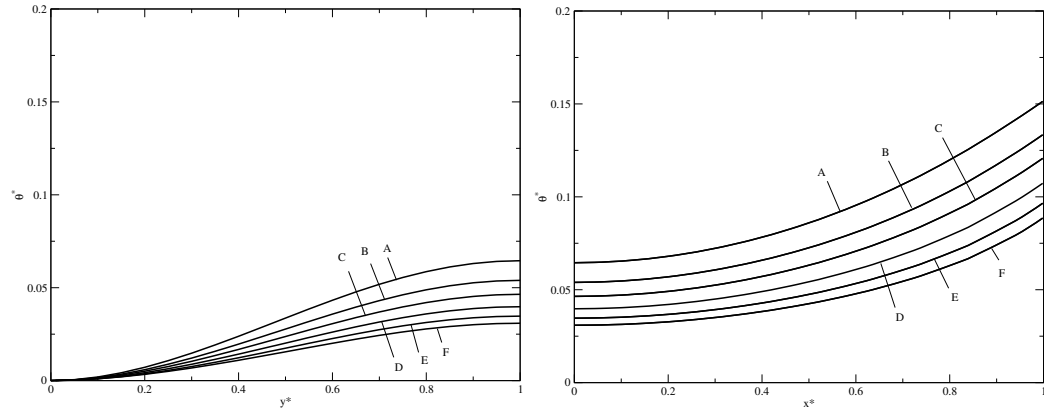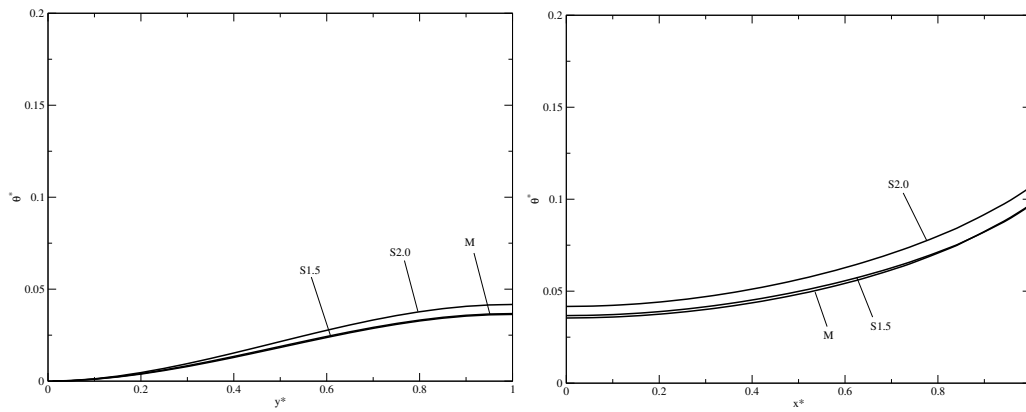

Figure 3.22: Triangular rod bundle with $\chi = 1.3$. Non-dimensional temperature θ^* over the vertical line *A-B* (left) and horizontal line *B-C* (right) for $Pe \approx 360$ (A) , 530 (B), 750 (C), 1030 (D) 1470 (E) and 1970 (F).
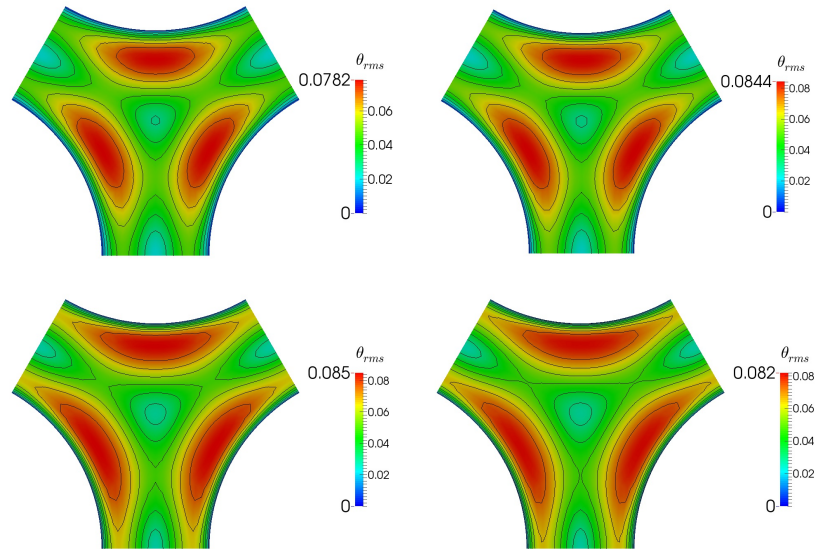
Figure 3.23: Triangular rod bundle with $\chi = 1.3$. Non-dimensional root-mean-square temperature fluctuation θ_{rms} for $Pe \approx 360$ (A), 530 (B), 1470 (E) and 1970 (F).

mm and $P = 1.3$, so $D = 10.66$ mm. The characteristic physical properties are defined in Table 3.1 and the equivalent hydraulic diameter $D_h \approx 7.07$ mm. Six different simulations with $Re \approx 14550$ (A), 21200 (B), 30100 (C), 41050 (D) 58700 (E) and 78700 (F) are presented, which correspond to an average velocity range of $0.25 - 2.0$ m/s in the considered geometry. These cases correspond to the mean velocity field $v \approx 0.336$ (A), 0.534 (B), 0.758 (C), 1.033 (D), 1.482 (E) and 1.92 (F) with corresponding Peclet numbers $Pe \approx 360$ (A) , 530 (B), 750 (C), 1030 (D) 1470 (E) and 1970 (F).

In order to analyze the temperature behavior, the solution T of the fully developed flow is written as a sum of three terms

$$T = \theta + T_c + \Delta T_m\, z\,, \tag{3.64}$$

where T_c is the constant temperature at the center of the inlet of the triangular rod bundle ($z = 0$) and ΔT_m the linear increase of temperature per unit of length in the vertical direction. In fully developed flow with constant heat flux on the wall the temperature grows uniformly on horizontal sections and linearly along the vertical direction. The slope of the linear growth ΔT_m can be easily computed with an energy balance as $\Delta T_m = \dot{q}/(C_p \dot{m})$ where $\dot{q}$ is the heat flux on the wall and $\dot{m}$ the mass flux through the triangular bundle. The non-dimensional value of temperature may be obtained in many ways. In this work we divide the temperature by $q D_{eq}/\lambda$, where q is the heat surface flux, D_{eq} the hydraulic diameter and λ the thermal conductivity. The non-dimensional temperature θ^* is therefore defined by $\theta^* = \theta\, \lambda/(qD)$. This non-dimensional variable θ^* resembles the inverse of the local Nusselt number. In the rest of the section we also set the inlet bundle center temperature T_c to zero.

In Figure 3.22 the non-dimensional temperature θ^* is shown over the lines A-B and B-C for $Pe \approx 360$ (A), 530 (B), 750 (C), 1030 (D), 1470(E), 1970 (F). The vertical line A-B is shown on the left and the horizontal line B-C on the right. At the point A the variable θ^* is zero, then increases to reach the middle point of the triangle side (B) and the wall point C. The temperature fluctuations are shown in Figures 3.23-3.24 by the non-dimensional root square mean temperature. We define the non-dimensional root square mean temperature θ_{rms} as $\theta_{rms} = \lambda\sqrt{2\,k_\theta}/qD_{eq}$. In Figure 3.23 one can see the non-dimensional root-mean-square temperature fluctuation θ_{rms} for the cases (A), (B), (E) and (F). The increasing values of Pe are reported from top-left to right-bottom. In the center of the triangular bundle k_θ has a local minimum and in the region between the center and the wall reaches its maximum. More details on temperature fluctuations can be seen in Figure 3.24 where the non-dimensional root-mean-square temperature θ_{rms}
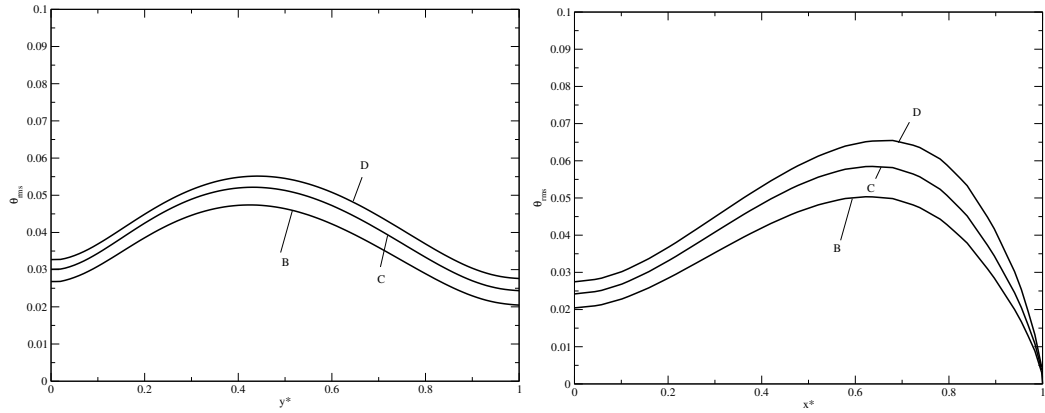
Figure 3.24:   Triangular rod bundle with $\chi = 1.3$. Non-dimensional root-mean-square temperature fluctuation θ_{rms} over the vertical line A-B (left) and horizontal line B-C (right) for $Pe \approx 530$ (B), 750 (C), 1030 (D).
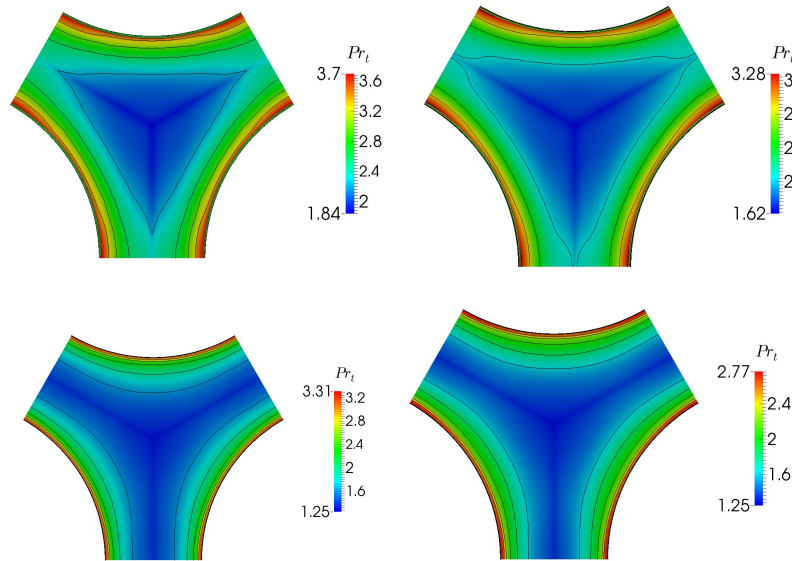
Figure 3.25:   Triangular rod bundle with $\chi = 1.3$. Turbulent Prandtl number Pr_t for $Pe \approx 360$ (A), 530 (B), 1470 (E) and 1970 (F).

is shown over the vertical line A-B and over the horizontal line B-C on the right and on the left respectively for the cases (B), (C) and (D). At the center point A, θ_{rms} is minimum, then it reaches a maximum approximately in the middle point of the segment A-B to decrease again to a new local minimum at B. Along the segment B-C, θ_{rms} reaches a maximum and tends to the boundary conditions $\theta_{rms} = 0$ at the wall point C.
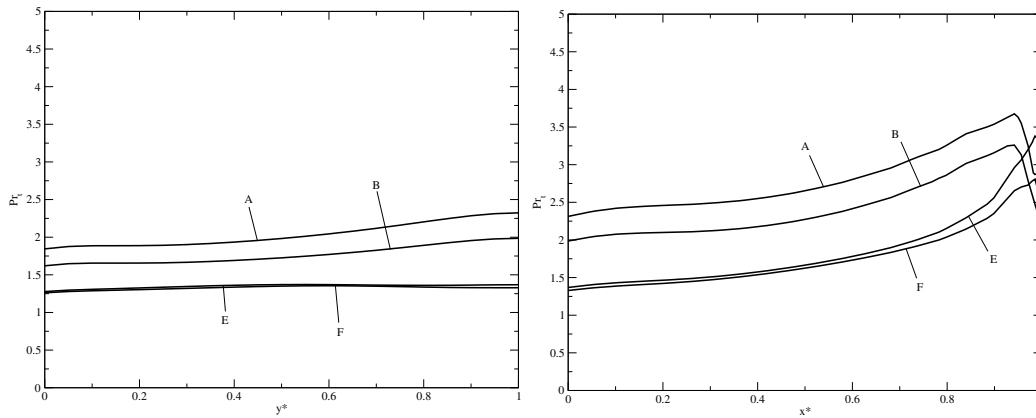
Figure 3.26: Triangular rod bundle with $\chi = 1.3$. Turbulent Prandtl number Pr_t over the vertical line A-B (left) and horizontal line B-C (right) for $Pe \approx$ 360 (A) $Pe \approx 530$ (B), 1470 (E) and 1970 (F).
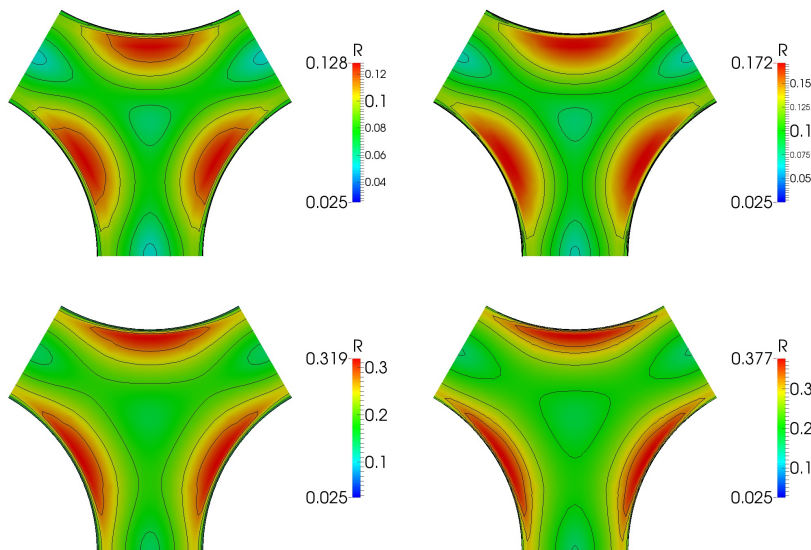
Figure 3.27: Triangular rod bundle with $\chi = 1.3$. Time ratio R for $Pe \approx 360$ (A), 530 (B), 1470 (E) and 1970 (F).

The turbulent Prandtl number Pr_t is shown in Figures 3.25-3.26. In Figure 3.25 one can see the behavior of turbulent Prandtl number for $Pe = 360$ (A), 530 (C), 1470 (E) and 1970 (F). The cases with increasing Pe number are reported from top-left to right bottom. In Figure 3.26 the turbulent Prandtl number Pr_t is shown over the lines A-B and B-C for $Pe \approx 530$ (B), 750 (C), 1470 (E) and 1970 (F). The turbulent Prandtl number Pr_t on the
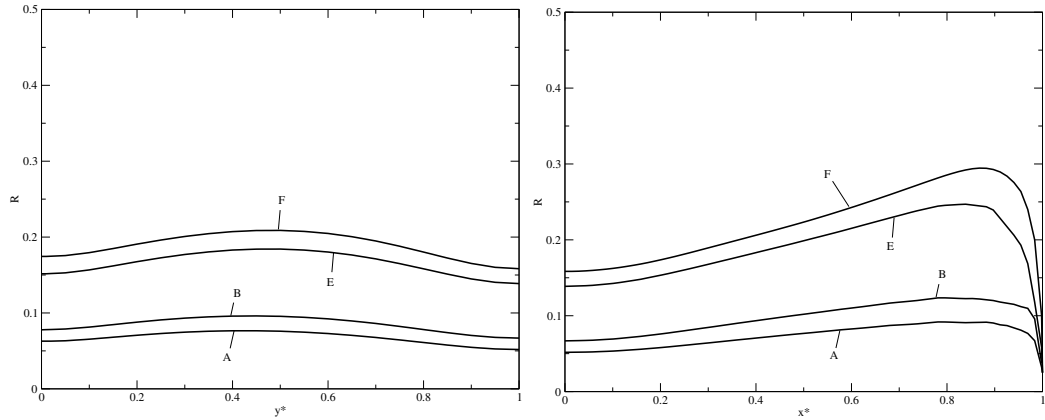
Figure 3.28:   Triangular rod bundle with $\chi = 1.3$. Time ratio R over the vertical line A-B (left) and horizontal line B-C (right) for $Pe \approx 360$ (A), 530 (B), 1470 (E) and 1970 (F).

vertical line A-B is shown on the left and the horizontal line B-C on the right as a function of the non-dimensional path. In the first case the value 0 corresponds to point A and the value 1 to the point B. It is worth to remark that the turbulent Prandtl number Pr_t is not constant but it shows a peak near the wall.

The time ratio R is defined as $R = \tau_t/\tau_u = \epsilon\,k_\theta/(\epsilon_\theta\,k)$ and it is a key parameter to define the turbulent Prandtl number and therefore the thermal diffusivity coefficient α_t. The time ratio R is shown in Figures 3.27-3.28 for different cases. In Figure 3.27 the ratio R can be seen over the bundle section for $Pe \approx 360$ (A), 530 (B), 1470 (E) and 1970 (F). We can see from this Figure that for higher velocity the time ratio R increases. A more detailed view is reported in Figure 3.28 where R is shown over the lines A-B and B-C for $Pe \approx 530$ (B), 750 (C), 1030 (D). On the left of Figure 3.28 one can see the time ratio R on the line A-B as a function of the non-dimensional path. At 0 (point A) R has a local minimum. Then it reaches a maximum to approach again to a local minimum value at 1 (point B). Along the B-C segment R takes higher values near the wall and decreases to the boundary conditions on the wall itself.

In Figures 3.29-3.31 one can see a comparison of non-dimensional temperature θ^* for $Pe = 1230$ and different turbulence models: k_θ-ϵ_θ and simple eddy diffusivity model (SED) with different constant Pr_t. We briefly recall the definition of the SED model. This model is based on the assumption of a constant turbulent Prandtl number which allows a direct computation of the turbulent thermal diffusivity from the eddy viscosity through equation (2.2). The value of Pr_t has to be defined and here we use $Pr_t = 1.5$ and $Pr_t = 2$.
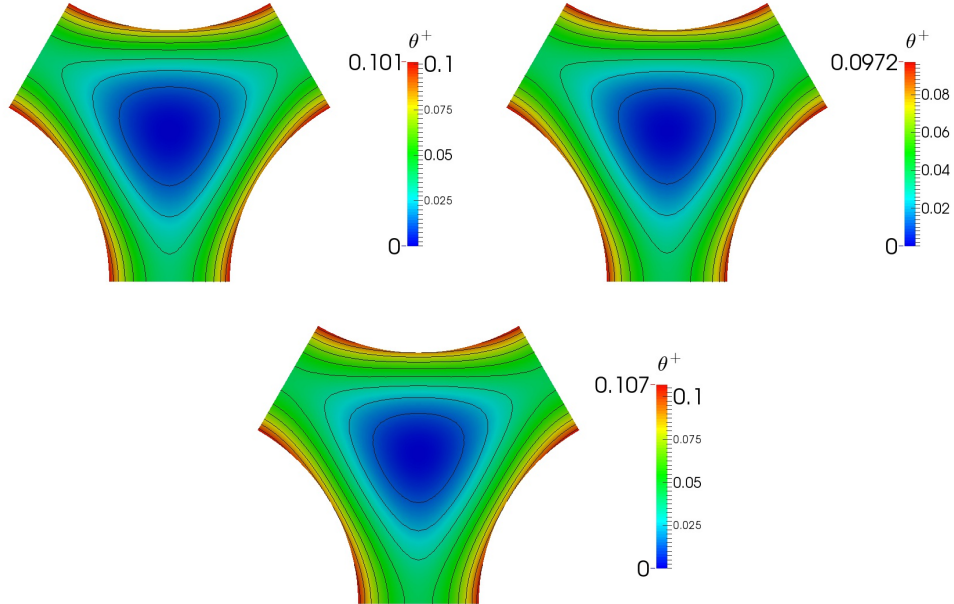
Figure 3.29: Triangular rod bundle with $\chi = 1.3$. Non-dimensional temperature θ^* for $Pe = 1230$ and different turbulence models: (from the top left to the bottom right) k_θ-ϵ_θ, SED model with $Pr_t = 1.5$ and with $Pr_t = 2.0$.
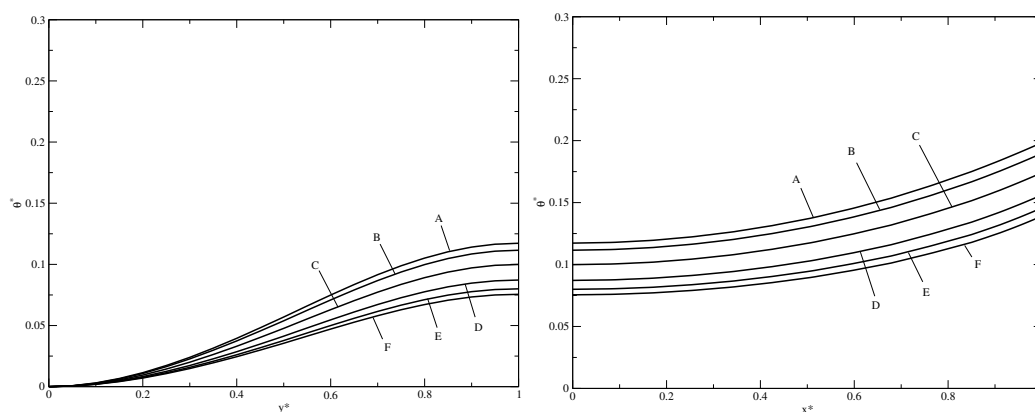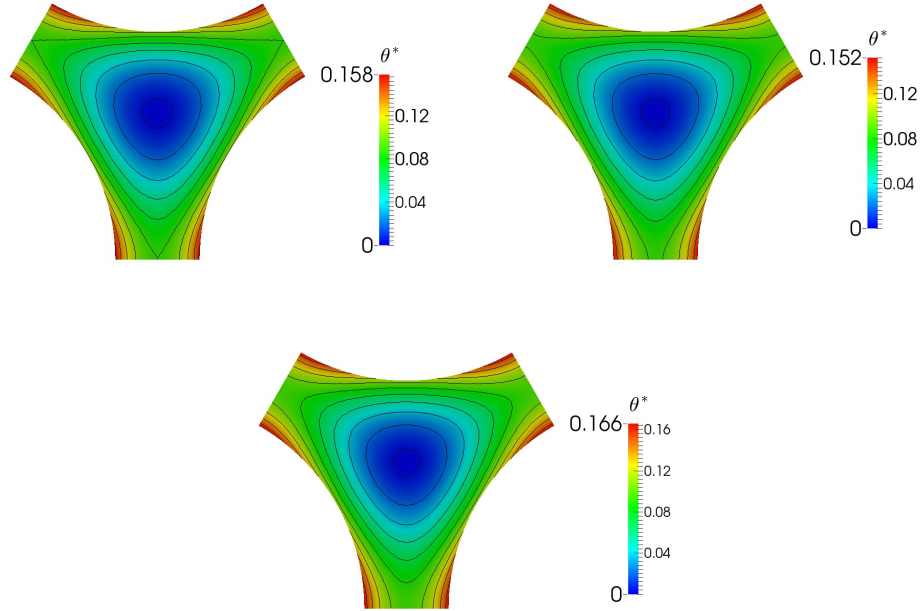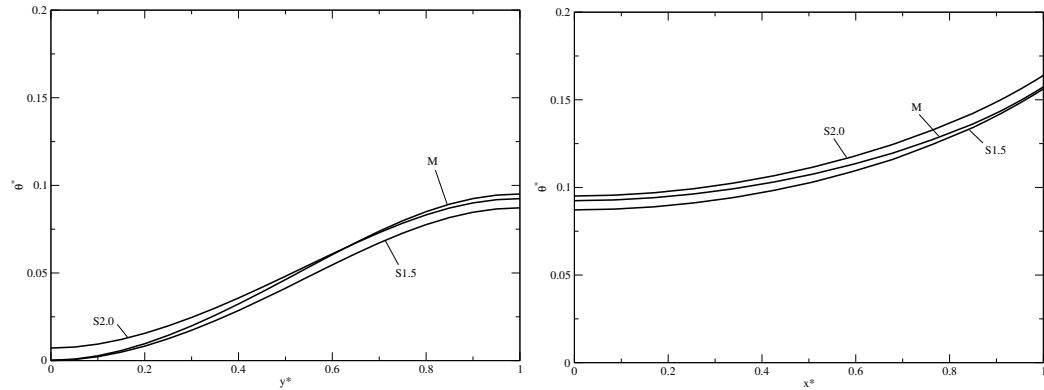

Figure 3.30: Triangular rod bundle with $\chi = 1.3$. Non-dimensional temperature θ^* over the vertical line A-B (left) and horizontal line B-C (right) for $Pe = 1230$ (D) and different turbulence models: (from the top left to the bottom right) k_θ-ϵ_θ (M), SED model with $Pr_t = 1.5$ (S1.5) and with $Pr_t = 2.0$ (S2.0).

In Figure 3.29, from the left top to the bottom right, non-dimensional
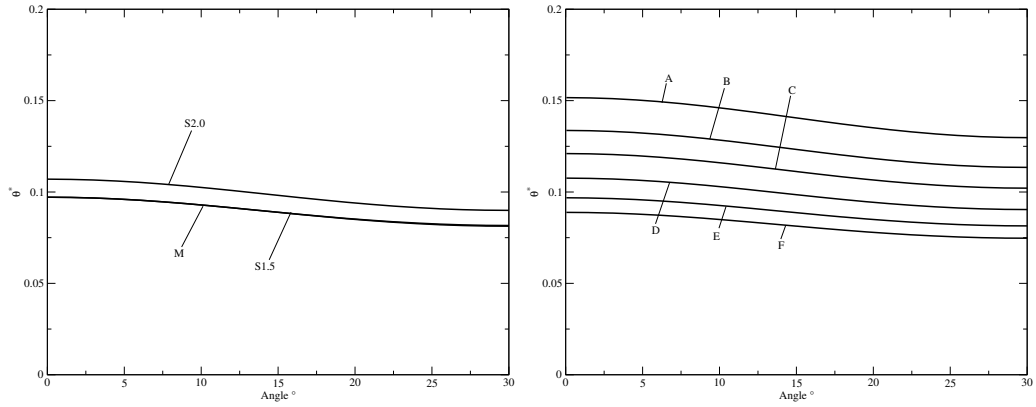
Figure 3.31:   Triangular rod bundle with $\chi = 1.3$. On the left non-dimensional temperature θ^* over the arch C-D with $Pe = 1230$ for different turbulence models: k_θ-ϵ_θ (M), SED model with $Pr_t = 1.5$ (S1.5) and with $Pr_t = 2.0$ (S2.0). On the right non-dimensional temperature θ^* over the arch C-D for different $Pe \approx 270$ (A) , 530 (B), 750 (C), 1030 (D) 1470 (E) and 1970 (F).

$< w >_{av}$ (m/s)	Pe	$< Pr_t >_{av}$
0.267	266	2.64
0.366	364	2.49
0.534	531	2.18
0.757	752	1.91
1.033	1026	1.79
1.238	1230	1.75
1.482	1468	1.73
1.92	1968	1.68

Table 3.2:   Triangular rod bundle with $\chi = 1.3$. Average turbulent Prandtl number $< Pr_t >_{av}$ as a function of average axial velocity $< w >_{av}$.

temperature θ^* is shown on the outlet exit section for three different cases: k_θ-ϵ_θ, SED model for $Pr_t = 1.5$ and $Pr_t = 2.0$. The contour lines are obtained by dividing the range in ten equal intervals. The temperature distribution of the k_θ-ϵ_θ model is between the SED model with $Pr_t = 1.5$ and $Pr_t = 2.0$. In Figure 3.30 the same non-dimensional temperature θ^* is shown over the lines A-B (left) and B-C (right) respectively, while in Figure 3.31 the non-dimensional temperature θ^* is plotted over the arch C-D. On the left of this Figure the temperature distributions for these different cases are labeled by M (k_θ-ϵ_θ), S1.5 (SED model for $Pr_t = 1.5$) and S2.0 (SED model for
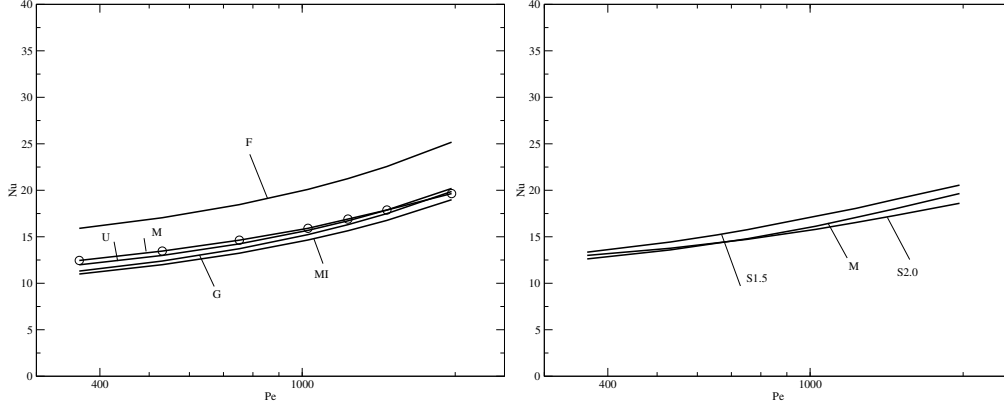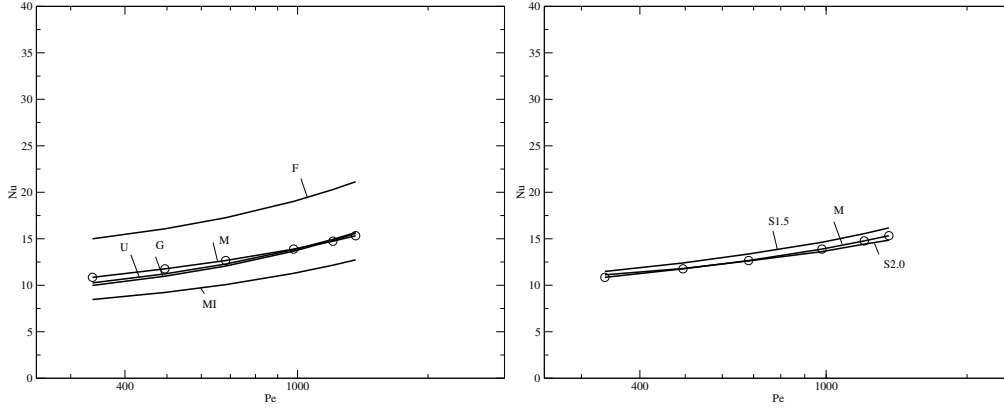
Figure 3.32: Triangular rod bundle with $\chi = 1.3$. Nusselt number as a function of Peclet number (left) from Friedland (F), Ushakov (U), Graber (G), Mikityuk (MI) correlations and k-ϵ-k_θ-ϵ_θ model (M) and for different turbulence models (right): k-ϵ-k_θ-ϵ_θ (M), SED model with $Pr_t = 1.5$ (S1.5) and with $Pr_t = 2$ (S2.0).

$Pr_t = 2.0$).

The computation of the Nu number allows us to compare the results obtained with the k-ϵ-k_θ-ϵ_θ model and experimental correlations. The Nusselt number is computed with the bulk temperature T_b and the average wall temperature T_{wm} as

$$Nu = \frac{\dot{q} \, D_{eq}}{(T_{wm} - T_b)\lambda} \qquad T_b = \frac{\int_\Omega T \, \mathbf{v} \cdot \mathbf{n} \, d\Omega}{\int_\Omega \mathbf{v} \cdot \mathbf{n} \, d\Omega} \qquad T_{wm} = \frac{\int_{\Gamma_w} T \, d\Gamma}{\int_{\Gamma_w} d\Gamma} \, . \qquad (3.65)$$

We remark that the temperature is not constant on the rod wall and the integral (3.65) should be computed with care. On the right of Figure 3.31 the non-dimensional temperature θ^* over the arch C-D is shown for $Pe \approx 270$ (A), 530 (B), 750 (C), 1030 (D) 1470 (E) and 1970 (F). As one can see from this figure the rod average temperature T_{wm} changes with Pe number and it is a function of the angle. By observing the behavior of the temperature along the arch C-D it is difficult to see a point that can be representative of the average rod temperature, so an integral as the one reported in (3.65) has to be computed precisely.

Finally the Nusselt number for the case $\chi = P/D = 1.3$ is investigated and compared with different correlations. On the left of Figure 3.32 the Nusselt number as a function of Peclet number from Friedland (F), Ushakov (U), Graber (G), Mikityuk (MI) correlations is shown. It is important to remark that Ushakov (U) and Graber (G) correlations are in very good agreement with the k-ϵ-k_θ-ϵ_θ model (M). It is easy to see also how the other heat transfer

	$Pe = 750$
Model	Nu
Friedland (F)	17.52
$Prt = 1.5$	15.72
$Pr_t = 2$	14.63
k-ϵ-k_θ-ϵ_θ	14.63
Ushakov (U)	14.24
Graber (G)	13.71
Mikityuk (MI)	13.23

	$Pe = 1030$
Model	Nu
Friedland (F)	21.25
$Prt = 1.5$	18.20
k-ϵ-k_θ-ϵ_θ	17.07
$Pr_t = 2$	16.74
Ushakov (U)	16.71
Graber (G)	16.30
Mikityuk (MI)	15.65

	$Pe = 1470$
Model	Nu
Friedland (F)	22.56
$Prt = 1.5$	19.09
Ushakov (U)	17.87
k-ϵ-k_θ-ϵ_θ	17.78
Graber (G)	17.49
$Pr_t = 2$	17.43
Mikityuk (MI)	16.76

Table 3.3: Triangular rod bundle with $\chi = 1.3$. Nusselt number for different turbulence models and comparison with different correlations: k-ϵ-k_θ-ϵ_θ, SED ($Pr_t = const$) model, Ushakov, Graber and Mikityuk (data fitting) correlation.

turbulence models perform on the same cases. On the right of Figure 3.32 the Nusselt number is reported as a function of Peclet for k-ϵ-k_θ-ϵ_θ (M) and SED model with $Pr_t = 1.5$ (S1.5), $Pr_t = 2$ (S2.0). It can be seen that the simple eddy viscosity (SED) model with an appropriate coefficient Pr_t in the range of $(1.5 - 2)$ can give quite good results in this geometry and for this range of Peclet. The k-ϵ-k_θ-ϵ_θ model lies between the line with $Pr_t = 2$ and $Pr_t = 1.5$. This model approaches to $Pr_t = 1.5$ when Pe number increases. An approximate evaluation of the constant turbulent Prandtl number Pr_t for the SED model can be found in many papers [26, 27] but a guess value can be taken also from the average Pr_t number computed from the k-ϵ-k_θ-ϵ_θ model as reported in Table 3.2 on the bottom. The values reported in Table 3.2 are close to those required approximately by the SED model. In this case the average values of the Pr_t decrease with higher velocity as required for SED simple eddy diffusivity models used with constant values. For a detailed comparison among turbulence models and experimental correlations one can refer to Table 3.3. Three cases are reported for $Pe = 750$, 1030 and

1470. In Table 3.3 we report the Nusselt number calculated with k-ϵ-k_θ-ϵ_θ and SED ($Pr_t = const$) model, Ushakov, Graber and Mikityuk correlations. It is worth to remark that the k-ϵ-k_θ-ϵ_θ model gives very good results for all these three cases and the Nusselt number is located between the values computed with the SED model with $Pr_t = 2.0$ and $Pr_t = 1.5$.

Triangular rod bundle with different $\chi = P/D$

In this section we present the results of triangular rod bundle heat transfer simulations with different χ. In Figure 3.33 the geometries are shown for the studied pitch-to-diameter ratios $\chi = 1.2$, 1.3 and 1.5. The equivalent hydraulic diameter is very different between these geometries and this can be appreciated in Figure 3.33.

Since we have already presented the results for $\chi = 1.3$ in the previous

Figure 3.33: Triangular rod bundle geometries for different χ. From left to right $\chi = 1.2$, 1.3 and 1.5.

Figure 3.34: Triangular rod bundle with $\chi = 1.2$. Non-dimensional temperature θ^* over the vertical line A-B (left) and horizontal line B-C (right) for $Pe \approx 340$ (A) , 500 (B), 680 (C), 980 (D) 1210 (E) and 1360 (F).

Figure 3.35:   Triangular rod bundle with $\chi = 1.2$. Non-dimensional temperature θ^* for $Pe \approx 980$ and three different turbulence models: (from the top left to the bottom right) k_θ-ϵ_θ, SED model for $Pr_t = 1.5$ and $Pr_t = 2.0$.

Figure 3.36:   Triangular rod bundle with $\chi = 1.2$. Non-dimensional temperature θ^* over the line A-B (left) and B-C (right) for $Pe \approx 980$ and three different turbulence models: k_θ-ϵ_θ (M), Kays (K), and SED model for $Pr_t = 1.5$ (S1.5) and $Pr_t = 2.0$ (S2.0).

Section it is important to compare now the results for $\chi = 1.2$ and 1.5. First we analyze the case $\chi = 1.2$, which is characterized by the same diameter

Figure 3.37: Triangular rod bundle with $\chi = 1.2$. On the left Nusselt number as a function of Peclet number from Friedland (F), Ushakov (U), Graber (G), Mikityuk (MI) correlations and k-ϵ-k_θ-ϵ_θ model (M). On the right the Nusselt number as a function of Peclet number for k-ϵ-k_θ-ϵ_θ (M), Kays (K) and SED model with $Pr_t = 1.5$ (S1.5), $Pr_t = 2$ (S2.0).

$D = 8.4$ mm but different pitch $P = 9.84$ mm, that results in an equivalent hydraulic diameter $D_h \approx 4.82$ mm. The characteristic physical properties are the same defined in Table 3.1 with $Pr = 0.025$. For this configuration we consider cases with average velocities in the range of 0.5 to 2 m/s. Six different simulations with $Re \approx 13470$ (A), 19780 (B), 27310 (C), 39180 (D) 48260 (E) and 54470 (F) are presented. These cases correspond to the mean velocity field $v \approx 0.497$ (A), 0.73 (B), 1.008 (C), 1.446 (D), 1.781 (E) and 2.01 (F) with corresponding Peclet numbers $Pe \approx 340$ (A) , 500 (B), 680 (C), 980 (D) 1210 (E) and 1360 (F).

The non-dimensional temperature θ^* for $\chi = 1.2$ is reported in Figure 3.34 for these six cases over the lines A-B and B-C (refer to Figure 3.20 for the location of these lines). The distribution of θ^* along the vertical line A-B is reported on the left of Figure 3.34 and along B-C on the right. With this geometry the drop in temperature is higher if compared with the case $\chi = 1.3$ which implies a less efficient heat transfer. This fact can be explained by comparing the equivalent hydraulic diameters of these different geometries.

Different turbulence models have been used for these simulations and a comparison of the temperature is reported in Figures 3.35-3.36 for the test case with $Pe = 980$. In Figure 3.35 one can see the non-dimensional temperature θ^* over the section of the triangular rod bundle for three different turbulence models. From the top left to the bottom right the temperature profiles and the corresponding contour lines for k_θ-ϵ_θ, SED model with $Pr_t =$
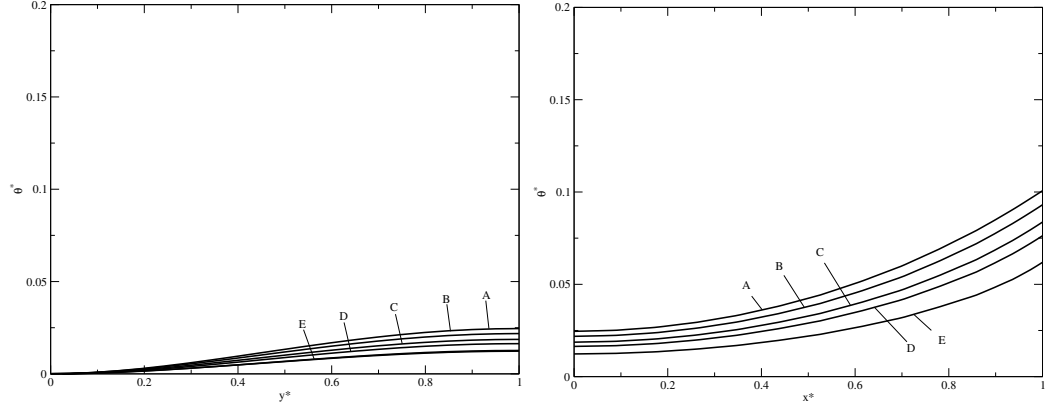
Figure 3.38:   Triangular rod bundle with $\chi = 1.5$. Non-dimensional temperature θ^* over the vertical line *A-B* (left) and the horizontal line *B-C* (right) for $Re \approx 17800$ (A), 26100 (B), 40400 (C), 53300 (D) and 68600 (E).

1.5 and $Pr_t = 2.0$ are shown. The contour lines are obtained by dividing the θ^* range in ten equal intervals over the section. The k_θ-ϵ_θ model shows a temperature that lies between the SED models with constant turbulent Prandtl number 2.0 and 1.5. We can see the temperature distribution θ^* in more details in Figure 3.36 over the line *A-B* and *B-C* on the left and on the right, respectively. In this Figure three different turbulence models are compared: the k_θ-ϵ_θ (M) the simple diffusivity model with $Pr_t = 1.5$ (S1.5) and $Pr_t = 2.0$ (S2.0).

Finally we show the Nusselt number for this geometry calculated using the k_θ-ϵ_θ and SED model and compare it with available experimental correlations for the heat transfer, namely Friedland, Ushakov, Graber and Mikityuk correlations for $\chi = 1.2$. In Figure 3.37 the Nusselt number is plotted as a function of Peclet number. On the left a comparison among Friedland (F), Ushakov (U), Graber (G) and Mikityuk (MI) experimental correlations and k-ϵ-k_θ-ϵ_θ model (M) is shown. On the right the comparison is between different turbulence models: k-ϵ-k_θ-ϵ_θ (M) and SED model with $Pr_t = 1.5$ (S1.5) and $Pr_t = 2$ (S2.0). Friedland correlation (with $\psi = 1$) predicts a very high heat transfer, while all the other correlations and turbulence models show a similar behavior, except from Mikityuk correlation which predicts a lower Nusselt number.

The triangular rod bundle case with $\chi = 1.5$ is characterized by $D = 8.2$ mm and $P = 12.3$ mm which corresponds to an equivalent hydraulic diameter $D_h = 12.1$ mm. This high hydraulic diameter allows a high heat transfer and a more uniform temperature distribution in the section of the rod bundle. In this geometry five different simulations with $Re \approx 17800$ (A), 26100 (B),
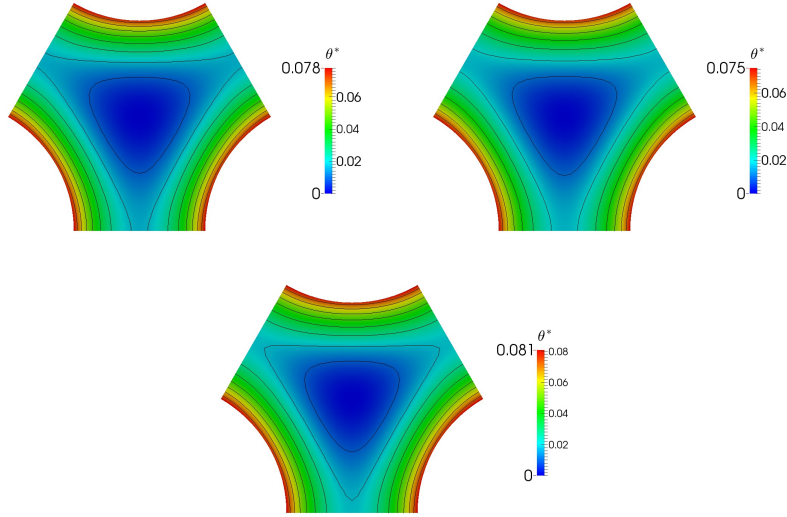
Figure 3.39:   Triangular rod bundle with $\chi = 1.5$. Non-dimensional temperature θ^* for $Re \approx 53300$ (D) and three turbulence models: from the top left to the bottom right, k_θ-ϵ_θ, SED model with $Pr_t = 1.5$ and $Pr_t = 2.0$.
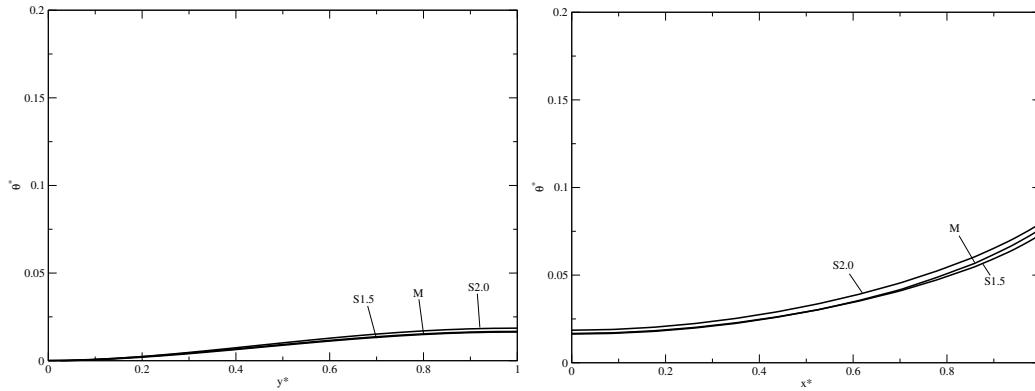
Figure 3.40:   Triangular rod bundle with $\chi = 1.5$. Non-dimensional temperature θ^* over the lines *A-B* (left) and *B-C* (right) for $Re \approx 53300$ (D) and three turbulence models: from the top left to the bottom right, k_θ-ϵ_θ (M), SED model with $Pr_t = 1.5$ (S1.5) and $Pr_t = 2.0$ (S2.0).

40400 (C), 53300 (D) and 68600 (E) have been performed. They correspond to a simulated velocity range 0.26-1 m/s in the rod bundle configuration. The Peclet numbers for these five cases are $Pe \approx 450$ (A), 650 (B), 1010 (C), 1340 (D) and 1720 (E). In order to characterize the temperature distribution, in Figure 3.38 we have shown the non-dimensional temperature θ^* over the
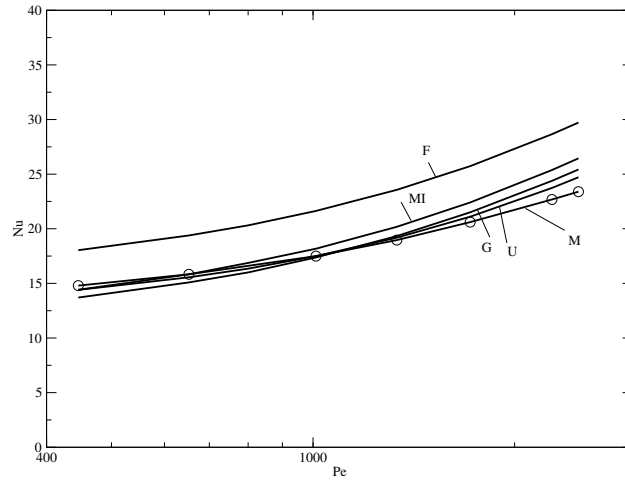
Figure 3.41:   Triangular rod bundle with $\chi = 1.5$. Nusselt number as a function of Peclet number for Friedland (F), Ushakov (U), Graber (G), Mikityuk (MI) correlations and k-ϵ-k_θ-ϵ_θ model (M).
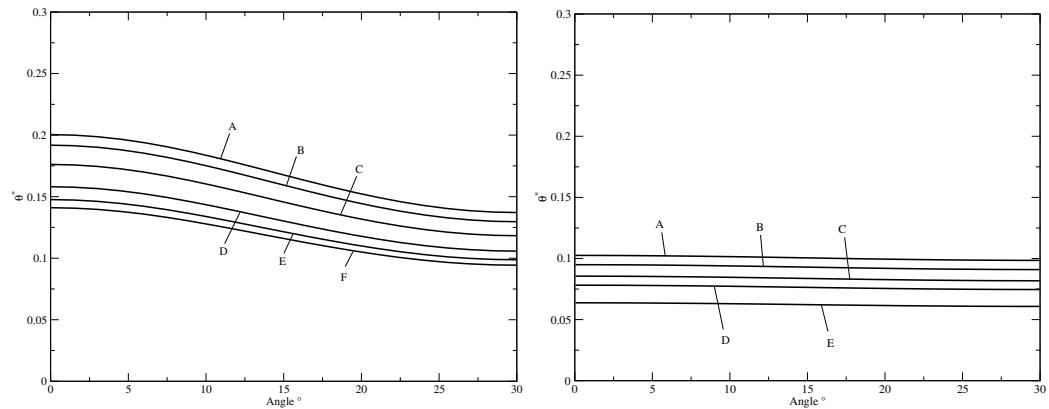
Figure 3.42: Non-dimensional temperature θ^* over the arch C-D for $\chi = 1.2$ on the left for all the different test cases A-F (Pe range of 340 to 1360) and for $\chi = 1.5$ on the right for the different cases A-E (Pe range of 450 to 1720).

lines A-B (left) and B-C (right) for all the cases simulated. As one can see, the temperature is lower and more uniform on the domain if compared with the $1.2 - 1.3$ cases.

A comparison among different turbulence models is reported in Figures 3.39-3.40 for the case D with $Pe \approx 1340$. In Figure 3.39 the non-dimensional temperature θ^* is shown over a triangular rod section for three different models: k-ϵ-k_θ-ϵ_θ and simple eddy diffusivity (SED) model with $Pr_t = 1.5$ and 2. In Figure 3.39 the results obtained with the k-ϵ-k_θ-ϵ_θ and the SED

$< w >_{av}$ (m/s)	Pe	$< Pr_t >_{av}$
0.497	340	2.2
0.73	500	2.125
1.008	680	1.94
1.446	980	1.789
1.781	1200	1.7388
2.01	1360	1.7218

$< w >_{av}$ (m/s)	Pe	$< Pr_t >_{av}$
0.2615	450	2.435
0.3824	650	2.09
0.592	1010	1.871
0.7817	1330	1.723
1.006	1720	1.6688

Table 3.4: Average axial velocity $< w >_{av}$, Peclet number and average turbulent Prandtl number $< Pr_t >_{av}$ for $\chi = 1.2$ (left) and 1.5 (right).

model with constant turbulent Prandtl number $Pr_t = 1.5$ and $Pr_t = 2.0$ are reported from the top left to the bottom right for the test case with $Re \approx 53300$ (D). The θ^* non dimensional temperature is reported with equally subdivided contours for all the turbulence models used. In Figure 3.40 the non-dimensional temperature θ^* is plotted over the vertical line A-B on the left and over the horizontal line B-C on the right. The results are labeled (M) for the k-ϵ-k_θ-ϵ_θ and (S1.5) and (S2.0) for the SED model with constant turbulent Prandtl number of 1.5 and 2.0. In this Figure it can be seen that the SED model with these two values of turbulent Prandtl number shows a similar behavior as the four parameter k-ϵ-k_θ-ϵ_θ model.

We can now present a comparison between the heat transfer predicted by experimental correlations and by the four parameter turbulence model for the triangular rod bundle with $\chi = 1.5$. In Figure 3.41 the Nusselt number is shown as a function of Peclet number for Friedland (F), Ushakov (U), Graber (G) and Mikityuk (MI) correlations and for the k-ϵ-k_θ-ϵ_θ turbulence model (M) for comparison. The experimental correlations give quite similar results for this case except from Friedland correlation which is quite higher. We remark that the Friedland correlation values have been computed with $\psi = 1$ ($Pr_t = 1$). The four parameter model predicts a little lower Nusselt number value for higher Peclet numbers than that of the Ushakov correlation while for intermediate Peclet numbers gives similar results.

It is very interesting to compare temperature and Nusselt number among different geometries of triangular rod bundles in order to understand better the different heat transfer behavior. This comparison is carried on in Figures 3.42-3.43 and Tables 3.4-3.5. In Figure 3.42, the non-dimensional temperature θ^* over the arch C-D is shown for different χ and for all the cases simulated. On the left θ^* is shown for $\chi = 1.2$ and on the right for $\chi = 1.5$. The cases with $\chi = 1.2$ show a higher temperature on the wall than cases with $\chi = 1.5$, considering similar Peclet numbers. Moreover, the cases with

$v = 1.45 m/s$	$Pe = 980$
Model	Nu
Friedland (A)	19.02
$Prt = 1.5$	14.62
k-ϵ-k_θ-ϵ_θ	$\boxed{13.89}$
Graber (D)	13.83
Ushakov (C)	13.67
$Pr_t = 2$	13.62
Mikityuk (E)	11.28

$v = 0.78 m/s$	$Pe = 1330$
Model	Nu
Friedland (A)	23.57
Mikityuk (E)	20.18
$Prt = 1.5$	20.00
Graber (D)	19.33
Ushakov (C)	19.19
k-ϵ-k_θ-ϵ_θ	$\boxed{18.87}$
$Pr_t = 2$	18.57

Table 3.5:   Nusselt number calculated with different turbulence models and with experimental correlations for reference cases $\chi = 1.2$ and 1.5. On the left $\chi = 1.2$ test case with $Pe = 980$ and on the right $\chi = 1.5$ test case with $Pe = 1330$.
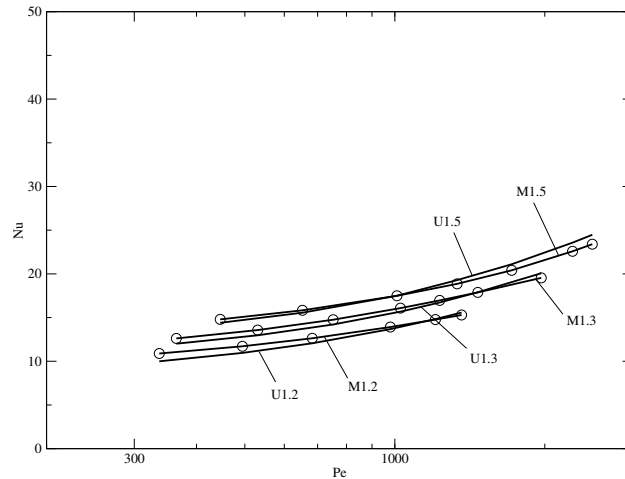
Figure 3.43:   Comparison between triangular bundles with different χ. Nusselt number from k-ϵ-k_θ-ϵ_θ model for $\chi = 1.2$ (M1.2), 1.3 (M1.3) and 1.5 (M1.5) and from Ushakov experimental correlation for $\chi = 1.2$ (U1.2), 1.3 (U1.3) and 1.5 (U1.5).

$\chi = 1.2$ show a much variable temperature on the wall, while this is nearly constant for the cases with $\chi = 1.5$. Care must be taken when integrating the wall temperature over the arch for calculating the Nusselt number over the section for geometries with low χ because of this high variability. This is true also for experimental measurements in order to obtain a proper definition of the wall temperature.

In Table 3.4 turbulent Prandtl number calculated with the k-ϵ-k_θ-ϵ_θ model

P/D	Min err $[Nu]$	Max err $[Nu]$	range[Pe]
1.2	0	0.9	350-1800
1.3	0	0.6	360-2200
1.5	0	1.2	400-2800

Table 3.6: Errors for different pitch-to-diameter ratio χ between the Ushakov correlation and the k-ϵ-k_θ-ϵ_θ turbulence model.

and averaged over the section are reported for all the cases simulated with $\chi = 1.2$ on the left and with $\chi = 1.5$ on the right. The average Pr_t decreases with increasing Peclet number and it remains in the range $1.6 - 2.4$ for all the test cases. The Nusselt number is compared for different correlations and turbulence models in Table 3.5 between two cases with different χ. It can be seen from these data that the Nusselt number calculated with the four parameter model lies between the results obtained with the SED model with $Pr_t = 1.5$ and $Pr_t = 2$.

Finally in Figure 3.43 the Nusselt numbers calculated with the k-ϵ-k_θ-ϵ_θ turbulence model are shown with the Ushakov correlation for different pitch-to-diameter ratios. An increase of the parameter χ increases the Nusselt number. This Figure shows that the four parameter turbulence model predicts a heat transfer quite similar to the one predicted by Ushakov correlation. In Table 3.6 we show the maximum and minimum errors between the Ushakov correlation and the k-ϵ-k_θ-ϵ_θ turbulence model for different pitch-to-diameter ratios $\chi = P/D$ and Pe numbers. The Nusselt number differs with slightly higher Nu in the low Peclet range and lower Nu in the high Peclet range. Since Ushakov correlation is now the most recommended correlation for liquid metal flows in triangular rod bundles the four parameter model can be considered a valid tool for the prediction of heat transfer for this geometry in this range of Pe numbers.

3.2.4 Square rod bundle

In this section we report the numerical results obtained for the simulations of fully developed turbulent flows of a heavy liquid metal with $Pr = 0.025$ in square lattice bare rod bundle geometries with different pitch-to-diameter P/D ratio.

The physical properties and geometrical parameters employed for the simulations are reported in Table 3.7. These data are representative of a Lead-Bismuth Eutectic at the reference temperature of about 520 K with a corresponding Prandtl number of 0.025 [34]. In these simulations all the physical properties are considered to be constant with temperature.

Square lattice bare rod bundle with $\chi = 1.22$

The first geometry we consider is characterized by $\chi = 1.22$ with a corresponding hydraulic diameter of 7.3 mm. We made six simulations with an average fluid velocity of 0.51 (A), 0.74 (B), 1.04 (C), 1.48 (D), 1.82 (E) and

Parameter	Symbol	Value	Unit of Measure
Dynamic Viscosity	μ	0.00184	Pa s
Mass Density	ρ	10340	Kg/m^3
Thermal Conductivity	λ	10.7272	W/(m K)
Specific Heat Capacity	C_p	145.75	J/(Kg K)
Rod Diameter	D	8.2	mm
P/D Ratios	χ	1.22 - 1.3 - 1.5	

Table 3.7: Physical properties and geometrical parameters employed in the simulations.
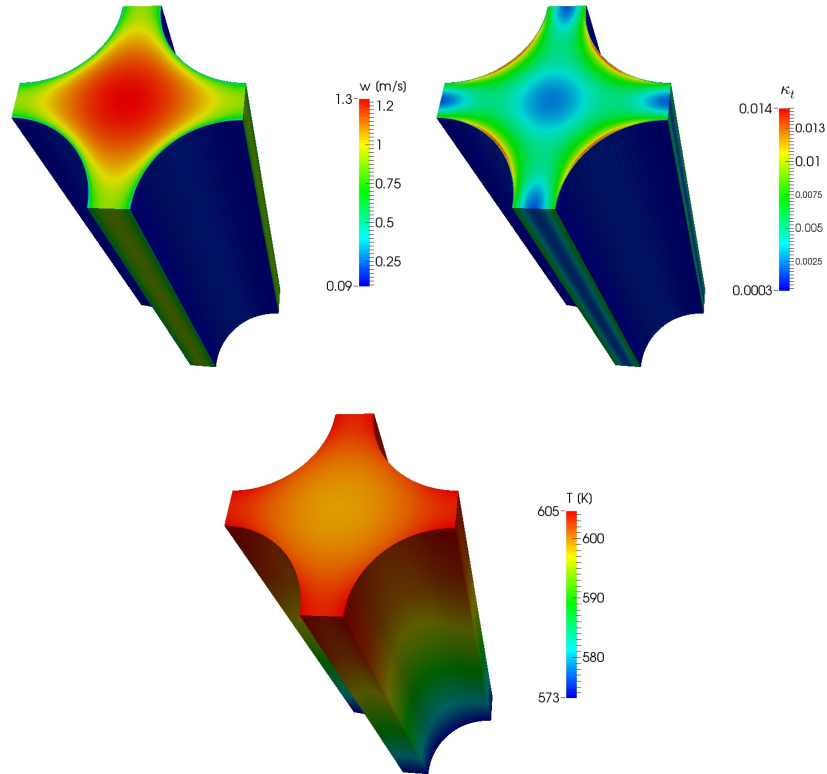
Figure 3.44: Square lattice bare rod bundle with $\chi = 1.22$. Velocity, turbulence kinetic energy and temperature for the test case C with $Pe = 1070$.
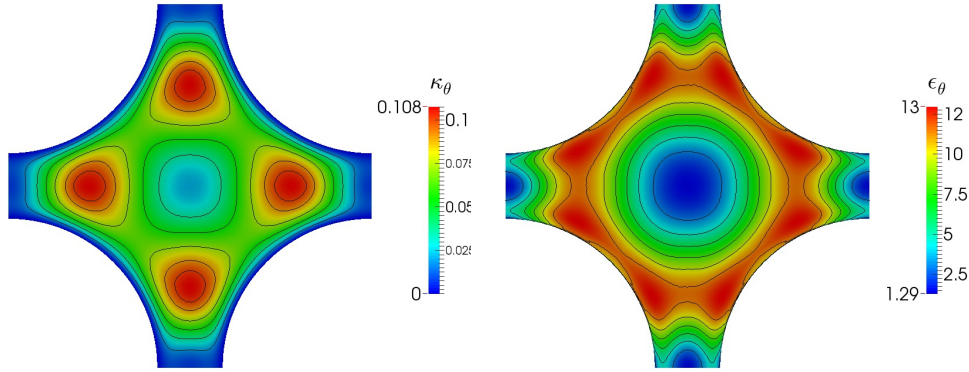
Figure 3.45: Square lattice bare rod bundle with $\chi = 1.22$. Average square temperature fluctuation and its dissipation for the test case C with $Pe = 1070$.
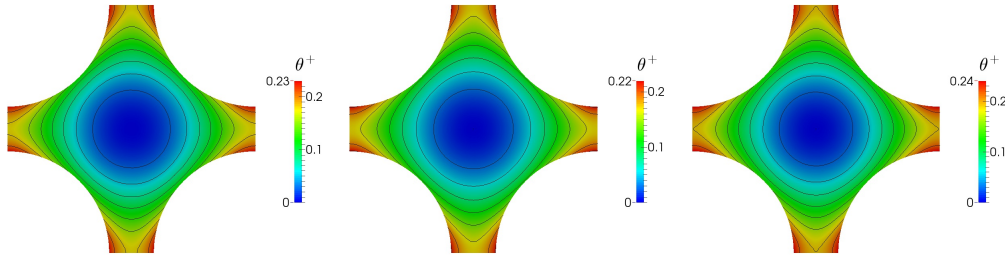
Figure 3.46: Square lattice bare rod bundle with $\chi = 1.22$, test case C. Non-dimensional temperature θ^+ for different turbulence model: from left to right four parameters turbulence model and SED model with $Pr_t = 1.5$ and 2.

2.22 m/s (F). The corresponding Peclet numbers are approximately 520 (A), 760 (B), 1070 (C), 1520 (D), 1870 (E) and 2280 (F). In Figure 3.44 the velocity, the turbulent kinetic energy and the temperature are visible in the three-dimensional geometry for the test case C with $Pe = 1070$. The geometry is scaled with a factor of $1/100$ on the azimuthal axis in order to better show the results. The flow is simulated as dynamically fully developed, so the velocity and turbulent kinetic energy are flat along the axis of the channel, while the thermal development of the flow is visible as the temperature rises along the channel. In Figure 3.45 the average square temperature fluctuation and its dissipation are reported on a slice in the fully developed region for test case C. The main difference with respect to dynamical turbulent variables is the length of the thermal boundary layer which appears to be very deep inside the channel. In Figure 3.46 the non-dimensional temperature θ^+ is reported for the test case C with $Pe = 1070$ to compare different tur-
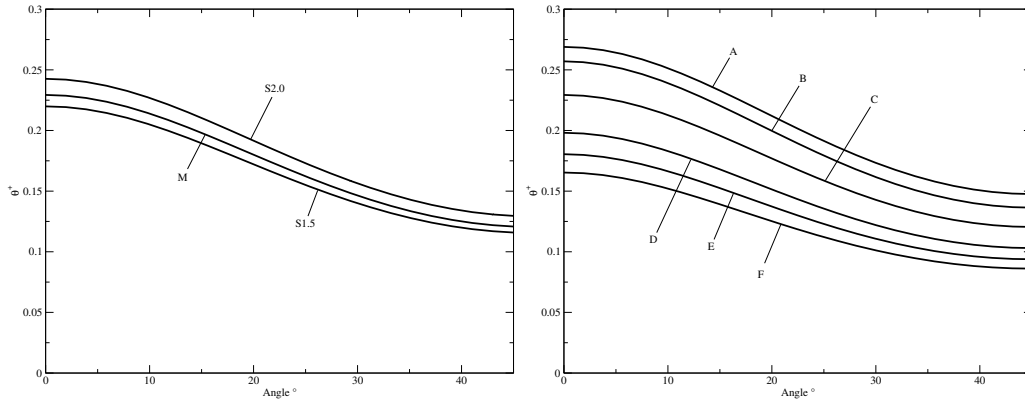
Figure 3.47: Square lattice bare rod bundle with $\chi = 1.22$. On the left non-dimensional temperature θ^+ as a function of the angle on the rod arc for test case C and different turbulence model: four parameter turbulence model (M) and SED model with $Pr_t = 1.5$ (S1.5) and 2 (S2.0). On the right non-dimensional temperature θ^+ as a function of the angle on the arc for all the test cases studied.

bulence models. The non-dimensional temperature is obtained dividing the difference $T - T_r$ by $(q_w \cdot D_h)/\lambda$ where q_w is the wall heat flux and D_h the hydraulic diameter. As one can see from this Figure the result of the four parameter turbulence model shows a maximum temperature that lies between SED model results obtained with $Pr_t = 1.5$ and $Pr_t = 2$. As we show in the following a similar result is obtained in term of Nusselt number. Finally we report in Figure 3.47 the non dimensional fluid temperature on the rod arc as a function of the angle in degree unit. The considered arc is an eighth of the rod total circumference. On the left the non dimensional temperature θ^+ is reported for test case C and for the three different turbulence model, the four parameter and the SED model with $Pr_t = 1.5$ and $Pr_t = 2$. On the right θ^+ is reported on the same position for all the test cases studied. It can be seen from this Figure that the temperature computed with the four parameter model lies between the temperature obtained with the SED model with $Pr_t = 2$ and 1.5. Moreover as the Peclet number increases the average temperature on the wall decreases and it becomes more uniform.

As already pointed out the most important heat transfer parameter from an engineering point of view is the asymptotic Nusselt number of the flow. We can compute this quantity for different turbulence models and compare it with the experimental correlations introduced in Section 2.3.3. In Table 3.8 the Nusselt numbers for all the test cases simulated and for the different turbulence models are reported. In the last column it is reported the

Test Case	SED $Pr_t = 2$	SED $Pr_t = 1.5$	Four parameter	$\langle \mathbf{Pr_t} \rangle$
A	9.13	9.68	9.57	1.616
B	9.96	10.71	10.16	1.511
C	10.95	11.93	11.31	1.431
D	12.36	13.72	12.87	1.421
E	13.27	14.85	13.92	1.400
F	14.16	15.95	14.99	1.395

Table 3.8: Square lattice bare rod bundle with $\chi = 1.22$. Nusselt number for different turbulence models for all the test cases simulated. In the last column average turbulent Prandtl number computed with the four parameter turbulence model.
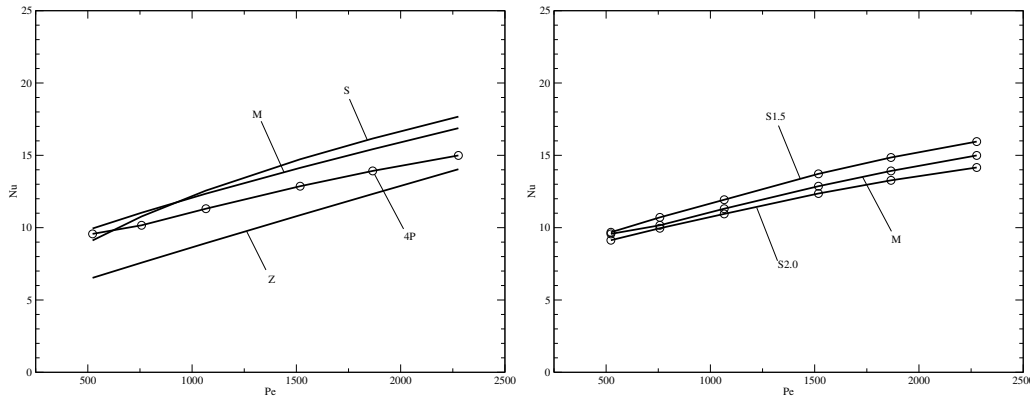
Figure 3.48: Square lattice bare rod bundle with $\chi = 1.22$. On the left asymptotic Nusselt number as a function of Peclet number computed with the four parameter turbulence model (4P) compared with Subbotin (S), Mikityuk (M) and Zhukov (Z) correlations. On the right asymptotic Nusselt number as a function of Peclet number for different turbulence models: four parameter turbulence model (M) and SED model with $Pr_t = 1.5$ (S1.5) and 2 (S2.0).

average turbulent Prandtl number computed with the four parameter turbulence model. It can be seen that the average Pr_t decreases as the Peclet number of the flow increases. Moreover it is important to remark that even if $\langle Pr_t \rangle$ is very close to 1.5 for test case B the resulting Nusselt numbers are quite different; this is due to the fact that Pr_t variations over the domain are more important than its average value. The integral heat transfer is highly affected by a change of Pr_t in the region near the wall. However the average value of Pr_t can give an overall estimate of the dissimilarity between the thermal and the dynamical turbulent boundary layers. The Nusselt number computed with the turbulence models are compared with the experimental

heat transfer correlations in Figure 3.48. On the left the results obtained with the four parameter model are compared with Subbotin, Mikityuk and Zhukov correlations. The BREST report correlation is omitted here because of its similarity with Zhukov one. On the right the Nusselt number computed with different turbulence models are reported and compared. The Nusselt numbers computed with the four parameter model lie between the experimental correlations. Moreover as the constant Pr_t of SED model decreases a higher heat transfer is predicted.

Square lattice bare rod bundle with $\chi = 1.3$

The second geometry we analyze is the square lattice bare rod bundle with pitch-to-diameter ratio $\chi = 1.3$. The rod diameter is kept constant at 8.2 mm

Test Case	$< \mathbf{w} >$ [m/s]	Pe	$\langle \mathbf{Pr_t} \rangle$
A	0.442	590	1.615
B	0.574	760	1.506
C	0.925	1230	1.423
D	1.19	1580	1.398
E	1.56	2070	1.360
F	1.96	2610	1.351

Table 3.9: Square lattice bare rod bundle with $\chi = 1.3$. Peclet numbers and average velocities of the six test cases studied. In the last column average turbulent Prandtl number for the four parameter turbulence model.
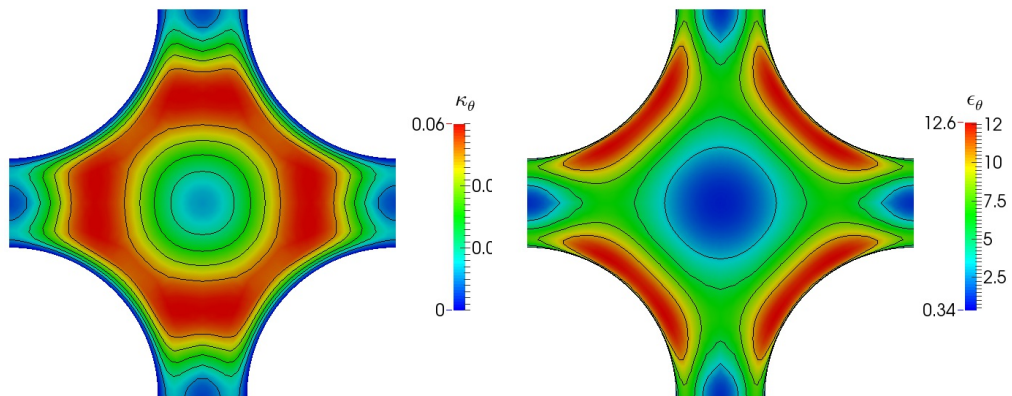
Figure 3.49: Square lattice bare rod bundle with $\chi = 1.3$. Average square temperature fluctuation and its dissipation for the test case D with $Pe = 1580$.
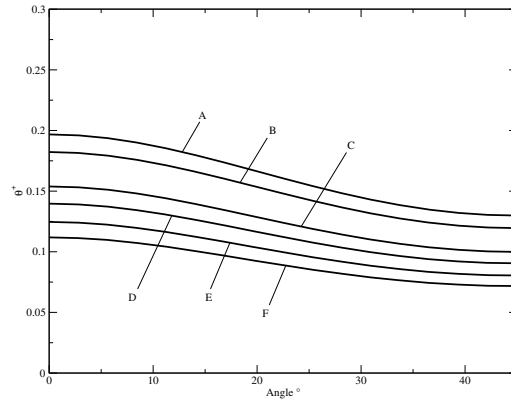
Figure 3.50: Square lattice bare rod bundle with $\chi = 1.3$. Non-dimensional temperature θ^+ on the rod arc as a function of the angle for all the test cases studied.
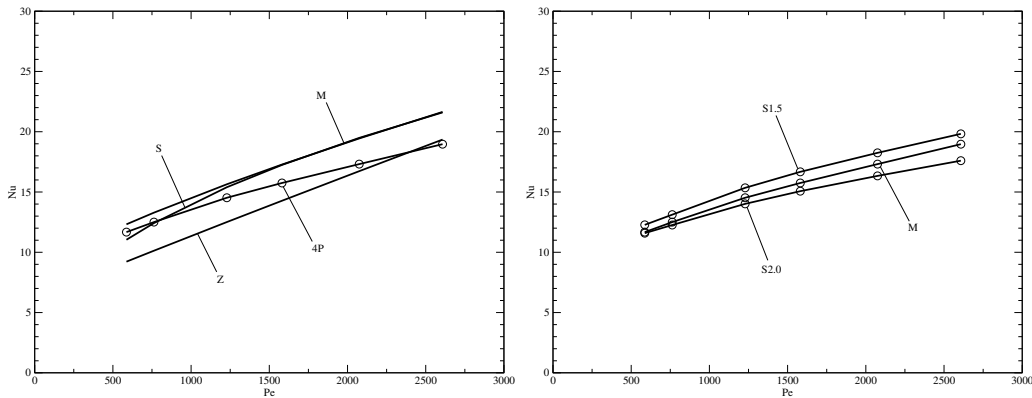
Figure 3.51: Square lattice bare rod bundle with $\chi = 1.3$. On the left asymptotic Nusselt number as a function of Peclet number computed with the four parameter turbulence model (4P) compared with Subbotin (S), Mikityuk (M) and Zhukov (Z) correlations. On the right asymptotic Nusselt number as a function of Peclet number for different turbulence models: four parameter turbulence model (M) and SED model with $Pr_t = 1.5$ (S1.5) and 2 (S2.0).

so the channel has a hydraulic diameter of 9.4 mm. We have studied six test cases with average velocities in the range of 0.4 to nearly 2 m/s. The Peclet numbers corresponding to the average velocities in our geometrical configuration for all the test cases are reported in Table 3.9 in the first columns. In the last column of the same Table the average turbulent Prandtl number in the fully developed region as computed with the four parameter turbulence model is reported for all the test cases. We remark the decreasing of Pr_t

with increasing Pe as it happens in the test cases with $\chi = 1.2$. In Figure 3.49 the averaged square temperature fluctuation k_θ and its dissipation are reported on a slice for the test case D with $Pe = 1580$.

We can now analyze the temperature behavior on the rod wall for this geometry. In Figure 3.50 we report the non-dimensional temperature θ^+ obtained with the four parameter model as a function of the angle for all the six test cases. The mean values are lower for this geometry with respect to $\chi = 1.2$ cases, and the temperature slope is smoother. Indeed it is known that with lower pitch-to-diameter ratios the temperature on the rod is less uniform and so more care has to be taken from an experimental point of view when low pitch-to-diameter geometries are considered because the measured wall temperature could not be a good estimate of the average wall temperature.

Finally we report and compare the asymptotic Nusselt numbers as computed with the SED and the four parameter models and as predicted by experimental heat transfer correlations. In Figure 3.51 on the left the Nusselt number computed with the four parameter model is compared with the experimental heat transfer correlations by Subbotin, Mikityuk and Zhukov. The predictions of the turbulence model lie in between the experimental correlations. However there is a quite different slope in the line of Nu(Pe) given by the numerical results with respect to the experimental correlations. On the right of Figure 3.51 a comparison between turbulence models is reported. The results of the four parameter model lie between the results of the SED model with $Pr_t = 1.5$ and 2. Starting from an average $Pr_t \approx 2$ computed by the four parameter model with a Nusselt number very similar to the one predicted by the SED model with $Pr_t = 2$, as the average Pr_t decreases the heat transfer predicted increases, tending to be more close to the SED model with $Pr_t = 1.5$. The same behavior of the SED model as noted above is found in this case.

Square lattice bare rod bundle with $\chi = 1.5$

The last geometry we analyze is the square lattice bare rod bundle with $\chi = 1.5$. This channel has $P = 6.15$ mm and $D_h = 15.3$ mm. The hydraulic diameter of this last geometry is high and this results in a higher heat transfer. In Figure 3.52 the average square temperature fluctuation and its dissipation are reported for the test case D with $Pe = 2210$. In this Figure it is visible the difference in the geometry shape and that the maximum of the average square temperature fluctuation is nearer to the rod wall, more similar to the turbulent specific kinetic energy. We performed seven test cases in this geometry with a range of Peclet number of 700 to 3700. The corresponding average velocities are reported in the second column of Table 3.10. In the
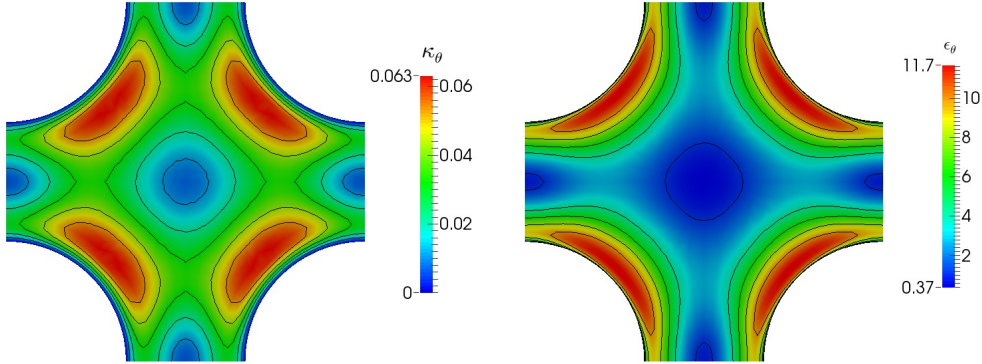
Figure 3.52: Square lattice bare rod bundle with $\chi = 1.5$. Average square temperature fluctuation and its dissipation for test case D with $Pe = 2210$.

Test Case	$\langle \mathbf{w} \rangle$ [m/s]	**Pe**	$\langle \mathbf{Pr_t} \rangle$
A	0.324	700	1.639
B	0.531	1140	1.444
C	0.774	1660	1.391
D	1.031	2210	1.380
E	1.245	2670	1.364
F	1.525	3280	1.330
G	1.754	3770	1.309

Table 3.10: Square lattice bare rod bundle with $\chi = 1.5$. Peclet numbers and average velocities of the seven test cases studied. In the last column average turbulent Prandtl number for the four parameter turbulence model.

last column of the same Table the average turbulent Prandtl numbers are reported. We see that for low Peclet numbers in this case Pr_t is higher than in geometries with lower χ.

In Figure 3.53 on the left the non-dimensional temperature θ^+ on the rod wall is reported as a function of the angle of the arc. We see a very flat profile due to the large hydraulic diameter of this geometry. For this kind of geometry the wall temperature can be measured with less care because the profile is nearly flat. Moreover the average wall temperatures are lower than in the previous cases. On the right of the same Figure the asymptotic Nusselt number is reported as a function of Peclet number as computed with the four parameter turbulence model and as predicted by Subbotin, Mikityuk, BREST and Zhukov correlations. In this case the BREST report correlation gives results quite different from Zhukov correlation, so it is reported in
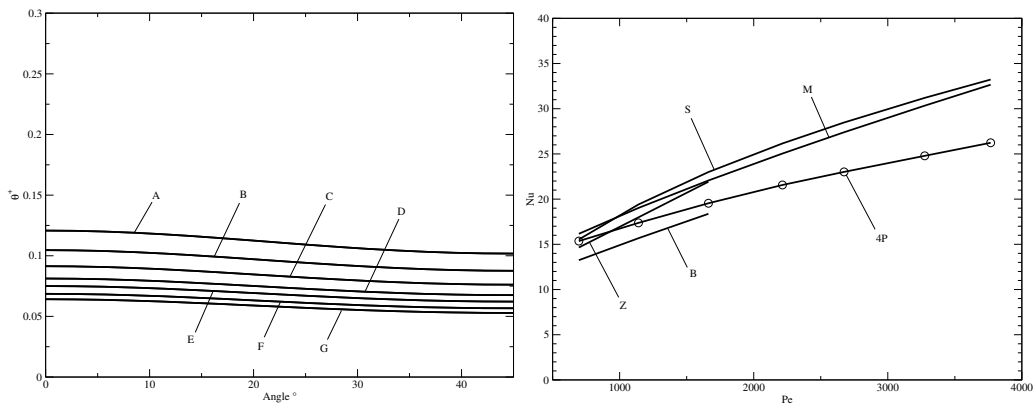
Figure 3.53:   Square lattice bare rod bundle with $\chi = 1.5$. On the left non-dimensional temperature θ^+ on the rod arc as a function of the angle for all the seven test cases studied. On the right asymptotic Nusselt number as a function of Peclet number computed with the four parameter turbulence model (4P) compared with Subbotin (S), Mikityuk (M), BREST (B) and Zhukov (Z) correlations.

the Figure. The turbulence model seems to be more conservative than the experimental correlations, with the only exception of BREST report one which predicts a lower heat transfer for the range of Peclet for which it is proposed.

Chapter 4

Turbulence model k-ω-k_θ-ω_θ

This Chapter is devoted to the description of a k-ω-k_θ-ω_θ four parameter turbulence model derived from the k-ϵ-k_θ-ϵ_θ formulation reported in Chapter 3. In the first Section the derivation of this model is presented together with some remarks on the improvements made in this new formulation with respect to k-ϵ one. Some numerical results are reported in the second Section and compared with results obtained with the k-ϵ model, with DNS data and with experimental correlations for the integral heat transfer.

4.1 Mathematical formulation

For convenience, we summarize briefly here the full mathematical model of the RANS equations for incompressible heavy liquid metal flows. The RANS equations read

$$\nabla \cdot \mathbf{u} \;=\; 0 \,, \tag{4.1}$$

$$\rho \frac{\partial \mathbf{u}}{\partial t} + \rho(\mathbf{u} \cdot \nabla)\mathbf{u} \;=\; \nabla \cdot \sigma - \nabla \cdot \tau + \rho \mathbf{g} \,, \tag{4.2}$$

$$\rho C_p \left(\frac{\partial T}{\partial t} + (\mathbf{u} \cdot \nabla) T \right) \;=\; \nabla \cdot \mathbf{q} - \nabla \cdot \mathbf{q}_\theta + Q \,, \tag{4.3}$$

where $\mathbf{u}$ is the averaged velocity of the fluid and T is the averaged temperature. The tensors σ and $\mathbf{q}$ are the usual viscous stress and heat flux and they are modeled using Navier-Stokes constitutive law for viscous fluids and Fourier law for heat conduction.

$$\sigma \;:=\; -p\mathbf{I} + \mu \mathbf{D} \quad \text{with} \quad \mathbf{D} := \nabla \mathbf{u} + \nabla \mathbf{u}^T \tag{4.4}$$

$$\mathbf{q} \;:=\; -\lambda \nabla T \,. \tag{4.5}$$

Two new terms appear after the averaging process, namely the Reynolds stress tensor τ and the turbulent heat flux $\mathbf{q}_\theta$, defined as the averaged product of the fluctuating components of velocity with itself and velocity with temperature. These terms are calculated as

$$\tau = \rho \overline{\mathbf{u}'\mathbf{u}'} \quad , \quad \mathbf{q}_\theta = \rho C_p \overline{\mathbf{u}'T'} \,. \tag{4.6}$$

Instead of solving the transport equations for the Reynolds stress tensor and for the turbulent heat flux we approximate these terms with the eddy diffusivity model as

$$\tau \;=\; -\nu_t \left(\nabla \mathbf{u} + \nabla \mathbf{u}^T \right) + \frac{2k}{3}\,\mathbf{I}\,, \tag{4.7}$$

$$\mathbf{q}_\theta \;=\; -\alpha_t \,\nabla T\,, \tag{4.8}$$

where the eddy diffusivity of momentum ν_t and the heat eddy diffusivity α_t must be properly defined in the turbulence model. We assume them as a function of the turbulence kinetic energy k and two characteristic time scales, namely τ_{lu}, for dynamical turbulence, and $\tau_{l\theta}$, for thermal turbulence. The eddy viscosity and the eddy diffusivity are then defined as

$$\nu_t := C_\mu \, k \tau_{lu}\,, \quad \alpha_t := C_\theta \, k \tau_{l\theta}\,, \tag{4.9}$$

where $C_\mu = 0.09$ and $C_\theta = 0.1 = C_\mu/0.9$. The ratio between the two eddy diffusivities is defined as the turbulent Prandtl number, which is $Pr_t = \nu_t/\alpha_t$.

The time scale of dynamical turbulence is defined in the same way as in Chapter 3, namely

$$\tau_{lu} = f_{1\mu}\, A_{1\mu} + f_{2\mu}\, A_{2\mu}\,, \tag{4.10}$$

where the functions $f_{1\mu}$, $A_{1\mu}$, $f_{2\mu}$ and $A_{2\mu}$ are appropriate for modeling the near wall behavior. We set

$$f_{1\mu} = (1 - \exp(-0.0714\, R_\delta))^2 \tag{4.11}$$

$$A_{1\mu} = \tau_u \tag{4.12}$$

$$f_{2\mu} = f_{1\mu}\, \exp(-2.5 \times 10^{-5}\, R_t^2) \tag{4.13}$$

$$A_{2\mu} = \tau_u \, \frac{5}{R_t^{3/4}} \tag{4.14}$$

where $R_t = k^2/\nu\epsilon$ and $R_\delta = \delta(\epsilon\nu)^{1/4}/\nu$ with δ the distance from the wall. The time scale of thermal turbulence shows slight changes in the values of some constants with respect to the one defined in Chapter 3

$$\tau_{l\theta} = f_{1\theta}\, B_{1\theta} + f_{2\theta}\, B_{2\theta}\,, \tag{4.15}$$

with $f_{1\theta}$, $B_{1\theta}$, $f_{2\theta}$ and $B_{2\theta}$ appropriate functions. We set

$$f_{1\theta} = (1 - \exp(-0.0714\,\frac{R_\delta}{\sqrt{Pr}}))\,(1 - \exp(-0.0714\,R_\delta)) \qquad (4.16)$$

$$B_{1\theta} = \tau_u\,C_\infty \qquad (4.17)$$

$$f_{2\theta}\,B_{2\theta} = \tau_u\left(f_{2a\theta}\,\frac{2\,R}{R + C_\gamma} + f_{2b\theta}\sqrt{\frac{2\,R}{Pr}}\,\frac{1.3}{\sqrt{Pr}R_t^{3/4}}\right), \qquad (4.18)$$

where $C_\gamma = 0.3$, $C_\infty = 0.75$, $f_{2a\theta} = f_{1\theta}\,\exp(-4{\cdot}10^{-6}\,R_t^2)$, $f_{2b\theta} = f_{1\theta}\,\exp(-2.5{\cdot}10^{-5}\,R_\delta{}^2)$.

To obtain a k-ω formulation of the turbulence model introduced in Chapter 3 we define the variables ω and ω_θ, as the specific dissipation rate of k and k_θ. These new variables are defined as:

$$\omega = \frac{\epsilon}{C_\mu k}, \qquad \omega_\theta = \frac{\epsilon_\theta}{C_\mu k_\theta}. \qquad (4.19)$$

By algebraically substituting the definitions (4.19) in the system of equations (3.8-3.15-3.24-3.26) we obtain

$$\frac{\partial k}{\partial t} + \mathbf{u}\cdot\nabla k = \nabla\cdot\left[\left(\nu + \frac{\nu_t}{\sigma_k}\right)\nabla k\right] + P_k - C_\mu\,k\,\omega, \qquad (4.20)$$

$$\frac{\partial \omega}{\partial t} + \mathbf{u}\cdot\nabla\omega = \nabla\cdot\left[\left(\nu + \frac{\nu_t}{\sigma_\epsilon}\right)\nabla\omega\right] + \frac{2}{k}\left(\nu + \frac{\nu_t}{\sigma_\epsilon}\right)\nabla k\cdot\nabla\omega +$$
$$+ (c_{\epsilon 1} - 1)\frac{\omega}{k}P_k - C_\mu\,(c_{\epsilon 2}f_\epsilon - 1)\,\omega^2, \qquad (4.21)$$

$$\frac{\partial \kappa_\theta}{\partial t} + \mathbf{u}\cdot\nabla\kappa_\theta = \nabla\cdot\left[\left(\alpha + \frac{\alpha_t}{\sigma_\theta}\right)\nabla\kappa_\theta\right] + P_\theta - C_\mu\,\kappa_\theta\,\omega_\theta, \qquad (4.22)$$

$$\frac{\partial \omega_\theta}{\partial t} + \mathbf{u}\cdot\nabla\omega_\theta = \nabla\cdot\left[\left(\alpha + \frac{\alpha_t}{\sigma_\theta}\right)\nabla\omega_\theta\right] + \frac{2}{\kappa_\theta}\left(\alpha + \frac{\alpha_t}{\sigma_\theta}\right)\nabla\kappa_\theta\cdot\nabla\omega_\theta +$$
$$+ (c_{p1} - 1)\frac{\omega_\theta}{\kappa_\theta}P_\theta + c_{p2}\frac{\omega_\theta}{k}P_k - (c_{d1} - 1)\,C_\mu\omega_\theta^2 - c_{d2}C_\mu\omega\omega_\theta. \qquad (4.23)$$

For the k-ω turbulence model the coefficients $c_{\epsilon 1}$, $c_{\epsilon 2}$ and the function f_ϵ are the same used in the k-ϵ model. For the k_θ-ω_θ thermal turbulence model the coefficient c_{p2} and the function c_{d2} are the same used in the k_θ-ϵ_θ model, while c_{p1} and c_{d1} have been set to 1.025 and 1.1. In a k-ω formulation the time scales of turbulence can be simply computed as $\tau_u = (C_\mu\,\omega)^{-1}$ and $\tau_\theta = (C_\mu\,\omega_\theta)^{-1}$, so the time ratio becomes $R = \omega/\omega_\theta$. Using this model we can avoid the variables coupling in the boundary conditions which occurs in k-ϵ formulation, as we prove now.

We can study the near wall behavior of the turbulent variables by using Taylor series expansion near the wall. By applying this expansion to k, ϵ, k_θ and ϵ_θ in the case of zero temperature fluctuations on the wall we obtain the following expressions

$$k_w = \frac{1}{2}\, a\, \delta^2, \qquad \epsilon_w = \nu \frac{k_w}{\delta^2}, \qquad k_{\theta w} = \frac{1}{2}\, a_\theta\, \delta^2, \qquad \epsilon_{\theta w} = \alpha \frac{k_{\theta w}}{\delta^2}, \quad (4.24)$$

where δ is the distance from the wall and a and a_θ are constant values that depend on the velocity and temperature fluctuations. In this case we cannot impose exact Dirichlet boundary conditions on ϵ and ϵ_θ because the values k_w and $k_{\theta w}$ are not known *a priori*. A Neumann boundary condition is imposed for k and k_θ while a Dirichlet boundary condition depending on the value of k and k_θ as computed in the previous iteration is employed for ϵ and ϵ_θ, see Chapter 3. This algorithm can lead to convergence issues if oscillations of the solutions on the wall do generate.

The near wall Taylor series expansion of ω and ω_θ is

$$\omega_w = \frac{2\nu}{C_\mu \delta^2}, \qquad \omega_{\theta w} = \frac{2\alpha}{C_\mu \delta^2}. \qquad (4.25)$$

As can be seen in (4.25) it is now possible to impose exact Dirichlet boundary conditions for ω and ω_θ near the wall because the terms on the right hand side are known values. In this case we have no coupling between the variables on the wall boundary condition and the solution of this system is more robust and stable. As it can be seen, in both formulations the time scale ratio R on the wall is equal to the molecular Prandtl number of the fluid while the turbulent kinetic energy k and the mean square temperature fluctuation k_θ tend to zero on the wall.

4.2   Numerical simulations

In the next Sections we report the numerical results of fully developed turbulent flow simulations in different geometries. The physical properties of the fluid are reported in Table 4.1. These properties are representative of Lead-Bismuth-Eutectic and other heavy liquid metal fluids with a molecular Prandtl number of $Pr = 0.025$. The two geometries studied here are two simple two dimensional geometries used commonly for model validation purposes. The results are compared with DNS data for the plane channel and with the experimental correlation by Kirillov for the pipe flow heated with constant heat flux.

4.2.1 Plane channel

In this section we report numerical results obtained for a fully developed turbulent flows in plane channel geometry. This geometry is chosen because it is

Physical properties of LBE fluid

Viscosity	μ	0.00184 Pa s
Density	ρ	10340 Kg/m^3
Thermal conductivity	λ	10.72 W/(m K)
Heat specific capacity	C_p	145.75 J/(Kg K)

Table 4.1: Physical parameters used in the CFD simulations.
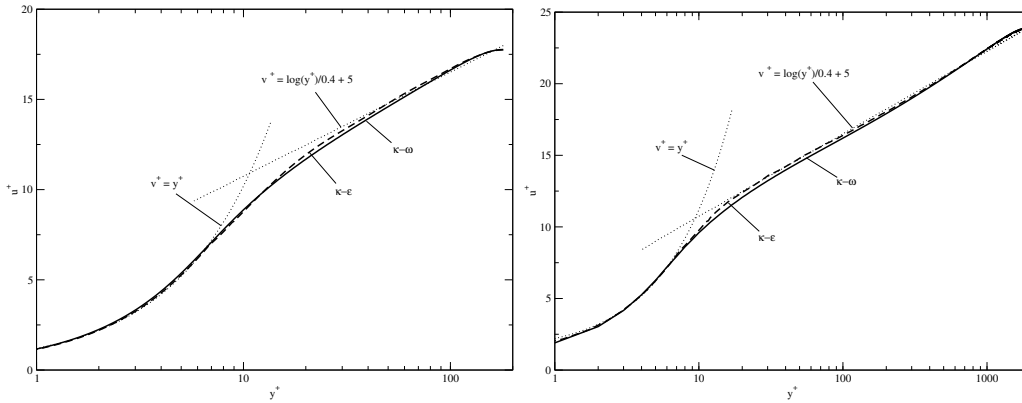
Figure 4.1: Plane case. Mean velocity distribution for $Re \approx 5500$ (left) and $Re \approx 86200$ (right) as computed with k-ϵ and k-ω model.
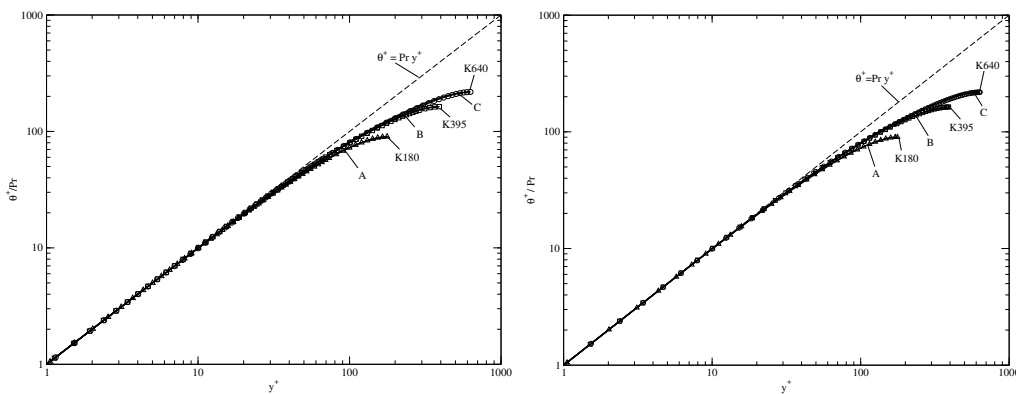
Figure 4.2: Plane case. Comparison of the temperature distribution θ^+/Pr obtained with k-ϵ (left) and k-ω model (right), with DNS data. DNS data are reported for $Re_\tau = 180$ (K180), $Re_\tau = 395$ (K395) and $Re_\tau = 640$ (K640).
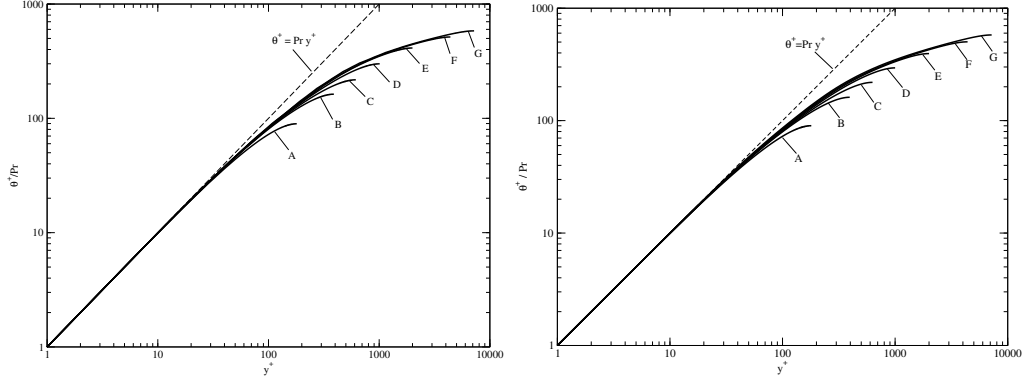
Figure 4.3: Plane case. Temperature distribution θ^+/Pr for different velocities $Re \approx 5500$ (A), 13500 (B), 23250 (C), 40100 (D), 86200 (E), 203900 (F) and 344800 (G). On the left the results were obtained with the k-ϵ-k_θ-ϵ_θ model while on the right the results were obtained with k-ω-k_θ-ω_θ model

very simple and many DNS data are available for this flow. We consider two plates located at a distance $L = 0.0605$ m and with infinite dimensions in the other directions. On the wall a uniform heat flux of 360000 W/m^2 is applied. We can solve this problem in two dimensions with periodic boundary conditions on the inlet and outlet of the channel, see Section 3.2.1 for more details. The results of the k-ω-k_θ-ω_θ model are compared with the ones obtained with the k-ϵ-k_θ-ϵ_θ model and with DNS data from Kawamura database, see [56] and references therein. The fields in DNS data are usually reported in non dimensional form. The dimensionless temperature is defined as $\theta^+ = \theta/T_\tau$, where T_τ is the friction temperature calculated as $T_\tau = q/(u_\tau \rho C_p)$ and θ is the difference between the temperature and the linear behavior characteristic of the fully developed flow, $\theta = T - T_{w0} - x \, \Delta T_b$. T_{w0} is the reference inlet wall temperature which is assumed to be zero. By using the temperature θ instead of T we can impose periodic boundary conditions on θ when the flow is fully developed.

Seven simulations have been performed with Reynolds number of $Re \approx$ 5500 (A), 13500 (B), 23250 (C), 40100 (D), 86200 (E), 203900 (F) and 344800 (G). They correspond to the friction Reynolds number of 180 (A), 395 (B), 640(C) , 1010 (D), 2000 (E), 4400 (F) and 7200 (G). In Figure 4.1 the non dimensional mean velocity profiles obtained with the k-ω and with the k-ϵ model $u^+ = \mathbf{u}/u_\tau$ are reported as a function of the non dimensional wall distance $y^+ = y u_\tau/\nu$ for two test cases, namely the case $Re \approx 5500$ (A) and $Re \approx 86200$ (E). The friction velocity u_τ is defined as $u_\tau = \sqrt{\tau_w/\rho}$ with τ_w the wall shear stress. The k-ω model reproduces well the linear and logarithmic behaviors of the velocity, namely $u^+ = y^+$ and $u^+ = \log(y^+)/0.4 + 5$.
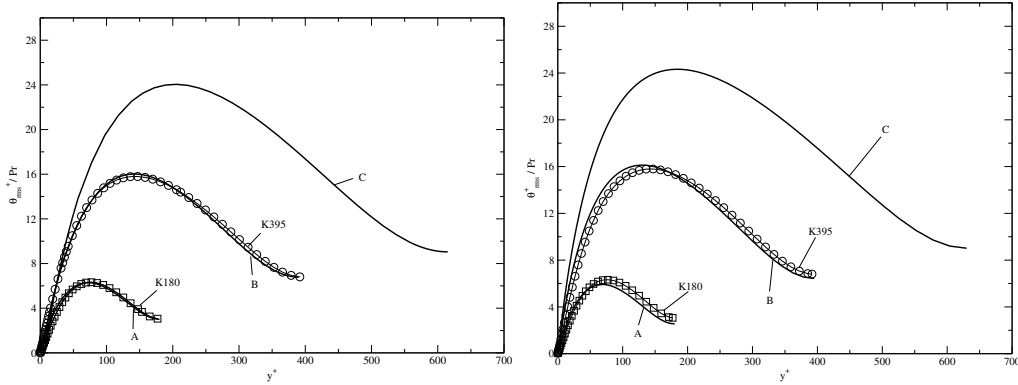
Figure 4.4: Plane case. The root-mean-square temperature fluctuations θ_{rms}^+ for different $Re \approx 5500$ (A), 13500 (B), 23250 (C) and comparison with DNS corresponding data (K180) and (K395). On the left results with the k-ϵ model, on the right k-ω model.
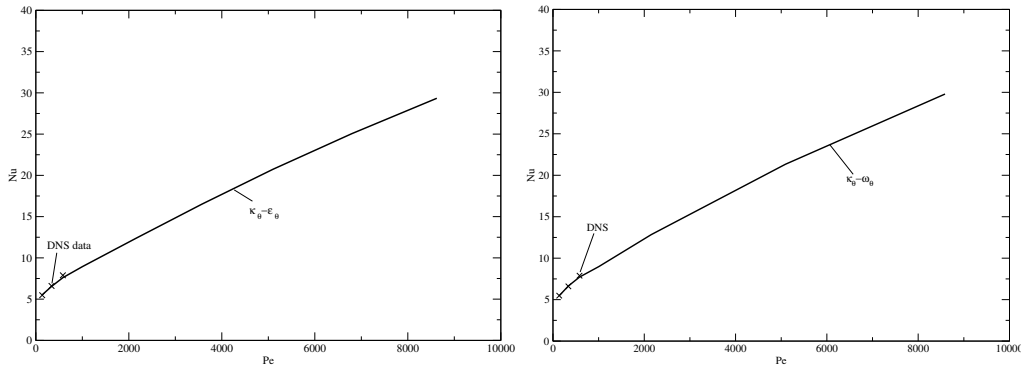
Figure 4.5: Plane case. Nusselt number (thick line) and DNS values (cross) for different Peclet numbers. On the left results with the k-ϵ model, on the right k-ω model.

Comparing the results obtained with k-ω model with the ones obtained with k-ϵ we can observe only a slight difference between them in the buffer region. In Figure 4.2 the non dimensional temperature θ^+ is reported as a function of y^+ and divided by the Prandtl number. The temperature profiles for the cases $Re_\tau = 180$, $Re_\tau = 395$ and $Re_\tau = 640$, are compared with DNS data from Kawamura [56]. The data obtained with the four parameter models agree very well with the DNS ones. The non dimensional temperature profiles of all the simulated cases are reported in Figure 4.3. The results obtained with the k-ω-k_θ-ω_θ, Figure 4.3 (right), show no relevant differences with the k-ϵ-k_θ-ϵ_θ ones, Figure 4.3 (left).

The root-mean-square temperature fluctuation $\theta_{rms} = \sqrt{2k_\theta}$ is an important variable needed to evaluate the time ratio R and the turbulent heat diffusion coefficient α_t. In Figure 4.4 the non dimensional $\theta_{rms}^+ = \theta_{rms}/T_\tau$ is reported for the k-ϵ (left) and k-ω (right) formulation of the model and it is compared with DNS data for $Re_\tau = 180$ and 395. Very similar results to DNS data are obtained with both the turbulence models, a slight difference in the prediction of the position of the peak can be seen between the two models but the overall result is very good. The Nusselt number is the most important non dimensional number in engineering heat transfer calculations and it quantifies the heat transfer effectiveness. It is defined as $Nu = qD_h/(\lambda\Delta T)$ where D_h is the hydraulic diameter of the geometry and ΔT is the difference between the average wall temperature and the bulk temperature, defined as the average temperature on the section of the flow with respect to velocity. In Figure 4.5 the Nusselt number calculated with the k-ϵ (left) and k-ω (right) four parameter turbulence models is reported as a function of Peclet number $Pe = Re\,Pr$. DNS data are reported as well for comparison. The first two points matches very well while the third (corresponding to $Re \approx 23250$ (C)) seems to slightly underestimate the DNS result.

4.2.2   Cylindrical channel

As a second test we simulate a fully developed turbulent flow in a cylindrical pipe with diameter $D = 0.0605$. The physical properties of the simulated flow are reported in Table 4.1. For this geometrical case we compare our results with DNS data, which are available only for the case $Re_\tau = 170$, and
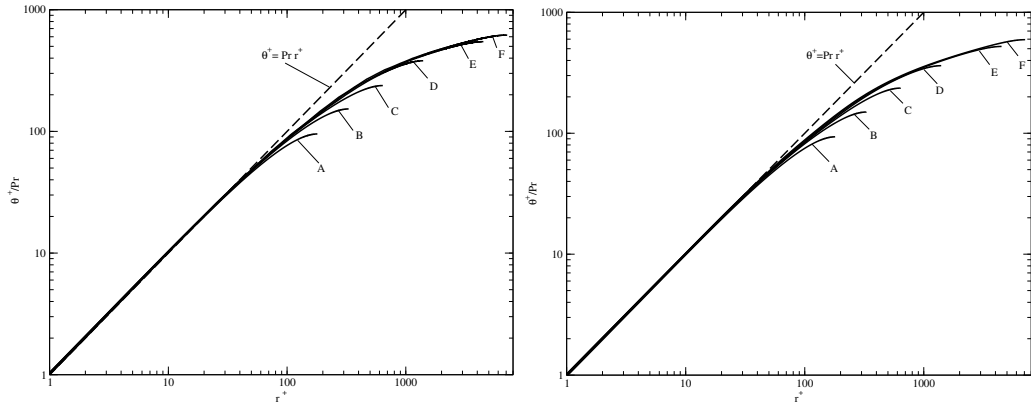
Figure 4.6: Cylinder case. Temperature distribution θ^+/Pr for $Re \approx 5500$ (A), 11150 (B), 23750 (C), 57500 (D), 213000 (E) and 345000 (F). Results obtained with k-ϵ-k_θ-ϵ_θ (left) and k-ω-k_θ-ω_θ (right) model.
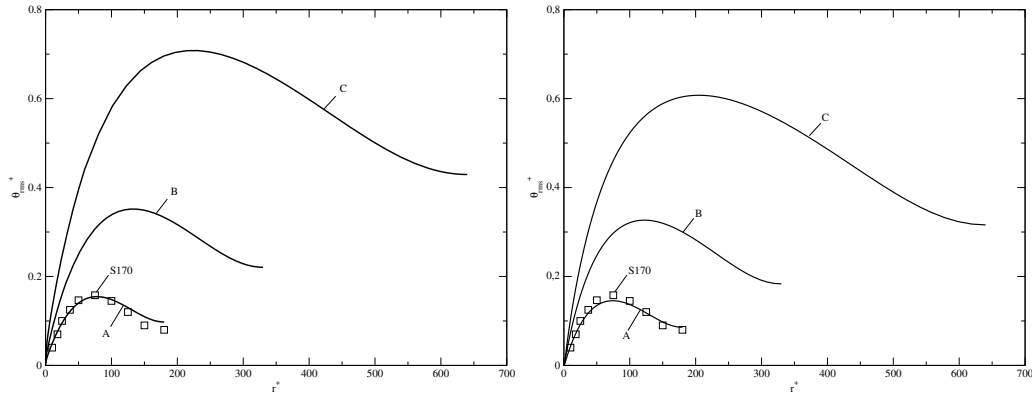
Figure 4.7: Cylinder case. Non-dimensional root-mean-square temperature fluctuation θ_{rms}^+ for $Re \approx 5500$ (A), 11150 (B) and 23750 (C) and comparison with DNS data for $Re_\tau = 170$ (S170). On the left the results were obtained with the k-ϵ model while on the right they were calculated with the k-ω model.
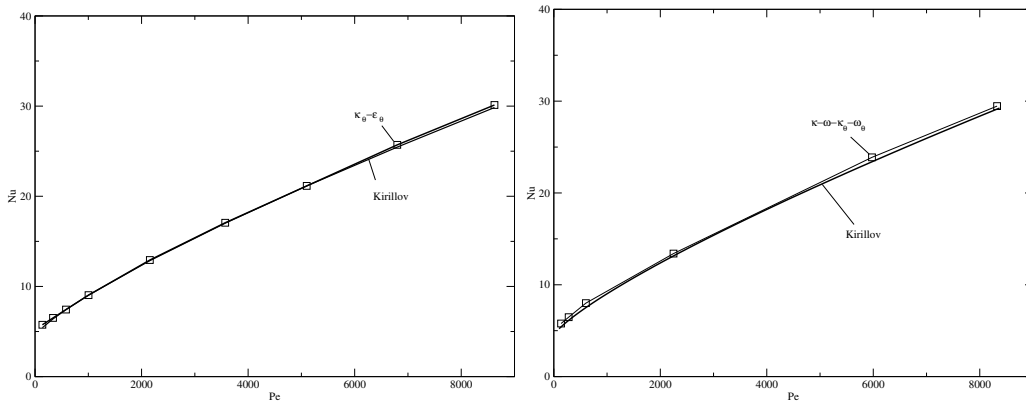
Figure 4.8: Cylinder case. Nusselt number (square) and Kirillov correlation for cylindrical geometry (thick line). On the left results obtained with the k-ϵ model while on the right calculated with the k-ω model.

with Kirillov heat transfer correlation

$$Nu = 4.5 + 0.018 \, Pe^{0.8} \,. \tag{4.26}$$

This is the reference correlation for this class of fluids in cylindrical geometry [62, 100] and it is claimed to be valid for $10^4 < Re < 5 \cdot 10^6$.

We performed six simulations over a wide range of Reynolds numbers, namely $Re \approx 5500$ (A), 11150 (B), 23750 (C), 57500 (D), 213000 (E) and 345000 (F) corresponding to $Re_\tau = 180$ (A), 395 (B), 640 (C), 1400 (D), 4500

(E) and 7150 (F). In Figure 4.6 the non dimensional temperature divided by the Prandtl number θ^+/Pr is reported for all the simulated cases, as a function of the non dimensional wall distance $r^+ = ru_\tau/\nu$. Comparing Figure 4.6 (right) with Figure 4.6 (left) we can see that the k-ω results are very close to the k-ϵ ones. The linear behavior of the non dimensional temperature field is well reproduced in all the simulated cases.

The non-dimensional root-mean-square temperature fluctuation θ^+_{rms} for $Re \approx 5500$ (A), 11150 (B) and 23750 (C) is compared with DNS data for $Re_\tau = 170$ (S170) in Figure 4.7. A good agreement with the DNS data is obtained with both models. Comparing the k-ϵ results with the k-ω ones, for the cases $Re_\tau = 395$ and $Re_\tau = 640$ one can see some differences between the models but there are no reference results to compare with. The Nusselt number for these simulations is reported in Figure 4.8. The square dots are the results obtained with the four parameter turbulence model, while the thick line is Kirillov correlation. On the left the results are reported for the k-ϵ model while on the right for the k-ω model. The matching between the numerical results and the correlation is almost perfect at any velocity for the k-ϵ model while little discrepancies can be seen for the k-ω model at very high velocities.

Part II

Adjoint Optimal Control

Chapter 5

Introduction to adjoint optimal control theory

Optimization of industrial devices and control of complex systems in engineering is a very common and old research field. Starting from the simplest wheel shape problem to the control of power plants or flap position for lift control in airplanes, optimization and control are pervasive subjects in engineering. Linear feedback methods are commonly employed to operate complex systems like turbine valves-heat exchanger in power stations and are used in electronic applications in the railway or automotive industries [48, 95]. Multi-objective optimization and sensitivities-based optimal control are other interesting research fields that find applications ranging from engineering design to financial predictions of market shares. The literature on these subjects is wide, the interested reader is referred to [28, 67, 90, 91] and to references therein for a first approach to these interesting subjects.

In this work we focus on adjoint based methods, which have been proven to be a good approach for the optimal control of complex problems in which Computational Fluid Dynamics simulations can be performed on the system of interest [45, 46, 47, 77, 113]. Adjoint optimal control theory has gained popularity in the last several years because of the growth of computational power that allows this type of problems to be applied in many industrial and research fields. The mathematical background of this theory is strong, since it has been studied from a mathematical point of view from several years, but applications of this theory to very complex problems are still lacking. In optimal control theory different types of controls, such as distributed, boundary and shape controls are considered, see for a review [47]. In the first one, source terms are used as control parameters in the whole domain to attain a specific objective. Due to practical issues it can be difficult to set control devices inside the system and this type of control cannot often be

used in real-life applications. In such cases the boundary control may be a possible approach. In this setting the control is a boundary condition on the domain, such as a temperature or heat flux on a wall or a fluid injection or suction. However, boundary control is more challenging than the distributed one, from the theoretical point of view and in the development of feasible computational algorithms. The last one we mention is the shape control in which the geometrical properties of the system can be changed in order to obtain the desired result. A common application of this type of control is airplane and car wings design [44].

In this Chapter we describe the theory and the methods to obtain and solve the optimality system in a general adjoint optimal control framework. In the following two Chapters we describe the application of this theory to two problems relevant for CFD studies of liquid metal systems. The first is a temperature boundary optimal control problem in which a desired temperature is set in a region of the domain and the controlling parameter is the temperature on some boundaries of the domain. The second is a velocity-turbulence distributed optimal control problem in which the objective is set as a velocity matching profile or a turbulence increase or decrease and the control is realized through a distributed force acting on the fluid. Together with the mathematical derivation and study of the optimality systems, numerical results are reported to prove the feasibility of this approach to industrially relevant problems.

5.1   Optimal control setting

To set up an optimal control problem we first need to specify the objective of the optimization and the way in which we aim at controlling the system. The objective functional has to be defined mathematically using the state variables of the system and appropriate functions or integration domains to improve the objective definition. The control can be a distributed force, a boundary condition or a geometrical parameter that determines the domain shape. The purpose of the optimization is to find a minimum of the objective functional, subjected to the state system constraint, by changing the control. This is a typical constrained optimization problem. The Lagrange multiplier method allows to obtain an unconstrained optimization problem by introducing a set of new Lagrange multiplier functions. These parameters multiply the constraint equations and the full Lagrangian is written as the sum of these terms and the objective functional. Finally to find a local minimum one can use the first-order necessary conditions of null variations of the Lagrangian with respect to all the variables involved. This is a very

brief summary of how an adjoint optimal control problem can be solved, we describe now in more detail how this procedure can be applied to a simple reference problem.

As an example to which apply the method, consider a system such as a metal sheet or bar subjected to heat treating that we would like to heat in a specific way by applying heat sources on it. In order to write this objective in a mathematical way we could compute the expression

$$\mathcal{J}(T) = \int_\Omega (T - T_d)^2 d\Omega \,, \tag{5.1}$$

where Ω is the domain of the sheet or bar and T_d is the desired temperature that we want to reach on the metal in order to properly treat it. The square is needed in order to avoid error cancellation during the integration over the whole domain Ω. The temperatures T and T_d could be functions of space and time but in this discussion we consider only steady state solutions that can vary in space, otherwise the integral in (5.1) should be performed also in the treatment time and the derivation of the optimality system would become more complex. As already said, the control is performed using heat sources that can be spatially controlled, so the equation modeling this problem is the heat conduction equation for a material with λ as thermal conductivity and Q the heat source

$$\nabla \cdot (\lambda \nabla T) + Q = 0 \qquad \forall x \in \Omega \,, \tag{5.2}$$

that has to be completed with appropriate boundary conditions, such as

$$\lambda \nabla T \cdot \mathbf{n} = q_w \qquad \text{on} \quad \Gamma_n \tag{5.3}$$

$$T = T_b \qquad \text{on} \quad \Gamma_d \,. \tag{5.4}$$

If this boundary value problem is written in a weak form by multiplying (5.2) with a test function ϕ defined in an appropriate space

$$\phi \in V_{\Gamma_d} = \{\phi \in H^1(\Omega) : \phi = 0 \quad \text{on} \quad \Gamma_d\} \,, \tag{5.5}$$

integrating over the whole domain Ω and performing the integration by parts on the Laplacian term, the boundary value problem is expressed in a complete formulation as

$$-\int_\Omega \lambda \nabla T \cdot \nabla \phi \, d\Omega + \int_{\Gamma_n} q_w \, \phi \, d\Omega + \int_\Omega Q \, \phi \, d\Omega = 0 \qquad \forall \phi \in V_{\Gamma_d} \,. \tag{5.6}$$

This equation is the state system for the problem of interest written in weak form.

The boundary value problem expressed by (5.2-5.4) or (5.6) can be seen as the constraint to the state variables T and Q in the optimal control setting. In general one still has to limit the control Q in some way because otherwise the problem could become unbounded and Q could assume infinite values in some points of the domain. From a mathematical point of view this corresponds to Q being in a distribution space of functions not square integrable over Ω. To solve this problem one can limit directly the value of the control with an additional constraint in the form

$$Q < Q_{max}\,,$$

or the definition of the L_2 norm of a function can be used in order to keep this norm bounded for Q and so not allowing Q to be a distribution. Therefore in the objective functional (5.1) we add a term containing the L_2 norm of Q penalized with a parameter β

$$\mathcal{J}(T,Q) = \frac{1}{2}\int_{\Omega}(T-T_d)^2\,d\Omega + \frac{\beta}{2}\int_{\Omega}Q^2\,d\Omega\,. \qquad (5.7)$$

By doing so the cost of using a control Q is kept in the optimal control setting and this cost can be tuned by changing the parameter β. If a large value of β is chosen than the optimization algorithm cannot improve the reference state too much because the cost of increasing the control Q is very high and a local minimum of this functional is likely to be found near the reference state. On the other hand, if a small value of β is used the optimization algorithm can use high values of the control Q and therefore the local minimum can be found far from the reference state.

The problem just described is a typical example of a distributed optimal control where the control is performed through a source in the state equation. Another possibility we mentioned is to use a boundary control. In this case a boundary condition is the control of the system, like a heat flux or a temperature on a surface or a fluid velocity on an inlet of a channel. The main difference in this case for the setting up of the optimal control problem is that one boundary condition is unknown, so the space of the test function has to be chosen properly. The objective functional shows some differences because the control is defined on a surface, so the regularization integral is performed on the controlled surface. Quite often in this case the control is not defined in a simple square integrable function space but usually additional requirements on the regularity of the control are considered. If we wish to have the control in H^1 we need to bound the whole H^1 norm, so the derivative of the control is included in the objective functional with another penalization parameter. Considering the problem (5.2-5.4) described above

we could think to obtain the desired temperature on the sheet by changing the boundary temperature T_b. In this case the state equation becomes

$$\nabla \cdot (\lambda \nabla T) = 0 \qquad \forall x \in \Omega \,, \tag{5.8}$$

with boundary conditions

$$\lambda \nabla T \cdot \mathbf{n} = q_w \qquad \text{on} \quad \Gamma_n \tag{5.9}$$

$$T = g \qquad \text{on} \quad \Gamma_d \,. \tag{5.10}$$

The objective functional for this problem is

$$\mathcal{J}(T, g) = \frac{1}{2} \int_{\Omega} (T - T_d)^2 \, d\Omega + \frac{\beta}{2} \int_{\Gamma_d} g^2 \, d\Gamma + \frac{\gamma}{2} \int_{\Gamma_d} \nabla g \cdot \nabla g \, d\Gamma \,, \tag{5.11}$$

where the parameter γ is to be set different from zero if a smooth solution on the controlled surface Γ_d is looked for. It should be clear that in general a boundary control is weaker than a distributed one because the boundary condition can affect only a small portion of the domain and if the objective is set in a region far from this boundary it could be impossible to obtain good improvements on the reference case. However in many real industrial applications, boundary control is the only one possibility because it might be impossible to operate in the domain interior for physical or practical reasons. Therefore the study of both distributed and boundary control can give useful insights and have practical relevance in different cases.

The shape control is the third possibility that is considered in the field of adjoint optimal control. In this setting a geometrical parameter or a function defining the shape of a part of the domain can be changed in order to obtain the desired objective. Typical examples of these problems are the shape changing of airplane wings or compressor and turbine blades. In this thesis we do not consider this type of control but focus on distributed and boundary control.

In the example described above the objective functional has been defined to assess a simple temperature matching profile over the whole domain but it is possible to use a weight function to set the desired objective in a specific region of the domain. There are also many other possibilities to define different functionals based on the state variables. To name a few we recall velocity matching profile, mass flow rate changing, minimum drag or maximum lift, increase or decrease of turbulent mixing, minimum heat flux magnitude or in some directions, and others. Any quantity of interest to engineering design that can be expressed through the state variables or their gradient can be used in the functional. This possibility opens wide opportunities to the use of

this approach in several industrial fields where a well defined mathematical model of the problem exists and it can be solved numerically with not too much computational expenses. We remark that this method is used to find a local minimum and that the solution of a problem with a complex objective functional and/or state system could be very hard. In principle we do not have information on the properties of the functional and many minimums can exist. This method, in contrast to other global optimization techniques, can be used only to get improvements on a reference state and not to find the global optimal solution to the problem, unless this is the only minimum of the functional. However, in many practical situations an improvement on a reference state is what is needed because too big changes on the design cannot be performed for physical or practical reasons. In these cases this method could prove useful for the optimal design of engineering devices.

5.2   Optimality system

The optimality system is a system of equations that allows to find the optimal state and control for a given optimal control problem, i.e. an objective functional and a type of control. This system of equations consists of the first order optimality conditions and can be found with the use of the Lagrange multiplier method. To describe the Lagrange multiplier method we apply it to the distributed optimal control problem set up in the previous section in order to obtain the optimality system composed of the first order necessary conditions. We write the full Lagrangian of the problem that is composed of the objective functional and of the constraint multiplied by the Lagrange multiplier ϕ

$$\mathcal{L}(T, Q, \phi) = \frac{1}{2} \int_{\Omega} (T - T_d)^2 \, d\Omega + \frac{\beta}{2} \int_{\Omega} Q^2 \, d\Omega + \tag{5.12}$$
$$\int_{\Omega} [\nabla \cdot (\lambda \nabla T) + Q] \, \phi \, d\Omega \,.$$

To obtain the first-order necessary conditions we derive $\mathcal{L}(T, Q, \phi)$ with respect to the three variables T, Q, and ϕ and then we set to zero these three components of the gradient in order to find a local minimum,

$$\frac{\delta \mathcal{L}}{\delta T} = 0$$
$$\frac{\delta \mathcal{L}}{\delta Q} = 0 \tag{5.13}$$
$$\frac{\delta \mathcal{L}}{\delta \phi} = 0 \,.$$

The variation of the Lagrangian with respect to the variation of one of its variables is called Fréchet derivative and can be defined as

$$\frac{\delta \mathcal{L}}{\delta T} = \lim_{\epsilon \to 0} \frac{\mathcal{L}(T + \epsilon \delta T, Q, \phi) - \mathcal{L}(T, Q, \phi)}{\epsilon} \,, \qquad (5.14)$$

where the variation δT of the temperature is arbitrary. This derivative is different from the ordinary derivative of a function because the value of the derivative depends on the variation δT [47]. By computing the first of the three first-order necessary conditions (5.13) we get

$$\frac{\delta \mathcal{L}}{\delta T} = \int_\Omega (T - T_d) \, \delta T + \int_\Omega \nabla \cdot (\lambda \nabla \delta T) \, \phi \, d\Omega = 0 \qquad \forall \delta T \in H^1(\Omega), \quad (5.15)$$

when the derivative is taken with respect to Q we get

$$\frac{\delta \mathcal{L}}{\delta Q} = \beta \int_\Omega Q \, \delta Q + \int_\Omega \delta Q \, \phi \, d\Omega = 0 \qquad \forall \delta Q \in H^1(\Omega), \qquad (5.16)$$

and the last variation in ϕ is

$$\frac{\delta \mathcal{L}}{\delta \phi} = \int_\Omega [\nabla \cdot (\lambda \nabla T) + Q] \, \delta \phi \, d\Omega = 0 \qquad \forall \delta \phi \in H^1(\Omega). \qquad (5.17)$$

The equations (5.15-5.17) form the optimality system that can be used to find (T, Q, ϕ) for which the objective functional (5.7) is stationary and subject to the constraint (5.2). We can analyze this system to get some useful information. For example (5.17) is a weak form of the state equation (5.2) and if we assume $\delta \phi \in V_{\Gamma_d}(\Omega)$ and perform an integration by parts substituting the value of $\lambda \nabla T = q_w$ on the surface Γ_n in the surface integral we recover (5.6). The (5.16) is an algebraic equation in the control Q and thus, since δQ is arbitrary, it can be easily solved by assuming

$$Q = -\frac{\phi}{\beta} \,. \qquad (5.18)$$

The first variation is the adjoint equation and it has to be solved for ϕ. Performing an integration by parts we get

$$\int_\Omega (T - T_d) \, \delta T - \int_\Omega \lambda \nabla \phi \cdot \nabla \delta T \, d\Omega + \int_\Gamma \lambda \nabla \delta T \cdot \mathbf{n} \, \phi \, d\Gamma = 0 \qquad (5.19)$$
$$\forall \delta T \in H^1(\Omega) \,,$$

that is the adjoint equation for the Lagrange multiplier ϕ. Since δT is the variation of the temperature T we can safely assume that this variation is

zero where the temperature is fixed with a Dirichlet boundary condition, so from (5.4) $\delta T \in V_{\Gamma_d}(\Omega) \subset H^1(\Omega)$. Moreover, by taking the variation of (5.3) we get $\nabla \delta T \cdot \mathbf{n} = 0$ on Γ_n since q_w is a constant. To obtain the dual or natural boundary conditions of the adjoint equations together with the strong form of it we have to perform another integration by parts on the volume integral of the gradient product,

$$\int_\Omega (T - T_d)\,\delta T + \int_\Omega \nabla \cdot (\lambda \nabla \phi)\,\delta T\,d\Omega - \int_{\Gamma_n} \lambda \nabla \phi \cdot \mathbf{n}\,\delta T\,d\Gamma + \qquad (5.20)$$

$$\int_{\Gamma_d} \lambda \nabla \delta T \cdot \mathbf{n}\,\phi\,d\Gamma = 0 \qquad \forall \delta T \in V_{\Gamma_d}(\Omega)\,,$$

where the considerations on δT have been taken into account. The dual boundary conditions are obtained by setting to zero the surface integrals that appear in (5.20). On Γ_n the normal gradient of ϕ is zero, on Γ_d the value of ϕ is zero. The adjoint boundary value problem in strong form can be written as

$$\nabla \cdot (\lambda \nabla \phi) + (T - T_d) = 0 \qquad \forall x \in \Omega\,, \qquad (5.21)$$

$$\lambda \nabla \phi \cdot \mathbf{n} = 0 \qquad \text{on} \quad \Gamma_n \qquad (5.22)$$

$$\phi = 0 \qquad \text{on} \quad \Gamma_d\,, \qquad (5.23)$$

since the variations δT are arbitrary. If we compare the problem (5.21-5.23) with (5.2-5.4) we understand that the adjoint variable ϕ satisfies an equation of heat transfer with the same thermal conductivity of the state temperature and a source equal to the difference between the temperature and the desired temperature. Moreover the boundary conditions of this equation are the same as in the state problem but they are homogenous. This is a typical feature of adjoint problems, in the regions where a Dirichlet b.c. is imposed in the state system the adjoint system presents a homogenous Dirichlet b.c., while in the regions where a Neumann b.c. is used, the adjoint system has an homogenous Neumann b.c..

5.3   Solution of the optimality system

Once the optimality system has been obtained it has to be solved in order to find the optimal solution. In principle a fully coupled solution of this system, a one-shot approach, is the first and best solution that comes to mind. For the optimality system obtained in the previous section, with a very simple and linear equation if λ does not depend on T, and an adjoint equation with the same operator, this approach could be the best. Moreover in this case

---

Algorithm 1 Steepest descent algorithm to find the optimal solution

---

1: **function** FIND OPTIMAL
2:     set a state T^0 satisfying (5.17) with $Q^0 = 0$ ▷ *Setup of the reference state*
3:     compute the functional $\mathcal{J}^0$ in (5.11)
4:     set $r^0 = r_0$
5:     **for** $i = 1 \to i_{max}$ **do**
6:         Solve equation (5.20) to obtain the adjoint state ϕ^i
7:         **for** $j = 1 \to j_{max}$ **do**
8:             compute the control $Q^i = Q^{i-1} - r^{i,j}\,\phi^i/\beta$
9:             solve (5.17) for the state $T^{i,j}$ with the new control Q^i.
10:           compute the new functional $\mathcal{J}^{i,j+1}$ in (5.11)
11:           **if** $\|\mathcal{J}^{i,j} - \mathcal{J}^i\|/\mathcal{J}^i < \tau$ **then**
12:              convergence reached   ▷ *end of the algorithm*
13:           **else if** $\mathcal{J}^{i,j} > \mathcal{J}^i$ **then**
14:              set $r^{i,j+1} = 2/3\,r^{i,j}$, $j = j+1$ and go to 8   ▷ *loop on j again*
15:           **else if** $\mathcal{J}^{i,j} < \mathcal{J}^i$ **then**
16:              set $r^{i,j+1} = 3/2\,r^{i,j}$, $i = i+1$ and go to 6   ▷ *loop on i again*
17:           **end if**
18:         **end for**
19:     **end for**
20: **end function**

---

we can simply substitute the definition of the control Q from (5.16) to (5.17) and solve the optimality system for T and ϕ only. A numerical solution of this system in a two-dimensional or either three-dimensional case is not a big task and so a one-shot approach is a fast and reliable way to obtain the solution in this case. However this straightforward solution could not be the best or possible at all in some cases.

In Chapter 7 we study a distributed optimal control for a state system composed of four equations coupled in a strong non-linear way through the definition of the eddy viscosity. When the optimality system is derived it becomes clear that a system composed of at least nine non-linearly coupled equations cannot be easily solved with a one-shot approach. Moreover one has to keep in mind that the numerical solution of a system with so many equations becomes very quickly too much expensive if a mesh with a high number of nodes is used. On the contrary by solving the equations in a segregated way the number of nodes can be increased without affecting too much the computational expense of the solver. In this and other cases an algorithm for the segregated solution of the optimality system has to be developed. To simplify the description we report the steepest descent algorithm

to solve the distributed optimal control problem introduced in Section 5.2. This algorithm can be used for other adjoint optimal control problems by changing appropriately the definition of the state and adjoint equations and the control computations.

After the initialization of the reference state, Algorithm 1 is composed of two main loops. In the outer loop i the adjoint system is solved to obtain the adjoint given a state of the main variable. In the inner loop j the state system is solved using different step increases of the control by using the adjoint computed at iteration i. Once a solution is obtained the functional is computed using its definition (5.11) and it is compared with its value as computed in the reference state for iteration $i = 1$ or in the preceding i iteration for $i > 1$. If a decrease in the functional is obtained we save the control and proceed with another i iteration. If the functional does not decrease, the step size is decreased and the state system is solved again in another j iteration with this different control based on the new step size until a decrease in the functional is obtained or no more improvements can be obtained. The Algorithm continues the search until a tolerance on the difference between the two functionals $\mathcal{J}^{i,j} - \mathcal{J}^i$ is reached. The value of this tolerance is τ and it can be set to 10^{-6}, for example. The value of r^0 must be smaller than 1 and usually it can be set to $r^0 = \beta$. This algorithm requires several solutions of the state and adjoint systems in order to find the optimal control, however it does not need a great amount of memory which is limited to a standard state or adjoint simulation.

More complex algorithms that uses information from the Hessian of the functional are currently being developed [113]. These algorithms should be faster and more precise in the search of the minimum with respect to the simple Algorithm 1, but are much more complex and require a great amount of memory in addition to keep information from previous iterations of the algorithm. In this thesis we focus on different and complex applications of adjoint optimal control to obtain new optimality systems instead of developing algorithms to solve these optimality systems.

In the following Chapters we report the derivation of the optimality system for a temperature boundary optimal control problem and for the distributed control of a turbulent flow modeled by a two equation RANS closure. The method used is exactly the same as the one reported here and it is applied to a boundary control or to a quite complex system of equations. In order to understand the following Chapters one has to keep in mind the steps that have been explained in this very simple case and that are applied to more complex problems in the following Chapters.

Chapter 6

Temperature optimal control

In this Chapter we consider an optimal boundary control problem for the temperature equations with velocity computed with Navier-Stokes system [24, 55]. Heat convection is regarded as the dominant physical mechanism for heat transfer and the effects of temperature on velocity and pressure, such as buoyancy, are neglected. We consider a boundary optimal control problem for the temperature equation where the control is performed through the boundary conditions of temperature on well defined parts of the boundary and the objective functional is given in the following form

$$\mathcal{J}(T, g) = \frac{1}{2} \int_{\Omega} (T(\mathbf{x}) - T_d)^2 \, w(\mathbf{x}) \, d\Omega + \frac{\beta}{2} \int_{\Gamma_c} g^2 \, d\Gamma + \qquad (6.1)$$
$$\frac{\lambda}{2} \int_{\Gamma_c} \nabla g \cdot \nabla g \, d\Gamma \,,$$

where $T(\mathbf{x})$ is the temperature distribution, T_d is the desired temperature, $w(\mathbf{x})$ is a weight function that can be used to improve the control, Γ_c is the surface on which the control is imposed and g is the controlled temperature. This functional consists of three terms: the objective and two regularization terms. The two parameters β and λ can be used to impose a more smooth controlled temperature. In particular if both parameters are different from zero the function g is differentiable, $g \in H^1(\Gamma_c)$ while for vanishing λ we have only square integrability, $g \in L^2(\Gamma_c)$. We consider and analyze three cases. In the first case we set $\lambda = 0$ and use standard Lagrangian quadratic elements. As it is proven in next Section, g is the trace of the gradient of the adjoint variable, so it is difficult to evaluate directly its numerical values. To overcome this difficulty we rewrite the boundary control equation in a volumetric form. In the second case we still set $\lambda = 0$ and use discontinuous Galerkin method [9, 29]. In the first two approaches we solve the optimality system with a fully coupled one-shot algorithm, which is very efficient

and fast. In the third case we consider the full functional and find a solution in more regular spaces, $g \in H^1(\Gamma_c)$. We solve this optimality system in a segregated way with standard quadratic elements for all state-adjoint variables.

6.1   Optimality System

Let Ω be an open set with boundary Γ. The optimality system on Ω can be obtained by minimizing the objective functional under the constraints imposed by the energy equation and the Navier-Stokes system. The Navier-Stokes equations for an incompressible Newtonian flow are

$$\nabla \cdot \mathbf{u} = 0 \,, \tag{6.2}$$
$$\rho(\mathbf{u} \cdot \nabla)\mathbf{u} = -\nabla p + \mu \nabla^2 \mathbf{u} \,, \tag{6.3}$$

where μ is the dynamical viscosity, ρ the density and p the pressure. The steady state energy equation together with the boundary conditions can be written as

$$(\mathbf{u} \cdot \nabla)T = \alpha \nabla^2 T \tag{6.4}$$
$$\frac{\partial T}{\partial n} = d \qquad \text{on} \quad \Gamma_n$$
$$T = g \qquad \text{on} \quad \Gamma_c \,,$$

where $\mathbf{u}$ is the fluid velocity and α is the constant fluid thermal diffusivity. We assume that the value of the heat flux d is given. The optimal control problem consists in finding the best possible g in order to minimize the functional (6.1). In this optimal control problem the velocity behaves as a given field computed with the Navier-Stokes equations (6.2-6.3). Therefore we do not consider the possibility of varying the fluid velocity to obtain the desired objective and the optimal control setting comprises only the energy equation and the objective functional (6.1).

The mathematical properties of the optimal control problem for the energy system, such as existence and smoothness of the solution, are well known, so we apply the Lagrange multiplier method without proving the existence of the solution and the differentiability of the Lagrangian functional. The interested reader can see an example of this procedure applied to a more complex problem in the next Chapter 7 or in the very comprehensive book [47].

The total Lagrangian of the problem is composed of the objective functional and the energy equation multiplied by the appropriate Lagrangian

multiplier,

$$\mathcal{L}(T, \theta, g) = \mathcal{J}(T, g) + \int_{\Omega} [(\mathbf{u} \cdot \nabla)T - \alpha \nabla^2 T] \, \theta \, d\Omega \,. \tag{6.5}$$

Following the method depicted in Chapter 5 we can obtain the optimality system for this problem. We set the Fréchet derivatives of (6.5) with respect to all the variables involved to zero and obtain the weak form of the optimality system

$$\int_{\Omega} [(\mathbf{u} \cdot \nabla)T]\phi \, d\Omega + \int_{\Omega} \alpha \nabla T \cdot \nabla \phi \, d\Omega - \int_{\Gamma_n} \alpha \nabla T \cdot n\phi \, d\Gamma = 0 \,, \tag{6.6}$$

$$\forall \phi \in H^1_{\Gamma_c}(\Omega)$$

$$\int_{\Omega} \theta \, [(\mathbf{u} \cdot \nabla)\psi] \, d\Omega + \int_{\Omega} \alpha \nabla \theta \cdot \nabla \psi \, d\Omega - \int_{\Gamma_n} \alpha \, \nabla \theta \cdot n\psi \, d\Gamma = \tag{6.7}$$

$$\int_{\Omega} (T - T_d)\psi \, d\Omega \,, \qquad \forall \psi \in H^1(\Omega)$$

$$\int_{\Gamma_c} \beta \, g\chi \, d\Gamma + \int_{\Gamma_c} \lambda \nabla g \cdot \nabla \chi \, d\Gamma = \int_{\Gamma_c} \alpha \nabla \theta \cdot n\chi \, d\Gamma \,, \quad \forall \chi \in H^{1/2}(\Gamma_c) \,. \tag{6.8}$$

The adjoint temperature θ is the Lagrange multiplier satisfying (6.7). The (6.8), defined only on the controlled surface, is the equation for the control temperature g. The functions $\chi \in H^{1/2}(\Gamma_c)$ are the restrictions of the test functions $\psi \in H^1(\Omega)$ over Γ_c. If one approximates the above spaces with the finite dimensional ones, the finite element approximation is obtained.

We now describe and compare three different approaches for the solution of the system (6.6-6.8). In the first case we set the parameter $\lambda = 0$ so we seek a solution for the controlled temperature in $L_2(\Gamma_c)$. In this case (6.8) can be solved by

$$T = g = \alpha \frac{\nabla \theta \cdot n}{\beta} \qquad \text{on } \Gamma_c \,. \tag{6.9}$$

Algorithm 2 Simple steepest descent algorithm

1: **function** FIND OPTIMAL BOUNDARY TEMPERATURE
2:     assign an initial condition $g^{(0)}$ for the temperature on Γ_c
3:     **for** $i = 1 \rightarrow i_{max}$ **do**
4:         solve energy equation (6.6) with the control $g^{(i)}$
5:         solve adjoint energy equation (6.7) with new T
6:         solve control equation (6.8) with new θ and update $g^{(i+1)}$
7:     **end for**
8: **end function**

Algorithm 3 Steepest descent algorithm

1: **function** FIND OPTIMAL BOUNDARY TEMPERATURE
2:     assign an initial condition $g^{(0)}$ for the temperature on Γ_c
3:     solve energy equation (6.6) with the control $g^{(0)}$ ▷ *Reference state*
4:     **for** $i = 1 \rightarrow i_{max}$ **do**
5:         solve adjoint energy equation (6.7)
6:         solve control equation (6.8) with new θ and update $g^{(i+1)}$
7:         compute the functional $\mathcal{J}(T, g)$ in (6.1) and assign an initial η
8:         **for** $j = 1 \rightarrow j_{max}$ **do**
9:             solve energy equation (6.6) with b.c. $(1 - \eta)\, g^{(i)} + \eta\, g^{(i+1)}$
10:             compute $\mathcal{J}^1(T, g)$ with the new temperature
11:             **if** $\mathcal{J}^1(T, g) < \mathcal{J}(T, g)$ **then**
12:                 Go to 5   ▷ *loop on i again*
13:             **else if** $\mathcal{J}^1(T, g) > \mathcal{J}(T, g)$ **then**
14:                 Compute $\eta = 0.5\,\eta$ and go to 9   ▷ *loop on j again*
15:             **else if** $\mathcal{J}^1(T, g) \approx \mathcal{J}(T, g)$ **then**
16:                 Convergence is reached   ▷ *End of the algorithm*
17:             **end if**
18:         **end for**
19:     **end for**
20: **end function**

In order to evaluate T from θ on Γ_c we can proceed in the following way. We first recall (6.8) with $\lambda = 0$,

$$\int_{\Gamma_c} \beta\, T \chi \, d\Gamma = \int_{\Gamma_c} \alpha \nabla \theta \cdot n \chi \, d\Gamma\,, \qquad \forall \chi \in H^{1/2}(\Gamma_c) \qquad (6.10)$$

which can be rewritten, using equation (6.7), as

$$\int_{\Gamma_c} \beta\, T\, \chi \, d\Gamma = \int_{\Omega} \theta\, [(\mathbf{u} \cdot \nabla)\psi]\, d\Omega + \int_{\Omega} \alpha\, \nabla \theta \cdot \nabla \psi \, d\Omega - \qquad (6.11)$$

$$\int_{\Omega} (T - T_d)\psi \, d\Omega \qquad\qquad \forall \psi \in H^1(\Omega)\,,$$

where the test function χ is the restriction of ψ on Γ_c. We remark that the temperature control (6.9) is the trace of the function $\nabla \theta$ which is difficult to evaluate numerically. The expression (6.11) allows an easy computation of $T = g$ on the boundary since all the right hand side functions are well defined on Ω.

In the second case we still assume $\lambda = 0$ and use the Discontinuous Galerkin method for the solution of the energy equation. Therefore we impose Dirichlet boundary conditions by setting $T = g$ on Γ_c. The use of

Discontinuous Galerkin is appropriate for this setting since we have $\beta \neq 0$ and the solution $g \in L^2(\Gamma_c)$. We remark that $\beta = 0$ implies $g \in H^{-1/2}(\Gamma_c)$ [46, 66, 79]. In the first two cases we solve the optimality system with a one-shot solver because the system is linear and the control g is computed implicitly.

In the third case we assume $\lambda \neq 0$ which implies $g \in H^1(\Gamma_c)$. In this case the differential equation (6.8) must be solved on the boundary. Extra boundary conditions over $\partial\Gamma_c$ must be enforced which can be arbitrarily chosen as $g = T_d$ on $\partial\Gamma_c$. We solve this optimality system in a segregated way with standard quadratic elements for all the three variables T, θ and g. In this case we do not use a one-shot solver and the equations are solved segregated so the simple Algorithm 2 could be used to obtain the final solution. We have found however that this algorithm does not converge monotonically and often convergence is not reached. One may introduce some changes to the algorithm to obtain a more stable solution process, see Algorithm 3. This algorithm is very similar to the one reported in Section 5.3 and in the numerical solution of the optimality system (6.6-6.8) it is proven that it can reduce strongly solution oscillations. For these reasons it has been used to obtain the numerical results reported in the next Section.

6.2 Numerical Results

In this section we report the numerical results obtained by solving the boundary optimal control problem for the energy equation, as described in Section 6.1, in different geometries and using different values of the parameters β and λ. In the following we refer to the three approaches to the solution of the optimality system as reported in Section 6.1 which are a one-shot solver with $\lambda = 0$ and standard quadratic elements, a one-shot solver with $\lambda = 0$ and a discontinuous Galerkin method and a segregated solution with $\lambda \neq 0$ using Algorithm 3.

We consider three geometries for the test problem cases. The first is a simple two-dimensional boundary layer plane flow, the others two are a two and a three-dimensional geometry with secondary flow injections at different temperatures. The objective functional in all cases is a desired constant temperature to be obtained in a specific region with support Ω_d where the weight function is defined $w(\mathbf{x}) \neq 0$. We report the temperature and velocity fields and the physical properties in non-dimensional values.
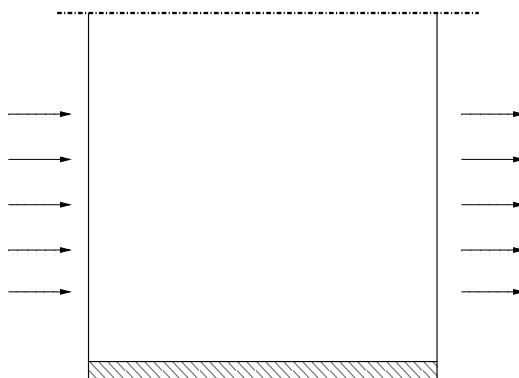
Figure 6.1: The plane boundary layer geometry. On the left inlet of the flow, on top symmetry axis, on bottom solid wall and on the right outlet.

Boundary layer flow

In this paragraph we analyze the behavior of different optimal control solvers in a simple laminar fully developed plane flow. The geometry is reported in Figure 6.1. With reference to this Figure we can define the inlet on the left side, the outlet on the right side, a symmetry plane on the top and the wall with the controlled temperature on the bottom. Two test cases have been studied with a different T_d. For the first test case the weight function is set to be $w(\mathbf{x}) = 1$ on the whole domain and we seek for an analytical solution: we impose a non-dimensional inlet temperature of 0.7 and we set $T_d = 0.7$. This case should serve as a benchmark for the optimal control solver. In the second test case we set $T_d = 1$ and still $w(\mathbf{x}) = 1$ on the whole domain. With this setting the solution is no longer analytical and the temperature develops as a boundary layer along the channel.

In the first test case the three approaches give slightly different solution results, as we can see in Figure 6.2. In this Figure the temperature profile on the controlled wall is reported as a function of the axial coordinate x for the three approaches and different values of the parameters β and λ. In the graph on top three temperature profiles for $\beta = 10^{-3}$ (dotted line) and $\beta = 10^{-6}$ (straight line) are reported as obtained with the one-shot solver and Discontinuous Galerkin method. It is clear that the controlling parameter β has a great importance in obtaining the correct solution. Using the Discontinuous Galerkin method convergence problems arise when imposing $\beta = 10^{-6}$, probably due to numerical errors. When β tends to zero the control is not a standard function anymore and therefore it becomes difficult to numerically represent a distribution. The result reported is the one with $\beta = 10^{-3}$ (dashed line). On the bottom we can see the results obtained by
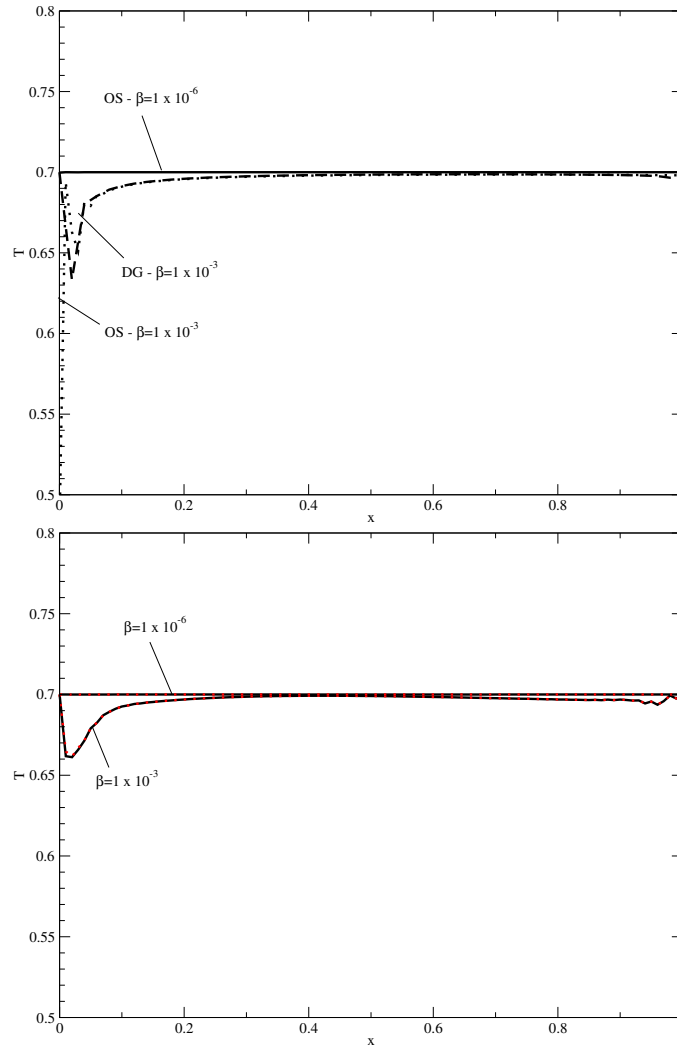
Figure 6.2: Plane boundary layer with $T_d = 0.7$, temperature on the wall. One-shot case with quadratic elements (OS) and Discontinuous Galerkin method (DG) (top) and $\lambda \neq 0$ case (bottom). In the last graph, dotted lines are for $\lambda = 10^{-6}$ while continuous for $\lambda = 10^{-3}$.

imposing $\lambda \neq 0$ and solving the control equation for g. By changing the parameter β one can obtain the correct solution, while by changing λ no relevant differences can be seen. The solution profiles obtained with this method are smoother than the ones obtained with $\lambda = 0$ as one can see by comparing the graphs on top and bottom of Figure 6.2.
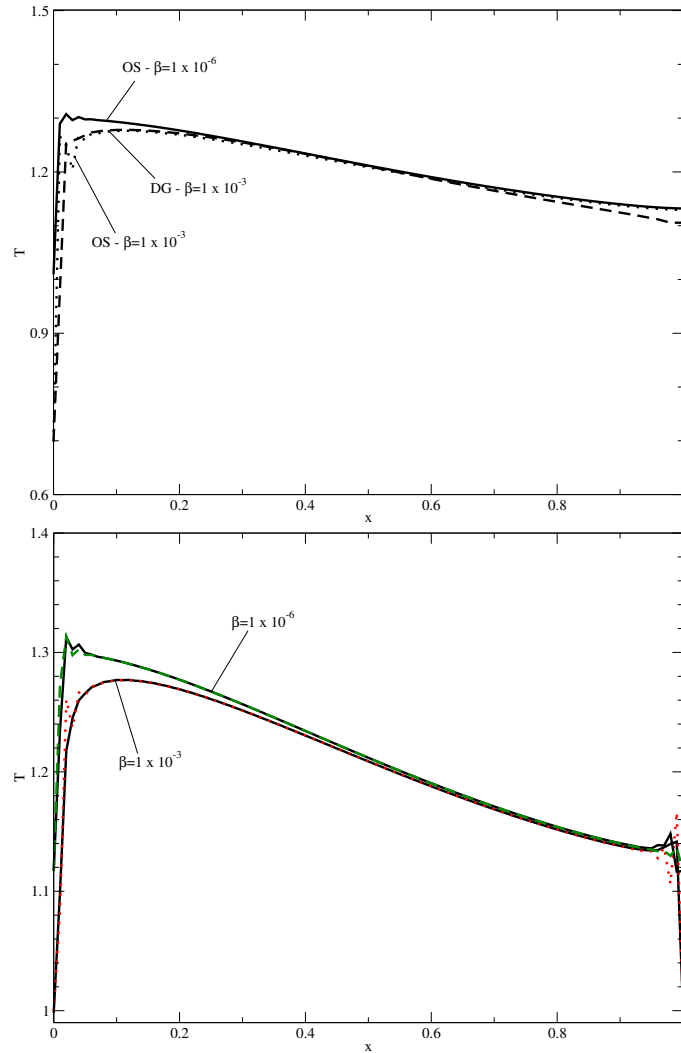
Figure 6.3: Plane boundary layer with $T_d = 1$, temperature on the wall. One-shot case with quadratic elements (OS) with $\beta = 10^{-3}$ (dotted), 10^{-6} (continuous) and Discontinuous Galerkin method (DG) with $\beta = 10^{-3}$ (dashed) on top. Segregated approach with $\lambda = 10^{-3}$ (continuous lines), $\beta = 10^{-3}$, $\lambda = 10^{-6}$ (dotted) and $\beta = 10^{-6}$, $\lambda = 10^{-6}$ (dashed) on the bottom.

In Table 6.1 the objective functional $\mathcal{J}'$ defined as

$$\mathcal{J}' = \frac{1}{2} \int_{\Omega} \left(T(\mathbf{x}) - T_d \right)^2 w(\mathbf{x}) \, d\Omega \,, \qquad (6.12)$$

is reported for the first test case, different solution approaches and β and λ values. It can be clearly seen that the most powerful control is achieved by
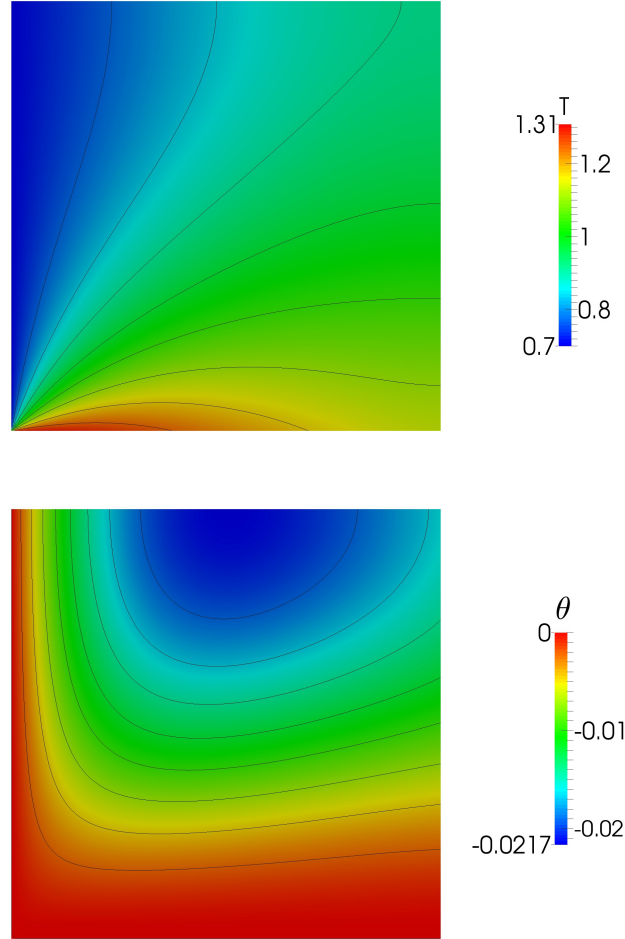
Figure 6.4: Plane boundary layer with $T_d = 1$, one-shot case with $\beta = 10^{-6}$. Temperature (top) and adjoint variable θ (bottom) contours obtained with ten equal subdivisions of the variable range.

setting $\beta = 10^{-6}$ and that the best result for this case is obtained with the segregated approach with $\lambda = 10^{-6}$. It must be taken into account that this method is much slower than the one-shot method in obtaining a convergent solution.

In the second set of test cases studied in this geometry with the weight function $w(\mathbf{x}) = 1$ and $T_d = 1$ the solution is no more analytical and a not uniform distribution of T and θ is obtained. We report the controlled solution and also some results for the adjoint temperature θ. In Figure 6.3 we show the profile of the temperature on the controlled wall as computed in

Solution Approach	$\mathcal{J}'$
One-shot $\beta = 10^{-3}$	2.23×10^{-06}
One-shot $\beta = 10^{-6}$	3.40×10^{-12}
Disc. Galerkin $\beta = 1 \times 10^{-3}$	1.63×10^{-06}
$\beta = 10^{-3}$ and $\lambda = 10^{-3}$	1.48×10^{-06}
$\beta = 10^{-3}$ and $\lambda = 10^{-6}$	1.46×10^{-06}
$\beta = 10^{-6}$ and $\lambda = 10^{-3}$	2.68×10^{-11}
$\beta = 10^{-6}$ and $\lambda = 10^{-6}$	2.57×10^{-12}

Table 6.1: Plane boundary layer with $T_d = 0.7$, objective functional computed with different solution approaches.

Solution Approach	$\mathcal{J}' \cdot 10^2$
One-shot $\beta = 10^{-3}$	1.0941
One-shot $\beta = 10^{-6}$	1.0936
Disc. Galerkin $\beta = 10^{-3}$	1.0921
$\beta = 10^{-3}$ and $\lambda = 10^{-3}$	1.0940
$\beta = 10^{-3}$ and $\lambda = 10^{-6}$	1.0940
$\beta = 10^{-6}$ and $\lambda = 10^{-3}$	1.0936
$\beta = 10^{-6}$ and $\lambda = 10^{-6}$	1.0936

Table 6.2: Plane boundary layer with $T_d = 1$, objective functional computed with different solution approaches.

all the three cases. On top the temperature profile is obtained with one-shot approach and Discontinuous Galerkin method while on the bottom with the segregated solver and g as additional variable. One-shot and DG method give quite similar results for the temperature profile: the controlled wall tends to increase the fluid temperature near the inlet while the temperature falls to 1.1 close to the outlet. The third approach shows ripples for cases with $\lambda = 10^{-6}$ and the profiles are different from the ones obtained with the other two approaches because near the outlet the temperature rises again. On the other hand, the profiles with $\lambda = 10^{-3}$ are smoother than the others.

In Figure 6.4 the temperature and adjoint variables are reported for the one-shot case with $\beta = 10^{-6}$. Near the axis of symmetry, very far from the wall, the control is difficult to be enforced and the maximum absolute value of θ is reached. On the other side, near the wall the control is very good and the adjoint variable vanishes in this region. Finally in Table 6.2 we report the values of the functional $\mathcal{J}'$ for this test case. We remark that the functional is several orders of magnitude higher than in the previous test case. This is due to the fact that an analytical optimal solution does not

exist in this setting. We can see also that the parameter β is less important for this range of values and the lowest objective functional is achieved with the Discontinuous Galerkin method.

Two-dimensional mixing channel

In this paragraph we report the numerical results obtained in a more complex geometry in order to show the capability of this optimal control solver in problems which are more similar to practical applications. We simulate a mixing channel in which a secondary flow injected from one side of the channel joins a main flow with different temperature. The objective of the problem
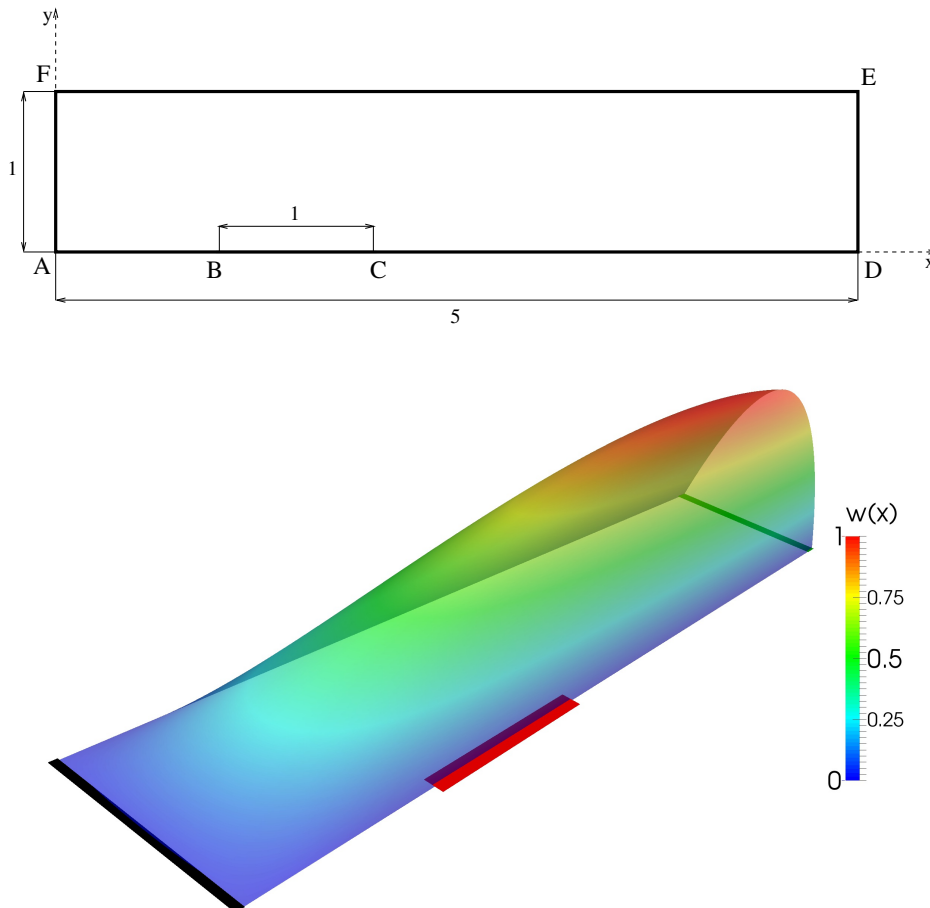
Figure 6.5: Mixing channel geometry (top) and weight function $w(x)$ (bottom). The segment AF (black on bottom) is the main flow inlet, BC (red on bottom) is the secondary flow inlet, DE (green on bottom) is the outflow.
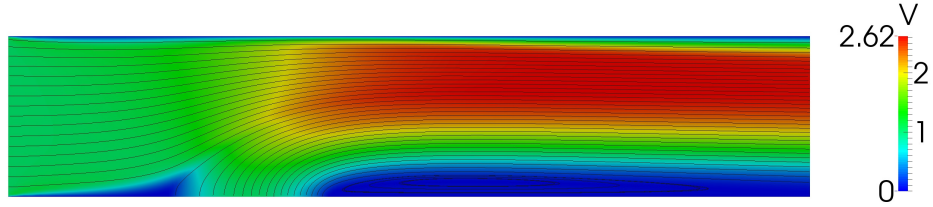
Figure 6.6: Velocity streamlines and velocity magnitude in the mixing channel.

is to obtain a desired temperature in the flow at the outlet of the channel lower than the inlet one $T_i = 1$ but still higher than the walls, $T_w = 0.5$. The desired temperature is then set to $T_d = 0.7$. Moreover we decide to assign great importance to the center of the channel near the outlet where the fluid velocity is higher by using the weight function $w(\mathbf{x}) = (8\,x - x^2)\,(y - y^2)/4$. This weight function is equal to 1 near the outlet and in the center of the channel and it decreases with a parabolic profile in the other directions to reach zero on the boundaries. In Figure 6.5 the geometry and the weight function are reported over the computational domain. In this Figure on top the geometry main dimensions are reported and the key regions are marked as follows: the segment AF is the inlet of the main flow, BC is the injection of the secondary flow with the controlled temperature and DE is the outlet. The other boundaries are solid walls with an assigned constant temperature. The characteristic parabolic shape of the weight function can be seen in Figure 6.5 on the bottom, where the main inlet is marked in black, the secondary inlet is red and the outlet is marked in green.

As mentioned above the Navier-Stokes equations are solved numerically with a finite element solver to obtain the velocity field before solving the optimality system. The horizontal velocity on the main inlet is set to a constant value of 1 while in the second injection boundary it is set with a parabolic profile. The Reynolds number of the flow based on the main inlet dimension and velocity is $Re = 1000$. In Figure 6.6 the velocity field is reported with flow streamlines and the velocity magnitude with colors. The effect of the injection flow can be clearly seen and a recirculation zone appears just after the injection region. With this velocity field we can solve the optimality system with different approaches as described before.

The one-shot approach with quadratic elements is very robust and the fully coupled solution with this approach is quite fast to obtain. The temperature and the adjoint variable fields, as obtained with the one-shot approach, are reported in Figure 6.7 for $\beta = 10^{-6}$. We can see, as expected,
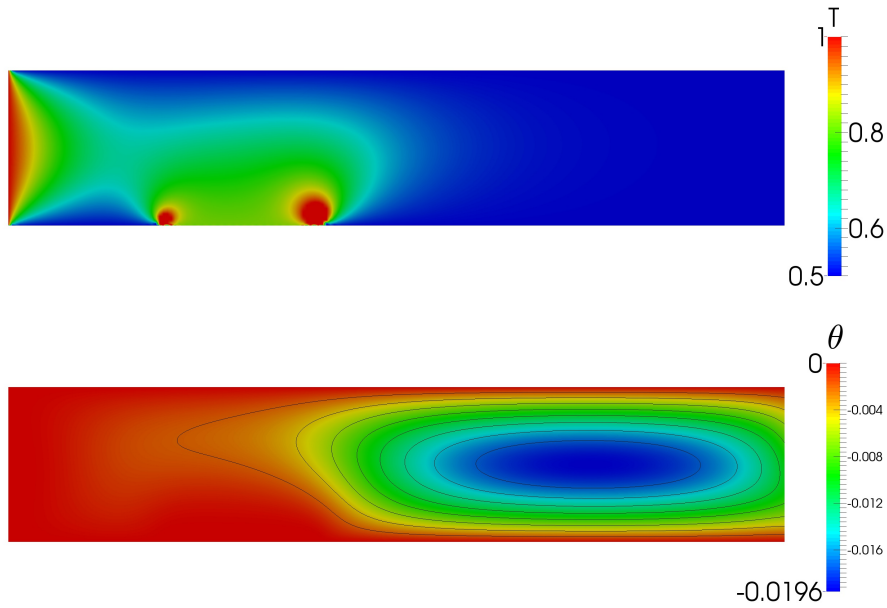
Figure 6.7: Temperature T (top) and adjoint variable θ (bottom) computed with first approach and $\beta = 10^{-6}$.
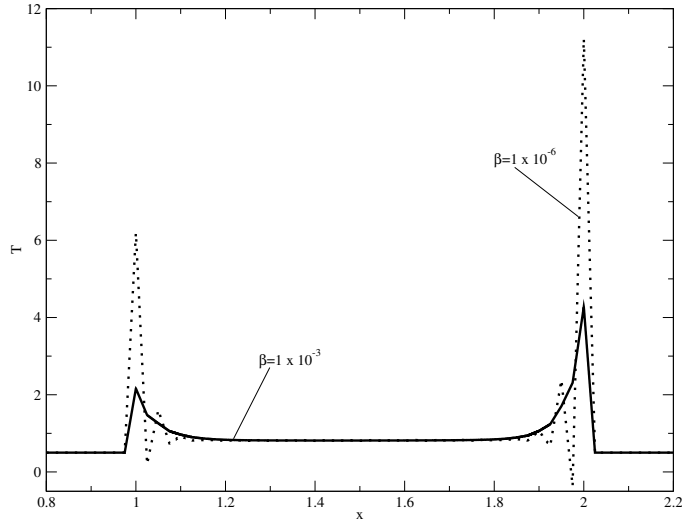
Figure 6.8: Temperature on the inlet line computed in the first case for $\beta = 10^{-3}$ (continuous line) and $\beta = 10^{-6}$ (dotted line).

that the region with high values of the modulus of the adjoint variable is the region where the weight function $w(x)$ is higher. With $\beta = 10^{-6}$ we can have a stronger control but the smoothness of the temperature on the
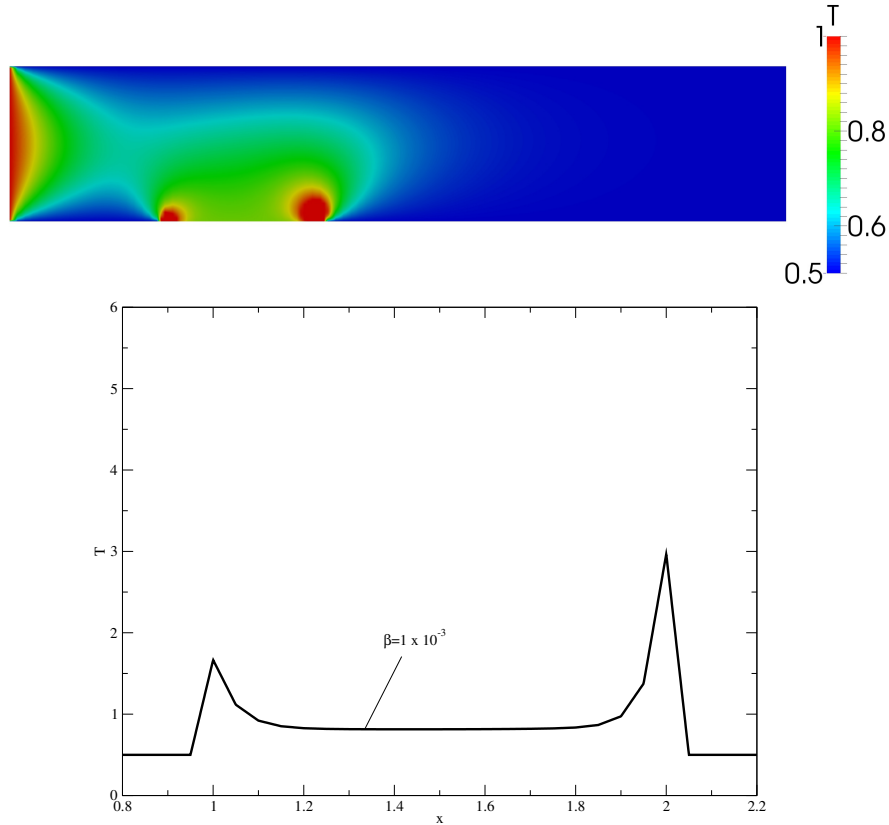
Figure 6.9: Temperature distribution on the whole domain (top) and on the inlet line (bottom) computed with Discontinuous Galerkin method and $\beta = 10^{-3}$.

controlled boundary decreases, as it can be seen in Figure 6.8. In this Figure the temperature is reported on the injection inlet line with coordinate x in the range of 0.8 to 2.2 for two values of $\beta = 10^{-3}$ and $\beta = 10^{-6}$. Strong oscillations of the temperature start to appear as the parameter β decreases under a certain value. On the contrary, with $\beta = 10^{-3}$, the temperature is quite smooth but it shows a sharp peak near the walls, where the inlet velocity $v \to 0$. The temperature distribution along the central region of the inlet flow is very similar for all different values of β.

The results obtained with the Discontinuous Galerkin method are reported in Figure 6.9. On top the temperature field is reported on the whole domain as computed with $\beta = 10^{-3}$ while on the bottom the temperature on the controlled inlet is shown as a function of the coordinate x in the range of 0.8 to 2.2. The result is quite similar to the one obtained with the first
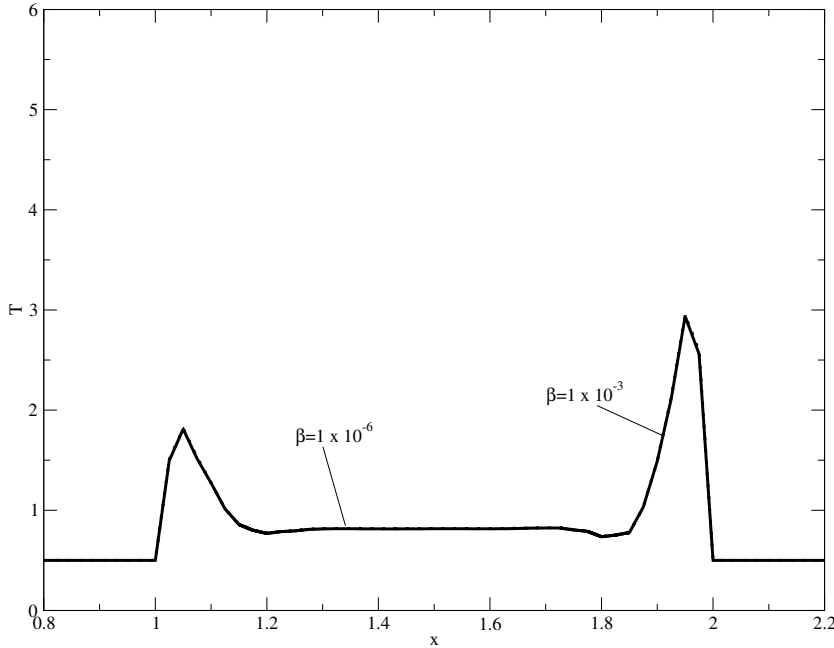
Figure 6.10: Temperature on the inlet line computed with third approach and $\beta = 10^{-3}$ (continuous) and $\beta = 10^{-6}$ (dotted), $\lambda = 10^{-3}$ in both cases.

Solution Approach	$\mathcal{J}' \cdot 10^{-2}$
One-shot $\beta = 10^{-3}$	3.3039
One-shot $\beta = 10^{-6}$	3.2960
Disc. Galerkin $\beta = 10^{-3}$	3.2890
$\beta = 10^{-3}$ and $\lambda = 10^{-3}$	3.3275
$\beta = 10^{-6}$ and $\lambda = 10^{-3}$	3.3270

Table 6.3: Two-dimensional mixing channel. Objective functional computed with different solution approaches and β-λ values.

approach showing sharp edges near the inlet wall and a flat non-dimensional temperature of around 0.8 in the center of the flow.

In Figure 6.10 we report the temperature profile on the inlet line as computed with the third approach solving directly a differential equation for g. We consider solutions with $\lambda = 10^{-3}$ and with $\beta = 10^{-3}$ and 10^{-6}. In this Figure two plots are reported with a straight continuous line for $\beta = 10^{-3}$ and with a dotted line for $\beta = 10^{-6}$. The results with varying β are quite similar, maybe due to the high value of λ. These profiles show similar peaks near the inlet walls as those obtained in the other two cases.

Finally we can compute the objective functional $\mathcal{J}'$ and compare the

results obtained with the different solvers. In Table 6.3 the functional is reported for the injection test case and for all the different approaches and β values employed. As already remarked, from this table one can see that by imposing a lower value of β the control is more effective. All the methods give quite similar values but the best result is obtained with the Discontinuous Galerkin method. The solution obtained with the segregated method is smoother and therefore the control loses effectiveness. For this reason it gives the worst results in term of functional $\mathcal{J}'$. The one-shot approach with quadratic elements lies between the other two. The result that gives high temperature oscillations near the wall corresponds to a low functional value.

Three-dimensional mixing channel

In this paragraph we report the numerical results obtained in a three dimensional test case. The geometry is a mixing channel with a main flow entering from the bottom and two injections of a fluid with controlled temperature on two sides of the box. The control problem can be summarized as a simple mixing flow heater exchanger with well defined geometry and flow rates and with the objective to increase the temperature of a main flow being able to inject fluid with controlled temperature from two specific locations.

The axial domain dimension is 5 while the other two dimensions x and y are 0.1. The injections are located between $z = 1.5$-2 and $z = $ 3-3.5 and are square and 0.05 wide. A three-dimensional view of the geometry is reported in Figure 6.11 with a scale factor of 0.1 in the axial direction. In this Figure the secondary injections are reported in red color while the walls are blue and the flow is directed from left to right. The main inlet velocity is 2 while the secondary injection velocities are 0.5 in the normal direction of the inlet giving a Reynolds number based on the square size and main inlet velocity of $Re = 2000$. The main inlet temperature and the wall temperature are assigned as 0.5, while the temperature of the two injection flows is controlled. The control objective is to obtain a constant temperature $T_d = 1$, higher than the main flow temperature, in the region near the outlet of the channel. This can be accomplished setting a weight function as

$$w(\mathbf{x}) = (0.12\, z^2 - 0.016\, z^3)(e^{\frac{ln(2)}{5}\, z} - 1)(40\, y - 400\, y^2)(40\, x - 400 x^2)\,.$$

This weight function is reported in Figure 6.11 with a geometrical scale factor of 0.1 in the axial direction and with ten equally spaced isosurfaces of the weight function in the range of 0 to 1.

The velocity field of the incompressible Navier-Stokes system can be solved separately from the optimality system, as explained before. The solution of the velocity and pressure fields requires a high computational cost
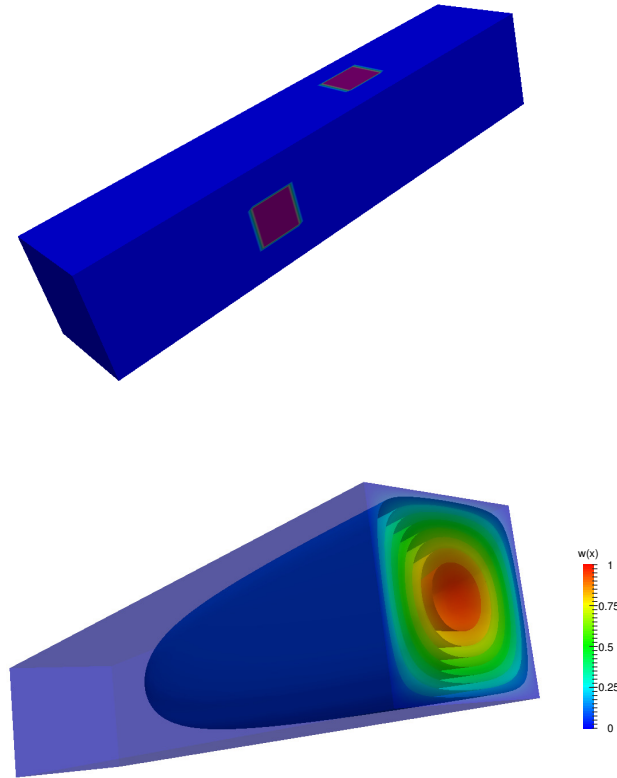
Figure 6.11: Three-dimensional mixing channel geometry with a scale factor of 0.1 in the axial direction (top), weight function on the same geometry (bottom). On the top the two flow injections are visible in red color and on the bottom ten equally subdivided isosurfaces for the weight function are reported. The flow is directed from left to right in both figures.

because of the three-dimensional problem and is obtained with a fully coupled solver. On top of Figure 6.12, the flow pattern is visible with the velocity streamlines reported on the three-dimensional domain and colored by the velocity magnitude. One can see the formation of vortices due to the lateral injections. A slice obtained at axial coordinate $z = 4$ is reported in Figure 6.12 on the bottom with the velocity vectors represented with arrows and colored by the velocity magnitude. The recirculation patterns are visible in this Figure and the flow on the outlet section is pushed towards a corner of the channel by two recirculation vortices.

For this test case the optimality system has been solved with the one-
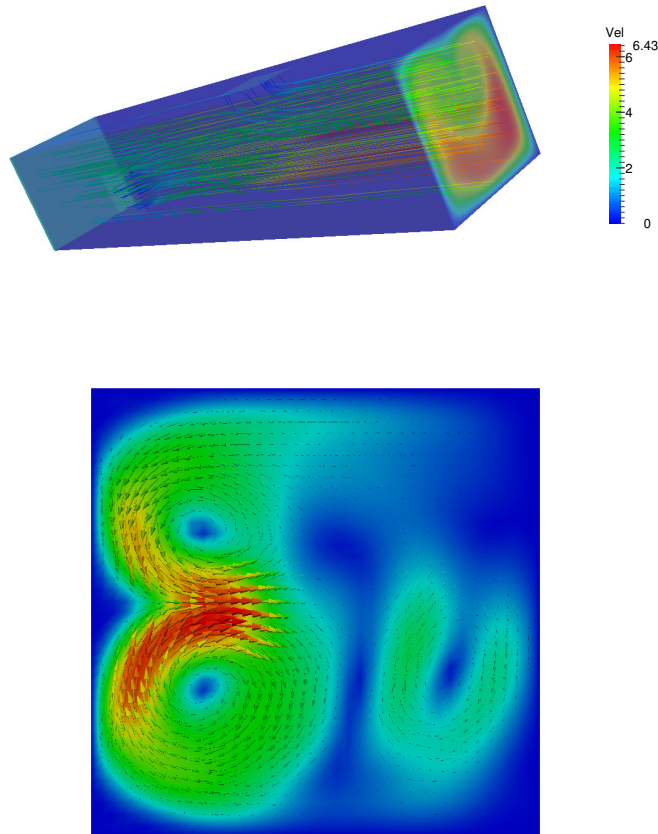
Figure 6.12: Velocity flow pattern of the three-dimensional mixing channel geometry. Velocity streamlines colored by the velocity magnitude (top) and velocity on a slice obtained at a constant axial coordinate $z = 4$ with arrows colored by velocity magnitude (bottom).

shot approach only, because of its robustness and fast convergence obtained in the other test cases. The temperature results obtained with $\beta = 0.1$ are reported in Figure 6.13. In this Figure the temperature is shown with ten equally subdivided isosurfaces on the domain clipped with a section normal to the x-axis on top and y-axis on the bottom. On top one can see the effect of the first injection located between $z = 1.5$-2 and on the bottom it can be seen the second injection located between $z = 3$-3.5. The control on the boundary tries to heat the flow by increasing temperature on the
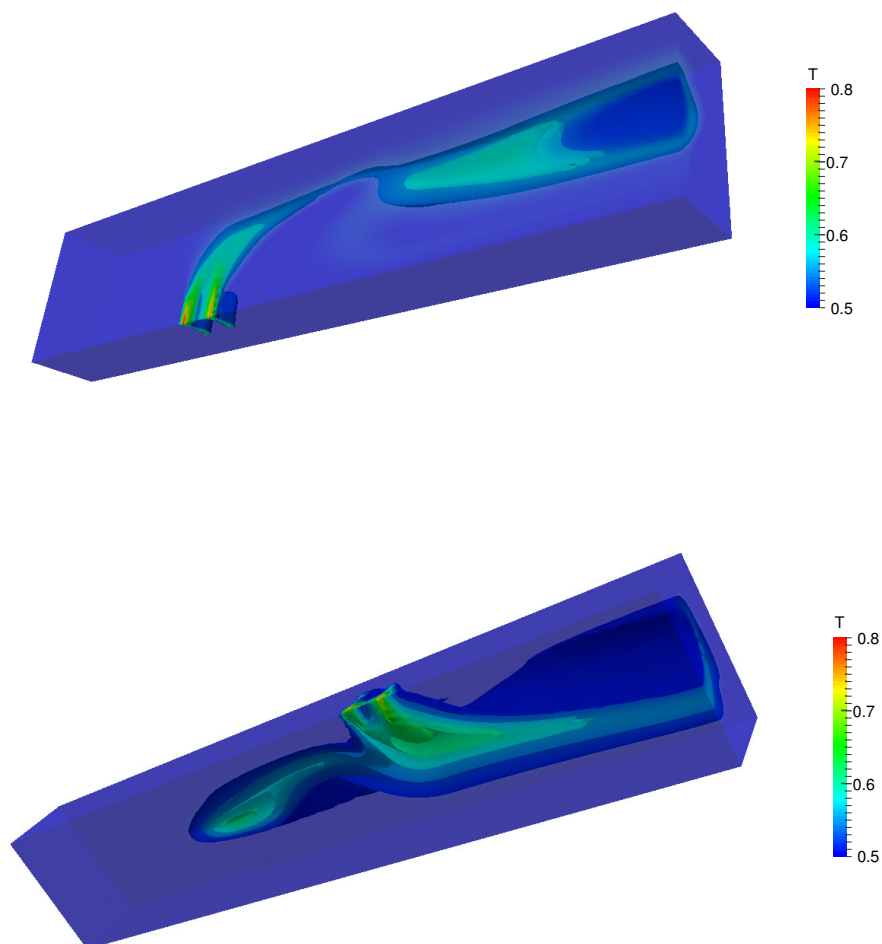
Figure 6.13: Temperature profile obtained with $\beta = 0.1$ in the three-dimensional mixing channel geometry. Ten equally spaced temperature iso-surfaces on half of the domain clipped with a section normal to the x-axis (top) and section normal to the y-axis (bottom).

two injections. The hotter fluid moves along the channel achieving a lower functional $\mathcal{J}'$.

It is interesting to study also the adjoint variable in order to better understand the control problem. Moreover this variable can give useful indications for an improved design. In Figure 6.14 the adjoint variable is reported with
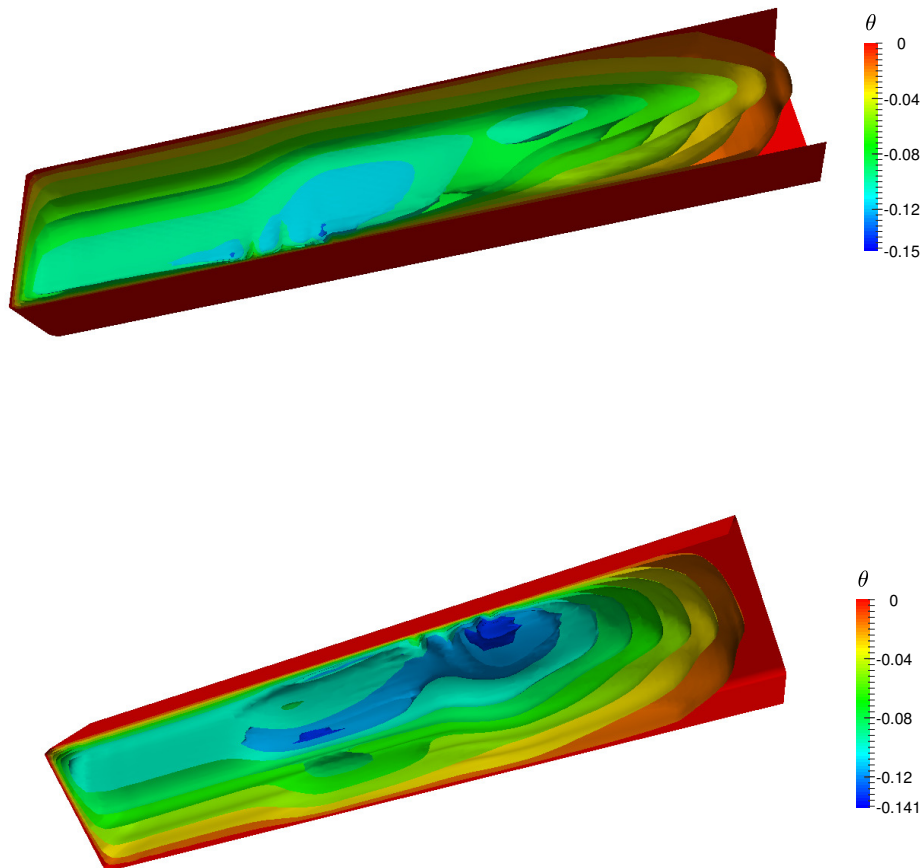
Figure 6.14: Adjoint variable profile obtained with $\beta = 0.1$ in the three-dimensional mixing channel geometry. Ten equally spaced temperature iso-surfaces on half of the domain clipped with a section normal to the x-axis (top) and section normal to the y-axis (bottom).

ten equally subdivided isosurfaces. On top the domain is clipped with a plane normal to the x-axis, on the bottom with respect to y-axis. The adjoint or importance function is higher in modulus where the control should act stronger in order to better achieve the desired result. We can see several regions where θ is higher, for example in front of the second injection which is
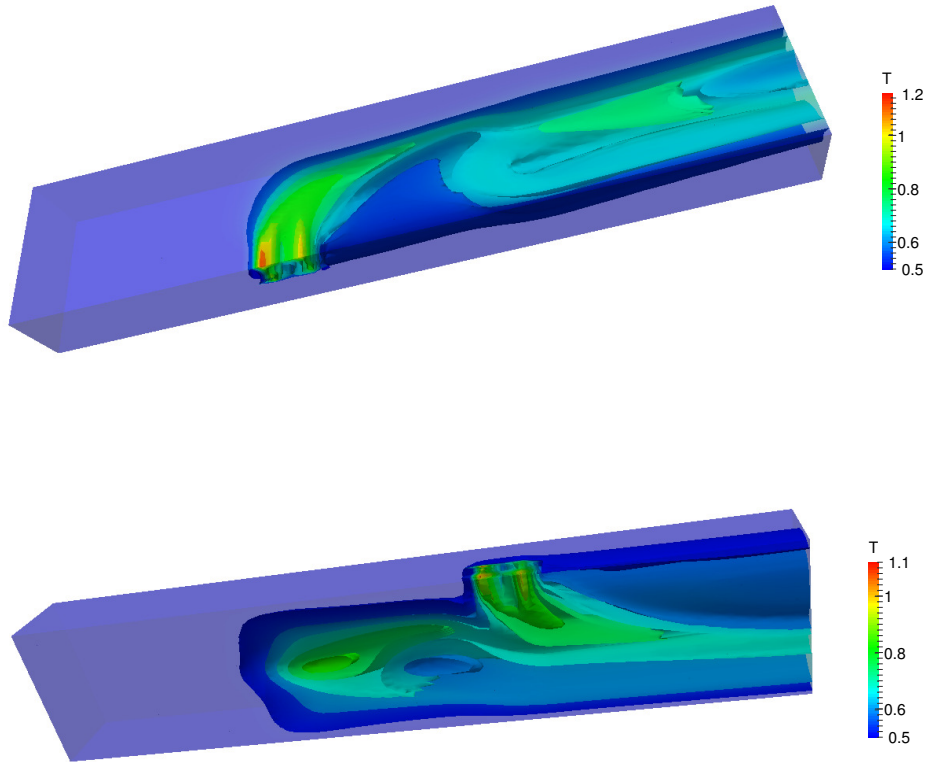
Figure 6.15: Temperature profile obtained with $\beta = 0.05$ in the three-dimensional mixing channel geometry. Ten equally spaced temperature iso-surfaces on half of the domain clipped with a section normal to the x-axis (top) and section normal to the y-axis (bottom).

near to the objective region and where the weight function is high. Another region where θ is quite high is towards the inlet of the channel. Here the weight function is nearly zero, so one possible explanation of this behavior could be the high velocity of the flow: changing the temperature near the inlet could control better the result than injecting fluid near the end of the channel due to advective effects. A possible way of taking into account this information could be to reformulate the problem by setting the injections upstream in the axial direction and solve again the optimality system with the new geometry. However here we are not interested in the best solution to this specific problem but in showing the information given from the solution
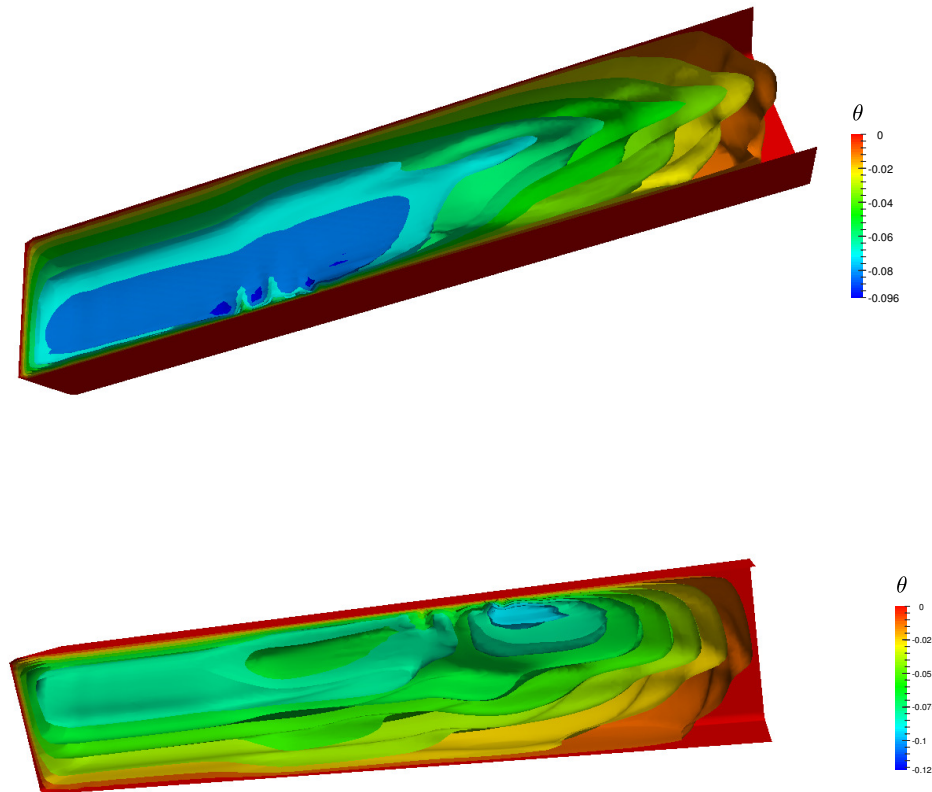
Figure 6.16: Adjoint temperature profile obtained with $\beta = 0.05$ in the three-dimensional mixing channel geometry. Ten equally spaced temperature isosurfaces on half of the domain clipped with a section normal to the x-axis (top) and section normal to the y-axis (bottom).

of the optimality system and in testing the use of adjoint optimal control algorithms, so we keep the same geometry for another test with different β.

By decreasing the parameter β to 0.05 the control acts stronger to decrease the objective functional because the solution T on the boundary can take higher values. In Figure 6.15 the temperature is reported with ten equally subdivided isosurfaces on the domain clipped with respect to the x (top) and y-axis (bottom). It can be seen from this Figure that the values attained by the temperature on the controlled surfaces are higher in modulus than the ones obtained by setting $\beta = 0.1$. The adjoint variable for this case is reported in Figure 6.16 and it is shown with ten equally subdivided
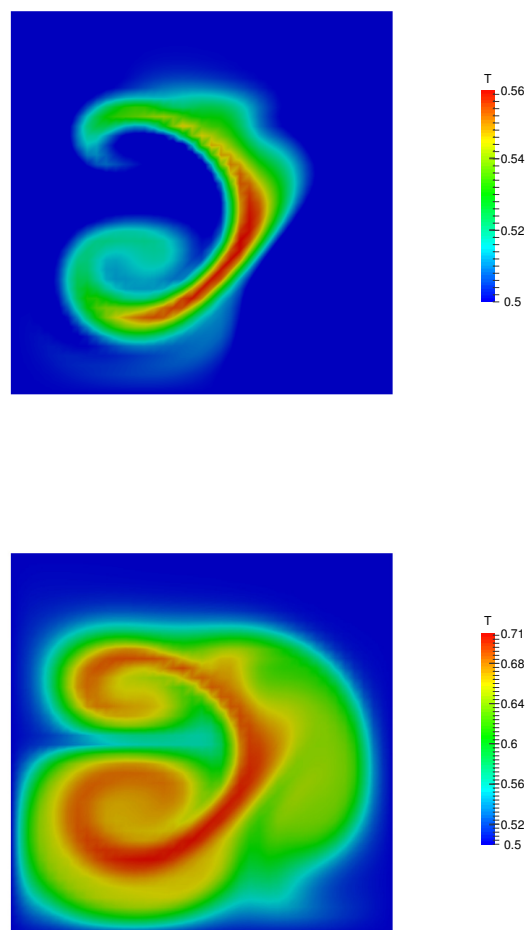
Figure 6.17: Temperature distribution on the outlet section of the three-dimensional mixing channel. Test case with $\beta = 0.1$ (top) and $\beta = 0.05$ (bottom).

isosurfaces. On top the domain is clipped with respect to the x-axis and on the bottom with respect to the y-axis. By decreasing β the adjoint variable becomes lower and the region where the control cannot act to reduce the objective functional is more visible. Clearly this is the entrance region, as we have already explained.

We can now compare the temperature distributions obtained on the outlet section for the two different values of β. The objective of the control is to

Solution Approach	$\mathcal{J}' \cdot 10^3$
One-shot $\beta = 0.1$	1.722
One-shot $\beta = 0.05$	1.054

Table 6.4: Three-dimensional mixing channel test case, objective functional computed with different β values.

obtain a higher temperature near the outlet region with more importance to the center of the channel, so we show the results in this region. On top of Figure 6.17 the temperature on a slice normal to the main flow at $z = 4$ obtained in the test case with $\beta = 0.1$ is reported, while on the bottom the one of $\beta = 0.05$. Over this section the vortices created by the two injections are well visible because the injected flow is hotter and the flow is too fast to allow a complete diffusion of heat in the fluid. Moreover we remark the different ranges of temperature with the different β, with the maximum temperature $T_{max} = 0.71$ obtained for $\beta = 0.05$ higher than the one obtained with $\beta = 0.1$, which is $T_{max} = 0.56$.

Finally in Table 6.4 we compare the objective functional computed on the results obtained with the one-shot approach and $\beta = 0.1$ and 0.05. It is clear the important effect of the regularization parameter β in achieving low functional values.

Chapter 7

Turbulence optimal control

The study of adjoint optimal control applied to the Navier-Stokes equations started several years ago. In spite of the computational difficulties, optimal control is nowadays commonly used in many fluid dynamics applications. Many works dealing with the distributed, boundary and shape control of Navier-Stokes equations exist in literature, [18, 44, 45, 46]. However the majority of these works refer to standard Navier-Stokes equations and a very high computational effort is needed to consider the effects of turbulence without modeling the averaged fields. Direct Numerical Simulation is currently the only way to take into account turbulence without applying filters or averaging to the fields.

In literature there are some studies dealing with the optimal control of modeled turbulent flows and different levels of approximation are used to account for turbulence effects in the optimal control setting. The simplest method which is often chosen is to consider the turbulent viscosity as "frozen" or independent on the control variable, [21, 106]. In this case no adjoint turbulent viscosity and turbulence model exist, so the computational effort is strongly decreased. Another common method to obtain information on the optimal turbulent flow without a too high computational cost is to use a lower level turbulence model, like a one-equation model. By doing so only one adjoint turbulence equation is obtained in the optimization process and the computations are faster, see [108, 118]. In work [118] the differences in the optimal solutions obtained with a complete model or with a frozen viscosity model are remarked. Some studies of the full adjoint two-equations turbulence model has been performed recently in the works [81, 94]. They deal with shape optimization problem by using automatic differentiation tools and adjoint approach for the k-ϵ model.

In this Chapter we aim at developing an adjoint optimal control setting for the Reynolds averaged Navier-Stokes system coupled with a two-equation

k-ω model. The objective is set in order to obtain two problems, a velocity matching or a turbulence enhancement or decreasing one. The control has been chosen as a distributed force in the domain which could be feasible with heavy liquid metals in fast nuclear reactors or other power systems. The objective functional is written as

$$\mathcal{J}(\mathbf{v}, k, f) = a\,\frac{1}{2} \int_\Omega \left(\mathbf{u} - \mathbf{u}_d\right)^2 \, d\mathbf{x} \,+ b\,\frac{1}{2} \int_\Omega \left(k - k_d\right)^2 \, d\mathbf{x} + \qquad (7.1)$$

$$\lambda\,\frac{1}{2} \int_\Omega \mathbf{f}^2 \, d\mathbf{x}\,,$$

where b is a non negative constant and a and λ positive. If $b = 0$ the objective functional can be used in a velocity matching profile problem, while $a \approx 0$ is to be used for a turbulence reduction or enhancement problem. It is important the introduction of the regularization term multiplied by the scalar λ. The choice of this parameter is a key point for the numerical solution of the problem because high values of λ can result in a poor control, while low ones usually lead to convergence issues due to the enlargement of the control space $\mathbf{f}$ to the space of distributions. The integral (7.1) is usually referred to as *cost functional* because it measures the difference between our objective and what we have actually achieved.

In the next Section we present the mathematical model of the RANS equations together with the k-ω model by Wilcox [112]. Three theorems are presented to prove the existence of solutions to the RANS system, which are needed in the following Section where some remarks are made on the mathematical properties of the control problem [78]. The optimality system is then derived using the Lagrange multiplier method described in Chapter 5. In the last Section some numerical results are reported to prove the feasibility of this method in complex industrial applications [77].

7.1   RANS system

The steady state RANS system coupled with the k-ω model consists of the following set of equations

$$\nabla \cdot \mathbf{u} = 0\,, \qquad (7.2)$$

$$(\mathbf{u} \cdot \nabla)\mathbf{u} + \nabla p - \nabla \cdot \left[(\nu + \nu_t)\mathbf{S}(\mathbf{u})\right] = \mathbf{f}\,, \qquad (7.3)$$

$$(\mathbf{u} \cdot \nabla)k - \nabla\left[(\nu + \sigma_k \nu_t) \cdot \nabla k\right] = S_k - \beta^*\, k\,\omega\,, \qquad (7.4)$$

$$(\mathbf{u} \cdot \nabla)\omega - \nabla\left[(\nu + \sigma_\omega \nu_t) \cdot \nabla \omega\right] = \alpha S_\omega - \beta \omega^2\,, \qquad (7.5)$$

where $\mathbf{f}$ is the force acting on the flow, p the total fluid pressure, ν the kinematic viscosity of the fluid and $\mathbf{S}$ the deformation tensor

$$\mathbf{S}(\mathbf{u}) := \nabla\mathbf{u} + \nabla\mathbf{u}^T . \tag{7.6}$$

The model coefficients and functions are [112]

$$\sigma_k = 0.6 \qquad\qquad \sigma_\omega = 0.5$$

$$\beta^* = 0.09 \qquad\qquad \alpha = \frac{13}{25}$$

$$\beta = 0.0708 .$$

In order to complete the system (7.2)-(7.5) the production term of the turbulent kinetic energy and its dissipation are usually modeled as

$$S_k = \nu_t \mathbf{S}(\mathbf{u}) : \nabla\mathbf{u} = \frac{1}{2}\nu_t \mathbf{S}^2(\mathbf{u}) \tag{7.7}$$

$$S_\omega = \frac{\omega}{k}\nu_t \mathbf{S}(\mathbf{u}) : \nabla\mathbf{u} = \frac{1}{2}\mathbf{S}^2(\mathbf{u}) , \tag{7.8}$$

with $\mathbf{S}^2(\mathbf{u}) = \mathbf{S}(\mathbf{u}) : \mathbf{S}(\mathbf{u})$ since $\nabla\mathbf{u}$ is symmetric and $\nu_t = k/\omega$. The key quantity ν_t is the turbulent or eddy viscosity which has to be defined in the turbulence model.

Standard regular Navier-Stokes solutions of (7.2)-(7.5) have the derivatives of the velocity field square integrable but not necessarily bounded. The k and ω equations have the typical pattern of the diffusion-reaction equations and therefore their solutions can be constrained inside a precise interval limited by the roots of the equation defined only by the right-hand-side non linear terms in (7.7)-(7.8). For example in an infinite medium with no advection and diffusion term (7.5) becomes

$$\frac{\alpha}{2}\mathbf{S}^2(\mathbf{u}) - \beta\,\omega^2 = 0 , \tag{7.9}$$

which has solution $\omega = \pm\sqrt{\alpha\mathbf{S}^2(\mathbf{u})/(2\beta)}$. Only the positive root should be considered but if $\nabla\mathbf{u}$ is not bounded then $\mathbf{S}(\mathbf{u})$ and ω are unbounded. In order to keep Navier-Stokes solutions in standard functional classes and the turbulent fields bounded in well defined intervals, we must regularize the modeling of the turbulence sources. Therefore we assume

$$S_k = \min\left[\frac{1}{2}\nu_t \mathbf{S}^2(\mathbf{u}), \beta^* k_{max,v}\omega\right] \tag{7.10}$$

$$S_\omega = \min\left[\frac{1}{2}\mathbf{S}^2(\mathbf{u}), \frac{\omega_{max,v}^2\beta}{\alpha}\right] , \tag{7.11}$$

where $k_{max,v}$ and $\omega_{max,v}$ are positive constants. This notation points out that $k_{max,v}$ and $\omega_{max,v}$ will be proven to be limits for k and ω fields while the label v suggests that these are volumetric bounds. The source model in (7.10)-(7.11) assures that, in the case of unbounded gradient velocity, the dissipation terms can cope with the turbulence sources and keep k and ω limited.

In k-ω model $\nu_t = k/\omega$, so if ω vanishes ν_t becomes singular. The existence of regular solutions of (7.4)-(7.5) when ν_t is an unbounded function is difficult to prove [97]. For this reason we assume

$$\nu_t = \min\left[\frac{k}{\omega}, \nu_{max}\right] . \tag{7.12}$$

The constants $k_{max,v}$, $\omega_{max,v}$ and ν_{max} can be chosen as large as needed in order to assure the regularity of the problem together with the accuracy of the physical solution. By doing so the solution of Navier-Stokes equations remains unchanged while only the turbulence source terms are modeled to avoid singularities.

We use a near-wall approach for the solution of the turbulence problem, so the RANS equations are integrated throughout the viscous layer where near-wall boundary conditions are imposed. By using Taylor expansion for the turbulence variables, with respect to the distance from the wall δ, we obtain for the tangential component v of the velocity and for the turbulence variables

$$v = \frac{\sigma_w}{\mu}\delta \qquad k = a_1\delta^2 \qquad \omega = \frac{2\,\nu}{\beta^*\delta^2}\,, \tag{7.13}$$

with a_1 constant and σ_w the stress on the boundary. For more details on the boundary conditions to be set with turbulence models see the discussion in Chapters 3 and 4.

7.1.1   Notations

Before introducing the boundary value problem, let us briefly recall some notations about functional spaces used here that have been defined in Chapter 1. We denote by $H^s(\mathcal{O})$, $s \in \Re$, the standard Sobolev space of order s with respect to the set $\mathcal{O}$, which is either the flow domain $\Omega \subset \Re^n$ ($n = 2, 3$), or its boundary Γ, or part of its boundary. Whenever m is a non-negative integer, the inner product over $H^m(\mathcal{O})$ is denoted by $(f, g)_m$ and (f, g) denotes the inner product over $H^0(\mathcal{O}) = L^2(\mathcal{O})$. Hence, we associate with $H^m(\mathcal{O})$ its natural norm $\|f\|_{m,\mathcal{O}} = \sqrt{(f, f)_m}$. Whenever possible, we will neglect the

domain label in the norm. For more details on these spaces, one can consult [7, 20].

For vector-valued functions and spaces, we use boldface notation. For example, $\mathbf{H}^s(\Omega) = [H^s(\Omega)]^n$ denotes the space of $\Re^n$-valued functions such that each component belongs to $H^s(\Omega)$. Of special interest is the space

$$\mathbf{H}^1(\Omega) = \left\{ v_i \in L^2(\Omega) \ \Big| \ \frac{\partial v_i}{\partial x_j} \in L^2(\Omega) \quad \text{for } i, j = 1, 2, 3 \right\}$$

equipped with the norm $\|\mathbf{v}\|_1 = (\sum_{i,j}(\|v_i\|_1^2 + \|\partial v_i/\partial x_j\|_1^2))^{1/2}$. We define the divergence-free space

$$\mathbf{V}(\Omega) = \left\{ \mathbf{u} \in \mathbf{H}^1(\Omega) \mid \nabla \cdot \mathbf{u} = 0 \right\}.$$

For $\Gamma_s \subset \Gamma$ with nonzero measure, we also consider the subspace

$$\mathbf{H}^1_{\Gamma_s}(\Omega) = \left\{ \mathbf{v} \in \mathbf{H}^1(\Omega) \mid \mathbf{v} = \mathbf{0} \quad \text{on } \Gamma_s \right\}.$$

Also, we write $\mathbf{H}^1_0(\Omega) = \mathbf{H}^1_\Gamma(\Omega)$. Let $(\mathbf{H}^1_{\Gamma_s})^*$ denote the dual space of $\mathbf{H}^1_{\Gamma_s}$. Note that $(\mathbf{H}^1_{\Gamma_s})^*$ is a subspace of $\mathbf{H}^{-1}(\Omega)$, where the latter is the dual space of $\mathbf{H}^1_0(\Omega)$. The duality pairing between $\mathbf{H}^{-1}(\Omega)$ and $\mathbf{H}^1_0(\Omega)$ is denoted by $\langle \cdot, \cdot \rangle$.

Let $\mathbf{g}$ be an element of $\mathbf{H}^{1/2}(\Gamma)$. It is well known that $\mathbf{H}^{1/2}(\Gamma)$ is a Hilbert space with norm

$$\|\mathbf{g}\|_{1/2,\Gamma} = \inf_{\mathbf{v} \in \mathbf{H}^1(\Omega); \, \gamma_\Gamma \mathbf{v} = \mathbf{g}} \|\mathbf{v}\|_1 \,,$$

where γ_Γ denotes the trace mapping $\gamma_\Gamma : \mathbf{H}^1(\Omega) \to \mathbf{H}^{1/2}(\Gamma)$. We let $(\mathbf{H}^{1/2}(\Gamma))^*$ denote the dual space of $\mathbf{H}^{1/2}(\Gamma)$ and $\langle \cdot, \cdot \rangle_\Gamma$ denote the duality pairing between $(\mathbf{H}^{1/2}(\Gamma))^*$ and $\mathbf{H}^{1/2}(\Gamma)$. From the definition of the dual norm, we have

$$\|\mathbf{s}\|_{-1/2,\Gamma} = \sup_{\mathbf{g} \in \mathbf{H}^{1/2}(\Gamma); \, \mathbf{g} \neq \mathbf{0}} \frac{\langle \mathbf{s}, \mathbf{g} \rangle_\Gamma}{\|\mathbf{g}\|_{1/2}} = \sup_{\mathbf{v} \in \mathbf{H}^1(\Omega); \, \mathbf{v} \neq \mathbf{0}} \frac{\langle \mathbf{s}, \gamma_\Gamma \mathbf{v} \rangle_\Gamma}{\|\mathbf{v}\|_1} \,.$$

Since the pressure is only determined up to an additive constant by the Navier-Stokes system with velocity boundary conditions, we define the space of square integrable functions having zero mean over Ω as

$$L^2_0(\Omega) = \left\{ p \in L^2(\Omega) \mid \int_\Omega p \, d\mathbf{x} = 0 \right\}.$$

In order to define a weak form of the Navier-Stokes-k-ω equations, we introduce the continuous bilinear forms

$$a(\nu; \mathbf{u}, \mathbf{v}) = \frac{1}{2} \int_\Omega \nu \, \mathbf{S}(\mathbf{u}) : \mathbf{S}(\mathbf{v}) \, d\mathbf{x} \qquad \forall \mathbf{u} \in \mathbf{H}^1(\Omega), \quad \forall \mathbf{v} \in \mathbf{H}^1_0(\Omega) \quad (7.14)$$

and

$$b(\mathbf{v}, q) = -\int_\Omega q\, \nabla \cdot \mathbf{v}\, d\mathbf{x} \qquad \forall\, q \in L_0^2(\Omega)\,, \quad \forall\, \mathbf{v} \in \mathbf{H}^1(\Omega) \qquad (7.15)$$

and the trilinear form

$$c(\mathbf{w}; \mathbf{u}, \mathbf{v}) = \frac{1}{2}\left[\int_\Omega [(\mathbf{w}\cdot\nabla)\mathbf{u}]\cdot\mathbf{v}\, d\mathbf{x} - \int_\Omega [(\mathbf{w}\cdot\nabla)\mathbf{v}]\cdot\mathbf{u}\, d\mathbf{x}\right] \qquad (7.16)$$
$$\forall\, \mathbf{w} \in \mathbf{V}(\Omega), \mathbf{u} \in \mathbf{H}^1(\Omega), \mathbf{v} \in \mathbf{H}_0^1(\Omega)\,.$$

The above definitions of the continuous bilinear forms are also valid for scalars with the appropriate mono dimensional operators, for example the form (7.14) becomes

$$a(\nu; u, v) = \int_\Omega \nu\, \nabla u \cdot \nabla v\, d\mathbf{x} \qquad \forall\, u \in H^1(\Omega),\ \forall\, v \in H_0^1(\Omega)\,. \qquad (7.17)$$

Obviously, given any $\nu \in L^\infty(\Omega)$, $a(\cdot,\cdot)$ is a continuous bilinear form on $\mathbf{H}^1(\Omega)\times\mathbf{H}_0^1(\Omega)$ and $b(\cdot,\cdot)$ is a continuous bilinear form on $\mathbf{H}^1(\Omega)\times L_0^2(\Omega)$; also $c(\cdot;\cdot,\cdot)$ is a continuous trilinear form on $\mathbf{H}^1(\Omega)\times\mathbf{H}^1(\Omega)\times\mathbf{H}_0^1(\Omega)$. For details concerning the function spaces we have introduced, one may consult [7, 109] while for details about the bilinear and trilinear forms and their properties see [39, 109] and Chapter 1.

7.1.2   The associated boundary value problem

We consider the formulation of the direct problem for the RANS system (7.2)-(7.3) and turbulence equations (7.4)-(7.5). A weak formulation of the Navier-Stokes-k-ω system is given as follows

given ν_{max}, $k_{max,v}$ and $\omega_{max,v}$ positive real constants and $\mathbf{f} \in \mathbf{H}^{-1}(\Omega)$, $\mathbf{g}_u \in \mathbf{H}^1(\Omega)$, $g_k \in H^1(\Omega)$, $g_\omega \in H^1(\Omega)$, find $(\mathbf{u}, p, k, \omega) \in \mathbf{H}^1(\Omega) \times L_0^2(\Omega) \times H^1(\Omega) \times H^1(\Omega)$ satisfying

$$\begin{cases} a(\nu + \nu_t; \mathbf{u}, \mathbf{v}) + c(\mathbf{u}; \mathbf{u}, \mathbf{v}) + b(\mathbf{v}, p) = \langle \mathbf{f}, \mathbf{v} \rangle & \forall\, \mathbf{v} \in \mathbf{H}_0^1(\Omega) \\[2mm] b(\mathbf{u}, q) = 0 & \forall\, q \in L_0^2(\Omega) \\[2mm] \langle \mathbf{u}, \mathbf{s} \rangle_\Gamma = \langle \mathbf{g}_u, \mathbf{s} \rangle_\Gamma & \forall\, \mathbf{s} \in \mathbf{H}^{-1/2}(\Gamma)\,, \end{cases} \qquad (7.18)$$

$$\begin{cases} c(\mathbf{u}; k, \psi) + a(\nu + \nu_t\sigma_k; k, \psi) = \langle S_k, \psi \rangle - (\beta^*\, k\omega, \psi) & \forall\psi \in H_0^1(\Omega) \\[2mm] \langle k, s_k \rangle_\Gamma = \langle g_k, s_k \rangle_\Gamma & \forall\, s_k \in H^{-1/2}(\Gamma) \\[2mm] c(\mathbf{u}; \omega, \phi) + a(\nu + \nu_t\sigma_\omega; \omega, \phi) = \langle \alpha\, S_\omega, \phi \rangle - (\beta\, \omega^2, \phi) & \forall\phi \in H_0^1(\Omega) \\[2mm] \langle \omega, s_w \rangle_\Gamma = \langle g_w, s_w \rangle_\Gamma & \forall s_w \in \mathbf{H}^{-1/2}(\Gamma)\,, \end{cases} \qquad (7.19)$$

where

$$\nu_t(k, \omega) = \min\left\{\frac{k}{\omega}, \nu_{max}\right\} \tag{7.20}$$

$$S_k(\mathbf{u}, k, \omega) = \min\left\{\nu_t \frac{\mathbf{S}^2(\mathbf{u})}{2}, \beta^* \omega\, k_{max,v}\right\} \tag{7.21}$$

$$S_\omega(\mathbf{u}, k, \omega) = \min\left\{\frac{\mathbf{S}^2(\mathbf{u})}{2}, \frac{\beta \omega_{max,v}^2}{\alpha}\right\}. \tag{7.22}$$

Existence and uniqueness results for solutions of the system (7.18) are contained in the following theorem; see, e.g., [44, 109].

Theorem 1. *Let Ω be an open, bounded set with Lipschitz-continuous boundary Γ. Let ν_t be a non-negative function in $L^\infty(\Omega)$, $\mathbf{f} \in \mathbf{H}^{-1}(\Omega)$ and $\mathbf{g}_u \in \mathbf{H}^1(\Omega)$. Then,*

i) there exists at least one solution $(\mathbf{u}, p) \in \mathbf{H}^1(\Omega) \times L^2(\Omega)$ of (7.18); and

ii) if

$$\nu > \nu_0(\Omega, \mathbf{f}, \mathbf{g}_u) \tag{7.23}$$

for some positive ν_0 whose value is determined by the given data, then the set of solutions of (7.18) consists of a single element.

Note that solutions of (7.18) exist for any value of the Reynolds number. However, ii) implies that uniqueness can be guaranteed only for "large enough" values of ν or for "small enough" data $\mathbf{f}$ and $\mathbf{g}_u$.

For the k-ω turbulence system we have a similar result for the existence of solutions to the non linear set of equations (7.19).

Theorem 2. *Let Ω be an open, bounded set with Lipschitz-continuous boundary Γ. Let $\mathbf{u}$ be in $\mathbf{V}(\Omega)$, g_k and g_ω in $H^1(\Omega) \cap L^\infty(\Omega)$ and ν_t, S_k, S_ω as in (7.20)-(7.22). Then,*

i) there exists at least one solution $(k, \omega) \in H^1(\Omega) \cap L^\infty(\Omega) \times H^1(\Omega) \cap L^\infty(\Omega)$ of (7.19);

ii) let $\omega_{max,v}$ and $k_{max,v}$ be positive real constants, and

$$k_{sup} = \sup\left\{\sup_\Gamma\{g_k\}, k_{max,v}\right\}$$

$$\omega_{inf} = \inf\left\{\inf_\Gamma\{g_\omega\}, \inf_\Omega\{\sqrt{\alpha S_\omega/\beta}\}\right\} \tag{7.24}$$

$$\omega_{sup} = \sup\left\{\sup_\Gamma\{g_\omega\}, \omega_{max,v}\right\}],$$

then

$$0 \leq k \leq k_{sup} \,, \tag{7.25}$$

$$0 \leq \omega_{inf} \leq \omega \leq \omega_{sup} \,. \tag{7.26}$$

Proof. Due to the theorem assumptions the proof of i) follows from standard techniques, see [38, 84, 97] for details. Therefore let us suppose that there is a solution $(k, \omega) \in H^1(\Omega) \times H^1(\Omega)$ and prove that $(k, \omega) \in L^\infty(\Omega) \times L^\infty(\Omega)$ with the bounds in ii).

The proof follows the basic framework for the maximum principle and the material in [84, 97]. Let $\phi \in H_0^1(\Omega)$ that can be decomposed as

$$\phi = \phi^+ - \phi^- \qquad \phi^+ = \sup(\phi, 0) \qquad \phi^- = \sup(-\phi, 0) \,. \tag{7.27}$$

A well known result in [105] states that both ϕ^+ and ϕ^- are in $H_0^1(\Omega)$ and are orthogonal, which means

$$(\phi^+, \phi^-) = (\nabla \phi^+, \nabla \phi^-) = 0 \,. \tag{7.28}$$

Furthermore if $\phi^- = 0$ then $\phi \geq 0$ or if $\phi^+ = 0$ then $\phi \leq 0$.

In order to prove the boundedness of k and ω we define $\widetilde{k}$ and $\widetilde{\omega}$ as

$$\tilde{k} = \begin{cases} k_{inf} & \text{if} \quad k \leq k_{inf} \\ k & \text{if} \quad k_{inf} \leq k \leq k_{sup} \\ k_{sup} & \text{if} \quad k \geq k_{sup} \end{cases} \,, \tag{7.29}$$

$$\widetilde{\omega} = \begin{cases} \omega_{inf} & \text{if} \quad \omega \leq \omega_{inf} \\ \omega & \text{if} \quad \omega_{inf} \leq \omega \leq \omega_{sup} \\ \omega_{sup} & \text{if} \quad \omega \geq \omega_{inf} \end{cases} \,, \tag{7.30}$$

with $k_{inf} = 0$. The $\widetilde{k}$ and $\widetilde{\omega}$ are the same functions as k and ω inside the proposed limits.

Now we introduce a similar k-ω problem where the non linear terms are regularized by $\widetilde{k}$ and $\widetilde{\omega}$ and prove that $\widetilde{k} = k$ and $\widetilde{\omega} = \omega$ are indeed solutions of the problem. We consider the following regularized problem

$$\begin{cases} c(\mathbf{u}; k, \psi) + a(\nu + \widetilde{\nu}_t \sigma_k; k, \psi) = \langle \widetilde{S_k}, \psi \rangle - (\beta^* \widetilde{k} \widetilde{\omega}, \psi) & \forall \psi \in H_0^1(\Omega) \\ \langle k, s_k \rangle_\Gamma = \langle g_k, s_k \rangle_\Gamma & \forall \, s_k \in H^{-1/2}(\Gamma) \\ c(\mathbf{u}; \omega, \phi) + a(\nu + \widetilde{\nu}_t \sigma_\omega; \omega, \phi) = \langle \alpha \, \widetilde{S_\omega}, \phi \rangle - (\beta \, \widetilde{\omega}^2, \phi) & \forall \phi \in H_0^1(\Omega) \\ \langle \omega, s_w \rangle_\Gamma = \langle g_w, s_w \rangle_\Gamma & \forall s_w \in \mathbf{H}^{-1/2}(\Gamma) \,, \end{cases} \tag{7.31}$$

where $\widetilde{\nu}_t = \nu_t(\widetilde{k}, \widetilde{\omega})$, $\widetilde{S}_k = S_k(\mathbf{u}, \widetilde{k}, \widetilde{\omega})$ and $\widetilde{S}_\omega = S_\omega(\mathbf{u}, \widetilde{k}, \widetilde{\omega})$. The problem (7.31) is the same as problem (7.19) inside the proposed interval.

We have that $\omega - \omega_{inf} = (\omega - \omega_{inf})^+ - (\omega - \omega_{inf})^-$ where $()^-$ and $()^+$ are the negative and positive operator functions respectively. Since $(\omega - \omega_{inf})^- \in H_0^1(\Omega)$ we can consider $-(\omega - \omega_{inf})^-$ as test function and obtain

$$c(\mathbf{u}; \omega, -(\omega - \omega_{inf})^-) = c(\mathbf{u}; -(\omega - \omega_{inf})^-, -(\omega - \omega_{inf})^-) = 0 \qquad (7.32)$$
$$a(\nu + \widetilde{\nu}_t \sigma_k; \omega, -(\omega - \omega_{inf})^-) = \qquad\qquad\qquad\qquad (7.33)$$
$$a(\nu + \widetilde{\nu}_t \sigma_k; -(\omega - \omega_{inf})^-, -(\omega - \omega_{inf})^-).$$

From (7.22), since $\omega_{inf}^2 \leq \inf_\Omega \{\alpha \widetilde{S}_\omega / \beta\}$ and $S_\omega(\mathbf{u}, \widetilde{k}, \widetilde{\omega}) \geq \omega_{inf}^2 \beta / \alpha$ for all $\widetilde{k}$ and $\widetilde{\omega}$, we have

$$(\alpha \widetilde{S}_\omega, -(\omega - \omega_{inf})^-) - (\beta \widetilde{\omega}^2, -(\omega - \omega_{inf})^-) = \qquad (7.34)$$
$$(\alpha \widetilde{S}_\omega - \beta \omega_{inf}^2, -(\omega - \omega_{inf})^-) \leq 0,$$

which implies

$$a(\nu + \widetilde{\nu}_t \sigma_k; (\omega - \omega_{inf})^-, (\omega - \omega_{inf})^-) \leq 0, \qquad (7.35)$$

and $(\omega - \omega_{inf})^- = 0$. Therefore we have $0 \leq \omega_{inf} \leq \omega$.
In a similar way using $(\omega - \omega_{sup})^+ \in H_0^1(\Omega)$ as test function we obtain

$$c(\mathbf{u}; \omega, (\omega - \omega_{sup})^+) = c(\mathbf{u}; (\omega - \omega_{sup})^+, (\omega - \omega_{sup})^+) = 0 \qquad (7.36)$$
$$a(\nu + \widetilde{\nu}_t \sigma_k; \omega, (\omega - \omega_{sup})^+) = a(\nu + \widetilde{\nu}_t \sigma_k; (\omega - \omega_{sup})^+, (\omega - \omega_{sup})^+). \qquad (7.37)$$

From (7.22), since $\omega_{sup}^2 \geq \sup_\Omega \{\alpha \widetilde{S}_\omega / \beta\}$ then $S_\omega(\mathbf{u}, \widetilde{k}, \widetilde{\omega}) \leq \omega_{sup}^2 \beta / \alpha$ for all $\widetilde{k}$ and $\widetilde{\omega}$, we have

$$(\alpha \widetilde{S}_\omega, (\omega - \omega_{sup})^+) - (\beta \widetilde{\omega}^2, (\omega - \omega_{sup})^+) = \qquad (7.38)$$
$$(\alpha \widetilde{S}_\omega - \beta \omega_{sup}^2, (\omega - \omega_{sup})^+) \leq 0,$$

which implies

$$a(\nu + \widetilde{\nu}_t \sigma_k; (\omega - \omega_{sup})^+, (\omega - \omega_{sup})^+) \leq 0, \qquad (7.39)$$

and $(\omega - \omega_{sup})^+ = 0$ or $\omega \leq \omega_{sup}$. This implies $\omega_{inf} \leq \omega \leq \omega_{sup}$ and $\omega = \widetilde{\omega} \in [\omega_{inf}, \omega_{sup}]$.

By following the same procedure as done for ω, we can prove that the turbulent kinetic energy k should be equal to $\widetilde{k}$. We can use $-(k - k_{inf})^- \in H_0^1(\Omega)$ as test function and obtain

$$c(\mathbf{u}; k, -(k - k_{inf})^-) = c(\mathbf{u}; -(k - k_{inf})^-, -(k - k_{inf})^-) = 0 \qquad (7.40)$$
$$a(\nu + \widetilde{\nu}_t \sigma_k; k, -(k - k_{inf})^-) = \qquad\qquad\qquad\qquad (7.41)$$
$$a(\nu + \widetilde{\nu}_t \sigma_k; -(k - k_{inf})^-, -(k - k_{inf})^-).$$

Since $k_{inf} = 0$ and $\widetilde{S}_k \geq 0$ then

$$(\widetilde{S}_k, -(k - k_{inf})^-) - (\beta^* \widetilde{k}\widetilde{\omega}, -(k - k_{inf})^-) = (\widetilde{S}_k, -k^-) \leq 0, \qquad (7.42)$$

which implies

$$a(\nu + \widetilde{\nu}_t \sigma_k; k^-, (k)^-) \leq 0, \qquad (7.43)$$

and $(k)^- = 0$ or $k \geq 0$.

Finally if we use $(k - k_{sup})^+ \in H_0^1(\Omega)$ as test function we have

$$c(\mathbf{u}; k, (k - k_{sup})^+) = c(\mathbf{u}; (k - k_{sup})^+, (k - k_{sup})^+) = 0 \qquad (7.44)$$
$$a(\nu + \widetilde{\nu}_t \sigma_k; k, (k - k_{sup})^+) = a(\nu + \widetilde{\nu}_t \sigma_k; (k - k_{sup})^+, (k - k_{sup})^+). \qquad (7.45)$$

From (7.24), since $\beta^* k_{sup} \widetilde{\omega} \geq \sup_\Omega\{\widetilde{S}_k\}$ then $\widetilde{S}_k \leq \beta^* k_{sup} \widetilde{\omega}$ we have

$$(\widetilde{S}_k, (k - k_{sup})^+) - (\beta \widetilde{k}\widetilde{\omega}, (k - k_{sup})^+) = \qquad (7.46)$$
$$(\widetilde{S}_k - \beta k_{sup}\widetilde{\omega}, (k - k_{sup})^+) \leq 0,$$

which implies

$$a(\nu + \widetilde{\nu}_t \sigma_k; (k - k_{sup})^+, (k - k_{sup})^+) \leq 0, \qquad (7.47)$$

and $(k - k_{sup})^+ = 0$ or $k \leq k_{sup}$. This implies $0 \leq k \leq k_{sup}$ and $k = \widetilde{k} \in [0, k_{sup}]$. $\qquad\square$

We remark that $\omega_{inf} = \inf\left\{\inf_\Gamma\{g_\omega\}, \inf_\Omega\{\sqrt{\alpha S_\omega/\beta}\}\right\}$ is zero if there is a region where $S^2(\mathbf{u}) = \mathbf{0}$. In this case, which is very usual, we have $k \in [0, k_{sup}]$ and $\omega \in [0, \omega_{sup}]$. With these bounds the ratio $\nu_t = k/\omega$ is non-negative but may be unbounded. The total kinematic viscosity $\nu + \nu_t$ is strictly positive. In order to have $\nu_t \in L^\infty(\Omega)$ the turbulence viscosity must be bounded by ν_{max} when ω vanishes.

By using the previous theorems we can prove an important result of the associated boundary value problem.

Theorem 3. *There exists a solution $(\mathbf{u}, p, k, \omega)$ of the associated boundary value problem in (7.18)-(7.22).*

Proof. The proof is obtained with standard techniques that can be found in [97]. We briefly describe the most important steps. In order to simplify the notation we assume $\mathbf{g}_u = \mathbf{0}$ and $g_k = g_\omega = 0$. Let $(\mathbf{u}_1, k_1, \omega_1) \in \mathbf{H}_0^1 \times H_0^1 \times H_0^1$

be given. Let $(\mathbf{u}_\eta, p_\eta)$ and (k_η, ω_η) be the state of the following Navier-Stokes-k-ω split problem

$$
\begin{aligned}
a(\nu + \nu_{t1}; \mathbf{u}_\eta, \mathbf{v}) + c(\mathbf{u}_1; \mathbf{u}_\eta, \mathbf{v}) + b(\mathbf{v}, p_\eta) &= \langle \mathbf{f}, \mathbf{v} \rangle && \forall\, \mathbf{v} \in \mathbf{H}_0^1(\Omega) \\
b(\mathbf{u}_\eta, q) &= 0 && \forall\, q \in L_0^2(\Omega) \quad (7.48) \\
c(\mathbf{u}_1; k_\eta, \psi) + a(\nu + \nu_{t1}\sigma_k; k_\eta, \psi) &= \langle S_{k1}, \psi \rangle - (\beta^* k_\eta \omega_\eta, \psi) && \forall \psi \in H_0^1(\Omega) \\
c(\mathbf{u}_1; \omega_\eta, \phi) + a(\nu + \nu_{t1}\sigma_\omega; \omega_\eta, \phi) &= \langle \alpha\, S_{\omega 1}, \phi \rangle - (\beta\, \omega_\eta \omega_\eta, \phi) && \forall \phi \in H_0^1(\Omega)
\end{aligned}
$$

where $\nu_{t1} = \nu_t(k_1, \omega_1)$, $S_{k1} = S_k(\mathbf{u_1}, k_1, \omega_1)$ and $S_{\omega 1} = S_\omega(\mathbf{u_1}, k_1, \omega_1)$. By using standard techniques and Theorem 2 we can prove the existence of a solution of the split system (7.48). Since $\|\nu_{t1}\|_\infty \leq \nu_{max}$ then $\|\mathbf{u}_\eta\|_1$ and $\|p_\eta\|_0$ are bounded uniformly by the constants C_u and C_p, respectively, for any $\mathbf{u}_1$ and ν_{t1}. By using Theorem 2 also $\|k_\eta\|_1$ and $\|\omega_\eta\|_1$ are uniformly bounded by the constants C_k and C_ω as functions of the given values $k_{max,v}$ and $\omega_{max,v}$.

Consider now the following mapping

$$
\mathcal{T} : \mathbf{D} = \mathbf{H}_0^1 \times H_0^1 \times H_0^1 \to \mathbf{A} = \mathbf{H}_0^1 \times H_0^1 \times H_0^1 \qquad (7.49)
$$
$$
\begin{cases}
\mathbf{u}_\eta = \mathbf{u}_\eta(\mathbf{u}_1, k_1, \omega_1) \\
k_\eta = k_\eta(\mathbf{u}_1, k_1, \omega_1) \\
\omega_\eta = \omega_\eta(\mathbf{u}_1, k_1, \omega_1).
\end{cases}
$$

We endow the product space $\mathbf{H}_0^1 \times H_0^1 \times H_0^1$ with the norm $\|(\mathbf{u}_1, k_1, \omega_1)\| = \|\mathbf{u}_1\| + \|k_1\| + \|\omega_1\|$. By using standard techniques it is possible to show that (7.49) is a continuous mapping with respect to this norm. For similar proofs see [97]. Let R denote the constant $R = C_u + C_k + C_\omega$ and let B_R be the ball of radius R. Since for all $(\mathbf{u}_1, k_1, \omega_1) \in \mathbf{D}$ we have $\|(\mathbf{u}_\eta, k_\eta, \omega_\eta)\| = \|\mathbf{u}_\eta\| + \|k_\eta\| + \|\omega_\eta\| < C_u + C_k + C_\omega = R$ then

$$
\mathcal{T}(\mathbf{B}_R) \subset \mathbf{B}_R. \qquad (7.50)
$$

Now we can use the Schauder fixed point theorem in order to prove the existence of the fixed point $(\mathbf{u}_1, k_1, \omega_1) = (\mathbf{u}_\eta, k_\eta, \omega_\eta)$ in the mapping $\mathcal{T}$. We recall briefly the theorem. Let $\mathbf{D}$ be a separated topological vector space, $\mathbf{B}_R \subset \mathbf{D}$ a convex subset, and $\mathcal{T}(\mathbf{B}_R) \to \mathbf{B}_R$ a continuous function on $\mathbf{B}_R$, equipped with the topology inherited from $\mathbf{D}$. Also let $\mathcal{T}(\mathbf{B}_R)$ be a compact subset of $\mathbf{B}_R$. Then $\mathcal{T}$ has a fixed point, namely, there exists $\mathbf{x} \in \mathbf{B}_R$ such that $\mathcal{T}(\mathbf{x}) = \mathbf{x}$. The theorem follows from the compactness of $\mathbf{B}_R$, which can be proven with standard techniques, see for example [97]. $\qquad \square$

7.2   Control problem

After having proven the existence of solution to the RANS equations coupled with the k-ω system with the bounds defined above, we can now study the optimal control problem. Given the extended boundary functions $g_k \in H^1(\Omega) \cap L^\infty(\Omega)$ and $g_\omega \in H^1(\Omega) \cap L^\infty(\Omega)$ and the positive constants $k_{max,v}$, $\omega_{max,v}$, ν_{max} we can define k_{sup}, ω_{sup} and ω_{inf}. The set of all admissible functions k and ω is determined by

$$\mathcal{Q}_{ad} = \big\{ (k,\omega) \in H^1(\Omega) \times H^1(\Omega) \mid \tag{7.51}$$
$$0 \le \omega_{inf} \le \omega \le \omega_{sup} \ \text{ and } 0 \le k \le k_{sup} \big\},$$

and set of all admissible functions ν_t by

$$\mathcal{H}_{ad} = \big\{ \nu_t \in L^2(\Omega) \mid \ \text{ such that } \nu_t \in [0, \nu_{max}] \big\}. \tag{7.52}$$

The optimal control problem can then be stated in the following way

Given g_k, $g_\omega \in H^1(\Omega) \cap L^\infty(\Omega) \subset \mathcal{Q}_{ad}$ and $\mathbf{g}_u \in \mathbf{H}^1(\Omega)$, find the control $\widehat{\mathbf{f}} \in L^2(\Omega)$ and $(\widehat{\mathbf{u}}, \widehat{p}, \widehat{k}, \widehat{\omega}, \widehat{\nu}_t, \widehat{S}_k, \widehat{S}_\omega)$ such that

$$\mathcal{J}(\widehat{\mathbf{u}}, \widehat{k}, \widehat{\mathbf{f}}) \le \mathcal{J}(\mathbf{u}, k, \mathbf{f}) \tag{7.53}$$

for all $(\mathbf{u}, p, k, \omega, \nu_t, S_k, S_\omega) \in \mathbf{H}^1(\Omega) \times L_0^2(\Omega) \times \mathcal{Q}_{ad} \times L^2(\Omega) \times L^2(\Omega) \times L^2(\Omega)$ satisfying the constraints (7.18)-(7.22) and the objective functional (7.1).

The admissible set of states and controls is given by

$$\mathcal{A}_{ad} = \{(\mathbf{u}, p, k, \omega, \nu_t, S_k, S_\omega, \mathbf{f}) \in$$
$$\mathbf{V}(\Omega) \times L_0^2(\Omega) \times \mathcal{Q}_{ad} \times L^2(\Omega) \times L^2(\Omega) \times L^2(\Omega) \times \mathbf{H}^{-1}(\Omega)$$
$$\text{such that } \mathcal{J}(\mathbf{u}, k, \mathbf{f}) < \infty \text{ and}$$
$$(\mathbf{u}, k, \omega, \mathbf{f}) \text{ satisfies (7.18)-(7.22) and (7.1)}\}.$$

We now turn to the question of the existence of optimal solutions for the problem in (7.53).

Theorem 4. *There exists at least one optimal solution $(\widehat{\mathbf{u}}, \widehat{p}, \widehat{k}, \widehat{\omega}, \widehat{\nu}_t, \widehat{S}_k, \widehat{S}_\omega, \widehat{\mathbf{f}}) \in \mathcal{A}_{ad}$ of the optimal control problem (7.53).*

Proof. The proof follows from standard techniques (see, e.g., [16] or [45]) and here we sketch the main idea. Let $\mathbf{f} = \mathbf{0}$ then we can solve the flow system $(\mathbf{u}, p, k, \omega, \nu_t, S_k, S_\omega, \mathbf{0})$. Since the set of admissible solutions $\mathcal{A}_{ad}$ is not

empty and the set of the values assumed by the functional is bounded from below, there exists a minimizing sequence $(\mathbf{u}_m, p_m, k_m, \omega_m, \nu_{tm}, S_{km}, S_{\omega m}, \mathbf{f}_m)$ in $\mathbf{V}(\Omega) \times L_0^2(\Omega) \times \mathcal{Q}_{ad} \times L^2(\Omega) \times L^2(\Omega) \times L^2(\Omega) \times \mathbf{H}^{-1}(\Omega)$. The sequences ν_{tm}, $S_{km}, S_{\omega m}$ are uniformly bounded in $L^2(\Omega)$ by construction. If the turbulence source terms $S_{km}, S_{\omega m}$ are bounded then also sequences k_m, ω_m are uniformly bounded in $\mathbf{H}^1(\Omega)$. Furthermore the functional value for the solution $\mathbf{f} = \mathbf{0}$ is a uniform bound for $\mathbf{u}_m$ and $\mathbf{f}_m$. Using a standard argument, we can extract sub sequences $(\mathbf{u}_n, p_n, k_n, \omega_n, \nu_{tn}, S_{kn}, S_{\omega n}, \mathbf{f}_n)$ that converge weakly to $(\widehat{\mathbf{u}}, \widehat{p}, \widehat{k}, \widehat{\omega}, \widehat{\nu}_t, \widehat{S}_k, \widehat{S}_\omega, \widehat{\mathbf{f}})$ [16, 45, 97]. By standard argument we can pass to the limit inside the linear and the nonlinear terms to prove that this satisfies the constraints. For details on Navier-Stokes one can see [45, 97] and for details on turbulence equations [97]. $\qquad\square$

In order to compute the optimal solution, we introduce the Lagrange multiplier method and define the optimality system.

7.2.1 The Lagrange multiplier method

In this section we show that the Lagrange multiplier technique is well posed and can be used to obtain the first-order necessary condition. Further, the Lagrangian map can be shown to be strictly differentiable for all values of the external force and this allows us to apply the Lagrange multiplier method to a wider range of problems and completes the theoretical treatment of the problem for arbitrary values of the viscosity. Also, this method gives a different and better theoretical insight into the control process, allowing us to write the inequality constraints in a different form.

First, we introduce auxiliary variables that allow us to transform the inequality constraints into equalities and then invoke well-known techniques for equality constrained minimization problems; see, e.g., [8] or [110]. We begin by replacing

$$\nu_t = \min\left\{\frac{k}{\omega}, \nu_{max}\right\}$$
$$S_k = \min\left\{\frac{\nu_t}{2}\mathbf{S}^2(\mathbf{u}), \beta^* k_{max,v}\omega\right\} \qquad (7.54)$$
$$S_\omega = \min\left\{\frac{1}{2}\mathbf{S}^2(\mathbf{u}), \frac{\omega_{max,v}^2\beta}{\alpha}\right\},$$

by

$$(k - \nu_t \omega)(\nu_{max} - \nu_t) = 0 \tag{7.55}$$

$$r_\nu^2 - (k - \nu_t \omega) - \omega\,(\nu_{max} - \nu_t) = 0$$

$$(\frac{\nu_t}{2}\mathbf{S}^2(\mathbf{u}) - S_k)(\beta^* k_{max,v}\omega - S_k) = 0 \tag{7.56}$$

$$r_k^2 - (\frac{\nu_t}{2}\mathbf{S}^2(\mathbf{u}) - S_k) - (\beta^* k_{max,v}\omega - S_k) = 0$$

$$(\frac{1}{2}\mathbf{S}^2(\mathbf{u}) - S_\omega)(\frac{\omega_{max,v}^2\beta}{\alpha} - S_\omega) = 0 \tag{7.57}$$

$$r_\omega^2 - (\frac{1}{2}\mathbf{S}^2(\mathbf{u}) - S_\omega) - (\frac{\omega_{max,v}^2\beta}{\alpha} - S_\omega) = 0\,,$$

for some $r_\nu, r_k, r_\omega \in L^2(\Omega)$. To better understand these constraints let us consider (7.55). If $r_\nu^2 > 0$ then $\nu_t = k/\omega < \nu_{max}$ or $\nu_t = \nu_{max} < k/\omega$ which implies (7.54), and viceversa if $k/\omega < \nu_{max}$ we have $\nu_t = k/\omega$ and $r_\nu^2 = (\nu_{max} - \nu_t) > 0$ or $k/\omega > \nu_{max}$ we have $\nu_t = \nu_{max}$ and $r_\nu^2 = (k - \nu_{max}\omega) > 0$. If $r_\nu^2 = 0$ then $\nu_t = \nu_{max} = k/\omega$. The same remark is true for the inequalities (7.56)-(7.57).

Now we compact all the constraint equations and the functional in two mappings in order to study their differential properties. It is convenient to define the following functional spaces

$$\widehat{\mathbf{B}}_1 = \mathbf{H}_0^1(\Omega) \times L_0^2(\Omega) \times \mathbf{L}^2(\Omega) \times \mathcal{Q}_{ad} \times \tag{7.58}$$
$$L^2(\Omega) \times L^2(\Omega)^2 \times (L^2(\Omega))^3\,,$$

$$\widehat{\mathbf{B}}_2 = \mathbf{H}^{-1}(\Omega) \times L_0^2(\Omega) \times \mathbf{H}^{1/2}(\Gamma) \times H^{-1}(\Omega) \times H^{1/2}(\Gamma) \times \tag{7.59}$$
$$H^{-1}(\Omega) \times H^{1/2}(\Gamma) \times L^1(\Omega)^6\,,$$

$$\widehat{\mathbf{B}}_3 = \mathbf{H}^{-1}(\Omega) \times L_0^2(\Omega) \times \mathbf{H}^{1/2}(\Gamma) \times H^{-1}(\Omega) \times H^{1/2}(\Gamma) \times \tag{7.60}$$
$$H^{-1}(\Omega) \times H^{1/2}(\Gamma) \times L^1(\Omega)^6\,,$$

and equip $\widehat{\mathbf{B}}_1$, $\widehat{\mathbf{B}}_2$ and $\widehat{\mathbf{B}}_3$ with the usual graph norms for the product spaces involved. The functional space $\widehat{\mathbf{B}}_1$ is set for the state variables $\widehat{\mathbf{b}} = (\widehat{\mathbf{u}}, \widehat{p}, \widehat{\mathbf{f}}, \widehat{k}, \widehat{\omega}, \widehat{\nu}_t, \widehat{S}_k, \widehat{S}_\omega, \widehat{r}_\nu, \widehat{r}_k, \widehat{r}_\omega)$. With this notation the constraints of the problem can be used to form the nonlinear mapping M from $\widehat{\mathbf{B}}_1$ to $\widehat{\mathbf{B}}_3$ defined by

$$M(\widehat{\mathbf{b}}) = \widehat{\mathbf{b}}^*$$

if and only if

$$
\begin{cases}
a(\nu + \nu_t; \widehat{\mathbf{u}}, \widehat{\mathbf{v}}) + c(\widehat{\mathbf{u}}; \widehat{\mathbf{u}}, \widehat{\mathbf{v}}) + b(\widehat{\mathbf{v}}, \widehat{p}) - \\
\qquad \int_\Omega \widehat{\mathbf{f}} \cdot \widehat{\mathbf{v}} \, d\mathbf{x} = \int_\Omega \mathbf{l}_1 \cdot \widehat{\mathbf{v}} \, d\mathbf{x} & \forall \widehat{\mathbf{v}} \in \mathbf{H}_0^1(\Omega) \\
b(\widehat{\mathbf{u}}, \widehat{z}) = \int_{\widehat{\Omega}} l_2 \, \widehat{z} \, d\mathbf{x} & \forall \widehat{z} \in L_0^2(\Omega) \\
\int_\Gamma (\widehat{\mathbf{u}} - \mathbf{g}_u) \cdot \widehat{\mathbf{s}}_u \, ds = \int_\Gamma \mathbf{l}_3 \cdot \widehat{\mathbf{s}}_u \, ds & \forall \widehat{\mathbf{s}}_u \in \mathbf{H}^{-1/2}(\Gamma) \\
a(\nu + \nu_t \sigma_k; \widehat{k}, \widehat{\phi}) + c(\widehat{u}; \widehat{k}, \widehat{\phi}) - \langle S_k, \widehat{\phi} \rangle + \langle \beta^* k\omega, \widehat{\phi} \rangle = \\
\qquad \int_\Omega l_4 \widehat{\phi} \, d\mathbf{x} & \forall \widehat{\phi} \in H_0^1(\Omega) \\
\int_\Gamma (\widehat{k} - g_k) \, \widehat{s}_k \, ds = \int_\Gamma l_5 \, \widehat{s}_k \, ds & \forall \widehat{s}_k \in \mathbf{H}^{-1/2}(\Gamma) \\
a(\nu + \nu_t \sigma_\omega; \widehat{\omega}, \widehat{\psi}) + c(\widehat{u}; \widehat{\omega}, \widehat{\psi}) - \alpha \, \langle S_\omega, \widehat{\psi} \rangle + \langle \beta \, \omega^2, \widehat{\psi} \rangle = \\
\qquad \int_\Omega l_6 \widehat{\psi} \, d\mathbf{x} & \forall \widehat{\psi} \in H_0^1(\Omega) \\
\int_\Gamma (\widehat{\omega} - g_\omega) \, \widehat{s}_w \, ds = \int_\Gamma l_7 \, \widehat{s}_w \, ds & \forall \widehat{s}_w \in \mathbf{H}^{-1/2}(\Gamma)
\end{cases}
\tag{7.61}
$$

$$
\begin{cases}
(\widehat{k} - \widehat{\nu}_t \widehat{\omega})(\nu_{max} - \widehat{\nu}_t) = l_{\nu 0} & \forall \mathbf{x} \in \Omega \\
\widehat{r}_\nu^2 - (\widehat{k} - \widehat{\nu}_t \widehat{\omega}) - \widehat{\omega}(\nu_{max} - \widehat{\nu}_t) = l_{\nu 1} & \forall \mathbf{x} \in \Omega \\
(\frac{\widehat{\nu}_t}{2} \mathbf{S}^2(\widehat{\mathbf{u}}) - \widehat{S}_k)(\beta^* k_{max,v} \widehat{\omega} - \widehat{S}_k) = l_{k0} & \forall \mathbf{x} \in \Omega \\
\widehat{r}_k^2 - (\frac{\widehat{\nu}_t}{2} \mathbf{S}^2(\widehat{\mathbf{u}}) - \widehat{S}_k) - (\beta^* k_{max,v} \widehat{\omega} - \widehat{S}_k) = l_{k1} & \forall \mathbf{x} \in \Omega \\
(\frac{1}{2} \mathbf{S}^2(\widehat{\mathbf{u}}) - \widehat{S}_\omega)(\frac{\omega_{max,v}^2 \beta}{\alpha} - \widehat{S}_\omega) = l_{\omega 0} & \forall \mathbf{x} \in \Omega \\
\widehat{r}_\omega^2 - (\frac{1}{2} \mathbf{S}^2(\widehat{\mathbf{u}}) - \widehat{S}_\omega) - (\frac{\omega_{max,v}^2 \beta}{\alpha} - \widehat{S}_\omega) = l_{\omega 1} & \forall \mathbf{x} \in \Omega
\end{cases}
,
$$

with $\widehat{\mathbf{b}}^* = (\mathbf{l}_1, l_2, \mathbf{l}_3, l_4, l_5, l_6, l_7, \mathbf{l}_\nu, \mathbf{l}_k, \mathbf{l}_\omega) \in \widehat{\mathbf{B}}_3$. The set of constraint equations in the optimal control problem can be expressed as

$$
M(\widehat{\mathbf{b}}) = \mathbf{0} \,.
$$

Given $\widehat{\mathbf{b}} \in \mathcal{A}_{ad}$, we define another nonlinear mapping $Q : \widehat{\mathbf{B}}_1 \to \Re \times \widehat{\mathbf{B}}_2$ by

$Q(\widehat{\mathbf{b}}) = \widehat{\mathbf{b}}^*$ if and only if

$$\begin{pmatrix} \mathcal{J}(\widehat{\mathbf{u}}, \widehat{k}, \widehat{\mathbf{f}}) - \mathcal{J}(\mathbf{u}_1, k_1, \mathbf{f}_1) \\ M(\widehat{\mathbf{b}}) \end{pmatrix} = \begin{pmatrix} a_1 \\ \widehat{\mathbf{b}}^* \end{pmatrix}. \tag{7.62}$$

7.2.2 Differentiability

These mappings are strictly differentiable, as it is shown in the following lemma. We recall the notion of strict differentiability (see [110]). Let X and Y denote Banach spaces, then the mapping $\varphi : X \to Y$ is strictly differentiable at $x \in X$ if there exists a bounded, linear mapping D from X to Y such that for any $\epsilon > 0$ there exists a $\delta > 0$ such that whenever $\|x - x_1\|_X < \delta$ and $\|x - x_2\|_X < \delta$ for $x_1, x_2 \in X$, then

$$\|\varphi(x_1) - \varphi(x_2) - D(x_1 - x_2)\|_Y \leq \epsilon \|x_1 - x_2\|_X. \tag{7.63}$$

The strict derivative D at the point $x \in X$, if it exists, will often be denoted by $D = \varphi'(x)$. The value of this mapping on an element $\widetilde{x} \in X$ will often be denoted by $\varphi'(x) \cdot \widetilde{x}$. In the next theorem we can identify $X = \widehat{\mathbf{B}}_1$ and $Y = \widehat{\mathbf{B}}_2$.

Lemma 1. *Let the nonlinear mappings $M : \widehat{\mathbf{B}}_1 \to \widehat{\mathbf{B}}_2$ and $Q : \widehat{\mathbf{B}}_1 \to \Re \times \widehat{\mathbf{B}}_2$ be defined by (7.61) and (7.62), respectively. Then, these mappings are strictly differentiable at the point $\widehat{\mathbf{b}} = (\widehat{\mathbf{u}}, \widehat{p}, \widehat{\mathbf{f}}, \widehat{k}, \widehat{\omega}, \widehat{\nu}_t, \widehat{S}_k, \widehat{S}_\omega, \widehat{r}_\nu, \widehat{r}_k, \widehat{r}_\omega) \in \widehat{\mathbf{B}}_1$ and its strict derivative is given by the bounded linear operator $M'(\widehat{\mathbf{b}}) : \widehat{\mathbf{B}}_1 \to \widehat{\mathbf{B}}_2$, where*

$$M'(\widehat{\mathbf{b}}) \cdot \widetilde{\mathbf{b}} = \overline{\mathbf{b}}$$

for all $\widetilde{\mathbf{b}} = (\widetilde{\mathbf{u}}, \widetilde{p}, \widetilde{\mathbf{f}}, \widetilde{k}, \widetilde{\omega}, \widetilde{\nu}_t, \widetilde{S}_k, \widetilde{S}_\omega, \widetilde{r}_\nu, \widetilde{r}_k, \widetilde{r}_\omega) \in \widehat{\mathbf{B}}_1$ and $\overline{\mathbf{b}} = (\overline{l}_1, \overline{l}_2, \overline{l}_3, \overline{l}_4, \overline{l}_5,$

$\bar{l}_6, \bar{l}_7, \bar{\mathbf{l}}_\nu, \bar{\mathbf{l}}_k, \bar{\mathbf{l}}_\omega) \in \widehat{\mathbf{B}}_2$ *if and only if*

$$
\begin{cases}
a(\widetilde{\nu}_t; \widehat{\mathbf{u}}, \widehat{\mathbf{v}}) + a(\nu + \nu_t; \widetilde{\mathbf{u}}, \widehat{\mathbf{v}}) + c(\widetilde{\mathbf{u}}; \widehat{\mathbf{u}}, \widehat{\mathbf{v}}) + c(\widehat{\mathbf{u}}; \widetilde{\mathbf{u}}, \widehat{\mathbf{v}}) \\
\qquad + b(\widehat{\mathbf{v}}, \widehat{p}) - \langle \widehat{\mathbf{f}}, \widehat{\mathbf{v}} \rangle = \displaystyle\int_{\widehat{\Omega}} \bar{\mathbf{l}}_1 \cdot \widehat{\mathbf{v}}\, d\mathbf{x} & \forall \widehat{\mathbf{v}} \in \mathbf{H}_0^1(\widehat{\Omega}) \\[4pt]
b(\widetilde{u}, \widehat{z}) = \displaystyle\int_{\widehat{\Omega}} \bar{l}_2\, \widehat{z}\, d\mathbf{x} & \forall \widehat{z} \in L_0^2(\widehat{\Omega}) \\[4pt]
\displaystyle\int_\Gamma (\widetilde{u} - \mathbf{g}_u) \cdot \widehat{s}_u\, ds = \int_\Gamma \bar{\mathbf{l}}_3 \cdot \widehat{s}_u\, ds & \forall \widehat{s}_u \in \mathbf{H}^{-1/2}(\Gamma) \\[2pt]
a(\widetilde{\nu}_t \sigma_k; \widehat{k}, \widehat{\phi}) + a(\nu + \nu_t \sigma_k; \widetilde{k}, \widehat{\phi}) + c(\widetilde{\mathbf{u}}; \widehat{k}, \widehat{\phi}) + \\
\qquad c(\widehat{\mathbf{u}}; \widetilde{k}, \widehat{\phi}) - \langle \widetilde{S}_k, \widehat{\phi} \rangle + \langle \beta^* \widetilde{k} \widehat{\omega}, \widehat{\phi} \rangle + \\
\qquad \langle \beta^* \widehat{k} \widetilde{\omega}, \widehat{\phi} \rangle = \displaystyle\int_\Omega \bar{l}_4 \widehat{\phi}\, d\mathbf{x} & \forall \widehat{\phi} \in H_0^1(\Omega) \\[4pt]
\displaystyle\int_\Gamma \widetilde{k}\, \widehat{s}_k\, ds = \int_\Gamma \bar{l}_5\, \widehat{s}_k\, ds & \forall \widehat{s}_k \in \mathbf{H}^{-1/2}(\Gamma) \\[2pt]
a(\widetilde{\nu}_t \sigma_\omega; \widehat{\omega}, \widehat{\psi}) + a(\nu + \nu_t \sigma_\omega; \widetilde{\omega}, \widehat{\psi}) + c(\widetilde{\mathbf{u}}; \widehat{\omega}, \widehat{\psi}) + c(\widehat{\mathbf{u}}; \widetilde{\omega}, \widehat{\psi}) - \\
\qquad \alpha \langle \widetilde{S}_\omega, \widehat{\psi} \rangle + \langle \beta\, 2 \widehat{\omega} \widetilde{\omega}, \widehat{\psi} \rangle = \displaystyle\int_\Omega \bar{l}_6 \widehat{\psi}\, d\mathbf{x} & \forall \widehat{\psi} \in H_0^1(\Omega) \\[4pt]
\displaystyle\int_\Gamma \widetilde{\omega}\, \widehat{s}_w\, ds = \int_\Gamma \bar{l}_7\, \widehat{s}_w\, ds & \forall \widehat{s}_w \in \mathbf{H}^{-1/2}(\Gamma)
\end{cases}
\tag{7.64}
$$

and for the turbulence sources by

$$
\begin{cases}
(\widetilde{k} - \widetilde{\nu}_t \widehat{\omega} - \widehat{\nu}_t \widetilde{\omega})(\nu_{max} - \widehat{\nu}_t) - \widetilde{\nu}_t(\widehat{k} - \widehat{\nu}_t \widehat{\omega}) = \bar{l}_{\nu 0} & \forall \mathbf{x} \in \Omega \\[4pt]
2\widetilde{r}_\nu \widehat{r}_\nu - (\widetilde{k} - \widetilde{\nu}_t \widehat{\omega} - \widehat{\nu}_t \widetilde{\omega}) + \widehat{\omega} \widetilde{\nu}_t + \widehat{\nu}_t \widetilde{\omega} = \bar{l}_{\nu 1} & \forall \mathbf{x} \in \Omega \\[4pt]
(\dfrac{\widetilde{\nu}_t}{2} \mathbf{S}^2(\widehat{\mathbf{u}}) + \widehat{\nu}_t \mathbf{S}(\widetilde{\mathbf{u}}) : \mathbf{S}(\widehat{\mathbf{u}}) - \widetilde{S}_k)(\beta^* k_{max,v} \widehat{\omega} - \widehat{S}_k) + \\
\qquad (\dfrac{\widehat{\nu}_t}{2} \mathbf{S}^2(\widehat{\mathbf{u}}) - \widehat{S}_k)(\beta^* k_{max,v} \widetilde{\omega} - \widetilde{S}_k) = \bar{l}_{k0} & \forall \mathbf{x} \in \Omega \\[4pt]
2\widetilde{r}_k \widehat{r}_k - (\dfrac{\widetilde{\nu}_t}{2} \mathbf{S}^2(\widehat{\mathbf{u}}) + \widehat{\nu}_t \mathbf{S}(\widetilde{\mathbf{u}}) : \mathbf{S}(\widehat{\mathbf{u}}) - \widetilde{S}_k) - \\
\qquad (\beta^* k_{max,v} \widetilde{\omega} - \widetilde{S}_k) = \bar{l}_{k1} & \forall \mathbf{x} \in \Omega \\[4pt]
(\mathbf{S}(\widetilde{\mathbf{u}}) : \mathbf{S}(\widehat{\mathbf{u}}) - \widetilde{S}_\omega)(\dfrac{\omega_{max,v}^2 \beta}{\alpha} - \widehat{S}_\omega)) - \\
\qquad \widetilde{S}_\omega(\dfrac{1}{2} \mathbf{S}^2(\widehat{\mathbf{u}}) - \widehat{S}_\omega) = \bar{l}_{\omega 0} & \forall \mathbf{x} \in \Omega \\[4pt]
2\widetilde{r}_\omega \widehat{r}_\omega - \mathbf{S}(\widetilde{\mathbf{u}}) : \mathbf{S}(\widehat{\mathbf{u}}) + 2\widetilde{S}_\omega = \bar{l}_{\omega 1} & \forall \mathbf{x} \in \Omega\,.
\end{cases}
\tag{7.65}
$$

Moreover, the strict derivative of Q at a point $\widehat{\mathbf{b}} \in \widehat{\mathbf{B}}_1$ is given by the bounded linear operator $Q'(\widehat{\mathbf{b}}) : \widehat{\mathbf{B}}_1 \to \Re \times \widehat{\mathbf{B}}_2$, where

$$Q'(\widehat{\mathbf{b}}) \cdot \widetilde{\mathbf{b}} = (\bar{a}, \bar{\mathbf{l}}_1, \bar{l}_2, \bar{\mathbf{l}}_3, \bar{l}_4, \bar{l}_5, \bar{l}_6, \bar{l}_7, \bar{\mathbf{l}}_\nu, \bar{\mathbf{l}}_k, \bar{\mathbf{l}}_\omega) \tag{7.66}$$

for all $\widetilde{\mathbf{b}} \in \widehat{\mathbf{B}}_1$ and $(\bar{a}, \bar{\mathbf{l}}_1, \bar{l}_2, \bar{\mathbf{l}}_3, \bar{l}_4, \bar{l}_5, \bar{l}_6, \bar{l}_7, \bar{\mathbf{l}}_\nu, \bar{\mathbf{l}}_k, \bar{\mathbf{l}}_\omega) \in \Re \times \widehat{\mathbf{B}}_2$ if and only if

$$\left(\begin{array}{c} \mathcal{J}'(\widehat{\mathbf{u}}, \widehat{\mathbf{f}}, \widehat{k}, \widehat{\omega}) \cdot (\widetilde{\mathbf{u}}, \widetilde{p}, \widetilde{\mathbf{f}}, \widetilde{k}, \widetilde{\omega}, \widetilde{\nu}_t, \widetilde{S}_k, \widetilde{S}_\omega, \ \widetilde{r}_\nu, \widetilde{r}_k, \widetilde{r}_\omega) \\ M'(\widehat{\mathbf{b}}) \cdot (\widetilde{\mathbf{u}}, \widetilde{p}, \widetilde{\mathbf{f}}, \widetilde{k}, \widetilde{\omega}, \widetilde{\nu}_t, \widetilde{S}_k, \widetilde{S}_\omega, \widetilde{r}_\nu, \widetilde{r}_k, \widetilde{r}_\omega) \end{array} \right) =$$

$$\left(\begin{array}{c} \bar{a} \\ (\bar{\mathbf{l}}_1, \bar{l}_2, \bar{\mathbf{l}}_3, \bar{l}_4, \bar{l}_5, \bar{l}_6, \bar{l}_7, \bar{\mathbf{l}}_\nu, \bar{\mathbf{l}}_k, \bar{\mathbf{l}}_\omega) \end{array} \right),$$

where

$$\mathcal{J}'(\widehat{\mathbf{b}}) \cdot \widetilde{\mathbf{b}} = a \int_\Omega (\widehat{\mathbf{u}} - \mathbf{u}_d) \cdot \widetilde{\mathbf{u}} \, d\mathbf{x} + b \int_\Omega \left(\widehat{k} - k_d \right) \widetilde{k} \, d\mathbf{x} + \lambda \int_{\mathbf{x}} \widehat{\mathbf{f}} \cdot \widetilde{\mathbf{f}} \, d\mathbf{x}.$$

Proof. The linearity of the operator M' is obvious and its boundedness follows from the continuity of the forms $a(\cdot; \cdot, \cdot)$, $b(\cdot, \cdot)$ and $c(\cdot; \cdot, \cdot)$. Likewise, the linearity and boundedness of the operator Q' are obvious. The fact that M' is the strict derivative of the mapping M also follows from the continuity of the trilinear form $c(\cdot; \cdot, \cdot)$ and bilinear form $a(\cdot; \cdot, \cdot)$. Indeed, given $\widehat{\mathbf{b}} = (\widehat{\mathbf{u}}, \widehat{p}, \widehat{\mathbf{f}}, \widehat{k}, \widehat{\omega}, \widehat{\nu}_t, \widehat{S}_k, \widehat{S}_\omega, \widehat{r}_\nu, \widehat{r}_k, \widehat{r}_\omega) \in \widehat{\mathbf{B}}_1$ we have that for any $\epsilon > 0$ and $\widehat{\mathbf{b}}_1, \widehat{\mathbf{b}}_2$ in $\widehat{\mathbf{B}}_1$, such that $\|\widehat{\mathbf{b}} - \widehat{\mathbf{b}}_1\|_{\widehat{\mathbf{B}}_1} < \delta$ and $\|\widehat{\mathbf{b}} - \widehat{\mathbf{b}}_2\|_{\widehat{\mathbf{B}}_1} < \delta$, with appropriate $\delta = \delta(\epsilon)$ we obtain

$$\|M(\widehat{\mathbf{b}}_1) - M(\widehat{\mathbf{b}}_2) - M'(\widehat{\mathbf{b}}) \cdot (\widehat{\mathbf{b}}_1 - \widehat{\mathbf{b}}_2)\|_{\widehat{\mathbf{B}}_2} \le \epsilon \|\widehat{\mathbf{b}}_1 - \widehat{\mathbf{b}}_1\|_{\widehat{\mathbf{B}}_1}.$$

The procedure is standard and the interested reader can see [44, 45, 72, 79] for similar proofs. Thus, the mapping M is strictly differentiable on all of $\widehat{\mathbf{B}}_1$ and its strict derivative is given by M'.

Using the strict differentiability of the mapping M it is then easy to show that the mapping Q is also strictly differentiable and that its strict derivative is given by Q'. $\qquad\square$

In order to prove the closure of the range of M' we need a result that claims the existence of the solution with a convection-diffusion equation of the following type

$$-\nabla \cdot (A\nabla T) + (\mathbf{u} \cdot \nabla)T + bT = f \qquad in \quad \Omega \tag{7.67}$$

$$T = T_1 \qquad on \quad \Gamma \tag{7.68}$$

This operator does not satisfy the coercivity property due to the presence of the convective terms and therefore the usual Lax-Milgram setting cannot be applied. Nevertheless, it is possible to claim the existence of the state solutions for the non-coercive elliptic case if the velocity field $\mathbf{u}$ is in $L^2(\Omega)$ [10, 31]. This existence result is obtained not in the Lax-Milgram setting but by using a Leray-Schauder Topological Degree argument.

Theorem 5. *Let $N_* = N$ when $N \geq 3$, $N_* \in]2, \infty[$ when $N = 2$. Consider the (7.67) with $b \in L^{N_*/2}(\Omega)$, $b \geq 0$ a.e. on Ω, $\mathbf{u} \in \mathbf{L}^{N_*}(\Omega)$, and $f \in (H^{-1}(\Omega))$. If A is a function which satisfies these two properties:*

   1. $\exists \, \alpha_A > 0$ such that $A(x)\xi \cdot \xi \geq \alpha_A |\xi|^2$ for a.e. $x \in \Omega$ and for all $\xi \in \Re$;

   2. $\exists \, \Lambda_A > 0$ such that $|A(x)| \leq \Lambda_A$ for a.e. $x \in \Omega$;

Then, there exists a unique solution $T \in H^1(\Omega)$ of (7.67).

Proof. The proof of this result is based on a Leray-Schauder Topological Degree argument and can be found in [31]. $\qquad\square$

We note that the Navier-Stokes system in (7.2)-(7.3) with Dirichlet boundary conditions has at least one solution $(\mathbf{u}, p) \in \mathbf{H}^1(\Omega) \times L_0^2(\Omega)$. The Sobolev compact embedding theorem implies $\mathbf{H}^1(\Omega) \hookrightarrow \mathbf{L}^q(\Omega)$ which holds for $1 \leq q < \infty$ when $N = 2$ and for $1 \leq q \leq 6$ when $N = 3$. The velocity solution $\mathbf{u} \in \mathbf{H}^1(\Omega)$ verifies the hypothesis in Theorem 5 both with $N = 2$ and with $N = 3$.

We remark also that, if one needs to use the Lax-Milgram setting, existence can be proven by assuming some condition on the velocity field $\mathbf{u}$. For instance, in the case of fully Dirichlet boundary conditions one can have coercivity with

$$-\frac{1}{2}\nabla \cdot \mathbf{u} + b \geq 0 \,. \tag{7.69}$$

This condition of additional regularity on the velocity field is not needed in the Leray-Lions setting [10].

Next, we prove some further properties of the derivatives of the mappings M and Q. It is worthwhile to note that r_ν, r_k and r_ω are zero when the differential equations in k and ω satisfy both limits at the same time. This is not a problem for the optimization if this happens over points or boundary regions with zero measure but it may be a problem if this is verified over domain with positive measure. For this reason let us introduce the following

subsets

$$\Omega_\nu = \left\{ \mathbf{x} \in \Omega \text{ such that } \nu_t = \nu_{max} = k/\omega \right\} \tag{7.70}$$

$$\Omega_{S_k} = \left\{ \mathbf{x} \in \Omega \text{ such that } S_k = \nu_t \mathbf{S}^2(\mathbf{u})/2 = \beta^* k_{max,v}\, \omega \right\} \tag{7.71}$$

$$\Omega_{S_\omega} = \left\{ \mathbf{x} \in \Omega \text{ such that } S_\omega = \mathbf{S}^2(\mathbf{u})/2 = \beta \omega_{max,v}^2/\alpha \right\}. \tag{7.72}$$

We use these sets to assure the validity of the Lagrangian multiplier technique around the region where the minimum point should be searched.

Lemma 2. *Let* $\widehat{\mathbf{b}} \in \widehat{\mathbf{B}}_1$ *denote a solution of the optimal control problem. Then, if the region* $\Omega_\nu \cup \Omega_{S_k} \cup \Omega_{S_\omega}$ *has zero measure, we have*

i) the operator $M'(\widehat{\mathbf{b}})$ *has closed range in* $\widehat{\mathbf{B}}_2$;

ii) the operator $Q'(\widehat{\mathbf{b}})$ *has closed range in* $\Re \times \widehat{\mathbf{B}}_2$;

iii) the operator $Q'(\widehat{\mathbf{b}})$ *is not onto* $\Re \times \widehat{\mathbf{B}}_2$.

Proof. In order to show i) we split the system (7.64-7.65) into three parts: the Navier-Stokes, the k-ω model and turbulence source constraint derivative operator system. Let us consider the Navier-Stokes derivative operator in (7.64) with $\nu_t \in L^\infty(\Omega)$ and $\nu + \nu_t > 0$. The question of the closeness of the range of the Navier-Stokes operator defined in $M' : \widehat{\mathbf{B}}_1 \to \widehat{\mathbf{B}}_2$ reduces to the like question for the inhomogeneous Stokes operator $\widetilde{\mathbf{S}} : \mathbf{H}^2(\Omega) \cap \mathbf{H}_0^1(\Omega) \times \mathbf{H}^1(\Omega) \cap L_0^2(\Omega) \to \mathbf{H}^{-1}(\Omega) \times L_0^2(\Omega) \times \mathbf{H}^{1/2}(\Gamma(\alpha))$ defined as $\widetilde{\mathbf{S}} \cdot (\widetilde{\mathbf{w}}, \widetilde{p}) = (\widetilde{\mathbf{l}}_1, \widetilde{l}_2, \widetilde{\mathbf{l}}_3)$ if and only if

$$\begin{cases} \nu a(\widetilde{\mathbf{w}}, \mathbf{v}) + b(\mathbf{v}, \widetilde{p}) - (\mathbf{v}, \widetilde{\mathbf{f}}) = \langle \widetilde{\mathbf{l}}_1, \mathbf{v} \rangle & \forall\, \mathbf{v} \in \mathbf{H}_0^1(\Omega) \\[2mm] b(\widetilde{\mathbf{w}}, z) = (\widetilde{l}_2, z) & \forall\, z \in L^2(\Omega) \\[2mm] \int_\Gamma (\widetilde{\mathbf{w}} - \mathbf{g}) \cdot \mathbf{s}\, ds = \int_\Gamma \widetilde{\mathbf{l}}_3 \cdot \mathbf{s}\, ds & \forall\, \mathbf{s} \in \mathbf{H}^{-1/2}(\Gamma), \end{cases} \tag{7.73}$$

where $\mathbf{f} \in \mathbf{L}^2(\Omega)$ and $\mathbf{g} \in \mathbf{H}^{1/2}(\Gamma)$. The fact that the operator $\widetilde{\mathbf{S}}$ has closed range in $\mathbf{H}^{-1}(\Omega) \times L_0^2(\Omega) \times \mathbf{H}^{1/2}(\Gamma)$ follows easily from well-known results for the Stokes equations; see, e.g., [109]. We can then conclude that the operator $\widetilde{\mathbf{S}}$ has closed range in $\widehat{\mathbf{B}}_2$, and, since the operator $M'(\mathbf{b})$ is a compact perturbation of the operator $\widetilde{\mathbf{S}}$, we have, from the Fredholm theory, that $M'(\mathbf{b})$ itself has closed range in $\widehat{\mathbf{B}}_2$.

Now we consider the k-ω system in M'. Since $\widehat{\mathbf{b}}$ is an optimal solution the system reduces to

$$
\begin{cases}
a(\nu + \nu_t \sigma_k; \widetilde{k}, \widehat{\phi}) + c(\widehat{\mathbf{u}}; \widetilde{k}, \widehat{\phi}) + \langle \beta^* \widehat{\omega} \widetilde{k}, \widehat{\phi} \rangle = \displaystyle\int_\Omega \bar{l}_4 \widehat{\phi} \, d\mathbf{x} - \\
\quad a(\widetilde{\nu}_t \sigma_k; \widehat{k}, \widehat{\phi}) - c(\widetilde{\mathbf{u}}; \widehat{k}, \widehat{\phi}) - \langle \beta^* \widetilde{\omega} \widehat{k}, \widehat{\phi} \rangle + \langle \widehat{S}_k, \widehat{\phi} \rangle \quad \forall \widehat{\phi} \in H_0^1(\Omega) \\[2mm]
\displaystyle\int_\Gamma \widetilde{k} \, \widehat{s}_k \, ds = \int_\Gamma \bar{l}_5 \, \widehat{s}_k \, ds \qquad\qquad\qquad\quad \forall \widehat{s}_k \in \mathbf{H}^{-1/2}(\Gamma) \\[2mm]
a(\nu + \nu_t \sigma_\omega; \widetilde{\omega}, \widehat{\psi}) + c(\widehat{\mathbf{u}}; \widetilde{\omega}, \widehat{\psi}) + \langle \beta \, 2 \widehat{\omega} \widetilde{\omega}, \widehat{\psi} \rangle = \displaystyle\int_\Omega \bar{l}_6 \widehat{\psi} \, d\mathbf{x} - \\
\quad a(\widetilde{\nu}_t \sigma_\omega; \widehat{\omega}, \widehat{\psi}) - c(\widetilde{\mathbf{u}}; \widehat{\omega}, \widehat{\psi}) + \langle \widehat{S}_\omega, \widehat{\psi} \rangle \qquad\quad \forall \widehat{\psi} \in H_0^1(\Omega) \\[2mm]
\displaystyle\int_\Gamma \widetilde{\omega} \, \widehat{s}_w \, ds = \int_\Gamma \bar{l}_7 \, \widehat{s}_w \, ds \qquad\qquad\qquad\quad \forall \widehat{s}_w \in \mathbf{H}^{-1/2}(\Gamma) \, .
\end{cases}
\tag{7.74}
$$

It is possible to show that $\widetilde{\omega}$-equation in (7.74) has a solution for all $\bar{l}_6$ and also that $\widetilde{k}$-equation can be solved for all $\bar{l}_4$. In fact since $\nu + \nu_t$ is a positive function in $L^\infty(\Omega)$ and thanks to the Sobolev compact embeddings $\mathbf{H}^1(\Omega) \hookrightarrow \mathbf{L}^q(\Omega)$ which holds for $1 \le q < \infty$ when $N = 2$ and for $1 \le q \le 6$ when $N = 3$, we have that $\mathbf{u} \in \mathbf{H}^1(\Omega)$ verifies the hypothesis in Theorem 5 both with $N = 2$ and with $N = 3$.

Finally we focus on the system (7.65) under the assumption that $\widehat{\mathbf{b}}$ is an optimal solution. From this we have that $\widehat{\mathbf{S}}^2(\widehat{\mathbf{u}})$ is bounded and $\widehat{\nu}_t \in L^\infty(\Omega)$. If we assume that the region $(\Omega_\nu \cup \Omega_k \cup \Omega_\omega) \cap \Omega$ has a measure zero then $\widehat{r}_\nu, \widehat{r}_k, \widehat{r}_\omega$ cannot be zero a.e. on the domain Ω. Therefore the equations can be solved a.e. in Ω for all $\mathbf{l}_\nu = (l_{\nu 0}, l_{\nu 1}) \in L^2(\Omega) \times L^2(\Omega)$, $\mathbf{l}_k = (l_{k0}, l_{k1}) \in L^2(\Omega) \times L^2(\Omega)$ and $\mathbf{l}_\omega = (l_{\omega 0}, l_{\omega 1}) \in L^2(\Omega) \times L^2(\Omega)$ as a function of $\widetilde{\nu}_t, \widetilde{r}_{\nu 1}$, $\widetilde{k}, \widetilde{r}_{k1}$ and $\widetilde{\omega}$ and $\widetilde{r}_{\omega 1}$, respectively.

Starting from i), the proof of ii) and iii) can be found easily by using the standard techniques in [42, 43, 45]. $\qquad\square$

The first-order necessary condition follows easily from the fact that the operator $Q'(\widehat{\mathbf{b}})$ is not onto $\Re \times \widehat{\mathbf{B}}_2$; see, e.g., [42, 46].

Theorem 6. *Let $\widehat{\mathbf{b}} \in \widehat{\mathbf{B}}_1$ be a solution of the optimal control problem, then there exists a nonzero Lagrange multiplier $\widehat{\mathbf{b}}_a = (\lambda_1, \widehat{\mathbf{u}}_a, \widehat{p}_a, \widehat{\mathbf{f}}_a, \widehat{k}_a, \widehat{\omega}_a, \widehat{\nu}_{ta}, \widehat{S}_{ka},$ $\widehat{S}_{\omega a}, \widehat{r}_{\nu a}, \widehat{r}_{ka}, \widehat{r}_{\omega a}) \in \Re \times \widehat{\mathbf{B}}_2^*$ satisfying the Euler equations*

$$
\lambda_1 \, \mathcal{J}'(\widehat{\mathbf{u}}, \widehat{k}, \widehat{\mathbf{f}}) \cdot \widetilde{\mathbf{b}} + \langle \widehat{\mathbf{b}}_a, M'(\widehat{\mathbf{b}}) \cdot \widetilde{\mathbf{b}} \rangle = 0 \qquad \forall \widetilde{\mathbf{b}} \in \widehat{\mathbf{B}}_1 \, ,
\tag{7.75}
$$

where $\langle \cdot, \cdot \rangle$ denotes the duality pairing between $\widehat{\mathbf{B}}_2$ and $\widehat{\mathbf{B}}_2^*$.

7.2.3   The optimality system

Next, we examine the first-order necessary condition (7.75) to derive an optimality system from which optimal states and controls may be determined.

Theorem 7. *Let* $\mathbf{b} \in \widehat{\mathbf{B}}_1$ *denotes a solution of the optimal control problem. Then, if the region* $\Omega_\nu \cup \Omega_{S_k} \cup \Omega_{S_\omega}$ *has zero measure,* $(\widehat{\mathbf{u}}_a, \widehat{p}_a, \widehat{\mathbf{f}}_a,)$ *are solutions of*

$$b(\widehat{\mathbf{u}}_a, \widetilde{p}) = 0$$

$$a(\nu + \nu_t; \widetilde{\mathbf{u}}, \widehat{\mathbf{u}}_a) + c(\widetilde{\mathbf{u}}; \widehat{\mathbf{u}}, \widehat{\mathbf{u}}_a) + c(\widehat{\mathbf{u}}; \widetilde{\mathbf{u}}, \widehat{\mathbf{u}}_a) + b(\widetilde{\mathbf{u}}, \widehat{p}_a) =$$

$$-a \int_\Omega \widetilde{\mathbf{u}} \, (\widehat{\mathbf{u}} - \mathbf{u}_d) - c(\widetilde{\mathbf{u}}; \widehat{k}, \widehat{k}_a) - c(\widetilde{\mathbf{u}}; \widehat{\omega}, \widehat{\omega}_a) +$$

$$a(\widehat{r}_{ka}\widehat{\nu}_t + \widehat{r}_{\omega a}; \widehat{\mathbf{u}}, \widetilde{\mathbf{u}}) - a(\widehat{S}_{ka}\widehat{\nu}_t \, (\beta^* k_{max,v} \, \widehat{\omega} - \widehat{S}_k) +$$

$$\widehat{S}_{\omega a} \, (\frac{\beta \omega^2_{max,v}}{\alpha} - \widehat{S}_\omega); \widehat{\mathbf{u}}, \widetilde{\mathbf{u}})$$

$$\lambda \langle \widehat{\mathbf{f}}_a, \widetilde{\mathbf{f}} \rangle = \langle \widehat{\mathbf{u}}_a, \widetilde{\mathbf{f}} \rangle \, ,$$

(7.76)

for all $(\widetilde{\mathbf{u}}, \widetilde{p}, \widetilde{\mathbf{f}})$ *in* $\mathbf{H}_0^1(\Omega) \times L_0^2(\Omega) \times \mathbf{L}^2(\Omega)$, $\widehat{k}_a, \widehat{\omega}_a$ *are solutions of*

$$a(\nu + \nu_t \sigma_k; \widetilde{k}, \widehat{k}_a) + c(\widehat{\mathbf{u}}; \widetilde{k}, \widehat{k}_a) + \langle \beta^* \, \widehat{k}_a \widehat{\omega}, \widetilde{k} \rangle =$$

$$-b \int_\Omega \left(\widehat{k} - k_d \right) \widetilde{k} \, d\mathbf{x} - \langle \widehat{\nu}_a - \widehat{r}_{\nu a}, \widetilde{k} \rangle$$

$$a(\nu + \nu_t \sigma_\omega; \widetilde{\omega}, \widehat{\omega}_a) + c(\widehat{\mathbf{u}}; \widetilde{\omega}, \widehat{\omega}_a) + \langle 2\beta \, \widehat{\omega} \widetilde{\omega}, \widehat{\omega}_a \rangle =$$

$$\langle -\widehat{r}_{\nu a} \widehat{\nu}_t + \widehat{\nu}_a \widehat{\nu}_t (\nu_{max} - \widehat{\nu}_t), \widetilde{\omega} \rangle - \langle \beta^* \, \widehat{k} \, \widehat{k}_a, \widetilde{\omega} \rangle -$$

$$\langle \widehat{S}_{ka} (\frac{\widehat{\nu}_t}{2} \mathbf{S}^2(\widehat{\mathbf{u}}) - \widehat{S}_k) - \widehat{r}_{ka}, \beta^* k_{max,v} \widetilde{\omega} \rangle \, ,$$

(7.77)

for all $(\widetilde{k}, \widetilde{\omega})$ *in* $\mathbf{H}_0^1(\Omega) \times \mathbf{H}_0^1(\Omega)$, $\widehat{\nu}_a, \widehat{S}_{ka}, \widehat{S}_{\omega a}$ *are solutions of the following algebraic equations*

$$\widehat{\nu}_a \left[\widehat{\omega}(\nu_{max} - \widehat{\nu}_t) + (\widehat{k} - \widehat{\nu}_t \widehat{\omega}) \right] =$$

$$\left[\nabla \widehat{\mathbf{u}} : \nabla \widehat{\mathbf{u}}_a + \sigma_k \nabla \widehat{k} \cdot \nabla \widehat{k}_a + \sigma_\omega \nabla \widehat{\omega} \cdot \nabla \widehat{\omega}_a \right] +$$

$$2\widehat{r}_{\nu a} \, \widehat{\omega} + \widehat{S}_{ka} \frac{\mathbf{S}^2(\widehat{\mathbf{u}})}{2} (\beta^* k_{max,v} \widehat{\omega} - \widehat{S}_k) - \widehat{r}_{ka} \frac{\mathbf{S}^2(\widehat{\mathbf{u}})}{2} \, ,$$

(7.78)

$$\widehat{S}_{ka} \left[(\beta^* k_{max,v} \, \widehat{\omega} - \widehat{S}_k) + (\frac{\widehat{\nu}_t}{2} \mathbf{S}^2(\widehat{\mathbf{u}}) - \widehat{S}_k) \right] = -\widehat{k}_a + \widehat{r}_{ka} \, ,$$

$$\widehat{S}_{\omega a} \left[(\frac{\beta \omega^2_{max,v}}{\alpha} - \widehat{S}_\omega) + (\frac{1}{2} \mathbf{S}^2(\widehat{\mathbf{u}}) - \widehat{S}_\omega) \right] = -\alpha \widehat{\omega}_a + 2\widehat{r}_{\omega a} \, ,$$

and $\widehat{r}_{\nu a}, \widehat{r}_{ka}, \widehat{r}_{\omega a}$ satisfy

$$\widehat{r}_{\nu a}\widehat{r}_\nu = 0 \qquad \widehat{r}_{ka}\widehat{r}_k = 0 \qquad \widehat{r}_{\omega a}\widehat{r}_\omega = 0 \, . \tag{7.79}$$

Proof. The first-order necessary condition (7.75) is equivalent to

$$\lambda_1 \Big(a \int_\Omega \widetilde{\mathbf{u}} \, (\widehat{\mathbf{u}} - \mathbf{u}_d) \, d\mathbf{x} + b \int_\Omega \widetilde{k} \left(\widehat{k} - k_d \right) d\mathbf{x} +$$

$$\lambda \int_{\mathbf{x}} \widetilde{\mathbf{f}} \cdot \widehat{\mathbf{f}} \, d\mathbf{x} \Big) + a(\widetilde{\nu}_t; \widehat{\mathbf{u}}, \widehat{\mathbf{u}}_a) + a(\nu + \nu_t; \widetilde{\mathbf{u}}, \widehat{\mathbf{u}}_a) +$$

$$c(\widetilde{\mathbf{u}}; \widehat{\mathbf{u}}, \widehat{\mathbf{u}}_a) + c(\widehat{\mathbf{u}}; \widetilde{\mathbf{u}}, \widehat{\mathbf{u}}_a) + b(\widehat{\mathbf{u}}_a, \widetilde{p}) - \langle \widetilde{\mathbf{f}}, \widehat{\mathbf{u}}_a \rangle + b(\widetilde{\mathbf{u}}, \widehat{p}_a) +$$

$$\int_\Gamma (\widetilde{u} - \mathbf{g}_u) \cdot \widehat{u}_a \, ds + a(\widetilde{\nu}_t \sigma_k; \widehat{k}, \widehat{k}_a) + a(\nu + \nu_t \sigma_k; \widetilde{k}, \widehat{k}_a) + c(\widetilde{\mathbf{u}}; \widehat{k}, \widehat{k}_a) +$$

$$c(\widehat{\mathbf{u}}; \widetilde{k}, \widehat{k}_a) - \langle \widetilde{S}_k, \widehat{k}_a \rangle + \langle \beta^* \, \widetilde{k}\widehat{\omega}, \widehat{k}_a \rangle + \langle \beta^* \, \widehat{k}\widetilde{\omega}, \widehat{k}_a \rangle + \int_\Gamma \widetilde{k} \, \widehat{k}_a \, ds +$$

$$a(\widetilde{\nu}_t \sigma_\omega; \widehat{\omega}, \widehat{\omega}_a) + a(\nu + \nu_t \sigma_\omega; \widetilde{\omega}, \widehat{\omega}_a) + c(\widetilde{\mathbf{u}}; \widehat{\omega}, \widehat{\omega}_a) + c(\widehat{\mathbf{u}}; \widetilde{\omega}, \widehat{\omega}_a) - \alpha \, \langle \widetilde{S}_\omega, \widehat{\omega}_a \rangle +$$

$$\langle \beta \, 2\widehat{\omega}\widetilde{\omega}, \widehat{\omega}_a \rangle + \int_\Gamma \widetilde{\omega} \, \widehat{\omega}_a \, ds + \langle \widehat{\nu}_a, (\widetilde{k} - \widetilde{\nu}_t \widehat{\omega} - \widehat{\nu}_t \widetilde{\omega})(\nu_{max} - \widehat{\nu}_t) - \widetilde{\nu}_t(\widehat{k} - \widehat{\nu}_t \widehat{\omega}) \rangle +$$

$$\langle \widehat{r}_{\nu a}, 2\widetilde{r}_\nu \widehat{r}_\nu - (\widetilde{k} - \widetilde{\nu}_t \widehat{\omega} - \widehat{\nu}_t \widetilde{\omega}) + \widetilde{\nu}_t \widehat{\omega} + \widetilde{\omega}\widehat{\nu}_t \rangle +$$

$$\langle \widehat{S}_{ka}, (\frac{\widetilde{\nu}_t}{2}\mathbf{S}^2(\widehat{\mathbf{u}}) + \widehat{\nu}_t \mathbf{S}(\widetilde{\mathbf{u}}) : \mathbf{S}(\widehat{\mathbf{u}}) - \widetilde{S}_k)(\beta^* k_{max,v}\widehat{\omega} - \widehat{S}_k) +$$

$$(\frac{\widehat{\nu}_t}{2}\mathbf{S}^2(\widehat{\mathbf{u}}) - \widehat{S}_k)(\beta^* k_{max,v}\widetilde{\omega} - \widetilde{S}_k)\rangle + \langle \widehat{r}_{ka}, 2\widetilde{r}_k \widehat{r}_k -$$

$$(\frac{\widetilde{\nu}_t}{2}\mathbf{S}^2(\widehat{\mathbf{u}}) + \widehat{\nu}_t \mathbf{S}(\widetilde{\mathbf{u}}) : \mathbf{S}(\widehat{\mathbf{u}}) - \widetilde{S}_k) - (\beta^* k_{max,v}\widetilde{\omega} - \widetilde{S}_k)\rangle +$$

$$\langle \widehat{r}_{\omega a}, 2\widetilde{r}_\omega \widehat{r}_\omega - \mathbf{S}(\widetilde{\mathbf{u}}) : \mathbf{S}(\widehat{\mathbf{u}}) \rangle + \langle \widehat{r}_{\omega a}, 2\widetilde{S}_\omega \rangle +$$

$$\langle \widehat{S}_{\omega a}, (\mathbf{S}(\widetilde{\mathbf{u}}) : \mathbf{S}(\widehat{\mathbf{u}}) - \widetilde{S}_\omega)(\frac{\omega_{max,v}^2 \beta}{\alpha} - \widehat{S}_\omega) - \widetilde{S}_\omega(\frac{1}{2}\mathbf{S}^2(\widehat{\mathbf{u}}) - \widehat{S}_\omega)\rangle = 0 \, ,$$

for all $\widehat{\mathbf{b}} = (\widehat{\mathbf{u}}, \widehat{p}, \widehat{\mathbf{f}}, \widehat{k}, \widehat{\omega}, \widehat{\nu}_t, \widehat{S}_k, \widehat{S}_\omega, \widehat{r}_\nu, \widehat{r}_k, \widehat{r}_\omega) \in \widehat{\mathbf{B}}_1$. In order to satisfy the integral on the boundary we set homogeneous Dirichlet boundary conditions for the adjoint variables $(\widehat{\mathbf{u}}_a, \widehat{p}_a, \widehat{k}_a, \widehat{\omega}_a)$. Furthermore we are free to choose $\lambda_1 = 1$. By extracting the terms involved in the same variation we obtain (7.76-7.79). $\qquad\square$

From (7.79) we note that if $\widehat{r}_k \neq 0$ then $\widehat{r}_{ka} = 0$. This is true also for $\widehat{r}_{\omega a}$

and $\widehat{r}_{\nu a}$. Therefore the final adjoint system reduces to

$$b(\widehat{\mathbf{u}}_a, \widetilde{p}) = 0 \,,$$

$$a(\nu + \nu_t; \widetilde{\mathbf{u}}, \widehat{\mathbf{u}}_a) + c(\widetilde{\mathbf{u}}; \widehat{\mathbf{u}}, \widehat{\mathbf{u}}_a) + c(\widehat{\mathbf{u}}; \widetilde{\mathbf{u}}, \widehat{\mathbf{u}}_a) + b(\widetilde{\mathbf{u}}, \widehat{p}_a) =$$

$$-a \int_\Omega \widetilde{\mathbf{u}} \, (\widehat{\mathbf{u}} - \mathbf{u}_d) \, d\mathbf{x} - c(\widetilde{\mathbf{u}}; \widehat{k}, \widehat{k}_a) - c(\widetilde{\mathbf{u}}; \widehat{\omega}, \widehat{\omega}_a) -$$

$$a(\widehat{S}_{ka}\widehat{\nu}_t \, (\beta^* k_{max,v} \, \widehat{\omega} - \widehat{S}_k) + \widehat{S}_{\omega a} \, (\frac{\beta \omega_{max,v}^2}{\alpha} - \widehat{S}_\omega); \widehat{\mathbf{u}}, \widetilde{\mathbf{u}}) \,,$$

$$a(\nu + \nu_t \sigma_k; \widehat{k}_a, \widetilde{k}) + c(\widehat{\mathbf{u}}; \widehat{k}, \widehat{k}_a) + \langle \beta^* \, \widehat{k}_a \, \widehat{\omega}, \widetilde{k} \rangle = -\langle \widehat{\nu}_a, \widetilde{k} \rangle - \qquad (7.80)$$

$$b \int_\Omega \left(\widehat{k} - k_d \right) \widetilde{k} \, d\mathbf{x}$$

$$a(\nu + \nu_t \sigma_\omega; \widetilde{\omega}, \widehat{\omega}_a) + c(\widehat{\mathbf{u}}; \widetilde{\omega}, \widehat{\omega}_a) + \langle 2\beta \, \widehat{\omega}\widehat{\omega}_a, \widetilde{\omega} \rangle =$$

$$\langle \widehat{\nu}_a \, \widehat{\nu}_t (\nu_{max} - \widehat{\nu}_t), \widetilde{\omega} \rangle -$$

$$\langle \beta^* \, \widehat{k} \, \widehat{k}_a, \widetilde{\omega} \rangle - \langle \widehat{S}_{ka}(\frac{\widehat{\nu}_t}{2} \mathbf{S}^2(\widehat{\mathbf{u}}) - \widehat{S}_k)\beta^* k_{max,v}, \widetilde{\omega} \rangle \,,$$

with control

$$\widehat{\mathbf{f}}_a = \frac{\widehat{\mathbf{u}}_a}{\lambda} \,, \qquad (7.81)$$

adjoint turbulent viscosity

$$\widehat{\nu}_a = \frac{\left[\nabla\widehat{\mathbf{u}} : \nabla\widehat{\mathbf{u}}_a + \sigma_k \nabla\widehat{k} \cdot \nabla\widehat{k}_a + \sigma_\omega \nabla\widehat{\omega} \cdot \nabla\widehat{\omega}_a \right] \widehat{S}_{ka}}{r_\nu^2}$$
$$\cdot \frac{\mathbf{S}^2(\widehat{\mathbf{u}})}{2}(\beta^* k_{max,v}\widehat{\omega} - \widehat{S}_k) \,, \qquad (7.82)$$

and adjoint turbulence sources

$$\widehat{S}_{ka} = -\frac{\widehat{k}_a}{r_k^2} \,, \qquad \widehat{S}_{\omega a} = -\frac{\alpha\widehat{\omega}_a}{r_\omega^2} \,. \qquad (7.83)$$

Furthermore in the case in which no bounds are reached and

$$\widehat{\nu}_t = \frac{k}{\omega} \,, \qquad \widehat{S}_k = \frac{\widehat{\nu}_t}{2} \mathbf{S}^2(\widehat{\mathbf{u}}) \,, \qquad \widehat{S}_\omega = \frac{1}{2} \mathbf{S}^2(\widehat{\mathbf{u}}) \,, \qquad (7.84)$$

the adjoint system (7.82-7.83) simplifies drastically.

To complete the optimality system definition we report the boundary conditions to be used for a generic turbulent flow simulations where the inlets are defined by the surface Γ_i, the outlets by Γ_o, the solid walls are

defined by Γ_w and a near wall approach is chosen. The boundary conditions for the state variables over the generic inlet Γ_i are

$$\mathbf{v} \cdot \mathbf{n} = \mathbf{v}_i \,, \qquad \mathbf{v} \cdot \mathbf{T} = 0 \,,$$
$$k = k_i \,, \qquad \omega = \omega_i \,,$$

and on the outlet Γ_o

$$(\nu + \nu_t)\mathbf{S}(\mathbf{v}) \cdot \mathbf{n} = 0 \,, \qquad \mathbf{v} \cdot \mathbf{T} = 0 \,, \qquad p = 0 \,,$$
$$\nabla k \cdot \mathbf{n} = 0 \,, \qquad \nabla \omega \cdot \mathbf{n} = 0 \,,$$

where $\mathbf{n}$ is the normal vector to the boundary surface and $\mathbf{T}$ the tangential tensor. If a near wall approach is chosen the boundary conditions on the solid wall Γ_w are

$$\mathbf{v} \cdot \mathbf{n} = 0 \,, \qquad (\nu + \nu_t)\mathbf{S}(\mathbf{v}) \cdot \mathbf{n} = \nu \frac{\mathbf{v} \cdot \mathbf{T}}{y_d} \,,$$
$$\nabla k \cdot \mathbf{n} = \frac{2\,k}{y_d} \qquad \omega = \frac{2\,\nu}{\beta^* \, y^2{}_d} \,.$$

The natural or dual boundary conditions for the optimality system in strong form can be obtained by setting to zero the surface integrals that contain unknown terms or non-integrable functions. Over the inlet Γ_i we set

$$\mathbf{v}_a = \mathbf{0} \,, \qquad k_a = 0 \,, \qquad \omega_a = 0 \,,$$

on the outlet Γ_o

$$(\nu + \nu_t)\mathbf{S}(\mathbf{v}_a) \cdot \mathbf{n} = -(\mathbf{v} \cdot \mathbf{n})\mathbf{v}_a \,, \mathbf{v}_a \cdot \mathbf{T} = 0 \,, \qquad p_a = 0 \,,$$
$$(\nu + \sigma_k \nu_t)\nabla k_a \cdot \mathbf{n} = -(\mathbf{v} \cdot \mathbf{n})k_a \,,$$
$$(\nu + \sigma_\omega \nu_t)\nabla \omega_a \cdot \mathbf{n} = -(\mathbf{v} \cdot \mathbf{n})\omega_a \,,$$

and on the wall Γ_w

$$\mathbf{v} \cdot \mathbf{n} = 0 \,,$$
$$(\nu + \nu_t)\mathbf{S}(\mathbf{v}_a) \cdot \mathbf{n} = \frac{\nu \mathbf{v}_a \cdot \mathbf{T}}{y_d} + 2[k_a \nu_t + \gamma_{a1} g(k, \mathbf{v})]\mathbf{v} \cdot \mathbf{T} \,,$$
$$\nabla k_a \cdot \mathbf{n} = 2\frac{k_a + \sigma_d \omega_a}{y_d} \,, \qquad \omega_a = 0 \,,$$

In order to obtain a finite element discretization of the optimality system the infinite dimensional functional spaces are replaced by finite dimensional spaces and a suitable basis for these spaces is chosen. We use

quadratic finite elements for all variables except the pressure which is assumed linear to satisfy the *inf-sup* condition needed as stability requirement for discrete Navier-Stokes approximations, see Chapter 1 for more details. Let $\mathbf{v}_h \in \mathbf{X}_h^2(\Omega) \subset \mathbf{H}^1(\Omega)$ and $p_h \in P_h(\Omega) \subset L_0^2(\Omega)$ be the quadratic and linear approximations for the fluid flow field. For the turbulence system we use quadratic approximations as $k_h \in X_h^2(\Omega) \subset H^1(\Omega)$ and $\omega_h \in X_h^2(\Omega) \subset H^1(\Omega)$. Similar approximations are used for the adjoint variables. With this assumption the weak form of the optimality system can be split into the incompressible Navier-Stokes system with the k-ω turbulence model and their adjoint equations. The first block of equations consists of the Navier-Stokes system

$$\int_\Omega \nabla \cdot \mathbf{v}_h \psi_h d\Omega = 0 \qquad \forall \psi_h \in P_h \,, \tag{7.85}$$

$$\int_\Omega \Big[[(\mathbf{v}_h \cdot \nabla)\mathbf{v}_h] \cdot \mathbf{w}_h - p_h \nabla \cdot \mathbf{w}_h + (\nu + \nu_t)\mathbf{S}(\mathbf{v_h}) : \nabla \mathbf{w}_h - \mathbf{f}_h \cdot \mathbf{w}_h \Big] d\Omega \tag{7.86}$$

$$- \int_{\Gamma_w} \left[\frac{\nu}{y_d}(\mathbf{v}_h - (\mathbf{v}_h \cdot \mathbf{n})\mathbf{n}) \cdot \mathbf{w}_h \right] d\Gamma = 0 \qquad \forall \mathbf{w}_h \in \mathbf{X}_h^2 \,,$$

and its adjoint set of equations

$$\int_\Omega \nabla \cdot \mathbf{v}_{ha} \psi_{ha} d\Omega = 0 \qquad \forall \psi_{ha} \in P_h \,, \tag{7.87}$$

$$\int_\Omega \Big[[(\mathbf{w}_{ha} \cdot \nabla)\mathbf{v}_h] \cdot \mathbf{v}_{ha} + [(\mathbf{v}_h \cdot \nabla)\mathbf{w}_{ha}] \cdot \mathbf{v}_{ha} - p_{ha}\nabla \cdot \mathbf{w}_{ha}+ \tag{7.88}$$

$$(\nu + \nu_t)\mathbf{S}(\mathbf{v_{ha}}) : \nabla \mathbf{w}_{ha} + k_{ha}(\delta \mathbf{v} \cdot \nabla)k_h + \omega_{ha}(\mathbf{w}_{ha} \cdot \nabla)\omega_h+$$

$$a\,(\mathbf{v}_h - \mathbf{v}_d) \cdot \mathbf{w}_{ha} - [k_{ha}\nu_t + \alpha\,\omega_{ha}]\,\mathbf{S}(\mathbf{v}_h) : \mathbf{S}(\mathbf{w}_{ha})+$$

$$- \gamma_{a1} \frac{g(k, \mathbf{v}_h)}{\mathbf{S}^2(\mathbf{v}_h)}\,\mathbf{S}(\mathbf{v}_h) : \mathbf{S}(\mathbf{w}_{ha}) \Big] d\Omega-$$

$$\int_{\Gamma_w} \left[\frac{\nu}{y_d}(\mathbf{v}_{ha} - (\mathbf{v}_{ha} \cdot \mathbf{n})\mathbf{n}) \cdot \mathbf{w}_{ha} \right] d\Gamma = 0 \,,$$

for all $\mathbf{w}_{ha} \in \mathbf{X}_h^2$. The terms $(\mathbf{v}_h - (\mathbf{v}_h \cdot \mathbf{n})\mathbf{n})$ and its dual are simply the tangential velocity. The second block of equations to be solved consists of

the turbulence system

$$
\int_\Omega \left[[(\mathbf{v}_h \cdot \nabla)k_h]\psi_h + (\nu + \sigma_k \nu_t)\nabla k_h \cdot \nabla \psi_h - P_{hk}\psi_h + \beta^* k_h \omega_h \psi_h \right] d\Omega +
$$

(7.89)

$$
- \int_{\Gamma_w} \frac{2\,k}{y_d} \psi_h \, d\Gamma = 0 \qquad\qquad \forall \psi_h \in X_h^2
$$

$$
\int_\Omega \left[(\mathbf{v}_h \cdot \nabla)\omega_h \varphi_h + (\nu + \sigma_\omega \nu_t)\nabla \omega_h \cdot \nabla \varphi_h + \right.
$$

(7.90)

$$
\left. \left[\beta \omega_h^2 + \frac{\sigma_d}{\omega_h}\nabla k_h \cdot \nabla \omega_h - \alpha \mathbf{S}^2(\mathbf{v}_h) \right] \varphi_h \right] d\Omega = 0 \qquad \forall \varphi_h \in X_h^2
$$

and the corresponding adjoint set of equations

$$
\int_\Omega \left[-[(\mathbf{v}_h \cdot \nabla)k_{ha}]\psi_h + (\nu + \sigma_k \nu_t)\nabla k_{ha} \cdot \nabla \psi_h + \beta^* k_{ha} \omega_h \psi_h + \right. \qquad (7.91)
$$

$$
\gamma_{a1}\, g(1, \mathbf{v}_h)\psi_h - \sigma_d \frac{\omega_{ha}}{\omega_h}\nabla \omega_h \cdot \nabla \psi_h + \frac{\gamma_{a2} - \nu_a\,(\nu_t - g)}{\omega_h}\psi_h +
$$

$$
\left. b\,(k_h - k_d)\psi_h \right] d\Omega - \int_{\Gamma_w} \frac{2\,k_{ha}}{y_d}\psi_h d\Gamma = 0
$$

$$
\int_\Omega \left[[(\mathbf{v}_h \cdot \nabla)\varphi_h]\omega_{ha} + (\nu + \sigma_\omega \nu_t)\nabla \omega_{ha} \cdot \nabla \varphi_h + \beta^* k_{ha} k_h \varphi_h + \right. \qquad (7.92)
$$

$$
2\beta \omega_{ha}\omega_h \varphi_h - \sigma_d \frac{\omega_{ha}}{\omega_h}\nabla k_h \cdot \nabla \varphi_h +
$$

$$
\left. \frac{\sigma_d\,\omega_{ha}}{\omega_h^2}\nabla k_h \cdot \nabla \omega_h \varphi_h - \frac{(\nu_a\,(\nu_t - g) - \gamma_{a2})\,k}{\omega_h^2}\varphi_h \right] d\Omega = 0 \,,
$$

for all $\psi_h \in X_h^2$, $\varphi_h \in X_h^2$. The system (7.85-7.92) is a finite element discretization of the optimality system (7.2-7.5), (7.80-7.83) when the boundary conditions are included. In the next section we solve the optimality system described here in some numerical cases.

7.3   Numerical Results

In this section we report some results obtained from the numerical solution of the optimality system described in the previous section. We use a segregated solver for the state and adjoint systems and the steepest descent Algorithm 4 for the optimal control solution. After the setup in which the first state solution is obtained, the Algorithm consists of two main loops, the outer

---

Algorithm 4 Steepest descent algorithm to find the optimal solution

---

1: **function** FIND OPTIMAL
2:      Set $\mathbf{f}^0 = 0, r^0 = \lambda$
3:      Set an initial state $(\mathbf{v}^0, p^0, k^0, \omega^0)$ satisfying (7.85-7.86) and (7.89-7.90)
4:      Compute the functional $\mathcal{J}^0$ in (7.1)   ▷ *Setup of the reference state*
5:      **for** $i = 1 \to i_{max}$ **do**
6:          Solve (7.87-7.88-7.91-7.92) for the adjoint state $(\mathbf{v}_a^i, p_a^i, k_a^i, \omega_a^i)$
7:          **for** $j = 1 \to j_{max}$ **do**
8:              Compute the control $\mathbf{f}^i = \mathbf{f}^{i-1} + r^{i,j} \mathbf{v}_a^i / \lambda$
9:              Solve (7.85-7.86) and (7.89-7.90) for the state $(\mathbf{v}^{i,j}, p^{i,j}, k^{i,j}, \omega^{i,j}, \nu_t^{i,j})$
10:             Compute the new functional $\mathcal{J}^{i,j+1}$ in (7.1)
11:             **if** $\|\mathcal{J}^{i,j+1} - \mathcal{J}^{i,j}\|/\mathcal{J}^{i,j} < toll$ **then**
12:                 Convergence of the optimal control problem reached   ▷ *End*
13:             **else if** $\mathcal{J}^{i,j+1} > \mathcal{J}^{i,j}$ **then**
14:                 set $r^{i,j+1} = 2/3\, r^{i,j}$ and go to 8   ▷ *loop on j again*
15:             **else if** $\mathcal{J}^{i,j+1} < \mathcal{J}^{i,j}$ **then**
16:                 set $r^{i,j+1} = 3/2\, r^{i,j}$ and go to 6   ▷ *loop on i again*
17:             **end if**
18:         **end for**
19:     **end for**
20: **end function**

---

with index i and the inner with index j. The loop j is nested inside the loop i after the adjoint system is solved. In the loop j the new control $\mathbf{f}$ is obtained by adding the previous value with a weighted contribution from the adjoint $\mathbf{v}_a$ computed at the current i-iteration. This weight function $r^{i,j}$ is initialized to λ and can be updated at every j iteration based on the value of the new computed functional. After the control $\mathbf{f}$ is updated, the state system is solved and the new functional is computed in order to compare this value with the previous one. If the relative difference between the two functionals is bounded by the tolerance *toll* then the searching for an optimal solution ends. If the new functional is greater than the old one, the value of r is too large and must be reduced. The new control $\mathbf{f}$ can be computed, then the state solution and another j-iteration is performed. When the new functional is less than the old one we have successfully performed a reduction in the functional with the current control $\mathbf{f}$, so the j-loop ends and a new i-iteration can start by solving the adjoint system with new velocity and turbulence fields. The algorithm stops when the two computed functionals are nearly identical and no more improvement is possible on the state system.

Some remarks need to be done on this algorithm. First we notice the high

computational cost needed by an adjoint based algorithm that solves many times the adjoint and state systems. In iterative methods it is very common to employ the last solution available as initial condition for the system solution in order to reduce the computational time. In this case however some care is needed because in the j-loop, if r is too big, the state solution can become very different from the solution at the begin of the j-loop and much time could be needed to obtain the correct solution with a much smaller r. The strategy adopted in this work has been to reset the state solution at the same value after every not successful j iteration. In the algorithm the state system is solved many times, while the adjoint one less often. Keeping in mind also that the adjoint system could be harder to solve numerically, one could use a faster projection algorithm for the RANS solution which is performed many times and a fully coupled and robust solver for the adjoint system. Comparing this algorithm with higher order ones where for example second order information through a Hessian computation are available, we can assume that this is more robust and suitable for this specific optimal control problem because of RAM limitations [47, 113]. However in the future more complex algorithms could be assessed to obtain possible improvements.

In the rest of this section we report the results obtained for some test cases for different parameters a, b and λ in two and three-dimensional geometries. Two cases are simulated: a two dimensional plane channel with a developing flow and a three dimensional channel with a more complex geometry. In the first case we test the optimal control solver for both a velocity matching and a turbulence enhancement problem, while in the three dimensional channel we study the turbulence reduction-enhancement problems. Different values of the parameter λ are chosen in the range of 0.1 to 0.001. In the following we report all the physical properties, dimensions and results in non-dimensional units.
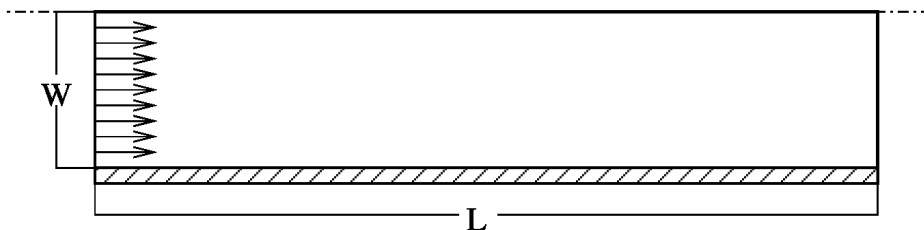
Figure 7.1: Plane channel geometry. Inlet on the left, outlet on the right, wall on the bottom and symmetry axis on top.

7.3.1   Plane Channel

In this section we solve the optimal control Algorithm 4 in two-dimensional geometry for the velocity-matching profile case and for the turbulence enhancement problem. We refer to the first case as case (a) and to the latter as case (b). The plane channel geometry is reported in Figure 7.1. The half-channel width W is 1 and the length L is 5. The x-axis is set along the flow direction while the transverse one is y-axis. The inlet is set on the left of the channel and a simple velocity uniform profile $\mathbf{v} = (1, 0)$ boundary condition
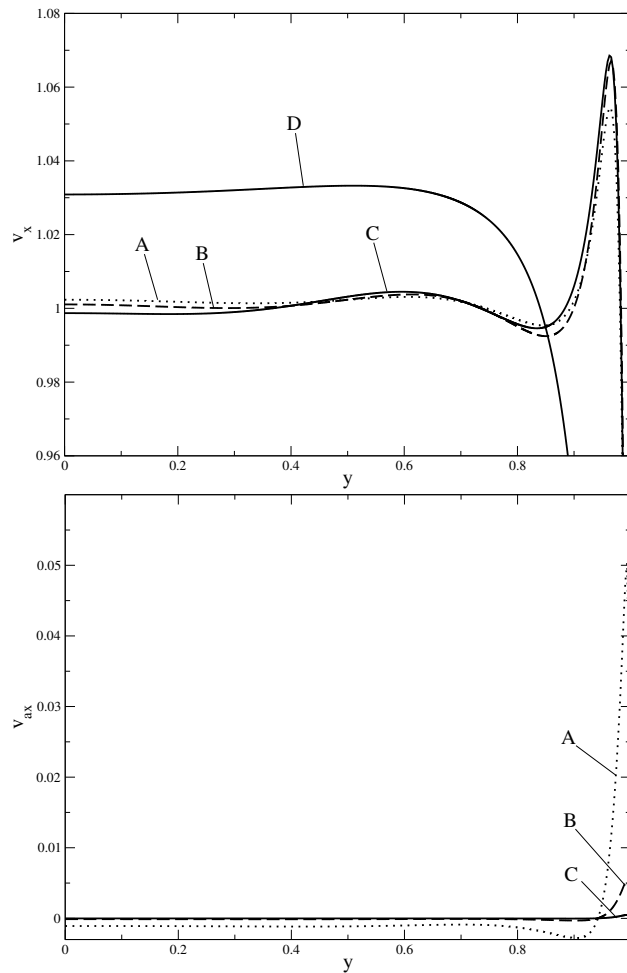
Figure 7.2: Case (a). On top axial velocity v_x in the plane channel geometry, profile on a line at $x = 4$. On the bottom adjoint axial velocity profile v_{ax} on the same line. Result (A) obtained with $\lambda = 0.1$, (B) with $\lambda = 0.01$ and (C) with $\lambda = 0.001$. Profile (D) on top obtained with no control.
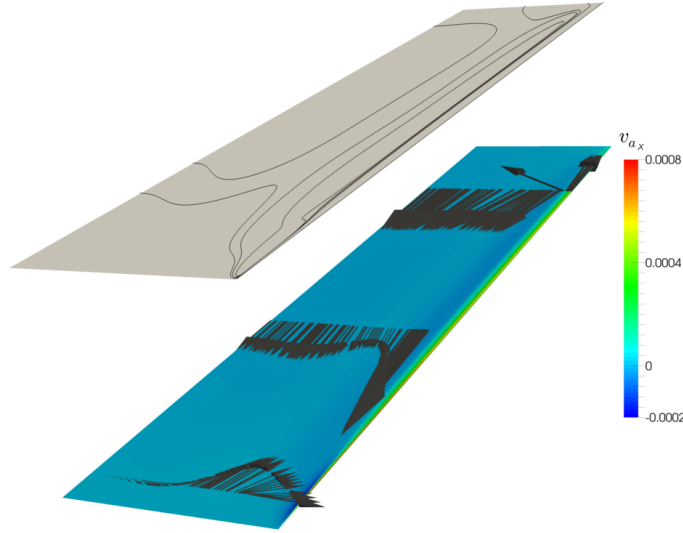
Figure 7.3: Case (a). Iso-surface contours (top) and vector field (bottom) of the adjoint axial velocity v_{ay} for $\lambda = 0.001$.

is imposed here, while on the right a standard outflow boundary condition is set. On the symmetry axis a homogenous Neumann boundary condition is set for v_x, v_{ax}, k, ω, k_a and ω_a and zero value for v_y and v_{ay} on the same symmetry axis. On the wall we use the near-wall boundary conditions as defined in Section 7.1.

The kinematic viscosity is the main physical parameter of this problem. Defining the Reynolds number based on the modulus of the inlet velocity $U = 1$ and on the half-width of the channel $W = 1$, $Re = UW/\nu$, we can consider different Reynolds numbers by changing the molecular viscosity ν. For this test case we set $Re = 10,000$ that implies a not fully developed flow at the outlet of the channel.

For the velocity matching case (a) we choose the desired velocity $\mathbf{v}_d = (1, 0)$ and $\lambda = 0.1$, 0.01 and 0.001. When λ is smaller the control can act stronger and achieve low values of the objective functional. In Figure 7.2, on top, the velocity v_x profiles on a line at $x = 4$ obtained with decreasing λ are reported. The lines (A-C) show the profile of the controlled velocity and line (D) is the reference result with no control. In the central region, as λ decreases, the velocity approaches a unitary uniform value and the matching is better achieved. Due to vanishing boundary conditions on the wall the
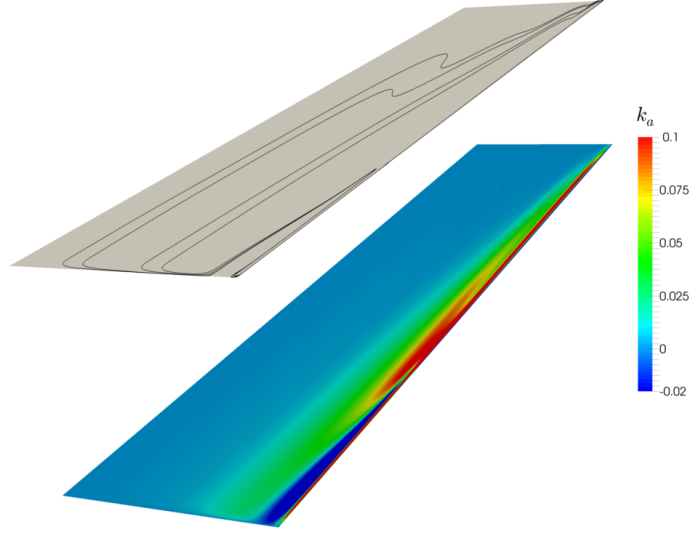
Figure 7.4: Case (a). Iso-surface contours (top) and scalar field (bottom) of the adjoint turbulent kinetic energy k_a for $\lambda = 0.001$.

λ	∞	0.1	0.01	0.001
$\mathcal{J}(\mathbf{v}, \mathbf{v_a})$	0.015995	0.003803	0.003353	0.003318

Table 7.1: Case (a). Objective functionals computed with no control ($\lambda = \infty$) and different λ values in the velocity matching profile problem, plane channel.

control cannot act efficiently in the near-wall region and therefore the source term $(\mathbf{v} - \mathbf{v}_d)$ and the adjoint variable are substantially large. In Figure 7.2, on the bottom, the profile of the adjoint velocity v_{ax} is reported for three values of λ showing a strong peak near the wall and flat profile in the center-channel region with negative values that decrease the fluid velocity. In this Figure we can see different values of v_{ax} obtained with decreasing λ, (lines A-C). In order to understand this behavior we must consider that the control $\mathbf{f}$ is scaled by the value of λ, so a smaller adjoint velocity is needed to obtain the same effect on the fluid velocity with decreasing λ.

In Figures 7.3-7.4 several equally subdivided contours of the adjoint variables $\mathbf{v}_a$ and k_a are reported for $\lambda = 0.001$. The interaction between the adjoint velocity and the adjoint turbulent kinetic energy is shown. The most important source for k_a seems to be the tensor double product of the velocity
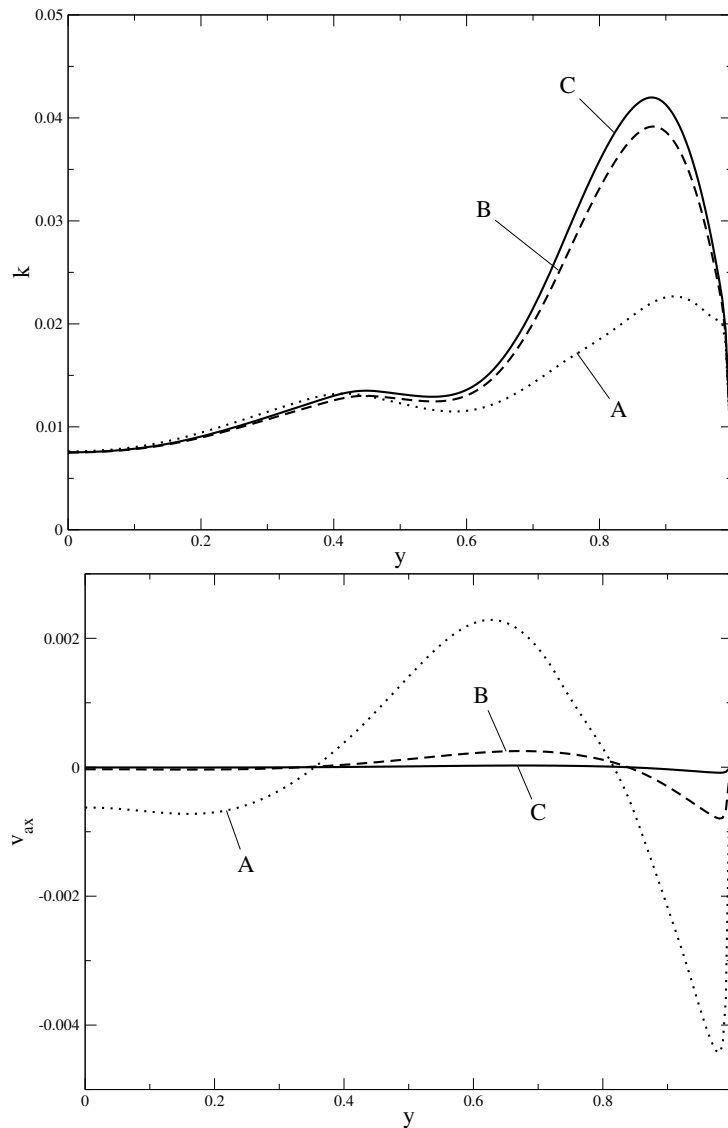
Figure 7.5: Case (b). Turbulence kinetic energy k (top) and adjoint axial velocity v_{ax} (bottom) profiles along the line $x = 4$ for different $\lambda = 0.1$ (A), 0.01 (B) and 0.001 (C).

derivatives and its adjoint. However the non linearity of the equations implies high complexity and the physical meaning of this variable in the context of velocity matching profile is difficult to be understood.

Finally in Table 7.1 the objective functionals are reported as computed in the velocity matching profile problem for the different λ values. As one can see, by decreasing λ a more effective control is attained and the objective
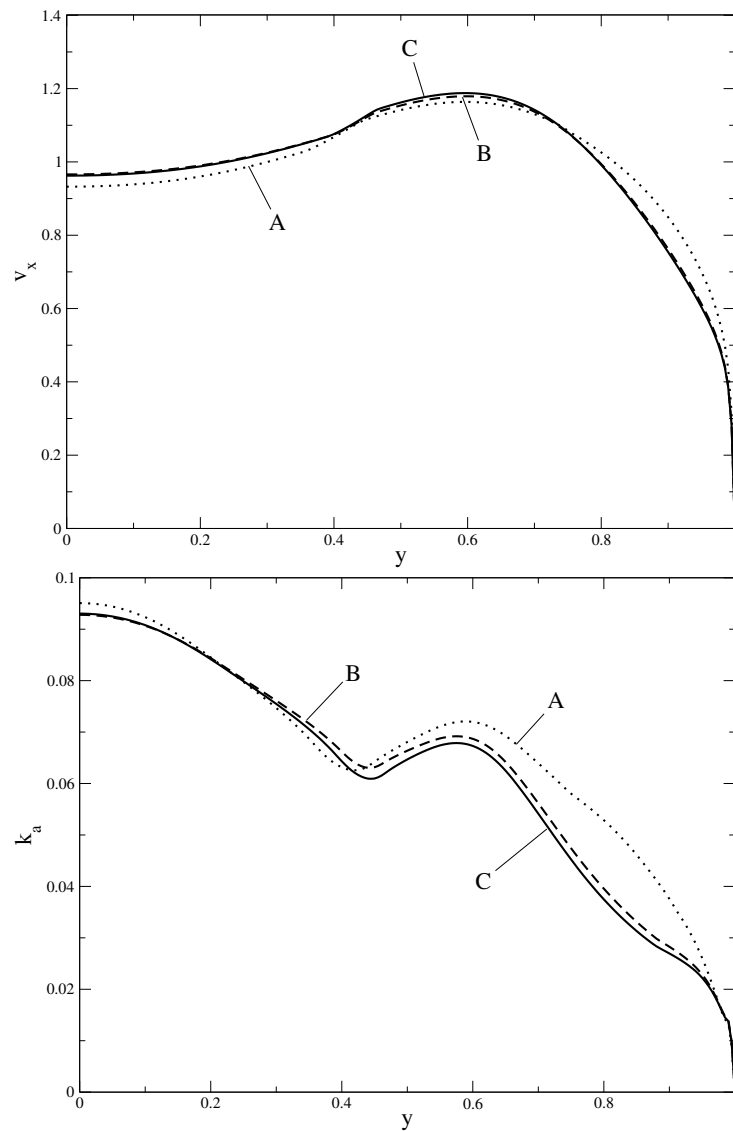
Figure 7.6: Case (b). Axial velocity v_x (top) and adjoint turbulent kinetic energy k_a (bottom) profiles along the line $x = 4$ for different $\lambda = 0.1$ (A), 0.01 (B) and 0.001 (C).

functional becomes smaller. Moreover by decreasing λ from 0.1 to 0.01 a great improvement is obtained while this is less evident when decreasing λ from 0.01 to 0.001.

In order to test the optimal control solver with $a = 0$, $b = 1$ in equation (7.1) we choose a turbulence enhancement problem and set the desired value k_d to 0.1 because the turbulence energy in the test case without control
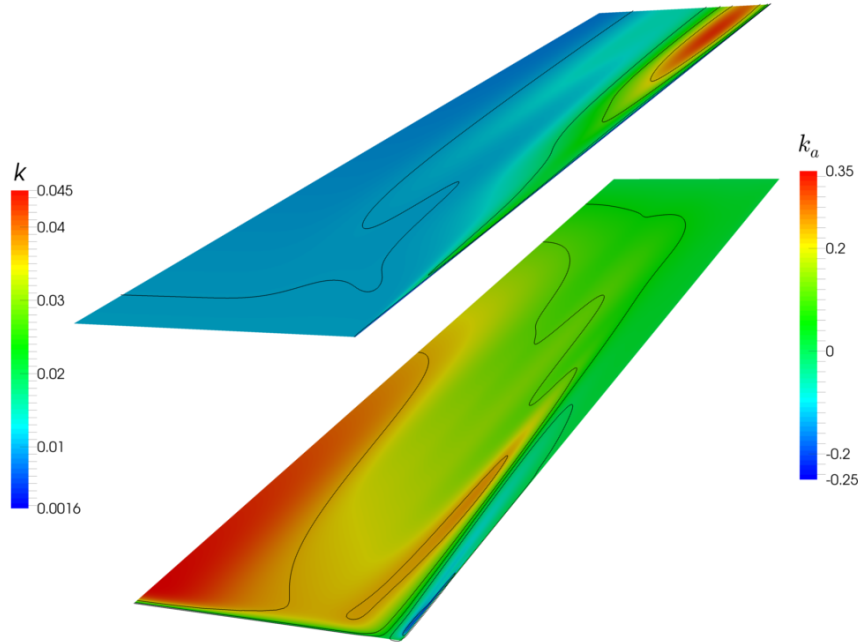
Figure 7.7: Case (b). Iso-surface contours of turbulent kinetic energy k (top) and adjoint turbulent kinetic energy k_a (bottom) for $\lambda = 0.001$.

is always smaller than this value. The regularization parameter λ of this case (b) is set to 0.1, 0.01 or 0.001. In Figure 7.5, on top, the turbulence kinetic energy k is reported for the three values of λ along the line $x = 4$. On the bottom of the same Figure the axial adjoint velocity is reported for different values of λ. The control increases the value of the turbulence energy by applying a negative force near the wall and in the center of the channel, slowing down the fluid in these regions, and a positive force in the intermediate region accelerating the fluid. The same scaling behavior of the adjoint velocity with decreasing λ is obtained, as pointed out in the description of Figure 7.2.

The resulting axial velocity profile is reported in Figure 7.6 on top. As expected, the control slows down the fluid near the wall and in the center of the channel. It also accelerates the fluid in the intermediate region. By doing so the gradient of the velocity becomes higher and the turbulence intensity increases. In this Figure on the bottom we can see the profile of the adjoint

λ	0.1	0.01	0.001
$\mathcal{J}(k, \mathbf{v_a})$	0.02009	0.01894	0.01870

Table 7.2: Case (b). Objective functionals computed with different λ values in the turbulence enhancement problem, plane channel.

turbulence intensity k_a, reported for three values of λ. The main source term of k_a is the difference $k - k_d$ so where k_a is higher the objective functional is far from vanishing. By looking at this profile one can see that in the center of the channel the turbulence energy is too low. By decreasing λ we obtain better overall results, except from a small region near the center of the channel where no improvement can be obtained.

In this test case advective effects are important because the coupling between velocity and adjoint turbulent kinetic energy is weak. In Figure 7.7 on top the turbulent kinetic energy k is reported on the whole domain with several iso-surface contours for the test case with $\lambda = 0.001$. The highest turbulence intensity is obtained near the outlet of the channel and near the wall where the boundary layer is enlarged by the control. On the bottom of the same Figure the adjoint turbulence energy k_a is shown. On the inlet of the channel, near the center, the control is ineffective and k_a has a strong peak. Furthermore k_a is smaller in the regions near the outlet and the wall, where turbulence energy is higher. By looking at these results it can be easily understood that convection is strong and large values of control are needed to affect upstream regions.

Finally we report in Table 7.2 the objective functional for case (b) and different λ values. It is worthwhile to note the decreasing of the functional with the decreasing of λ and in particular in the range of 0.1 to 0.01.

7.3.2   Three dimensional channel

In this section we report the results of the simulations performed on a three-dimensional geometry that represents a closed channel with two obstacles. In Figure 7.8 the three-dimensional geometry of the channel is shown with the main flow direction along the z-axis. The flow enters at the bottom at $z = 0$, throughout a unitary square surface, with $\mathbf{v} = (0, 0, 0.1)$ and a Reynolds number of about $1,000$, and impacts on two solid walls to finally exit crossing the top section located at $z = 5$. The two obstacles consist of two slices in the middle of the channel. The first one is located at $z = 1.5$ and extends along the x-axis inside the channel for 0.4 and along the z-direction for 0.1. The second obstacle is set at $z = 2.5$ and extends along the y-axis for 0.5 and along the z-axis for 0.1.
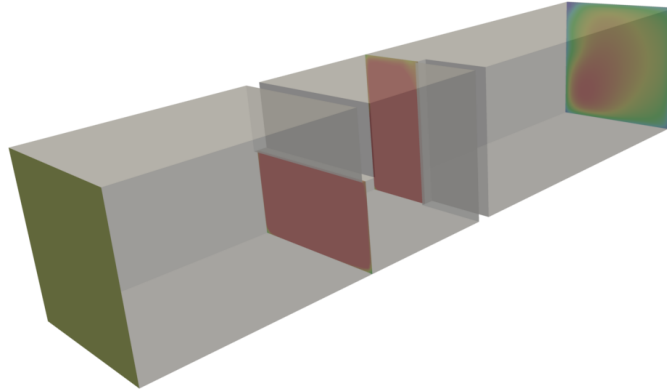
Figure 7.8: Three dimensional channel geometry. Inlet on the left, outlet on the right of the Figure. The two obstacle walls are visible where the corresponding fluid crossing sections are shown in red.
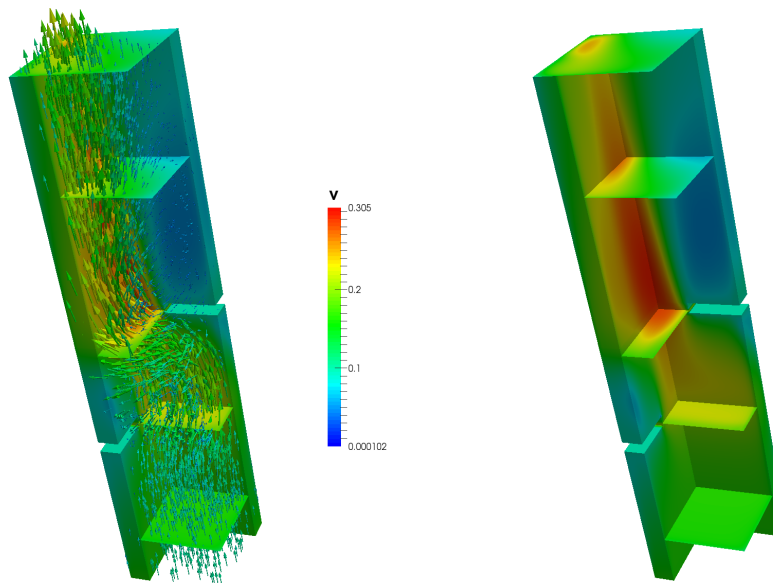
Figure 7.9: Three dimensional channel with no control. The velocity field (on the left) and the velocity magnitude (on the right) are shown on the whole domain with arrows and colored by the magnitude.

The uncontrolled flow is reported in Figures 7.9-7.10. On the left of Figure 7.9 the velocity field is depicted with arrows colored by its magnitude. Two main vortices appear after the solid walls and the main flow is compressed at the corner of the channel where no solid walls are present. On the right
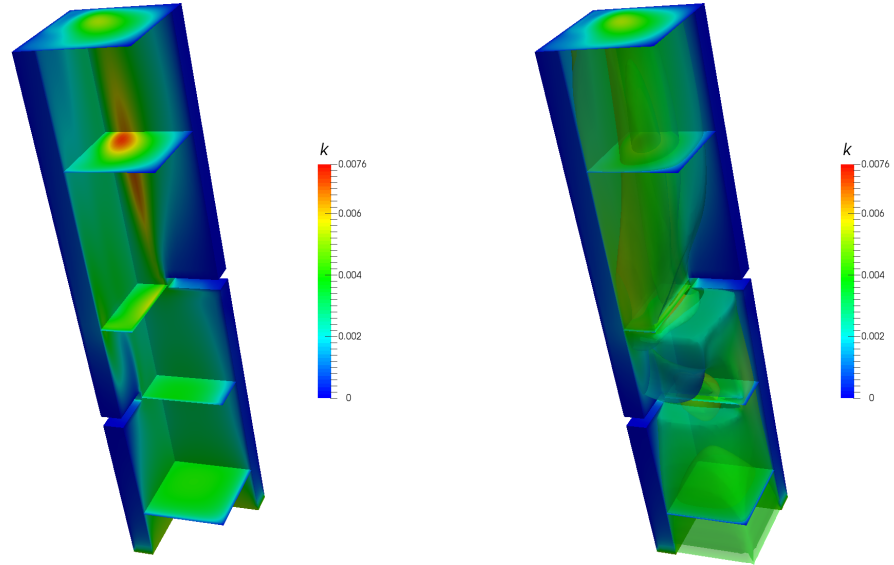
Figure 7.10: Three dimensional channel with no control. The turbulent kinetic energy k (on the left) and its iso-surface contours representing regions at similar k values (on the right) are represented with colors.

of the same Figure one can see the magnitude of the velocity field. In Figure 7.10 the turbulent kinetic energy k is shown on the left and its iso-surface contours representing regions at similar k values on the right. The second wall is a strong source of turbulence and a high amount of turbulent kinetic energy is produced in this region. The turbulence is then convected through the exit of the channel dissipating on the way. Another region where the turbulence level is high is near the inlet where a constant value of $k = 0.005$ is imposed on the inlet boundary.

In this geometry we study two control problems, a turbulence reduction and a turbulence enhancement problem. Concerning the first, we impose a desired value for the turbulent kinetic energy of $k_d = 0$ constant on the whole domain. As already explained, k_d could be chosen as a smooth function of the spatial coordinates but since in this case we are interested in a more general result we use a function constant with respect to the spatial coordinates. For the second problem we have to choose a high value for k_d, so based on the obtained values in the uncontrolled flow reported in Figure 7.9 we choose $k_d = 0.1$. The two test cases are simulated both with values of $\lambda = 0.01$ and $\lambda = 0.001$ to make a comparison.

In Figure 7.11 we report the results obtained for the turbulence reduction problem with $\lambda = 0.01$. On the left of this Figure the adjoint velocity
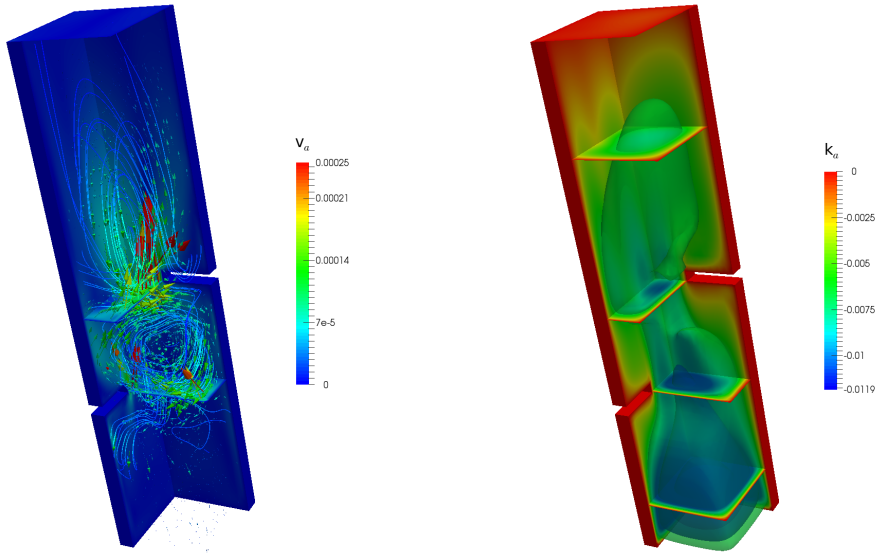
Figure 7.11: Three dimensional channel controlled for a turbulence reduction problem, $\lambda = 0.01$. On the left adjoint velocity reported with arrows colored by the adjoint velocity magnitude and with streamlines. On the right adjoint turbulent kinetic energy k_a shown with iso-surface contours representing regions at similar k_a values.

is reported and represented with arrows colored by the adjoint velocity magnitude. Moreover we report in this Figure some streamlines in the region between the walls to better show the control pattern. It can be seen that there are two main effects of the control in this region, the first is to push the flow behind the obstacle wall and the second is to slow down the flow in the region where it is faster. The adjoint turbulent kinetic energy k_a is reported on the right of the same Figure 7.11 with iso-surface contours. The adjoint k_a is negative on the whole domain and higher in modulus where the turbulence energy k is higher. Two main regions are visible, the area near the inlet of the flow and the one near the second wall.

A similar pattern for the adjoint variables is visible for the test case with $\lambda = 0.001$. In Figure 7.12 on the left the adjoint velocity is reported with arrows colored by the adjoint velocity magnitude and with some streamlines. The control pattern is similar to the one obtained for the case with $\lambda = 0.01$, the differences lie in the magnitude of the control due to the smaller λ and in a more complex and strong force in the region between the two walls. On the right of Figure 7.12 the adjoint turbulent kinetic energy k_a is reported with the same iso-surface contours to compare with Figure 7.11. It can be
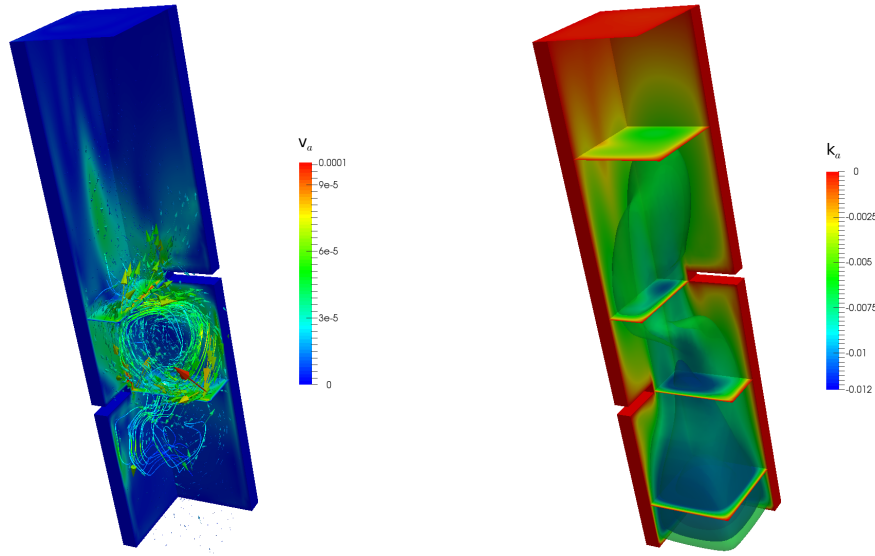
Figure 7.12: Three dimensional channel controlled for a turbulence reduction problem, $\lambda = 0.001$. On the left adjoint velocity reported with arrows colored by the adjoint velocity magnitude and with streamlines. On the right adjoint turbulent kinetic energy k_a shown with iso-surface contours representing regions at similar k_a values.

λ	∞	0.01	0.001
$\mathcal{J}(k, \mathbf{v_a}) \cdot 10^5$	2.068	1.244	1.110

Table 7.3: Objective functionals computed with no control and with different λ values in the turbulence reduction problem, three dimensional channel.

seen that a reduction in the modulus of k_a is obtained in the region near the second wall, while in the entrance region the values are nearly the same. This could be explained by considering that in a fluid flow where convective effects are important and the inlet velocity and turbulent kinetic energy are imposed, it is very difficult for the control to influence the upstream region.

Finally we can compare the results attained from the optimal control solver in the turbulence reduction problem with regard to the main variable, the turbulent kinetic energy k. In Figure 7.13 k is reported with several iso-k surface contours, on the left for the test case with $\lambda = 0.01$ and on the right for $\lambda = 0.001$. Comparing these Figures with Figure 7.9 on the right it can be seen that the objective is well attained in the region near the outflow where a strong reduction in the turbulence intensity is achieved. On the contrary, in the region near the inlet the control cannot act to decrease
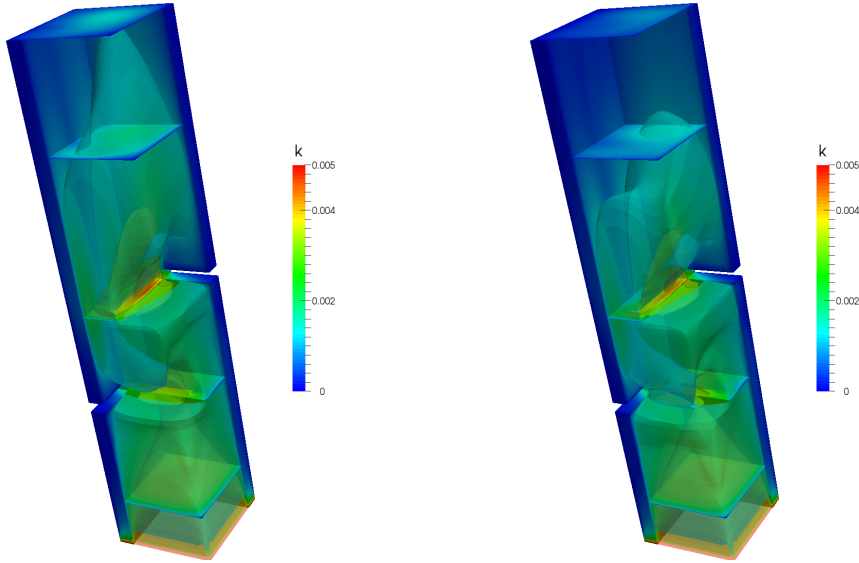
Figure 7.13: Three dimensional channel controlled for a turbulence reduction problem, on the left $\lambda = 0.01$, on the right $\lambda = 0.001$. On both sides the same iso-surface contours are reported, representing regions at similar k values.

the turbulence, because it is due to an upstream boundary condition. In Table 7.3 the objective functionals for the turbulence reduction problem as computed with no control and with $\lambda = 0.01$ and $\lambda = 0.001$ are reported. A clear decreasing of the functional is attained with the decreasing of λ, as expected.

The turbulence enhancement problem has been studied with $\lambda = 0.01$ and $\lambda = 0.001$. As already said for this test case we set $k_d = 0.1$ to set a limit to the maximum value of k. As we show in the results, the enhancing of turbulence is not limited to this value but the turbulence intensity can be increased more. However this value should be enough to prove the feasibility of our method. In Figure 7.14 the main flow patterns are visible for the test case with $\lambda = 0.001$. On the left of this Figure the velocity is reported with streamlines colored by the velocity magnitude, on the right the adjoint velocity field is reported in the same way. The control produces many vortices in order to increase turbulence in the flow and performs a suction from the outlet to increase the vorticity and the velocity gradients by applying an adverse force on the flow. The velocity flow field is complex and some helical vortices are located near the inlet and in the region before the outlet. Moreover the flow is strongly accelerated and a maximum velocity magnitude greater than 0.8 is present in some regions of the domain. This
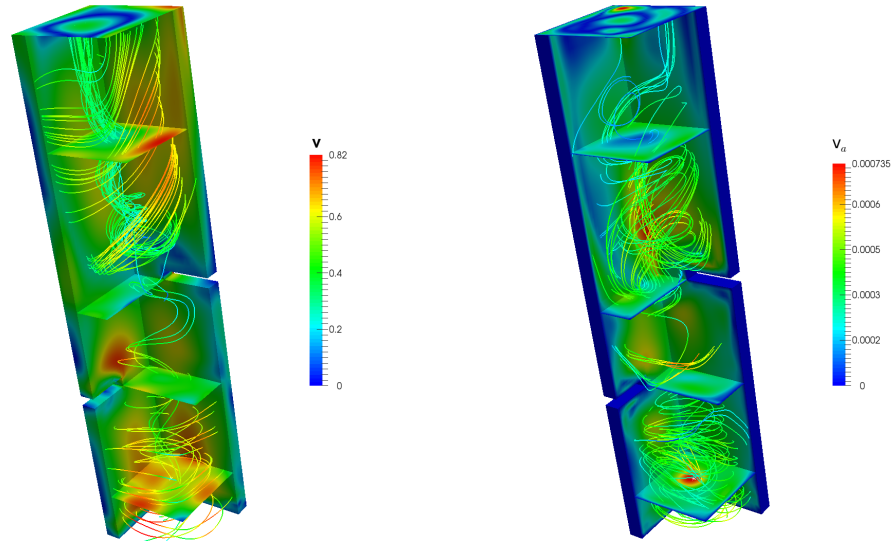
Figure 7.14: Three dimensional channel controlled for a turbulence enhancement problem, $\lambda = 0.001$. On the left velocity $\mathbf{v}$ reported with streamlines colored by the velocity magnitude. On the right adjoint velocity $\mathbf{v_a}$ reported with streamlines colored by the adjoint velocity magnitude.

λ	∞	0.01	0.001
$\mathcal{J}(k, \mathbf{v_a})$	0.023321	0.009826	0.002896

Table 7.4: Objective functionals computed with no control and with $\lambda = 0.01$ and $\lambda = 0.001$ in the turbulence enhancement problem, three dimensional channel.

value has to be compared with the maximum value of 0.3 which is reported in Figure 7.9 for the uncontrolled case. The suction performed on the outlet region does not produce a net variations of the total mass flow crossing the channel because of the incompressibility constraint, as can be demonstrated by computing the integrals of the velocity normal to the inlet and to the outlet of the channel and comparing the two values, which are both equal to 0.1.

The main result of the optimal control algorithm for the turbulence enhancement problem can be seen in Figure 7.15 where the turbulent kinetic energy is reported with several iso-surface contours. The turbulence is well spread and diffused in the whole domain and very high values of k are reached, a maximum of 0.145. These values and pattern of k have to be compared with the ones of the uncontrolled solution in Figure 7.9. Finally, in Table
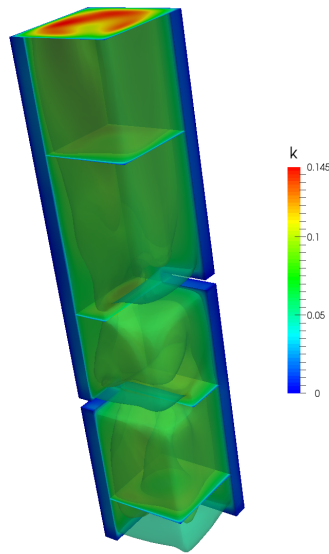
Figure 7.15: Three dimensional channel controlled for a turbulence enhance-
ment problem, $\lambda = 0.001$. Turbulence kinetic energy k reported with iso-
surface contours representing regions at similar k values.

7.4 the values of the objective functional for the turbulence enhancement
problem are reported as computed with no control and with $\lambda = 0.01$ and
$\lambda = 0.001$. The difference between the uncontrolled and controlled values is
very high and for the case $\lambda = 0.001$ reaches one order of magnitude, so the
objective can be considered very well achieved.

Conclusion

In this thesis we have presented several computational models that can be useful for the study and design of industrial devices in which liquid metals are used as working fluid and coolant. In the first Part, the closure of Reynolds Averaged Navier-Stokes equations for the turbulence modeling has been assessed by developing a new four-parameter turbulence model that takes into account dissimilarities between thermal and dynamical turbulent transport. In the second Part the adjoint optimal control theory has been used to develop algorithms based on the adjoint to solve two optimal control problems. The first is a temperature boundary optimal control and the second one a distributed optimal control for the RANS equations closed with a two-equation turbulence model. All these solvers have been implemented in a Finite Element computational platform and tested in several test cases. The numerical results reported in each Chapter show the effectiveness of these computational models in several interesting applications.

The turbulence model developed in k-ϵ or k-ω formulation has been validated in four geometries for a wide range of parameters such as Peclet numbers and pitch-to-diameter ratios for rod bundle geometries. In all these cases the model predictions in term of integral heat transfer are very close to experimental correlations widely used in literature, with the only exception of some square rod bundle simulations. The results have been also compared with DNS data and they show a very good agreement for local variables such as average temperature fluctuations and total heat flux. The improvements of the k-ω formulation are mostly numerical because this formulation allows for a more robust and stable convergence of the approximated solution. The results obtained with this formulation are comparable with the ones obtained with k-ϵ formulation. This model can be further improved in the future by assessing a logarithmic formulation of the model and could be tested in more complex geometries, like hexagonal rod bundles with grid spacers. The effect of buoyancy could be also taken into account for further improvements.

The results obtained implementing the adjoint optimal control algorithms for the temperature and turbulent flows control prove that this approach

is versatile and can be applied to complex problems. In the temperature boundary control Chapter 6 we have derived and solved an optimality system comparing three approaches to the solution of some test cases in two and three-dimensional geometries. The results have shown a fast and robust optimization process. One main result of the turbulence control Chapter 7 is the derivation of the optimality system for a two equation turbulence model together with a discussion and mathematical proof of the existence of solutions. Moreover the results have shown the power of this type of control that can achieve a strong reduction of the objective functional through a distributed force. This type of control can find applications in liquid metal flows where it is possible to actively control the fluid by means of electromagnetic forces. This study could be the ground for future applications of this approach to boundary control problems where the controlling parameters are boundary velocity profiles.

List of Figures

List of Tables

Bibliography

[1] (1997) Hdf group, hierarchical data format, version 5. Http://www.hdfgroup.org/HDF5/.

[2] (2016) École polytechnique de montréal, dragon-donjon codes. Http://www.polymtl.ca/nucleaire/en/logiciels/index.php.

[3] K. Abe, T. Kondoh, and Y. Nagano, "A new turbulence model for predicting fluid flow and heat transfer in separating and reattaching flows ii. thermal field calculations," *International Journal of Heat Mass Transfer*, vol. 38 (8), pp. 1467–1481, 1995.

[4] ——, "A two-equation heat transfer model reflecting second-moment closures for wall and free turbulent flows," *International Journal of Heat and Fluid Flow*, vol. 17, pp. 228–237, 1996.

[5] K. Abe and K. Suga, "Towards the development of a reynolds-averaged algebraic turbulent scalar-flux model," *International Journal of Heat and Fluid Flow*, vol. 22, pp. 19–29, 2001.

[6] E. O. Adamov and V. V. Orlov, "Naturally safe lead-cooled fast reactor for large-scale nuclear power," *Dollezhal RDIPE*, 2001.

[7] R. Adams, *Sobolev Spaces*. Academic Press, New York, 1975.

[8] V. Alekseev, V. Tikhomirov, and S. Fomin, *Optimal Control*. Consultants Bureau, New York, 1987.

[9] D. N. Arnold, F. Brezzi, B. Cockburn, and L. Marini, "Unified analysis of discontinuous galerkin methods for elliptic problems," *Journal on Numerical Analysis*, vol. 39 (5), pp. 1749–1779, 2002.

[10] E. Aulisa, G. Bornia, and S. Manservisi, "Boundary control problems in convective heat transfer with lifting function approach and multigrid vanka-type solvers," *Communications in Computational Physics*, vol. 18 (3), pp. 621–649, 2015.

[11] E. Aulisa, S. Manservisi, and P. Seshaiyer, "A computational multi-level approach for solving 2d navier-stokes equations over non-matching grids," *Computational Methods in Applied Mechanics and Engineering*, vol. 195, pp. 4604–4616, 2006.

[12] S. Balay, S. Abhyankar, M. F. Adams, J. Brown, P. Brune, K. Buschelman, L. Dalcin, V. Eijkhout, W. D. Gropp, D. Kaushik, M. G. Knepley, L. C. McInnes, K. Rupp, B. F. Smith, S. Zampini, and H. Zhang, "PETSc Web page," http://www.mcs.anl.gov/petsc, 2015. [Online]. Available: http://www.mcs.anl.gov/petsc

[13] ——, "PETSc users manual," Argonne National Laboratory, Tech. Rep. ANL-95/11 - Revision 3.6, 2015. [Online]. Available: http://www.mcs.anl.gov/petsc

[14] S. Balay, W. D. Gropp, L. C. McInnes, and B. F. Smith, "Efficient management of parallelism in object oriented numerical software libraries," in *Modern Software Tools in Scientific Computing*, E. Arge, A. M. Bruaset, and H. P. Langtangen, Eds. Birkhäuser Press, 1997, pp. 163–202.

[15] R. A. Bartlett, M. Heinkenschloss, D. Ridzal, and B. G. Waanders, "Domain decomposition methods for advection dominated linear-quadratic elliptic optimal control problems," *Computer Methods in Applied Mechanics and Engineering*, vol. 195, pp. 6428–6447, 2006.

[16] D. Bedivan, "Existence of a solution for complete least squares optimal shape problems," *Numerical Functional Analysis and Optimization*, vol. 18, pp. 495–505, 1997.

[17] V. Borishanski, M. Gotovski, and E. Firsova, "Heat transfer to liquid metals in longitudinally wetted bundles of rods," *Atomnaya Energiya*, vol. 6 (27), pp. 549–552, 1969.

[18] G. Bornia, M. D. Gunzburger, and S. Manservisi, "A distributed control approach for the boundary optimal control of the steady mhd equations," *Communications In Computational Physics*, vol. 14 (3), pp. 722–752, 2013.

[19] J. Bramble, *Multigrid methods.* Pitman Research Notes in Math, Longman, London, 1993, vol. 294.

[20] S. C. Brenner and L. R. Scott, *The mathematical theory of finite element methods.* Springer-Verlag, 2002.

[21] A. Carnarius, F. Thiele, E. Ozkaya, and N. R. Gauger, "Adjoint approaches for optimal flow control," *American Institute of Aeronautics and Astronautics, 5th Flow Control Conference*, 2010.

[22] O. CASCADE. (2015) Salome open source integration platform. Http://www.salome-platform.org/.

[23] CEA. (2016) Advanced safety code for pressurized water reactors. Http://www-cathare.cea.fr.

[24] D. Cerroni, S. Manservisi, and F. Menghini, "Numerical comparison of different solution methods for optimal boundary control problems in thermal fluid dynamics," *International Journal of Mechanics*, vol. 9, pp. 1–10, 2015.

[25] D. Cerroni, "Multiscale multiphysics coupling on a finite element platform," Ph.D. dissertation, University of Bologna, Italy, 2016.

[26] X. Cheng and N. Tak, "Cfd analysis of thermal-hydraulic behavior of heavy liquid metals in sub-channels," *Nuclear Engineering and Design*, vol. 236, pp. 1874–1885, 2006.

[27] ——, "Investigation on turbulent heat transfer to lead-bismuth eutectic flows in circular tubes for nuclear applications," *Nuclear Engineering and Design*, vol. 236, pp. 385–393, 2006.

[28] A. Chinchuluun, P. Pardalos, R. Enkhbat, and I. Tseveendorj, *Optimization and Optimal Control: Theory and Applications*, ser. Springer Optimization and Its Applications. Springer, 2010.

[29] B. Cockburn, G. E. Karniadakis, and C. W. Shu, *Discontinuous Galerkin Methods: Theory, Computation and Applications*, ser. Lecture Notes in Computational Science and Engineering. Springer, 2000, vol. 11.

[30] B. Deng, W. Wu, and S. Xi, "A near-wall two-equation heat transfer model for wall turbulent flow," *International Journal of Heat and Mass Transfer*, vol. 44, pp. 691–698, 2001.

[31] J. Droniou, "Non-coercive linear elliptic problems," *Potential Analysis*, vol. 17, pp. 181–203, 2002.

[32] M. Duponcheel, L. Bricteux, M. Manconi, G. Winckelmans, and Y. Bartosiewicz, "Assessment of rans and improved near-wall modeling for forced convection at low prandtl numbers based on les up to

$re_\tau = 2000$," *International Journal of Heat and Mass Transfer*, vol. 75, pp. 470–482, 2014.

[33] O. Dwyer, "Recent developments in liquid metal heat transfer," *Atomic Energy Review (Austria)*, vol. 4, pp. 3–92, 1965.

[34] C. Fazio, Ed., *Handbook on Lead-bismuth Eutectic Alloy and Lead Properties, Materials Compatibility, Thermal-hydraulics and Technologies.* OECD, 2015.

[35] J. Flesch, A. Fritsch, G. Cammi, L. Marocco, F. Fellmoser, J. Pacio, and T. Wetzel, "Construction of a test facility for demonstration of a liquid lead-bismuth-cooled 10 kw thermal receiver in a solar furnace arrangement - sommer," *Energy Procedia*, vol. 69, pp. 1259–1268, 2015.

[36] A. Friedland and C. Bonilla, "Analytical study of heat transfer rates for parallel flow of liquid metals through tube bundles, part ii," *AIChE Journal*, vol. 7 (1), pp. 107–112, 1961.

[37] E. Gabriel, G. E. Fagg, G. Bosilca, T. Angskun, J. J. Dongarra, J. M. Squyres, V. Sahay, P. Kambadur, B. Barrett, A. Lumsdaine, R. H. Castain, D. J. Daniel, R. L. Graham, and T. S. Woodall, "Open MPI: Goals, concept, and design of a next generation MPI implementation," in *Proceedings, 11th European PVM/MPI Users' Group Meeting*, Budapest, Hungary, September 2004, pp. 97–104.

[38] B. H. Gilding and R. Kersner, *Traveling Waves in Nonlinear Diffusion Convection Reaction.* Birkhäuser, Springer, New York, 2004.

[39] V. Girault and P. Raviart, *The Finite Element Method for Navier-Stokes Equations: Theory and Algorithms.* Springer, New York, 1986.

[40] V. Graber and M. Rieger, "Experimentelle untersuchung des warmeabergangs an flassigmetalle (nak) in parallel durchstraten rohrbandeln bei konstanter und exponentieller warmeflussdichteverteilung," *Atomkernenergie (ATKE)*, vol. 19, pp. 23–40, 1972.

[41] G. Grötzbach, "Challenges in low-prandtl number heat transfer simulation and modelling," *Nuclear Engineering and Design*, vol. 264, pp. 41–55, 2013.

[42] M. Gunzburger, L. Hou, and T. Svobodny, "Analysis and finite element approximations of optimal control problems for the stationary navier-stokes equations with dirichlet controls," *Mathematical Modelling and Numerical Analysis*, vol. 25, pp. 711–748, 1991.

[43] ——, *Optimal control and optimization of viscous, incompressible flow.* Cambridge University, New York, 1993.

[44] M. Gunzburger, H. Kim, and S. Manservisi, "On a shape control problem for the stationary navier-stokes equations," *Mathematical Modelling and Numerical Analysis*, vol. 34 (6), pp. 1233–1258, 2000.

[45] M. Gunzburger and S. Manservisi, "Analysis and approximation of the velocity tracking problem for navier-stokes flows with distributed control," *Journal of Numerical Analysis*, vol. 37 (5), pp. 1481–1512, 2000.

[46] ——, "The velocity tracking problem for navier-stokes flow with boundary control," *Journal on Control and Optimization*, vol. 39 (2), pp. 594–634, 2000.

[47] M. D. Gunzburger, *Perspectives in Flow Control and Optimization*, ser. Advances in Design and Control. SIAM, 2003.

[48] M. D. Gunzburger and S. Manservisi, "The velocity tracking problem for navier-stokes flow with linear feedback control," *Journal of Computer Methods in Applied Mechanics and Engineering*, vol. 189 (3), pp. 803–823, 2000.

[49] H. Hattori, A. Morita, and Y. Nagano, "Nonlinear eddy diffusivity models reflecting buoyancy effect for wall-shear flows and heat transfer," *International Journal of Heat and Fluid Flow*, vol. 27, pp. 671–683, 2006.

[50] H. Hattori, Y. Nagano, and M. Tagawa, "Analysis of turbulent heat transfer under various thermal conditions with two-equation models," *Engineering Turbulence Modeling and Experiments*, vol. 2, pp. 43–52, 1993.

[51] T. J. R. Hughes and A. Brooks, "Streamline upwind petrov-galerkin formulation for convection dominated flows with particular emphasis on the incompressible navier-stokes equations," *Computer Methods in Applied Mechanics and Engineering*, vol. 32, pp. 199–259, 1982.

[52] C. Hwang and C. Lin, "A low reynolds number two-equation k_t-ϵ_t model to predict thermal field," *International Journal of Heat and Mass Transfer*, vol. 42, pp. 3217–3230, 1999.

[53] M. Ibragimov, V. Subbotin, and P. Ushakov, "Investigation of heat transfer in the turbulent flow of liquid metals in tubes," *Atomnaya Energiya*, vol. 8 (1), pp. 54–56, 1960.

[54] M. Inagaki, H. Hattori, and Y. Nagano, "A mixed-timescale sgs model for thermal field at various prandtl numbers," *International Journal of Heat and Fluid Flow*, vol. 34, pp. 47–61, 2012.

[55] K. Ito and S. S. Ravindran, "Optimal control of thermally convected fluid flows," *Journal on Scientific Computing*, vol. 19 (6), pp. 1847–1869, 1998.

[56] H. Kawamura, H. Abe, and Y. Matsuo, "Dns of turbulent heat transfer in channel flow with respect to reynolds and prandtl number effects," *International Journal of Heat and Fluid Flow*, vol. 20, pp. 196–207, 1999.

[57] ——, "Surface heat-flux fluctuations in a turbulent channel flow up to $re_\tau = 1020$ with $pr = 0.025$ and 0.71," *International Journal of Heat and Fluid Flow*, vol. 25, pp. 404–419, 2004.

[58] H. Kawamura, K. Osaka, H. Abe, and H. Yamamoto, "Dns of turbulent heat transfer in channel flow with low to medium-high prandtl number fluids," *International Journal of Heat and Fluid Flow*, vol. 19, pp. 482–491, 1998.

[59] W. Kays, "Turbulent prandtl number - where are we," *Journal of Heat Transfer*, vol. 116, pp. 284–295, 1994.

[60] J. Kim and J. Moin, "Transport of passive scalars in turbulent channel flows," *Turbulent Shear Flows*, vol. 6, pp. 85–96, 1989.

[61] P. Kirillov, "Generalization of experimental data on heat transfer in molten metals," *Soviet Atomic Energy*, vol. 13 (5), pp. 1103–1106, 1963.

[62] P. Kirillov and P. Ushakov, "Heat transfer to liquid metals: specific features, methods of investigation, and main relationships," *Thermal Engineering*, vol. 48 (1), pp. 50–59, 2001.

[63] ——, "Liquid-metal heat transfer in rod bundles," *Thermal Engineering*, vol. 48 (2), pp. 127–133, 2001, translated from Teploenergetika.

[64] B. S. Kirk, J. W. Peterson, R. H. Stogner, and G. F. Carey, "`libMesh`: A C++ Library for Parallel Adaptive Mesh Refinement/Coarsening

Simulations," *Engineering with Computers*, vol. 22, no. 3–4, pp. 237–254, 2006.

[65] B. E. Launder, G. J. Reece, and W. Rodi, "Progress in the development of a reynolds-stress turbulence closure," *Journal of Fluid Mechanics*, vol. 37 (3), pp. 537–566, 1975.

[66] H. Lee and O. Imanuvilov, "Analysis of neumann boundary optimal control problems for the stationary boussinesq equations including solid media," *Journal on Control and Optimization*, vol. 39 (2), pp. 457–477, 2000.

[67] G. Leugering, S. Engell, A. Griewank, M. Hinze, R. Rannacher, V. Schulz, M. Ulbrich, and S. Ulbrich, *Constrained Optimization and Optimal Control for Partial Differential Equations*, ser. International Series of Numerical Mathematics. Birkhäuser Mathematics, Springer, 2012.

[68] N. Lorenzin and A. Abánades, "A review on the application of liquid metals as heat transfer fluid in concentrated solar power technologies," *International Journal of Hydrogen Energy*, 2016.

[69] R. Lyon, "Liquid metal heat transfer coefficients," *Chemical Engineering Progress*, vol. 47, pp. 75–79, 1951.

[70] ——, *Liquid-Metals Handbook*. Atomic Energy Comm., 1952.

[71] S. Lyons, T. Hanratty, and J. McLaughlin, "Direct numerical simulation of passive heat transfer in a turbulent channel flow," *International Journal of Heat and Mass Transfer*, vol. 34, pp. 1149–1161, 1991.

[72] S. Manservisi, *Some shape optimal control computations for Navier-Stokes flows*, ser. International Series of Numerical Mathematics. Birkhäuser Verlag, Basel/Switzerland, 2002, vol. 143, pp. 231–248.

[73] ——, "Numerical analysis of vanka-type solvers for steady stokes and navier-stokes flows," *Journal on Numerical Analysis*, vol. 44 (5), pp. 2025–2056, 2006.

[74] S. Manservisi and F. Menghini, "A cfd four parameter heat transfer turbulence model for engineering applications in heavy liquid metals," *International Journal of Heat and Mass Transfer*, vol. 69, pp. 312–326, 2014.

[75] ——, "Triangular rod bundle simulations of a cfd κ-ϵ-κ_θ-ϵ_θ heat transfer turbulence model for heavy liquid metals," *Nuclear Engineering and Design*, vol. 273, pp. 251–270, 2014.

[76] ——, "Cfd simulations in heavy liquid metal flows for square lattice bare rod bundle geometries with a four parameter heat transfer turbulence model," *Nuclear Engineering and Design*, vol. 295, pp. 251–260, 2015.

[77] ——, "Numerical simulations of optimal control problems for the reynolds averaged navier-stokes system closed with a two-equation turbulence model," *Computers and Fluids*, vol. 125, pp. 130–143, 2015.

[78] ——, "Optimal control problems for the navier-stokes system coupled with the k-ω turbulence model," *Computers and Mathematics with Applications*, 2016, available online 11 November 2015.

[79] S. Manservisi, "An extended domain method for optimal boundary control for navier-stokes equations," *International Journal of numerical analysis and modeling*, vol. 4 (3), pp. 584–607, 2007.

[80] M. Mareska and O. Dwyer, "Heat transfer in a mercury flow along bundles of cylindrical rods," *Journal of Heat Transfer*, vol. 2, pp. 180–186, 1964.

[81] A. C. Marta and S. Shankaran, "On the handling of turbulence equations in rans adjoint solvers," *Computers & Fluids*, vol. 74, pp. 102–113, 2013.

[82] R. Z. Mehran and B. T. Farzad, "Implicit algebraic model for predicting turbulent heat flux in film cooling flow," *International Journal for Numerical Methods in Fluids*, vol. 64, pp. 517–531, 2010.

[83] K. Mikityuk, "Heat transfer to liquid metal: Review of data and correlations for tube bundles," *Nuclear Engineering and Design*, vol. 239, pp. 680–687, 2009.

[84] B. Mohammadi and O.Pironneau, *Analysis of the k-epsilon turbulence model*, ser. Research in applied mathematics. John Wiley and Sons, New York, 1994.

[85] K. W. Morton, *Numerical Solution of Convection-Diffusion Problems*. Chapman & Hall, London, Glasgow, New York, 1996.

[86] Y. Nagano, H. Hattori, and K. Abe, "Modeling the turbulent heat and momentum transfer in flows under different thermal conditions," *Fluid Dynamics Research*, vol. 20, pp. 127–142, 1997.

[87] Y. Nagano, M. Kondoh, and M. Shimada, "Multiple time-scale turbulence model for wall and homogeneous shear flows based on direct numerical simulations," *International Journal of Heat and Fluid Flow*, vol. 18, pp. 346–359, 1997.

[88] Y. Nagano, C. Q. Pei, and H. Hattori, "A new low-reynolds-number one-equation model of turbulence," *Flow, Turbulence and Combustion*, vol. 63, pp. 135–151, 1999.

[89] Y. Nagano and M. Shimada, "Development of a two equation heat transfer model based on direct simulations of turbulent flows with different prandtl numbers," *Physics of Fluids*, vol. 8, pp. 3379–3402, 1996.

[90] B. Noack, M. Morzynski, and G. Tadmor, *Reduced-Order Modelling for Flow Control.* Springer, 2011.

[91] J. Nocedal and S. J. Wright, *Numerical Optimization*, ser. Springer Series in Operation Research and Financial Engineering. Springer, 2006.

[92] M. Ould-Rouiss, L. Redjem-Saad, G. Lauriat, and A. Mazouz, "Effect of prandtl number on the turbulent thermal field in annular pipe flow," *International Communications in Heat and Mass Transfer*, vol. 37 (8), pp. 958–963, 2010.

[93] J. Pacio, K. Litfin, A. Batta, M. Viellieber, A. Class, H. Doolaard, F. Roelofs, S. Manservisi, F. Menghini, and M. Böttcher, "Heat transfer to liquid metals in a hexagonal rod bundle with grid spacers: Experimental and simulation results," *Nuclear Engineering and Design*, vol. 290, pp. 27–39, 2015.

[94] E. Papoutsis-Kiachagiasa, A. Zymarisa, I. Kavvadiasa, D. Papadimitriou, and K. Giannakoglou, "The continuous adjoint approach to the k-ϵ turbulence model for shape optimization and optimal active control of turbulent flows," *Engineering Optimization*, vol. 47 (3), pp. 370–389, 2015.

[95] H. M. Park and W. J. Lee, "Feedback control of natural convection," *Computer Methods in Applied Mechanics and Engineering*, vol. 191 (8-10), pp. 1013–1028, 2001.

[96] M. Piller, "Direct numerical simulation of turbulent forced convection in a pipe," *International Journal for Numerical Methods in Fluids*, vol. 49, pp. 583–602, 2005.

[97] B. Rebollo and R. Lewandowski, *Mathematical and Numerical Foundations of Turbulence Models and Applications*, ser. Modeling and Simulation in Science, Engineering and Technology.   Springer, New York, 2014.

[98] L. Redjem-Saad, M. Ould-Rouiss, and G. Lauriat, "Direct numerical simulation of turbulent heat transfer in pipe flows: effect of prandtl number," *International Journal of Heat and Fluid Flow*, vol. 28 (5), pp. 847–861, 2007.

[99] F. Roelofs, A. Shams, I. Otic, M. Böttcher, M. Duponcheel, Y. Bartosiewicz, D. Lakehal, E. Baglietto, S. Lardeau, and X. Cheng, "Status and perspective of turbulence heat transfer modelling for the industrial application of liquid metal flows," *Nuclear Engineering and Design*, vol. 290, pp. 99–106, 2015.

[100] S. Saha, C. Chin, H. M. Blackburn, and A. Ooi, "The influence of pipe length on thermal statistics computed from dns of turbulent heat transfer," *International Journal of Heat and Fluid Flow*, vol. 32, pp. 1083–1097, 2011.

[101] A. Shams, F. Roelofs, E. Baglietto, S. Lardeau, and S. Kenjeres, "Assessment and calibration of an algebraic turbulent heat flux model for low-prandtl fluids," *International Journal of Heat and Mass Transfer*, vol. 79, pp. 589–601, 2014.

[102] E. Skupinski, J. Tortel, and L. Vautrey, "Determination des coefficients de convection d'un alliage sodium-potassium dans un tube circulaire," *International Journal of Heat and Mass Transfer*, vol. 8, pp. 937–951, 1965.

[103] C. A. Sleicher, A. S. Awad, and R. H. Notter, "Temperature and eddy diffusivity profiles in nak," *International Journal of Heat and Mass Transfer*, vol. 16, pp. 1565–1575, 1973.

[104] T. P. Sommer, R. M. C. So, and H. S. Zhang, "Heat transfer modeling and the assumption of zero wall temperature fluctuations," *Journal of Heat Transfer*, vol. 116, pp. 855–863, 1994.

[105] W. K. Stromquist, "Effect of wetting on heat transfer characteristics of liquid metals," *ORO-93*, 1953, university of Tennessee.

[106] A. Stück and T. Rung, "Adjoint rans with filtered shape derivatives for hydrodynamic optimisation," *Computers & Fluids*, vol. 47, pp. 22–32, 2011.

[107] V. I. Subbotin, P. A. Ushakov, P. L. Kirillov, M. H. Ibragimov, M. N. Ivanovski, E. M. Nomofilov, D. M. Ovechkin, L. N. Sorokin, and V. P. Sorokin, "Heat transfer in elements of reactors with a liquid metal coolant," *Proceedings of the 3rd International Conference on Peaceful Use of Nuclear Energy*, vol. 8, pp. 192–200, 1965.

[108] T. W. R. Taylorand, F. Palacios, K. Duraisamy, and J. J. Alonso, "A hybrid adjoint approach applied to turbulent flow simulations," *American Institute of Aeronautics and Astronautics, 21st AIAA Computational Fluid Dynamics Conference*, 2013.

[109] R. Temam, *Navier-Stokes equation.* North-Holland, Amsterdam, 1979.

[110] V. Tikhomirov, *Fundamental Principles of the Theory of Extremal Problems.* Wiley, Chichester, 1986.

[111] I. Tiselj, E. Pogrebnyak, C. Li, A. Mosyak, and G. Hetsroni, "Effect of wall boundary condition on scalar transfer in a fully developed turbulent flow," *Physics of Fluids*, vol. 13 (4), pp. 1028–1039, 2001.

[112] D. Wilcox, "Formulation of the k-omega turbulence model revisited," *AIAA Journal*, vol. 46 (11), pp. 2823–2838, 2008.

[113] Y. Yan and D. Keyes, "Smooth and robust solutions for dirichlet boundary control of fluid-solid conjugate heat transfer problems," *Journal of Computational Physics*, vol. 281, pp. 759–786, 2015.

[114] A. V. Zhukov, V. N. Leonov *et al.*, "An experimental study of heat transfer in the core of a brest-od-300 reactor with lead cooling on models," *Thermal Engineering*, vol. 49 (3), pp. 175–184, 2002, translated from Teploenergetika.

[115] O. Zienkiewicz and R. Taylor, *The Finite Element Method Volume 2: Solid Mechanics*, 5th ed. Butterworth-Heinemann Eds., 2000.

[116] ——, *The Finite Element Method Volume 3: Fluid Dynamics*, 5th ed. Butterworth-Heinemann Eds., 2000.

[117] O. Zienkiewicz, R. Taylor, and J. Zhu, *The Finite Element Method: Its Basis and Fundamentals*, 7th ed.   Butterworth-Heinemann Eds., 2013.

[118] A. S. Zymaris, D. I. Papadimitriou, K. C. Giannakoglou, and C. Othmer, "Continuous adjoint approach to the spalart-allmaras turbulence model for incompressible flows," *Computers & Fluids*, vol. 38, pp. 1528–1538, 2009.